London South Bank University

Establishing the role of surface chemistry and topography in determining wettability and the development of a novel assessment methodology for repellent surfaces

Ana Antelava

A thesis submitted in partial fulfilment of the requirements of London South Bank University for the degree of Doctor of Philosophy

This research programme was carried out in collaboration with

TWI Ltd.

July 2021

Preface

This dissertation is submitted for the degree of Doctor of Philosophy at the London South Bank University. It is based on the work carried out by the author at NSIRC, TWI Ltd between December 2017 and July 2021.

Declaration

I declare that the work reported in this dissertation is original, except where specific reference is made to the work of others. This dissertation has not been submitted in whole or in part for consideration for any other qualification. The work reported is the result of my own research under the supervision of Dr Alan Taylor (TWI Ltd.), Prof Geraldine G. Durand (London South Bank University), Dr Achilleas Constantinou (London South Bank University) and Dr Anna Wojdyla-Cieslak (TWI Ltd.). The experimental work was carried out at the National Structural Integrity Research Centre (NSIRC), TWI Ltd.

Ana Antelava

July 2021

Acknowledgments

Firstly, I would like to thank my industrial supervisor Dr Alan Taylor, whose expertise was immense in shaping my research work and knowledge on repellence. Thank you for supporting me through this challenging four years and providing mentorship and research guidance. I would like to thank my Director of Studies Prof. Geraldine Durand, who provided invaluable advice and always supported me. I am deeply thankful to my academic supervisor, Dr Achilleas Constantinou who introduced me to the world of research and motivated me in perusing a PhD programme. I am also thankful to Dr Anna Wojdyla-Cieslak from TWI Ltd for sharing insightful suggestions and giving me encouragement.

I would like to thank Lloyd's Register Foundation for providing financial sponsorship for this research project. Lloyd's Register Foundation helps to protect life and property by supporting engineering-related education, public engagement, and the application of research. Special thanks to Richard Dawson and Stuart Downie of Lloyd's Register Foundation for offering industrial mentorship.

I would like to thank LSBU and TWI teams for their support during my PhD: Aamna, Adam, Angelo, Alenka, Asish, Charlotte, Christina, Chris, Gaowei, Gillian, Golnaz, Heider, Maria, Marion, Marta, Mehrnaz, Nadia, Shenghui, Taraneh, Victoria, for your help and encouragement. Special thanks to Lewis, Steve, Jacob, and Alex for your support in the lab and teaching me how to run all the equipment.

Thanks to Dr Suela from LSBU for providing clarification and advice on the university guidelines.

These past four years were challenging, and I am very grateful to my friends who made my life happier. I will never forget the friends I made at NSIRC, TWI and Cambridge during my PhD years.

Finally, I would like to thank my family. My role model, my grandmother Emeritus Professor Nelly Antelava for inspiring me and introducing me to the science from the young age. My parents for loving me unconditionally and always supporting me. Thanks to my best friend, my sister Eka.

Abstract

Coatings and surfaces with repellence to a range of liquids can find application in aerospace, marine, construction, energy industries and many more. The reported research provides understanding of the relative roles of surface chemistry and surface roughness on repellence and has allowed the development of a new methodology for assessing wettability. A review on surface treatments and how they affect solid-liquid interaction by measuring the static and dynamic contact angle with a variety of polar and non-polar probe liquids has been presented. During this research, eleven coating systems (including fluorinated and non-fluorinated ones) were assessed for promoting repellence on planar/smooth surfaces and on substrates grit blasted to micro-level roughness (roughness average of 1 μm to 4 μm). To assess the impact of nano-scale and dual-scale roughness on repellence, the functionalised silica nanoparticles (fumed and synthesised by sol-gel) were incorporated into the coating system to build up the desired nano-scale topography (roughness average of 56 nm). This approach was undertaken in efforts to decouple the effects of surface roughness/topography on repellence from the surface chemistry contributions. The nano-scale topography provided high static contact angles, 128° and 93° with water and diiodo-methane respectively as probe liquids, this scale of roughness however, also exhibited high roll-off angles/or no roll-off even at 80° tilt. The micro-scale topography provided similar results. The combination of both nano and micro-scale topographies provided both high static contact angles (above 150°), low contact angle hysteresis and low roll-off tilts (below 10°) for water. However, this same combination of surface characteristics does not satisfy the conditions to achieve super repellence for probe liquids with lower surface tensions and different surface tension components (polar part/disperse part). The results in this study show that a high static contact angle with a probe liquid does not guarantee the abhesive behaviour. A novel assessment methodology has been proposed for the evaluation of repellence of surfaces. This approach helps to classify coatings and surface roughness characteristics according to their ability to repel various liquids not only in terms of static contact angles but also in terms of contact angle hysteresis, roll off tilt and film forming behaviour. It is proposed that droplet diameter is used as an indicator of a tendency of specific liquids to film formation. Whilst the critical parameters to achieving omniphobicity are still unclear, this work sheds light on the parameters that have to be considered and the methods to elucidate them.

List of symbols

A	True surface area
A_o	Nominal area
B	Bond number
D	Translational diffusion coefficient
F	Friction force
G	Measured fracture energy
F_E	External force
F_a	The force per unit of length acting on the advancing angle of the drop
F_k	Sticking force
F_r	The force per unit of length acting on the receding angle of the drop
G^b	The Gibbs free energy value
I_{SL}	Energy of adhesion per unit area between a liquid and a solid surface
Lc	Evaluation Length
P_d	Plate periphery
P	Capillary pressure
R	Radius of the curvature of the droplet
W	Work done
W_a	Work of adhesion
W_c	Work of cohesion
W_i	Work of wetting
a_d	Radius of curvature at the apex of the drop
k_B	Boltzmann's constant
r_f	The roughness ratio of the wet surface area
v_0	Velocity
α_c	Critical sliding angle (minimum tilt required for the droplet to move)
γ_L	Overall surface tension of the wetting liquid
γ_L^-	The base component of the surface tension of probe liquid
γ_L^+	The acid component of the surface tension of probe liquid
γ_L^D	Dispersive component of the surface tension of the wetting liquid
γ_L^P	Polar component of the surface tension of the wetting liquid
γ_{LV}	Liquid - vapour interfacial surface free energy

γ_S	Overall surface energy of the solid
γ_S^-	The base component of the surface energy of the solid
γ_S^+	The acid component of the surface energy of the solid
γ_S^D	Dispersive component of the surface energy of the solid
γ_{SL}	The interfacial tension between the solid and the liquid
γ_S^P	Polar component of the surface energy of the solid
γ_{SV}	Solid - vapour interfacial surface free energy
θ_A	Advancing contact angle
θ_R	Receding contact angle
θ_W	Apparent contact angle
θ_Y	Young's contact angle
λ_{LV}	Liquid surface tension at meniscus during the substrate dip coating
ΔW	Weight exerted on the plate
d(H)	Hydrodynamic diameter
h	Height gained by the liquid in capillary
R1	the radius of curvature at the point with coordinates (x, z).
T	Absolute temperature
η	Viscosity
λ	Wet film thickness
ρ	Density
ϕ	Other energy dissipating processes
a	Radius of the tube/capillary
b	Radius of the liquid in contact with solid
f	The fraction of solid surface wet by the liquid
g	Gravitational acceleration equal to 9.81 m/s^2
k	Capillary length
m	Mass of the droplet
r	Wenzel roughness factor
α	Tilt angle
γ_1	Surface free energy of phase 1
γ_2	Surface free energy of phase 2
θ	Contact angle between the liquid and the solid
π	Spreading pressure
ω	Width of the drop

R_{Sm}	Mean spacing
R_T	Maximum height of the profile
R_{Tm}	Average height of the profile
R_V	Maximum profile valley depth
R_Z	Ten-point average roughness
R_a	Roughness average
R_c	Average profile peak height
R_{dq} or RMS	Root mean square slope
R_{ku}	Kurtosis
R_{max}	Maximum profile peak height
R_q	Root mean square roughness
R_{sk}	Skewness

List of nomenclature

AFM	Atomic force microscopy
BA	Butyl acetate
BSE	Backscattered electrons
CA	Contact angle
CA [A]	Advanced contact angle
CA [R]	Receding contact angle
CAH	Contact angle hysteresis
CP [A]	Advanced contact point
CP [R]	Receding contact point
CPH	Contact Point Hysteresis
CVD	Chemical Vapour Deposition
D	Diameter of the droplet
DCA	Diiodo-methane contact angle
DCAH	Diiodo-methane contact angle hysteresis
DD	Diameter of diiodo-methane droplet
DLS	Dynamic light scattering
DOI	Distinctiveness of the image
DROT	Diiodo-methane roll off tilt
DSA	Drop shape analyser
FAS	(Heptadecafluoro–1,1,2,2–tetrahydrodecyl) trimethoxysilane
FAS-GPTS	3- Glicidoxypropyltrimethoxysilane
HMDZ	Hexamethyldisilazane
IPA	Isopropyl alcohol
KOH	Potassium hydroxide
Ku	Surface kurtosis
LST 30	Liquid surface tension at 30 mN/m
LST 30 CAH	LST 30 liquid contact angle hysteresis
LST 30 D	Diameter of LST 30 liquid droplet
LST 50	Liquid surface tension at 50 mN/m
LST 50 CAH	LST 50 liquid contact angle hysteresis
LST 50 D	Diameter of LST 50 liquid droplet

LST30 CA	LST 30 liquid contact angle
LST30 ROT	LST 30 liquid roll off tilt
LST50 CA	LST 50 liquid contact angle
LST50 ROT	LST 50 liquid roll off tilt
NIBS	Non-invasive backscatter detection
NVC	Non-volatile content
OFTES	3-(1,1,2,2,3,3,4,4-Octafluoropentyloxy)propyltriethoxysilane
OWRK	Owens, Wendt, Rabel and Kaelble
PD	Pendant drop
PdI	Polydispersity index
PSI	Phase shift Interference
PTFE	Polytetrafluoroethylene
ROT	Roll-off tilt
SA	Sliding angle
SAMs	Self-assembled monolayers
SE	Secondary Electrons
SEM	Scanning electron microscopy
SFE	Surface free energy
Sk	Surface skewness
SMS35	Silica nanoparticles synthesised by sol-gel method
SNPs	Silica nanoparticles
SS	Stainless steel
TEOS	Tetraethyl orthosilicate
TFTES	3-(1,1,2,2,-tetrafluoropropyloxy)propyltriethoxysilane
TGA	thermogravimetric analysis
TMS	Trimethylsilyl
VSI	Vertical Scanning Interferometry
WCA	Water contact angle
WCAH	Water contact angle hysteresis
WD	Diameter of water droplet
WLI	White light interferometry
WROT	Water roll off tilt
XPS	X-Ray Fluorescence

Table of Contents

List of Figures

List of Tables

CHAPTER 1. INTRODUCTION

1.1. Project background

This project was carried out under a PhD programme with the London South Bank University in partnership with The Welding Institute (TWI Ltd) and The National Structural Integrity Research Centre (NSIRC). The project was sponsored by Lloyd's Register Foundation (LRF).

The National Structural Integrity Research Centre (NSIRC) is a state-of-the-art postgraduate engineering facility based in Cambridge, UK, established by structural integrity specialist TWI. Its mission is to train the next generation of highly skilled engineers and scientists, who will become the future leaders of industry. The PhD programmes under NSIRC are a new model of postgraduate research driven by the needs of industry to accelerate the translation of science into industrially relevant products and services.

Lloyd's Register Foundation helps to protect life and property by supporting engineering-related education, public engagement and the application of research.

1.2. Research need

Surface contamination is an industrial problem that leads to loss of performance and increased maintenance costs. Numerous methods have been developed to prepare super-repellent coatings, but the retention of high levels of repellence in real world or operational environments has not yet been achieved. The development of surfaces that repel liquids has attracted lots of interest due to variety of possible applications in industry. The repellent / hydrophobic / oleophobic attributes of surfaces can find useful application in several industries; aerospace (Piscitelli *et al.*, 2020), marine (Genzer and Efimenko, 2006), wind energy (Dalili, Edrisy and Carriveau, 2009), solar panels (Ilse *et al.*, 2018), chemical plants, road infrastructure and many more (Esmeryan, 2020). A deeper understanding of the key chemical and topographic characteristics that dictate this behaviour would provide the enabler for the engineering of anti-contamination, anti-sticking and self-cleaning materials.

The terms hydrophobic and super-hydrophobic are most frequently used to describe repellent surfaces, although strictly speaking these terms only relate to interaction between the surface and water. As can be seen from Figure 1.1, the interest in hydrophobic as well as super-hydrophobic coatings has increased in the past 20 years and high volume of publications is

made each year. However, the area of super-repellent coatings starting to be identified specifically allowing separate identification of the publications that are differentiated by their authors. This field is still in the early stages of research and whilst the amount of published work is increased each year it is still small. Most of the research literature focuses on hydrophobicity rather than repellence to liquids with lower surface tensions due to which there is still no deep understanding of the design rules for surfaces that will be repellent not only for water but liquids with lower surface tensions too. This thesis will provide insight into those design rules.

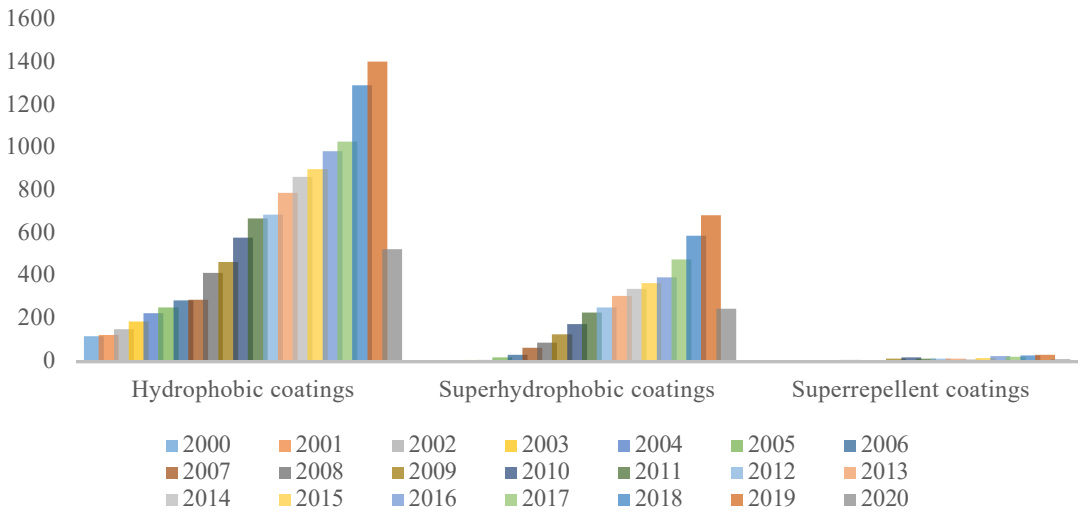

Figure 1.1. Recorded research articles corresponding to "hydrophobic coatings", "Superhydrophobic coatings" and "super repellent coatings "according to Scopus in the last 20 years (data retrieved on 02.05.20).

1.3. Aim of research

The aim of this research is to better understand the conditions that dictate super repellence, specifically to decouple the effect of surface chemistry from surface roughness and to develop a new methodology for assessing wettability.

1.4. Objectives

The specific objectives of this work were:

- To develop new assessment criteria for wettability evaluation of repellent and super repellent coatings that allows for the comparison of various surface treatments

- To evaluate, substrates with different levels of surface roughness treated with commercially available coatings and chemical functionalities to decouple the impact of surface chemistry (fluorinated and non-fluorinated) and topography, specifically:
    - minimum surface roughness
    - nano-scale topography
    - micro-scale topography
    - dual-scale topography
- To determine the best practise available for surface preparation method of glass and stainless steel that increases the adhesion strength between the substrate and the coating.
- To provide novel classification criteria of highly repellent coatings based on
    - The repellence not only for water but other probe liquids
    - Dynamic contact angle measurements as a function of tilt

1.5. Organisation of the thesis

The thesis is organised in 9 chapters.

Chapter 2 presents the background theory behind adhesion, repellence, concept of contact angles and surface free energy (SFE).

Chapter 3 presents the critical review of the associated literature providing the understanding of the state of art and identifying the knowledge gap.

Chapter 4 presents the experimental methodology and techniques used to characterise surfaces studied in this project. The assessment/characterisation methodology focused on the surface topography, surface chemistry and most importantly wettability to various liquids.

Chapter 5 presents the study on the effect of various surface chemistries on the repellence. The reported study was conducted on planar substrates with minimal surface roughness (roughness average less than 0.16μm) in order to minimise the effect of surface topography on repellence and mainly concentrate on the effect of surface chemistry achieved by treatments.

Chapter 6 reports the engineered surface topography in micro scale and its effect on wetting to a range of probe liquids, both polar and non-polar.

Chapter 7 reports the effect of nano-scale roughness on surface wettability and repellence to a variety of probe liquids.

Chapter 8 presents a new assessment approach for the repellence evaluation of coatings and surfaces. The proposed methodology helps to classify coatings and surface roughness characteristics according to their ability to repel various liquid.

Chapter 9 presents the conclusions drawn from this project and includes the suggestions for further work.

1.6. Conferences and publications

"Development of Super Repellent coatings" Oral Presentation. NSIRC 2020 Live (23rd July) 2020, Coating technologies session, online event.

"Development of repellent surfaces" Oral Presentation. 5th edition of the Smart Materials and Surfaces - SMS 2019 (23-25 October) 2019, Lisbon, Portugal.

"Development of repellent surfaces" Oral Presentation. 2nd International Conference on Nanomaterials Science and Mechanical Engineering - ICNMSME2019 (9-12 July) 2019, the University of Aveiro, Portugal.

"Development of Durable Super Repellent Coatings" Oral Presentation. National Structural Integrity Research Centre 2019 Annual Conference – NSIRC 2019 (2-3 July) 2019, Cambridge, United Kingdom.

"Development of Super Repellent Coatings" Oral Presentation at Young Scientist Lecture Competition session. Poster Presentation "Development of Super Repellent Coatings". NANOSMAT 2018 Conference (11-14 September) 2018 in Gdansk, Poland.

"Development of Durable Super Repellent Coatings" Poster Presentation. London South Bank University Postgraduate Research Summer School 2018 – (16-19 July), London, United Kingdom.

"Development of Durable Super Repellent Coatings" Poster Presentation. National Structural Integrity Research Centre 2018 Annual Conference – NSIRC 2018 (3-4 July) 2018, Cambridge, United Kingdom.

"Development of Durable Super Repellent Coatings" Poster Presentation. Lloyd's Register Foundation international conference 2018 (9-10 May) 2018, London, United Kingdom.

CHAPTER 2. BACKGROUND THEORY

2.1. Introduction

Zisman (1964) introduced the term "Abhesive", to describe materials which are applied to a solid to prevent adhesion to another solid. “Abhesion” is the converse of adhesion and is expressed as:

$$abhesion = \frac{1}{adhesion} \qquad 2.1$$

Adhesion of contaminants to the surface is an industrial problem that leads to significant loss of performance and increased operational and maintenance costs. There is no passive, durable and highly abhesive coating due to the inherent fragility of the current design approaches. Numerous methods have been developed to prepare a super-repellent coating; both top-down and bottom-up approaches to nanostructure formation have been attempted but retention of high levels of repellence has not been achieved yet. Self-cleaning coatings still suffer from numerous complications such as low mechanical stability and low durability (Wojdyla *et al.*, 2015; Dalawai *et al.*, 2020).

The abhesion of liquids and contaminants to a surface is an important property for many functional materials in the field of materials engineering, generally this property is referred to as repellence. The self-cleaning materials have the ability to repel liquids by forming spherical droplets that easily roll-off. This property is used in self-cleaning technology, as droplets can collect and remove contaminants when rolling off the surface.

Most of the studies and research focus on achieving optimum adhesion, however an understanding of abhesion or repellence fundaments is crucial for a number of industries. Understanding abhesion can assist in developing substrates with a range of properties: self-cleaning, anti-fouling, anti-icing, as well as oil-water separation, corrosion protection for various metals and drag reduction (Vazirinasab, Jafari and Momen, 2018).

The great focus that has been applied to the science and technology of adhesion has allowed considerable understanding of the underpinning mechanisms. The reciprocal nature of adhesion and abhesion implies that such an understanding can be used to assist the elucidation of the key factors that drive adhesion and perhaps even allow enhancement of

this behaviour. It seems that different mechanisms are active in different adhesive joints depending on a range of factors. There are six main theories describing the mechanisms of adhesion between surfaces (Dillard, Pocius and Chaudhury, 2002).

- **Adsorption mechanisms** involve secondary molecular forces; molecules near the interface are attracted to each other by London dispersion forces, dipole-dipole interactions, hydrogen bonding, or other secondary molecular forces.
- **The diffusion theory** of adhesion is based on the hypothesis that one material inter-diffuses into and with another.
- **Chemical reaction** theories propose that chemical reactions occur between the adhesive and the adherent forming primary chemical bonds.
- **The electrostatic force** model of adhesion assumes that the electrons within the adhesive and the adherend occupy different energy levels and electron transfer occurs across the surface. The two surfaces are attracted to each other as a result of these opposite charges.
- **The acid-base reaction theory** of adhesion has been proposed to explain a number of observed adhesive phenomena and is based on acid-base reactions at the surface.
- **Mechanical interlocking**

  Bond is achieved by transmission of force through friction along rough interfaces. Rougher surfaces, such as grit blasted metals, generally provide better interlock than smooth surfaces.

4 of the 6 mechanisms are related to surface chemistry, 2 are related to the interfacial contact area and of these two one is dictated by diffusion considerations. The approaches adopted to prevent adhesion focus on the reduction of the chemical attraction at the interface and the minimisation of the potential for chemical bonding between the adherends. In addition, the minimisation of the interfacial contact area can also be used to minimise the potential for chemical attraction. However, since chemical approaches, i.e. coatings, dominate the terminology associated with these is widely used as a generic descriptor of behaviour. Typically, coatings are described as hydrophobic (water repelling), oleophobic (oil repelling) or hygrophobic (liquid repelling). In industrial/technical terminology reference is often made to specific attributes e.g self-cleaning, anti-icing, anti-fouling, anti-microbial etc – these are sometimes referred to as the “anti-”properties.

Within this thesis the terms philic/phobic or repellent will be used as the generic term and will refer to the wettability of a solid surface by a probe liquid as determined by sessile drop assessment. This research project will provide a comprehensive review of chemical and

physical properties that influence abhesion and provide an assessment of hygrophobic treatments as well as coatings available on the market.

2.2. Abhesive surfaces in nature

Surfaces with high level of repellence exist naturally in the environment. Natural surfaces exist with varying degrees of wettability to water ranging between two extremes; super-hydrophilicity and super-hydrophobicity. Surfaces with these properties can be found in plant leaves, feathers of birds, legs/back/wings of insects and silk of spiders (Liu *et al.*, 2012).

Biological topography on the external surfaces of animals, insects, and plants are remarkably complex in terms of structure and composition to provide the necessary characteristics required for the environmental niche that is occupied. These natural structures offer insight into the design rules that underpin various behavioural characteristics. For example, the natural photonic structures in the Ophiuroidea "BrittleStar" and Morpho butterfly wings create optical effects that have inspired the design of innovative optical components that can also enhance hydrodynamic and aerodynamic performance. Sharks have microscopic grooves known as riblets that can reduce drag in turbulent flows. Another example of functional topography is needle-shaped microstructures on the legs of water striders that enable them to effortlessly move on water (Byun *et al.*, 2009).

The lotus leaf is the most well-known example of a super hydrophobic surface. Its ability to repel water is due to a combination of both surface physics and chemistry; the leaves have a micro-nanoscale hierarchical structure covered with epicuticalar wax. The wax provides hydrophobic surface chemistry while the dual-scale structure gives the rough surface topography (Quek, Magee and Low, 2017).

Possessing these properties helps with self-cleaning or collecting water droplets by integrating water vapour collection and transportation. Nature also has the ability to preserve these surface properties by self-healing. Bio-mimicking and understanding the features of these appealing interfaces has been an active research topic in the past few years (Liu *et al.*, 2012).

2.3. Concept of the work of Adhesion

Adhesion of contaminants/liquids to the surface is dependent on work of adhesion and surface energies. Even modest changes in their values can cause large changes in practical measured adhesion. For many years, their values have been deduced via contact angle

measurements. The work of adhesion is a concept of 19th century and in that period it was pointed out that the work of adhesion (W_a) was not the same as the adhesion measured in mechanical test (Packham, 1996). A measured fracture energy (G) consists of the thermodynamic term (W_a) and other energy dissipating processes (ϕ):

$$G = W_a + \phi \qquad 2.2$$

For an ideal adhesive surface, the G term can be regarded as the thermodynamic work of adhesion (W_a), which can be derived from the surface energies in the system. In fundamental terms, when there is mechanical interlocking occurring there is cohesive failure of the contacting media and the G term contains a contribution due to the work of cohesion (W_c) (Packham, 1996). G is a complex function consisting of three terms. In order to achieve good abhesion, the W_a term should be minimised, this is achieved by having a low surface free energy coating. The contribution from W_c is minimised by reducing the surface roughness, as will be discussed later.

The work of adhesion is the work that has to be done to separate two phases (1 and 2). It is defined as the free energy difference between two states that are in equilibrium with their own vapour (Packham, 1996):

$$W_a^* = \gamma_1 + \gamma_2 - \gamma_{12} \qquad 2.3$$

Where γ_1 is the surface free energy (SFE) of phase 1, γ_2 is the SFE of phase 2 and γ_{12} being their interfacial energy.

Similarly, the work of cohesion applies to a system with only one phase and it is expressed as follows:

$$W_c = 2\gamma_1 \qquad 2.4$$

Work of adhesion is also used to designate the free energy difference, between two phases 1 and 2 in contact at equilibrium and the two separate phases in the same enclosure at equilibrium with the vapour present. If the phases are liquid and solid, the work of adhesion can be expressed as (Packham, 1996):

$$W_a = \gamma_L + \gamma_S - \gamma_{SL} \qquad 2.5$$

γ_1 differs from γ_L by the spreading pressure, π, which represents the lowering of the surface energy of the material in vacuo by adsorption of the vapour (Packham, 1996). Thus;

$$W_a^* - W_a = \pi_1 + \pi_2 \qquad 2.6$$

Surface energies may be taken to be either Gibbs G or Helmholtz F free energies. In the former case the change considered in Figure 2.1 (Packham, 1996) takes place at constant pressure, in the latter at constant temperature.

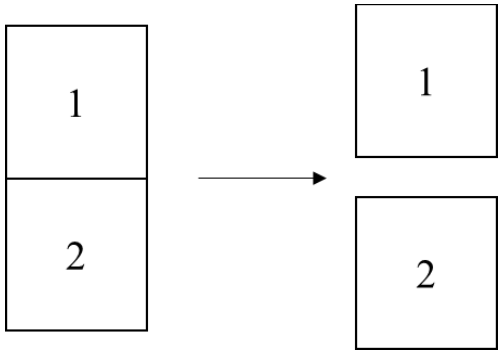

Figure 2.1 two phases 1 and 2 in contact at equilibrium and the two phases separate in the same enclosure at equilibrium (redrawn form Packham, 1996).

When taking γ as being Gibbs energy, the surface energy is defined as:

$$\text{Surface energy} = \gamma = G^s = [G - G^b]/A \qquad 2.7$$

Where A is the surface area, G is the Gibbs free energy in the system while G^b is the Gibbs free energy value if the all the constituents of the system were in the same state as they are in the bulk phase. With regard to the surface area, if the interface between the two phases is ideally flat, it is straightforward to define the interfacial area A. In practice, most of the surfaces exhibit a degree of roughness (Packham, 1996). The true area can be calculated using the Wenzel roughness factor:

$$r = \frac{A}{A_o} \qquad 2.8$$

Where A is the true area and A_o is the nominal area. This r factor can be easily substituted into the work of adhesion equation. However, for a fine roughness such calculation becomes unrealistic as we approach the molecular scale roughness.

2.4. Concept of contact angle and thermodynamic derivation

Contact angle measurements have been the principal method of calculating surface free energies. Various techniques are available for the calculations of critical surface tensions and they are based on the idea of using the equation derived by Thomas Young in 1805 (Lam *et al.*, 2002). Young's equation assumes that there is an equilibrium of the three interfacial tensions (liquid, solid and vapour):

Young's equation (2.9):

$$\gamma_{SV} = \gamma_{SL} + \gamma_{LV} \cos\theta \qquad 2.9$$

Where:

θ – Liquid contact angle

γ_{LV} – liquid - vapour SFE

γ_{SV} – solid - vapour SFE

γ_{SL} – solid - liquid interfacial free energy

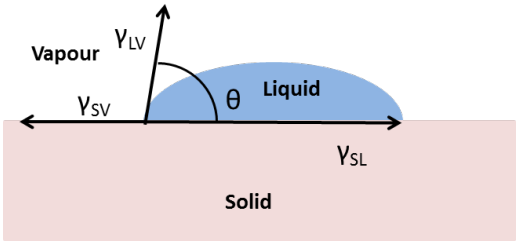

Figure 2.2 Young's equilibrium contact angle

Surface repellence to liquids is defined by Young's equilibrium (2.9) contact angle (CA), it is a specific contact angle that is formed between the solid and a liquid droplet when they come in contact (Figure 2.2) (Makkonen, 2017). It is considered that super repellent materials are characterised as those with a liquid contact angle exceeding 150 degrees (Figure 2.3) and the roll-off angle less than 10 degrees (Flink, Van Veggel and Reinhoudt, 2001). However, there are different opinions on how to classify hydro/oleo-phobic and hydro/oleo-philic surfaces. According to Young's equation a surface with a water contact angle larger than 90 degrees is hydrophobic. (Vogler, 1998) recommended repellency at 65 degrees, thus making a surface with CA above 65 degrees hydro/oleophobic (Figure 2.4). Using a surface force apparatus supported by ancillary techniques, attractive forces appear when two planes exhibit a contact angle above 65 degrees and repulsive below the 65 degrees (Li *et al.*, 2016). Liu *et al.* (2012) investigated the apparent and intrinsic contact angles of polymers and suggested an angle of 62.7 degrees to distinguish between hydrophobicity and hydrophilicity.

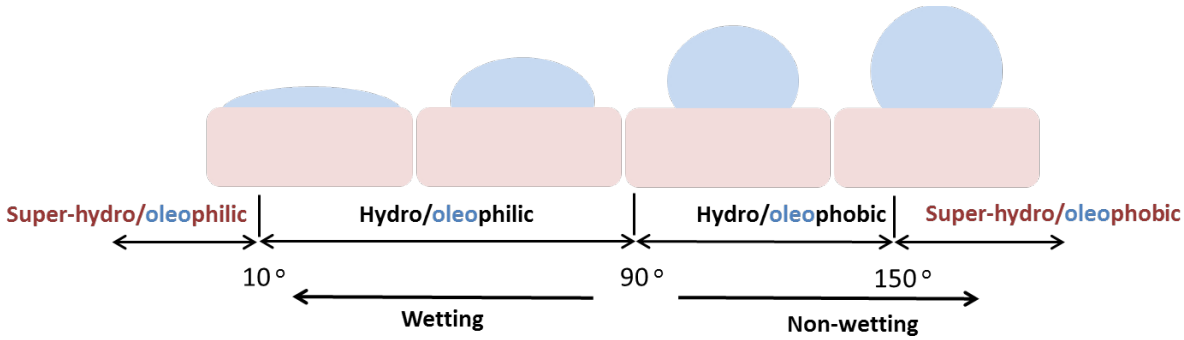

Figure 2.3 Classification of repellence according to Young's equation

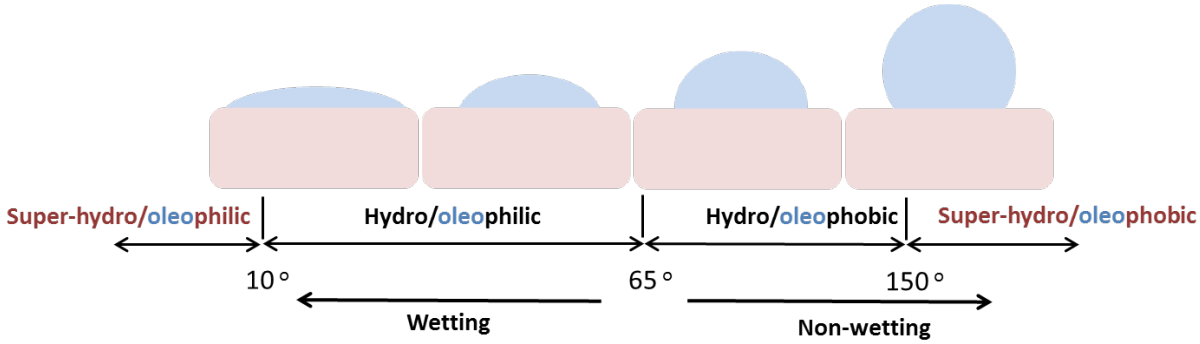

Figure 2.4 Classification of repellence according to Vogler et al. (1998)

Young's equation was originally described as a balance of three phases and their surface tensions. It was derived using the principle of minimising the total free energy of the system and thus it assumes that the interfacial surface tensions are scalar rather than tension vectors. It is assumed that these interfacial tensions can do work in order to move the contact line along the surface (Makkonen, 2016). The derivation of Young's equation assumes that the solid is chemically and physically inert and homogeneous. According to Young's equation a unique static contact angle is anticipated for a given liquid on a solid surface. However, in real life when a liquid wets a solid surface a range of contact angles is formed; the upper limit of the range being the advancing contact angle (θ_A) and the lower limit being the receding contact angle (θ_R) (Lam *et al.*, 2002). The difference between the advancing and receding contact angles is used as a measure of how well the liquid sticks to the surface and is known as contact angle hysteresis (CAH) as shown on Figure 2.5.

$$\theta_A - \theta_R = CAH \qquad 2.10$$

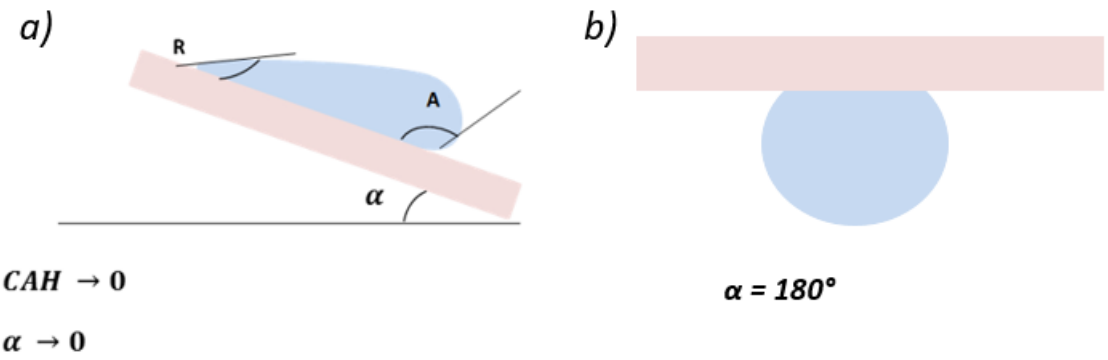

Figure 2.5 Contact angle hysteresis (CAH) on a tilted surface

The contact angle hysteresis has been studied extensively but the fundamental causes of its origin are still debatable and not completely agreed on. The origin of contact angle hysteresis has been credited to surface heterogeneity, metastable surface energetic states, molecular mobility, liquid penetration, surface swelling etc. Some studies showed the dependence of the liquid molecular size and solid/liquid contact time, which leads to liquid sorption and retention being causes of CAH (Lam *et al.*, 2002). Chibowski (2003) assumed that the hysteresis is due to the liquid film left behind the drop during retreating of its contact line.

Figure 2.5 shows two types of adhesion: a – low adhesion and b – high adhesion. In case of low adhesion, a droplet starts sliding when tilted, however there are some high adhesion cases that exhibit high static contact angle and no roll-off even at a tilt of 180°. This is known as the "petal effect" (Bhushan and Nosonovsky, 2010).

Contact angle hysteresis is an essential parameter in understanding liquid drop sliding on a tilted surface. When the surface is tilted, the drop's leading edge starts to move while the trailing edge remains pinned, the drop's shape starts to deform until a tilt angle is reached at which the drop slides down. When the drop starts sliding, the forces acting on the drop are its weight and the capillary force that results from the difference in the advancing and receding contact angles (Bouteau *et al.*, 2008). Furmidge (1962) proposed the following relationship between the weight of the drop and the difference between advancing and receding angles:

$$mg \sin \alpha_c = \omega \gamma_L (\cos \theta_r - \cos \theta_a) \qquad 2.11$$

Where m is the mass of the drop, g the gravitational acceleration, α_c the critical sliding angle (minimum tilt required for the droplet to move) and ω is width of the drop.

During sliding the drop exhibits a receding angle at the rear and a advancing at the front. This state gives a maximum value for the sticking force (Krasovitski and Marmur, 2005). The force per unit of length acting on the receding angle of the drop is:

$$F_r = \gamma_{SV} - \gamma_{SL} - \gamma_{LV} \cos\theta_r \qquad 2.12$$

The force acting on the advancing part is:

$$F_a = \gamma_{SV} + \gamma_{Lv} \cos\theta_a - \gamma_{SL} \qquad 2.13$$

Thus, the maximum sticking force can be derived as:

$$F_k = \gamma_{Lv}(\cos\theta_r - \cos\theta_a) \qquad 2.14$$

If this force is integrated along the contact line the following equation will be derived for the sticking force:

$$F_k = \pi\gamma_{Lv} R \sin\theta \, (\cos\theta_r - \cos\theta_a) \qquad 2.15$$

Where:

R – Radius of the curvature of the droplet

To make the droplets slide easily from a solid, the CAH has to be minimised and the average contact angle between the solid and the liquid has to be maximised (Quéré, 2008).

The work of adhesion can be related to the Young's contact angle by combining it with the young's equation, giving:

$$W_a = \gamma_L(1 + \cos\theta_Y) \qquad 2.16$$

It can be rewritten as

$$\frac{W_a}{\gamma_L} = 1 + \cos\theta_Y \qquad 2.17$$

And the work of adhesion can be plotted against young's contact angle. As can be seen from the graph (Figure 2.6) with increased contact angle, the work of adhesion decreases, thus it is easier to separate a liquid from a solid surface.

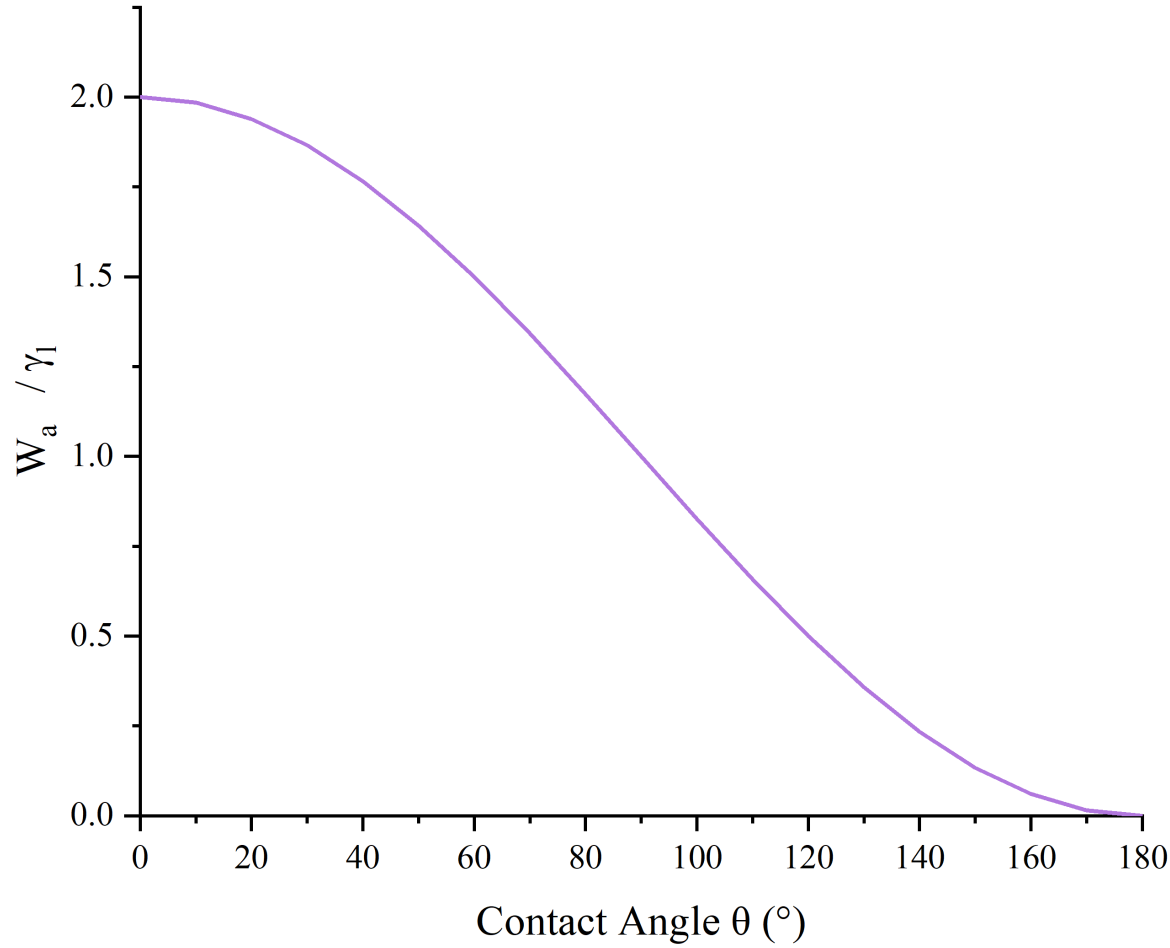

Figure 2.6 Work of adhesion as a function of contact angle

Surface tension is one of the parameters that determines the wettability of a material. Makkonen (2017) has described surface tension as a friction force in his paper. The Gibbsian surface thermodynamics state that work must be spent when creating new surface, and this work defines the thermodynamic surface energy γ ($\frac{J}{m^2}$). During the sliding of a droplet, when the substrate is tilted, the three-phase contact recedes along the surface and a new solid surface is created. Also, when the contact line advances, a new solid-liquid interface is created (Figure 2.7).

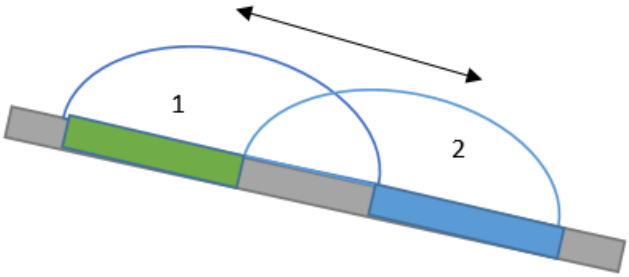

Figure 2.7. Creation of new interface while advancing and receding

It could be argued that the surface energy of the disappearing surface should be stored as the free energy on the other side of the contact line. The surface energy is a thermodynamic concept and it is a two dimensional interface. It is not related to the volume, thus when a contact line moves, the surface energy of a disappearing surface cannot be stored and thus is not transferred to the other side of the contact line. So, the surface energy of the disappearing surface should dissipate into thermal energy. Consequently, work is done when moving the contact line. This can be possible if there is a friction force F, against which the work is done. Makkonen (2017) shows in his paper that the friction force against which the work is done relates to the surface energy of the new surface interface that is created when moving the contact line:

$$\frac{F}{w} = \gamma \qquad 2.18$$

In Figure 2.7. when the contact line advances to the right and creates a new solid-liquid interface, the frictional tension is equal to the γ_{SL}. This frictional tension adds up to the existing static equilibrium tensions. In order to adjust the static force equilibrium in Young's equation to the new dynamic state, the arising frictional tension needs to be balanced by the change in the contact angle and thus (Makkonen, 2017):

$$\gamma_{SL} = \gamma_{LV}(\cos\theta - \cos\theta_a) \qquad 2.19$$

This state affects the contact angle because it is the only parameter that is free and can be altered to balance the system as other parameters such as surface tensions are constants.

When combining the Young's equation (equation 2.9) with equation 2.19, it gives us:

$$\gamma_{SV} = \gamma_{SL} + \gamma_{LV}\cos\theta_a + \gamma_{SL} \qquad 2.20$$

In a similar way, when the right side of the droplet moves to the left, more frictional tension is added due to work that has to be spent to create a new solid-vapour interface. This is balanced by the contact angle and can be represented as follows (Makkonen, 2017):

$$\gamma_{SV} = \gamma_{LV}(\cos\theta_r - \cos\theta) \qquad 2.21$$

The force equilibrium can be represented as:

$$\gamma_{SV} + \gamma_{SV} = \gamma_{SL} + \gamma_{LV}\cos\theta_r \qquad 2.22$$

The frictional parameters on the left side of equation 2.21 can be described as the work of wetting. If the contact angle does not change when the contact line is moved the work of wetting W_i equals $-\gamma_{SL}$ or $-\gamma_{SV}$ depending on the direction of movement when considering an irreversible process (Makkonen, 2017).

It is necessary to characterise the repellence of a material quantitatively, with precise determination of the static contact angle as well as the roll-off angle and the contact angle hysteresis (CAH). As the CAH plays an important role in the removal of the liquid from surface.

Several attempts were made to study contact angle hysteresis. Adam and Jessop (1925) included an external force in Young's equation. For advancing it is given as:

$$\gamma_{sv} - \gamma_{ls} = \gamma_{lv}cos\theta_a + F_E \qquad 2.23$$

And for receding:

$$\gamma_{sv} - \gamma_{ls} = \gamma_{lv}cos\theta_r - F_E \qquad 2.24$$

F_E is a friction force per unit length that acts on a triple contact line with equal intensity for advancing and receding angles.

Good and Girifalco (1960) gave a different interpretation for F_E.

$$F_a = \gamma_{lv}(cos\theta_Y - \cos\theta_a) \qquad 2.25$$

$$F_r = \gamma_{lv}(cos\theta_r - \cos\theta_Y) \quad 2.26$$

So, if friction force is the same at receding and advancing points, it can be defined as:

$$\theta_Y = \arccos\left(\frac{\cos\theta_r + \cos\theta_a}{2}\right) \quad 2.27$$

When two immiscible inert phases are brought together, they interact through physical adhesion. Under the ideal conditions, the work done for adhesion and abhesion of these surfaces would be equal. In real systems, hysteresis reflects deviation from idealised conditions. The advancing contact angle for a spreading liquid is larger than the receding angle and the difference between them is contact angle hysteresis.

Quéré (2002) derived a relationship between the CAH sticking force and the capillary force. The capillary force can be calculated by the following equation:

$$F_k = \pi b\gamma_{LV}(\cos\theta_r - \cos\theta_a) \quad 2.28$$

Where:

b- radius of the liquid contact with solid and it is related to the capillary length, k:

$$b \sim R^2 k \quad 2.29$$

Where k is:

$$\frac{1}{k} = \left(\frac{\gamma_{LV}}{\rho g}\right)^{0.5} \quad 2.30$$

According to Quéré (2002) the contact of a liquid with a solid is dependent on the size of the droplet. The drop sticks if the capillary force is larger than the weight of the particle.

Regardless of advances in the experimental methods and theoretical understanding of wettability, the contact angle hysteresis remains not completely understood and generally unpredictable for a range of liquids on surfaces. The contact angle hysteresis is mostly attributed to the physical and chemical heterogeneity of a surface.

2.5. Surface tension and surface free energy

As mentioned previously, surface energy and surface tension play a vital role in adhesion. Understanding of spreading and liquid–solid interaction is inadequate without the knowledge of solid–liquid interfacial free energy.

In the bulk phase of a liquid/solid each atom is surrounded by similar atoms and therefore there is no net force. However, atoms at the surface experience this only at one side of the interface and the difference arises from the asymmetric environment. In addition, other factors exerted by the environment act only on the outermost atoms (Giese and van Oss, 2002). Consequently, the atoms at the interface have different energy distribution and are in a higher energy state. This energy difference between the atoms in the bulk phase and at the interface is the surface tension or surface free energy (SFE).

In contrast to solids, liquids have an ability to rise or get depressed in capillary tubes. Due to the surface tension, liquids tend to contract to the smallest area possible. Laplace proved that surface tension is not an independent property and that its existence is a consequence of intermolecular forces that have a short range of action and the concentration of matter in the gas phase is smaller than in the liquid (Bikerman, 2012).

Measuring the SFE of liquids is straightforward as it is equal to its surface tension and there are various techniques for its determination. However, for solids only contact angle analysis is capable of yielding the surface or interfacial properties. Researchers have attempted to correlate solid SFE to measurable contact angles by developing empirical and semi-empirical models (Giese and van Oss, 2002).

SFE values have to be calculated from a set of liquid/solid contact angles, obtained by bringing various liquids with known surface tensions in contact with the solid. There are no universal set of liquids or methods for testing solid surfaces and when choosing probe liquids specific surface interactions, surface reactivity, and surface solubility need to be considered. There are various theories that can be applied when calculating the solid SFE. The value of the SFE depends on the theory used as well as the selected probe liquid. Review of the most commonly used models for the calculation of SFE is presented below.

2.5.1. Zisman Theory

Zisman theory is a one component model for solid SFE estimation. The method proposes the concept of ‘critical surface energy’ of a solid. It assumes the interfacial solid–liquid energy decreases to zero when the SFE of the solid and the surface tension of the liquid are

equal. It defines the SFE of the solid to be equal to the surface tension of the liquid that will completely wet the surface with a contact angle of 0° (W. A. Zisman, 1964).

The Zisman theory is best applied to non-polar surfaces. If the tested surface is even slightly polar the Zisman method becomes inadequate. This is because it attempts to characterise the SFE by taking into account just one parameter and it ignores liquid-solid surface interactions. An example of Zisman plot for characterising poly(methyl methacrylate) is shown below in Figure 2.8. The following contact angle and liquid surface tension data were obtained from Kruss TN-306.

Table 2-1 Liquid surface tension and contact angle data with poly(methyl methacrylate). Data from Kruss TN 306 (*Models for Surface Free Energy Calculation - Kruss TN 306*, 1999).

Probe liquid	Surface tension (mN/m)	Contact angle on poly(methyl methacrylate)	Dispersive component (mN/m)	Polar component (mN/m)
n-hexane	18.4	0.0	18.4	0.0
n-heptane	19.9	0.0	19.9	0.0
n-octane	21.3	0.0	21.3	0.0
n-decane	23.8	0.0	23.8	0.0
cyclohexane	25.5	0.0	25.5	0.0
n-tetradecane	26.4	0.0	26.4	0.0
toluene	28.4	0.0	26.1	2.3
nitro-methane	36.5	16.5	22.0	14.5
methyl benzoate	37.2	3.9	27.0	10.2
benzyl alcohol	39.0	15.1	30.3	8.7
ethylene glycol	47.7	46.7	26.4	21.3
formamide	57.0	64.1	22.4	34.6
glycerol	63.4	61.5	37.0	26.4
water	72.8	75.6	26.4	46.4

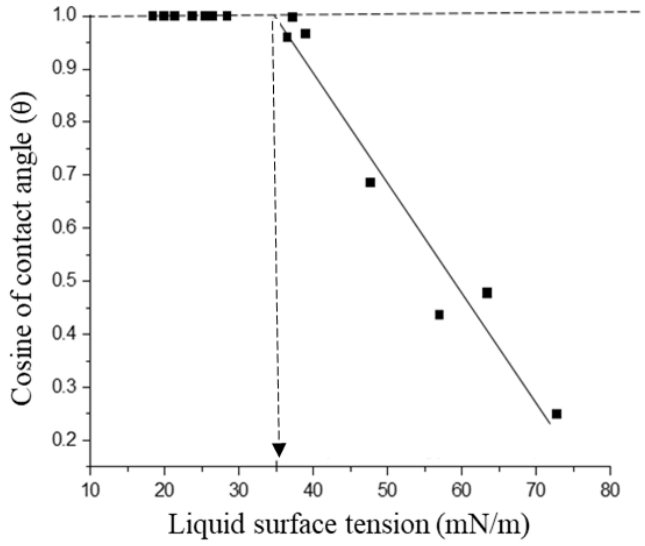

Figure 2.8 Zisman plot for poly(methyl methacrylate). Plotted using the data from Kruss TN306. (*Models for Surface Free Energy Calculation - Kruss TN 306*, 1999).

From the Zisman plot, the surface energy of poly(methyl methacrylate) is determined to be 35 mJ/m^2.

2.5.2. Owens/Wendt Theory

Owens/Wendt Theory is a two-component model. Owens and Wendt proposed SFE to consist of a polar and a dispersive component to account for polar interactions between solids and liquids. Theoretically, the dispersive component accounts for van der Waals and other non-site-specific interactions. While, the polar component takes into account hydrogen bonding, dipole-dipole, dipole-induced dipole and other interactions (Owens and Wendt, 1969).

The model is based on the following equations describing interactions between solids and liquids (*Models for Surface Free Energy Calculation - Kruss TN 306*, 1999):

Good's equation (Good and Girifalco, 1960):

$$\gamma_{SL} = \gamma_S + \gamma_L - 2(\gamma_L^D \gamma_S^D)^{\frac{1}{2}} - 2(\gamma_L^P \gamma_S^P)^{\frac{1}{2}} \qquad 2.31$$

Young's equation:

$$\gamma_S = \gamma_{SL} + \gamma_L \cos\theta \qquad 2.32$$

Where: γ_L- liquid surface tension, γ_L^D – dispersive component of the liquid surface tension, γ_L^P - polar component of the liquid surface tension, γ_S - SFE of the solid, γ_S^D - dispersive component of the solid's SFE , γ_S^P - polar component of the solid's SFE, γ_{SL} - the interfacial surface tension, and θ - the contact angle between the phases.

Owens and Wendt combined the Good's equation together with Young's equation:

$$\frac{\gamma_L\,(\cos\theta+1)}{2\,(\gamma_L^D)^{1/2}} = (\gamma_S^P)^{1/2}\,\frac{(\gamma_L^P)^{1/2}}{(\gamma_L^D)^{1/2}} + (\gamma_S^D)^{1/2} \qquad 2.33$$

Hence, if the contact angles are obtained for a range of liquids on a solid and the surface tension values are known together with their polar and dispersive parts. The data can be plotted to obtain the best fit line and using the gradient of the slope, the polar component of the SFE can be obtained using the equation above. An example of Owens/Wendt plot is shown below in Figure 2.9 with seven liquids used for the analysis from Table 2-1(*Models for Surface Free Energy Calculation - Kruss TN 306*, 1999). The results are an overall SFE for poly(methyl methacrylate) of 38.0 mJ/m^2 , with 5.7 mJ/m^2 (calculated from the slope) attributable to polar component and 32.3 mJ/m^2 to the dispersive one (calculated from the intercept with y-axis).

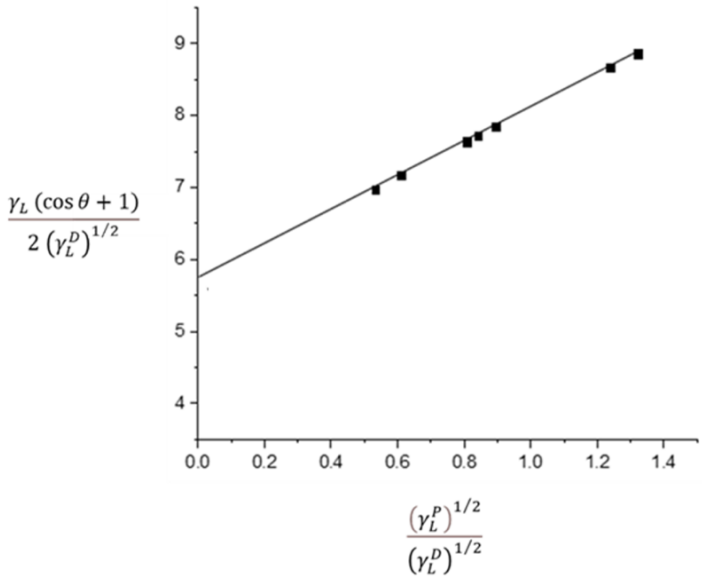

Figure 2.9 Owens/Wendt plot for poly(methyl methacrylate). Plotted using the data from Kruss TN306 (*Models for Surface Free Energy Calculation - Kruss TN 306*, 1999).

To use this theory, it is important to obtain the polar and dispersive component values of the liquid surface tension. This can be done using a standard reference surface such as PTFE. PTFE is assumed to have a SFE of 18.0 mJ/m^2 without any polar type interactions. This means that $\gamma_S = \gamma_D$ and $\gamma_P = 0$. Substituting these values into the primary Owens/Wendt equation yields the following equation (*Models for Surface Free Energy Calculation - Kruss TN 306*, 1999):

$$\gamma_L^D = \frac{\gamma_L^2(\cos\theta_{PTFE} + 1)^2}{72} \qquad 2.34$$

Where θ_{PTFE} is the probe liquid contact angle on PTFE

The dispersive surface tension component can be calculated if the overall surface tension is known. The polar component can be obtained by calculating the difference between the overall and dispersive surface tension components.

2.5.3. Fowkes Theory

Fowkes theory is also a two-component model for solid SFE. It is a widely used two component theory and as the Owens and Wendt's one needs a range of probe liquids to be assessed. Fowkes theory assumes a solid SFE to have two components; a dispersive component and a "non-dispersive" component. It is based on three equations describing the interactions between solid surfaces and liquids (Fowkes, 1964). These equations are as follows:

Young's Equation

$$\gamma_S = \gamma_{SL} + \gamma_L \cos\theta \qquad 2.35$$

Dupre's Definition of Adhesion Energy and

$$I_{SL} = \gamma_S + \gamma_L - \gamma_{SL} \qquad 2.36$$

Where I_{SL} is adhesion energy between a solid and a liquid

This adhesive energy can be separated into dispersive and non-dispersive components.

$$I_{SL} = 2[(\gamma_L^D)^{1/2}(\gamma_S^D)^{1/2} + (\gamma_L^P)^{1/2}(\gamma_S^P)^{1/2}] \qquad 2.37$$

These three equations are combined to yield:

$$(\gamma_L^D)^{1/2}(\gamma_S^D)^{1/2} + (\gamma_L^P)^{1/2}(\gamma_S^P)^{1/2} = \frac{\gamma_L(\cos\theta + 1)}{2} \quad 2.38$$

Assessing a solid with a probe liquid with only dispersive surface tension generates the following equation:

$$\gamma_S^D = \frac{\gamma_L(\cos\theta + 1)^2}{4} \quad 2.39$$

The dispersive component can be obtained from the contact angle data. The polar component of the solid SFE can be calculated by measuring the contact angle with the probe liquid containing both dispersive and non-dispersive surface tension components via Fowkes' equation. After obtaining both parts the overall value can be calculated as:

$$\gamma_S = \gamma_S^P + \gamma_S^D \quad 2.40$$

This theory can be applied to contact angle data from only two liquids. The adhesion energy foresees that the greatest adhesion will arise when a substrate with a given percentage of surface polarity is wet with the liquid that has the similar percentage of surface polarity (*Models for Surface Free Energy Calculation - Kruss TN 306*, 1999).

2.5.4. Van Oss theory

The van Oss theory is a three-component model, it separates the SFE into a dispersive, an acid and a base component. The dispersive component characterises the van der Waals interactions. The acid component characterises the tendency of the surface to interact with the liquids that have the ability to donate electron density thus act as basic and for the base component it is vice versa (Van Oss, Good and Chaudhury, 1986).

The primary equation is expressed as:

$$\gamma_L(\cos\theta + 1) = 2[(\gamma_L^D\gamma_S^D)^{1/2} + (\gamma_L^-\gamma_S^+)^{1/2} + (\gamma_L^+\gamma_S^-)^{1/2}] \quad 2.41$$

Where:

γ_L^+ is the acid component of the liquid surface tension

γ_L^- is the base component of the liquid surface tension

γ_S^+ is the acid component of the solid SFE

γ_S^- is the base component of the solid SFE

Three probe liquids must be used. The first one with only adispersive component in its surface tension. After which the following formula is used:

$$\gamma_L\,(\cos\theta + 1) = \; 2(\gamma_L^D \gamma_S^D)^{1/2} \qquad 2.42$$

Once the solid's dispersive component is obtained, the acid and base components can be calculated by contact angles with two more probe liquids in a similar way (liquids with just acid or base components) (*Models for Surface Free Energy Calculation - Kruss TN 306*, 1999).

2.6. Summary of SFE theories

Table 2-2 Summary of SFE theories. Surface type information from (*Models for Surface Free Energy Calculation - Kruss TN 306*, 1999)

Theory	Definition	Surface type
Zisman	One component model for solid SFE. Defines the solid's SFE to be equal to the surface tension of the liquid that will completely wet the surface. A range of probe liquids have to be used.	Suitable for non-polar surfaces
Owens/Wendt	Two component model that takes into account dispersive and polar interactions. A range of probe liquids have to be used.	Suitable for moderately polar surfaces
Fowkes	Two component model that takes into account a dispersive component and a non-dispersive component. Two probe liquids have to be used.	Suitable for coatings
Van Oss	Three component model that takes into account dispersive, acid and base components. Three probe liquids have to be used.	Suitable for ionic surfaces

2.7. Regimes of wetting and effect of surface roughness

As mentioned in the previous section, surfaces exhibit physical and chemical inhomogeneity. Thus, the idealised young's equation is not applicable for rough surfaces. Wenzel modified the Young's equation to account for this and introduced a roughness term. The wetting model assumes that the liquid is in complete contact with the solid (Figure 2.14 regimes of wetting) which makes it harder for the drop to roll off due to the larger interfacial contact area (Li *et al.*, 2016). The Wenzel wetting is described by the equation below:

$$\cos(\theta_W) = r\cos\theta_Y \qquad 2.43$$

Where:

θ_W – apparent contact angle

r- roughness ratio factor

θ_Y - Young's contact angle, the contact angle as defined for a perfect, smooth surface

Apparent contact angle (Wenzel contact angle) plotted as a function of the Young's contact angle is represented in Figure 2.10 where θ_w corresponds to the apparent contact angle measured on the surface while θ_Y is Young's contact angle corresponding to the intrinsic contact angle on a chemically and physically homogeneous surface. The effect of surface roughness depends on the roughness ratio introduced into equation 2.43. The roughness ratio r represents a perfectly homogeneous surface, values of 1.2 and 3 represent surfaces with increased roughness. The plot helps differentiate the regions of high wettability, repellence and super repellence. As can be seen from the plot, for θ_Y below 90° the measured θ_w is lower which means that the introduced roughness enhances wettability of the surface. For the repellent region, θ_Y above 90° the effect is opposite, repellence is enhanced and at a certain point of roughness ratio r it is possible to achieve θ_w in the region of super repellence, θ_w above 150°.

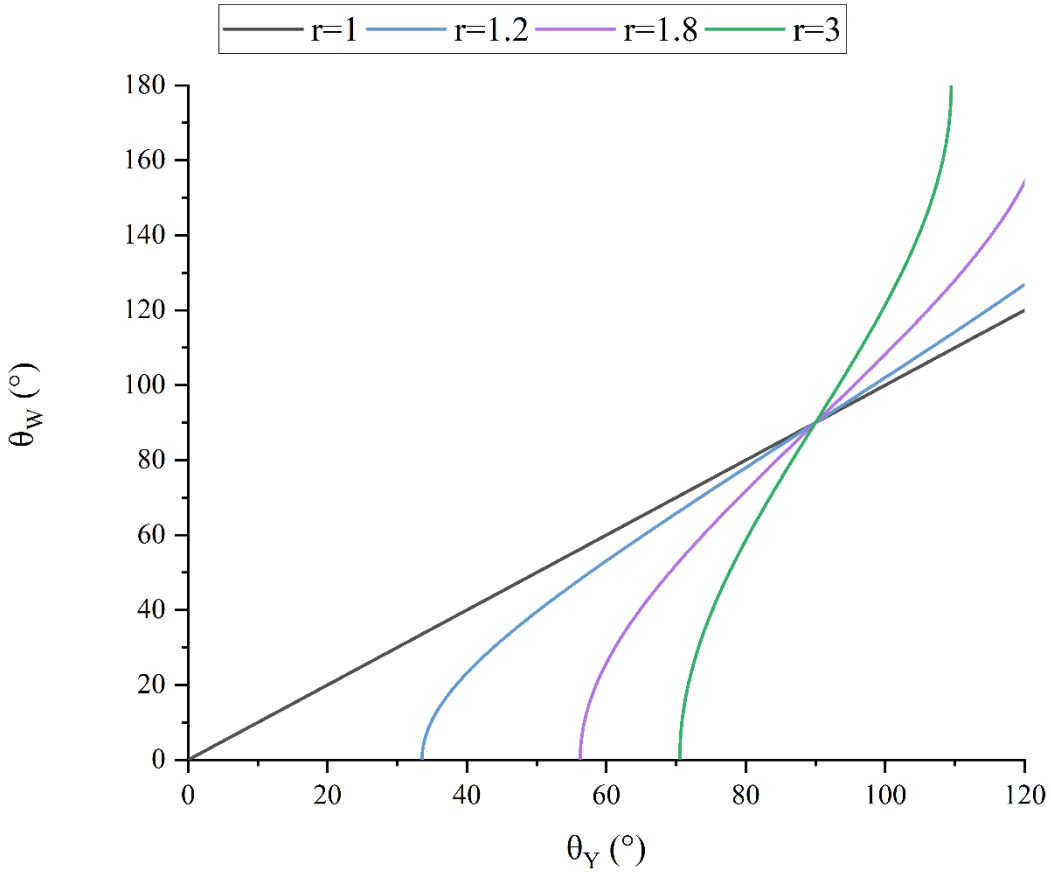

Figure 2.10 Representation of the Wenzel's apparent contact angle as a function of the Young's contact angle for the r values: 1, 1.2 and 3

Packham (1996) has studied the influence of surface roughness on adhesion. The complex interaction of surface chemistry and roughness, referring to both adsorption and mechanical interlocking theories of adhesion, are used to explain the increased adhesion resulting from micro or nano rough surfaces. It is well known that in order to achieve improved abhesion the specific surface area should be minimised. Packham discusses that liquid penetration into a capillary (roughness groove) can be derived by equating the spreading pressure of the liquid to the resisting pressure due to trapped air. At equilibrium, the distance, x, penetrated is given by:

$$x = k\left(1 - \left\{\frac{Pa}{2[2\gamma_l \cos\theta + Pa]}\right\}\right) \qquad 2.44$$

Where k is capillary length, P is the capillary pressure, a is the capillary radius, θ is the contact angle and γ_l is the surface tension of the liquid.

Another way to look at this phenomenon on the surface is to assume that roughness grooves act as capillaries. In the capillary rise of a liquid in the tube, the height (h) gained by the liquid can be determined by the equilibrium contact angle. This capillary effect is due to the fact that interfacial surface tension of solid with air is larger than that of solid with liquid. The liquid rises up to the height at which the interfacial surface tension balances the weight of the raised liquid in the capillary.

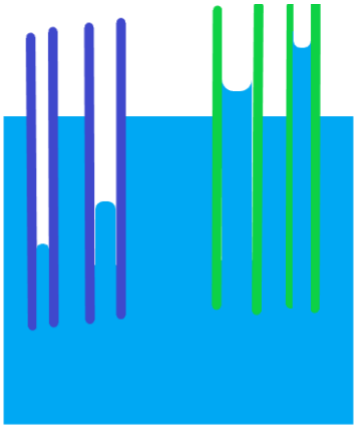

Figure 2.11 Capillary rise in hydrophilic (green) and hydrophobic (blue) tubes with different diameters

This capillary effect can be seen in Figure 2.11, green capillaries being hydrophilic (contact angle below 90°) and blue hydrophobic (contact angle above 90°). For hydrophilic capillaries immersed in water, the water is dragged up the capillary by surface tension until the weight of the water column displaced equals the drag from the surface tension. This effect is greater for capillaries (tubes) with smaller diameter. The opposite effect takes place at hydrophobic capillaries.

The height of the raised liquid can be calculated using the Jurin's height equation (Lautrup, 2011):

$$h = 2\frac{k}{a}\cos\theta \qquad 2.45$$

where:

k is capillary length

a is radius of the tube

Jurin's height equation is derived from the Young-Laplace equation for the capillary pressure:

$$P = \frac{2\gamma_{Lv}\cos\theta}{a} \qquad 2.46$$

Figure 2.12 and Figure 2.13 show the capillary rise as a function of capillary radius for water and for diiodo-methane. Diiodo-methane is liquid with lower capillary length (1.25mm) compared to water (2.71mm). As can be seen from the graph, the diiodo-methane exhibits lower capillary movement (r).

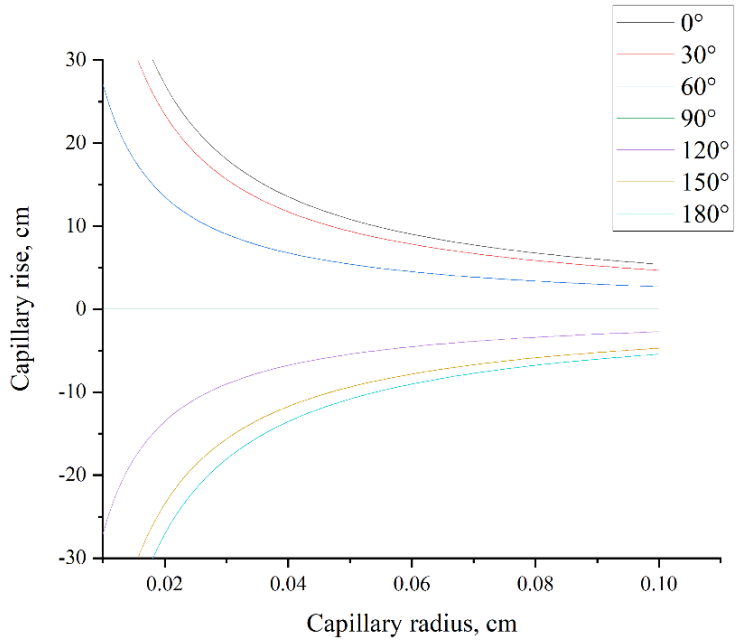

Figure 2.12 Capillary rise for water

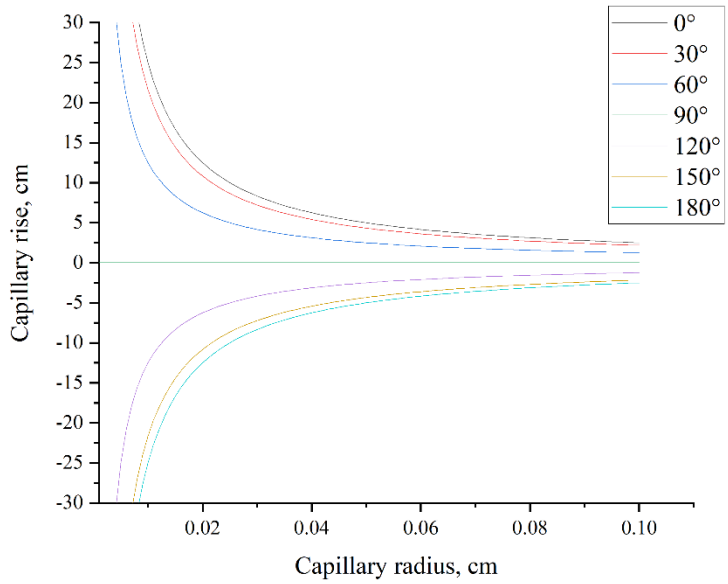

Figure 2.13 Capillary rise for Diiodo-methane

These equations will not necessarily hold in tiny capillaries. Although the capillary rise phenomenon does hold for very small diameter capillaries, it is not clear if it can be applied for nano-scale capillaries (Caupin *et al.*, 2008).

At the specific capillary radius and pressure it is more energetically favourable for the liquid not to penetrate into the roughness grooves (Lautrup, 2011) as it will minimise the interfacial contact area. Thus, a droplet exhibits local capillary action. Cassie and Baxter suggested a heterogeneous contact model where liquid does not penetrate into the roughness grooves of the material as there is an entrapped air and it just remains on top in the "Fakir state". In this wetting model the droplet sits on the composite surface, of air and solid (Li *et al.*, 2016) (Figure 2.14).

Equation for Cassie-Baxter wetting regime:

$$\cos(\theta_W) = r_f f \cos\theta + f - 1 \qquad 2.47$$

Where:

r_f- the roughness ratio of the wet surface area

f - the fraction of solid surface wet by the liquid

The Wenzel and Cassie-Baxter states can transit into each other under some conditions (Li *et al.*, 2016). When the fraction of solid surface wet by liquid, f, is equal to one and the roughness ratio, r_f, of the wet surface is equal to the roughness ratio, the Cassie-Baxter transforms into the Wenzel equation.

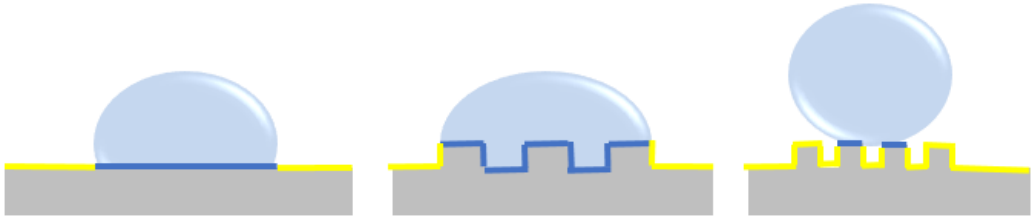

Figure 2.14 regimes of wetting; regions wetted (blue), non-wetted (yellow)

Contact angle is a simplistic method that is easily measured using optical goniometry. The proposed wetting models assume ideal conditions, also it is possible for the liquid not be at a chemical or physical equilibrium state during the contact angle measurements. The concept of metastable states was first introduced by Derjaguin. Further development of this important idea has provided a basis for the deeper understanding of contact angle hysteresis (Lam *et al.*, 2001). The contact angle varies along the three-phase contact line for a liquid drop deposited on a rough surface. Contact angles are measured macroscopically for droplets millimetres in size, due to this global contact points known as apparent contact angles are reported instead of the local ones (Jaroslaw W. Drelich, 2019). As the real surfaces are never chemically and physically homogeneous, Gibbs energy varies for each local contact angle. A droplet can exhibit one of the metastable states. Both apparent receding and advancing angles are metastable angles as they might change to different values by physical stimuli. The most stable contact angle is at the lowest Gibbs energy (Jaroslaw W. Drelich, 2019).

CHAPTER 3. LITERATURE REVIEW

3.1. Introduction

The research reported in this thesis is trying to identify the design rules for the development of super repellent coatings. Covering the topics of surface chemistry and topography to decouple their individual contributions to the level of the surface abhesion. This chapter is a critical review of the associated literature providing the understanding of the state of art and identifying the knowledge gap.

3.2. Super repellence in nature

Fabrication of super repellent coatings is an inspiration from nature. Biological topography on the external surfaces of animals, insects, and plants are remarkably advanced and practical, with abilities to perform multiple functions. These natural structures offer insights into the design of functional artificial surfaces.

Classical example of super hydrophobicity is lotus leaves, which is used to emphasise the importance of surface chemistry and surface topography. This behavior of water droplets rolling off the surface is mainly due to the combination of rough micro-nanostructure and low SFE waxy materials on their surfaces. This concept was well elaborated by Barthlott and Neinhuis (1997) and the characterisation of about 200 water repellent species was presented. They reported that the water penetrates between those trichomes lacking wax crystals due to the hydrostatic pressure of a water droplet. However, it was difficult to ascertain whether water-repellence depends on the very dense arrangement of wax crystals. It was presumed that the scale of epidermal papillae or trichomes seems to be less important as long as wax crystals are present on the surface as the main causes of water-repellence are epicuticular waxes. Conversely, surface analyses have shown the necessity of surface structures. The hydrophobic properties are extremely dependent on roughness as described by the Wenzel and Cassie–Baxter equations (Wenzel, 1936; Cassie and Baxter, 1944). The properties and functions of the materials in nature arise from the structural arrangement of simple building blocks, rather than the chemical diversity (Eder, Amini and Fratzl, 2018). In nature the superhydrophobic design forms four general groups: pillar like and dome shape, varied shape of a few micrometres in one dimension, hair or setae usually longer than 5 μm with a much smaller diameter, and hierarchical organization that is a combination of these elements (Nguyen-Tri *et al.*, 2019).

In 2011, Guo *et al.* studied natural superhydrophobic surfaces. The obtained SEM images showed that lotus leaf surface is uniformly textured with 3–10 um size protrusions and valleys with 70–100 nm nanometer-sized particles of a hydrophobic wax-like material. Surface also had a random distribution of 50nm nano-sticks. Comparable surface structure and wetting property was also observed on the rice leaf. Rice leaf exhibited the papillae with average diameter of about 5–8um arranged in one-dimensional order on the surface. Nano-scale pins that trap air were also observed on the surface. In addition to lotus leaf and rice leaf, taro leaf shows super-hydrophobicity with a hierarchical structure. Its unique micro-structure displays uniformly distributed elliptic protrusions with average diameter of 10um together with nanoscale pins resulting in a hierarchical structure.

However, surface topography does have its limitations. Herminghaus (2000) described that when Cotinus coggygria Scop leaf is submerged at a depth of 20 cm for a few seconds it loses its repellence. Similar observations were made with other leaves, such as Cercis siliquastrum L. or Ginkgo biloba L. The layer of air trapped by the papillae/surface structures often mentioned as plastron disappears under hydrostatic pressure. While plastron can remain stable when exposed to small amounts of water, at a certain point the hydrostatic pressure makes it unstable, and the wetting regime transitions from Cassie state to Wenzel state. One of the examples of the stable plastron is shown in Springtails. They usually live in a polluted environments containing decaying organic matter and their skin not only shows super hydrophobicity but also exhibits super olephobic behaviour. Its oleophobicity can prevent a range of organic liquids from wetting its skin. This behaviour also results in a plastron which remains stable even after immersion in water, organic liquids and even ethanol. The scanning electron microscope (SEM) image of Springtail's skin revealed that it has numerous bristles and rhombic meshes of interconnected nano-granules that result in a re-entrant topography (Yong *et al.*, 2017).

Another interesting surface hydrophobic and oleophobic behaviour from the nature can be observed in fish scales. Fish have an ability of swimming in oil - contaminated water without staining their scales. This ability is derived by scales having super oleohobicity in surrounding environment containing water. Fish scales are made up of hydrophilic calcium phosphate and protein, coated by mucus layer. The scale also consists of dual – scale roughness composed of rough micropapillae. This combination of surface chemistry and topography results in fish scale being super hydrophilic and super oleophilic in air having contact angles with these liquids close to zero. However, immersion in water leads to the

transition in wettability and the scales start to exhibit superoleophobicity. This is caused by water being trapped in surface structures generating super – oil repellent surface (Yong *et al.*, 2017).

As observed from nature it is imperative to assess the thermodynamic robustness of the surface and understand that the wettability can transition depending on the surrounding environment and liquids involved.

3.3. Robustness

Coating/surface "Robustness" is the ability of the surface to withstand adverse conditions or rigorous testing. This term can refer to different aspects but the main ones are chemical, mechanical and thermodynamic robustness. These areas are tested differently by resistance to mechanical abrasion or chemical attack. For the super repellent surfaces, tests are performed to determine the effect on contact angle, roll off angle and contact angle hysteresis. Some studies have focused on applying hydrostatic pressure to Cassie state of the surface to determine its stability to compression, tests, immersion tests, impact of the droplet tests.

The robustness in this thesis will be referred to the thermodynamic one rather than mechanical or chemical one. It will assess the ability of the surface to maintain Cassie state when exposed to probe liquid blends with low liquid surface tensions.

3.4. Application of repellent surfaces

The repellence to a range of liquids is one of the key surface properties of materials and it can play an important part in a range of practical or industrial applications. The artificial repellent / hydrophobic / oleophobic attributes of surfaces can find useful application in industry. The uses of superhydrophobic surfaces are not limited to anti-fouling, self-cleaning, anti-icing, drag reduction and anti-fogging applications. The oleophobic coatings / surfaces, can be used in marine anti-fouling, fluid power systems, anti-oil treatment of oil pipelines, mould – release, resistance against wax deposition in fuel oil tanks, anti-crawling materials and against bio-adhesion (Valipour M., Birjandi and Sargolzaei, 2014).

3.5. Designing repellence

Learning from nature, low SFE wax is essential for the plants, animals, insects, etc. to maintain their ability to repel water. The SFE determines the degree of surface wettability. Low energy surfaces exhibit reduced intermolecular attractive forces. Hence, spreading of

the liquid on the surface is reduced along with any physical or chemical bonds which result in low adhesion levels. Interaction of the materials takes place at the molecular level interface, due to this the properties of the surface depend on its molecular composition and orientation (Arkles, Pan and Mi Kim, 2009).

Surfaces to be rendered repellent/hydrophobic generally are polar with hydrogen bonding sites. A hydrophobic coating or surface treatment needs to eliminate hydrogen bonding sites and prevent polar surfaces/sites from interaction with water by creating a non-polar surface. The surface hydroxyl groups are the active sites for hydrogen bonding. The hydroxyl groups can be ousted by bond formation with organosilanes. Examples of materials commonly used for such purposes are the polymethylsiloxanes; the high molecular weight fatty acids, amines, amides, and alcohols; various types of highly fluorinated fatty acids and alcohols; and the fluorocarbon resins (Arkles, Pan and Mi Kim, 2009).

Zisman (1964) found that the SFE depends on the constituent groups in polymers, as follows: CH2 (36mN/m) > CH3 (30 mN/m) > CF2 (23 mN/m) > CF3 (15 mN/m). He also reported that the replacement of a single fluorine atom by a hydrogen atom in a terminal -CF 3 group doubles the critical surface energy. The fluoroalkylsilane molecule is bifunctional with a silane termination which will bond to many different types of substrates whilst a highly fluorinated chain is terminated with a CF3 group at the other end. Fluorinated groups migrate to the outer surface in the coating as it is thermodynamically more favourable to minimise the SFE. After molecular bonding with the substrate, the fluorinated chain forms self-assembled monolayers (SAMs) on substrates. Perfluorinated alkanes are known to have lower water solubilities than the corresponding hydrocarbons, while they also exhibit high level of lipophobicity. The though-provoking observation regarding the increased hydrophobicity is that the free energy of hydration per unit hydrophobic surface area is similar for both hydrocarbons and fluorocarbons. C-F bond exhibits higher dipole moment than the C-H bond and owing to that a stronger binding with dipolar water might be anticipated. The dispersion interactions of C-F are expected to be more attractive than those of C-H with water due to the polarizability of F in the C-F bond being higher than in the C-H bond. The fluorocarbon surface could be argued to be more hydrophilic. However, the fluorocarbon with a molecular cross-section of 28.3 $Å^2$ occupies more volume in water than the corresponding hydrocarbon with molecular cross-section of 18.9 $Å^2$. Therefore, the work done to form a cavity to hold a fluorocarbon offsets the expected free-energy value from greater energetic interactions with water. In terms of the hydrophobic fluorinated coatings,

this argument does not apply, and it might be predicting that such surface is more hydrophilic than a hydrocarbon surface, in contrast to experimental observations. It is also not clear whether there is an additional "polar hydrophobic" effect (Dalvi and Rossky, 2010).

3.6. Review of experimentally obtained repellent surfaces

As mentioned in chapter 2, high level of repellence is achieved by the appropriate selection and combination of surface roughness and surface chemistry of the substrate / coating. Various methods are available to fabricate such surfaces. They are generally classed into two categories: bottom-up and top-down approach. Nevertheless, the combination of both approaches can also be used in order to build up dual scale roughness. The top – down approach can be used to achieved micro – scale roughness after which the nano – scale roughness can be added via bottom – up techniques. The bottom-up approach may involve processes such as sol-gel, self-assembly, electrostatic spinning, chemical vapour deposition and so on. The Top-down method includes plasma treatment, lithography patterning, template method, etching method etc. The more detailed description of several techniques for both categories is provided below.

3.6.1. The bottom-up approach

The bottom-up approach refers to the addition of material to the surface in order to create a specific topography or roughness. It generally involves forming a complex surface by addition of materials via sol-gel method, layer by layer deposition, chemical vapour deposition and electrochemical deposition. Chemical vapour deposition is a method in which gaseous reactants are deposited on a substrate to form a non-volatile film (Subhash Latthe *et al.*, 2012). The precursor such as silane is evaporated and allowed to react with the surface to functionalise it or create a thin film. The advantage of this method is that can be used on a range of substrates, both rough and planar. However, it requires time, special equipment and is not feasible for large surfaces. The layer-by-layer approach is a solution-dipping method. It can be used to produce multi-layered films on the substrate and can be used to build up roughness (for example nanoparticle addition). Electrochemical processes such as anodizing, electrodeposition and galvanic deposition can also be used for the formation of repellent surfaces by the bottom-up approach. Electrospinning is used to produce the continuous nanofibers or filaments from polymers. Fibres with diameter ranging from nanometre to submicron scale can be extruded (Subhash Latthe *et al.*, 2012). Which are useful in achieving high levels of surface roughness to obtain repellence. The sol-gel method involves the hydrolysis reaction of metal alkoxide groups followed by the condensation

reaction. The sol-gel method is described in detail in Chapter 7, where it was used to fabricate silica nanoparticles to be used as nano-additives to build up nano-scale roughness on the substrate. The advantage of the nano-additives is that they can be incorporated into the coating (Jeevahan *et al.*, 2018).

3.6.2. The top-down approach

The top – down methods refers to the material removal / roughening process for the surface fabrication. Techniques such as lithography, laser treatment, templating, micromachining, plasma treatments, blasting, etching, etc. are considered top – down approaches for the fabrication of repellent surfaces. In the templating technique, a template is prepared after which a coating material is filled and pressed against the template so a pattern can be formed. The technique is used to produce polymeric repellent materials. Photolithography technique provides a better control over the surface structuring and is generally used to create micro and nano patterns. It is used to produce complex topographies such as circular or square pillars with a range of diameters and spacings. The method involves irradiating a light (or X-ray, electron beam, etc. can also be used) through a mask onto a photoactive polymer after which exposed or unexposed polymer is removed to produce a copy of the patterned mask. Another top – down method frequently used is etching in which a chemical reaction is used to erode a material to produce a roughened surface. Etching method could involve chemical etching, laser etching and plasma etching (Jeevahan *et al.*, 2018). Another method that can be used is grit blasting and it is described in detail in Chapter 6.

3.6.3. Limitation of the fabrication methodologies

The artificial fabrication of bio-mimetic super repellent structures can be performed but due to its complexity its application in industry is limited and not feasible. Most of the described methods require strict conditions, complex processes involving expensive materials, meaning that it is complicated to scale them up for practical application. Therefore, developing other facile methods for fabrication of super abhesive surfaces is required. Learning from nature and understanding the specific combination of surface chemistry together with surface roughness that creates a repellent surface will enable creation of super-repellent surfaces for various liquids. Table 3-1 reviews experimentally obtained repellent surfaces on glass and stainless steel by various researchers. The focus is on glass and stainless steel as those are the substrates studied in the PhD project. The table highlights which physical and chemical treatments were used and what was the result of those

treatments in terms of water contact angle, as it is the most reported definition of repellence level.

Table 3-1 Review of experimentally obtained repellent surfaces

Substrate	**Chemical treatment**	**Physical treatment**	**Water contact angle (º)**	**Sliding angle (º)**	**Reference**
Glass	Hexadecyltriethoxysilane	No treatment	100		(Dopierala *et al.*, 2013)
Glass	OFTES	No treatment	80		
Glass	TFTES	No treatment	90		
Glass	10% solution of octafluorosilane dissolved in 1:2 water–methanol mixture	Mix of silica sol with Aerosil 300 with 7 nm	163		
Glass	10% solution of octafluorosilane dissolved in 1:2 water–methanol mixture	Mix of silica sol and Aerosil 130 with the particle diameter 16 nm	150		
Stainless steel		n/a - R_a 2.2 (±0.6) nm	47		(Kaynak *et al.*, 2017)
Stainless steel	dipodal silanes F-8 and F-12		>110		
Mild steel panels	pristine silicone resin	No treatment	93	60	

Mild steel panels		Silicone resin incorporated with metal silicates (nanosilica, nanotitania and aluminium stearate)	157	28	(Anitha, S. and Mayavan, 2018)
Austenitic stainless steel (type AISI 304)	Fluorination with trichloro (1H,1H,2H,2H-perfluorooctyl) silane	Etching with Hydrofluoric acid	166	5	(Kim *et al.*, 2018)
Austenitic stainless steel (type AISI 304)	Fluorination with trichloro (1H,1H,2H,2H-perfluorooctyl) silane	Etching with Hydrofluoric acid followed with etching with NaCl	168	2	
Glass	1H,2H,2H-perfluorotetradecyltriethoxysilane	N/A	110		(Marczak *et al.*, 2016)
Glass	PTFE thin films deposited by pulsed laser deposition time 30 min	RMS 10 nm	96		(Alawajji, Kannarpady and Biris, 2018)

Glass	PTFE thin films deposited by pulsed laser deposition time 60 min	RMS 36.4 nm	151		
Stainless steel 304	Immersed into stearic acid solution (0.05 mol/L) for 1 h at room temperature.	fSiO2-assisted Hydrofluoric acid etching	162		(Zhang *et al.*, 2020)
The stainless-steel wire mesh substrates (#300)	FAS-GPTS modification	polyurethane–SiO2 nanoparticle coating and wire mesh substrate	a water / oil contact angles of 159 / 140°	3 / 10	(Yousefi *et al.*, 2018)
Low carbon steel Q panels	The fluoroalkyl silane used was F8815, provided by Dynasylan	Polyurethane base surface treated with optimised oxygen/ argon plasma	153		(West *et al.*, 2016)
Glass substrates and aluminum coupons	Polydimethylsiloxane–silica nanocomposite double layer coating with fluoroalkyl silane as topcoat.		158 – 160		(Basu, Dinesh Kumar and Anandan, 2012)

The 304 stainless steel discs	3-(1,1,2,2,3,3,4,4-Octafluoropentyloxy)propyltriethoxysilane and methanol at a 5:95 vol ratio	KOH solution	108 and 103		(Szubert *et al.*, 2018)
The 304 stainless steel discs	No treatment	No treatment	90		
K9 glass or silicon substrates	HMDS	Hollow silica nanoparticles	156		(Tao *et al.*, 2016)
Glass	Epoxy coating		73		(Lei *et al.*, 2018)
Glass	Epoxy coating + heptadecafluorodecyl triethoxysilane treatment		113		

3.7. Summary and knowledge gap

Understanding the specific combination of surface chemistry together with surface roughness that creates a repellent surface will enable creation of super-repellent surfaces for various liquids. Table 3-1 reviews experimentally obtained repellent surfaces on glass and stainless steel by various researchers. Most of the papers studying repellent substrates focus on hydrophobicity and use high water contact angle as the main definition of repellence. Thus, it is hard to assess the performance of the given treatments with non-polar probe liquids and liquids with lower surface tensions.

The highest water contact angle achieved on the planar glass surface from the reviewed literature is 110º (Table 3-1). Which is obtained by treating the surface with perfluorotetradecyltriethoxysilane. Water contact angle higher than 110 º is achievable by roughening the substrate or by applying a nanocomposite coating. With incorporated surface roughness the water contact angles reported are higher than 150º. Which demonstrate the importance of surface topography on the enhancement of repellence. From the literature review, most research is concentrated on super hydrophobicity and static contact angle measurements with water. However, to obtain super repellence liquid-surface interaction has to be studied for a variety of liquids; polar, non-polar and low surface tension liquids. As discussed in Chapter 2, high static contact angles do not mean that there will be no pinning on the liquid on the surface (petal effect) or that roll-off angle and contact angle hysteresis will be low.

This thesis will review the following aspects to address the identified knowledge gap:

- Decouple effect of surface chemistry and surface topography on repellence
    - Smooth substrates
    - Micro-scale
    - Nano-scale
    - Dual-scale
- Study the effect of fluorinated and non-fluorinated treatments on repellence
- Develop a new assessment criteria for wettability evaluation of repellent surfaces
    - Assess wettability as a function of surface tilt
    - Evaluate repellence with variety of probe liquids

CHAPTER 4. EVALUATION METHODOLOGY

4.1. Overview

In this chapter, techniques used to characterise obtained surfaces are described. Surfaces with planar (chapter 5), engineered (chapter 6) and nano-scale roughness (chapter 7) were prepared and treated with fluorinated and non-fluorinated treatments to promote repellence. The assessment/characterisation methodology focused on the surface topography, surface chemistry and most importantly wettability to various liquids. An illustrative description of used methodology is presented in Figure 4.1.

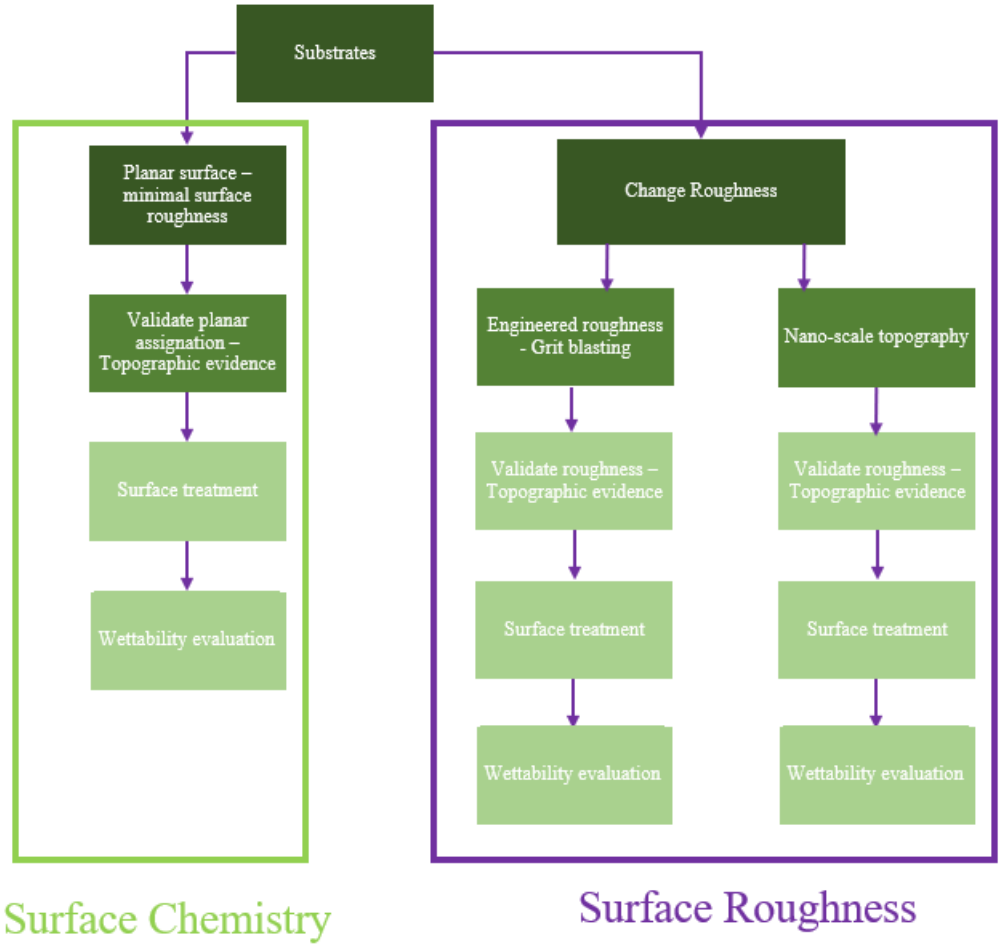

Figure 4.1 Evaluation methodology

4.2. Substrates used and surface preparation

For the evaluation of the planar surfaces glass substrates and stainless steel coupons with 2B and mirror finish were used. Glass was selected as a substrate because it exhibits minimal surface roughness, and its topographic characteristics should not have an effect on repellence. Stainless steel 304 with the mirror finish was obtained from Just Stainless, Resurgem Ltd. Stainless steel 304 (SS304) coupons with 2B surface finish were obtained from Q-lab corporation. The data from the manufacturer suggests that the chemical composition of SS 304 steel panels is 0.60% max manganese, 0.15% max carbon, 0.030% max phosphorus, 0.035% max sulphur. The roughness of the selected substrates was evaluated by a range of profilometers and microscopes to validate their planar assignation.

4.2.1. Grit blasting

For the engineered roughness grit blasting was chosen to generate substrates with different levels of roughness. It was intended that the process would minimise variability that might arise from surface treatments such as chemical etching and provide reproducible method. The grit blasting process used different sizes of alumina abrasive media particles. The grit sizes used were 240, 220, 100, 60 and 36 that were blasted at different pressures of 40,40, 40, 50 and 70 psi respectively. The blasting was performed as a single pass to avoid over blasting the samples. SS304 coupons with 2B finish were used as a basis for grit blasting treatment. Figure 4.2 shows the simplified schematic of grit blasting process; the abrasive particles of a specific size are blasted onto the substrate under specific pressure (Figure 4.3) to increase the roughness.

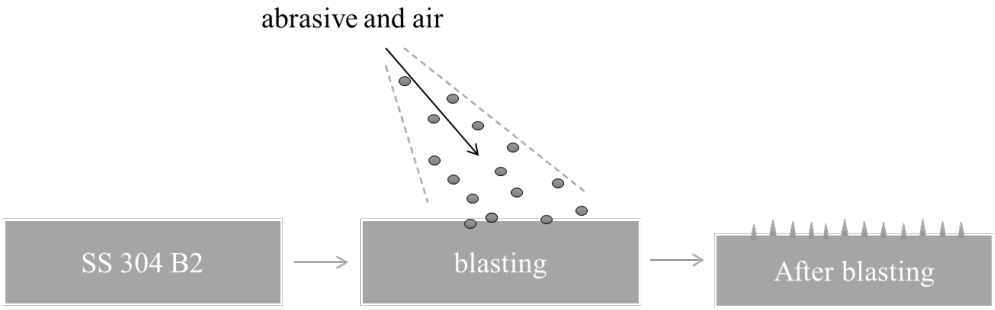

Figure 4.2 Grit blasting process

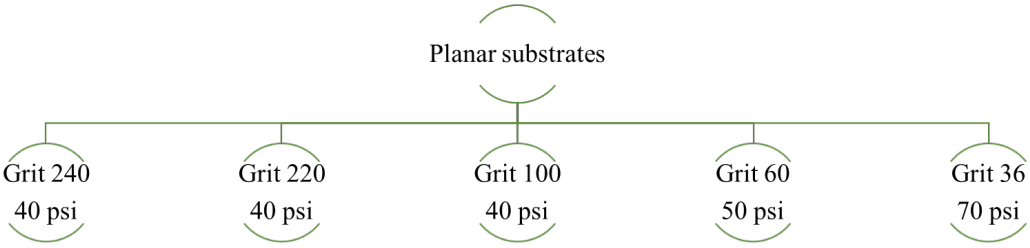

Figure 4.3 Sizes of grit used and blasting pressures

The substrates obtained exhibited different levels of topographic characteristics and glossiness as can be seen in Figure *4.4*.

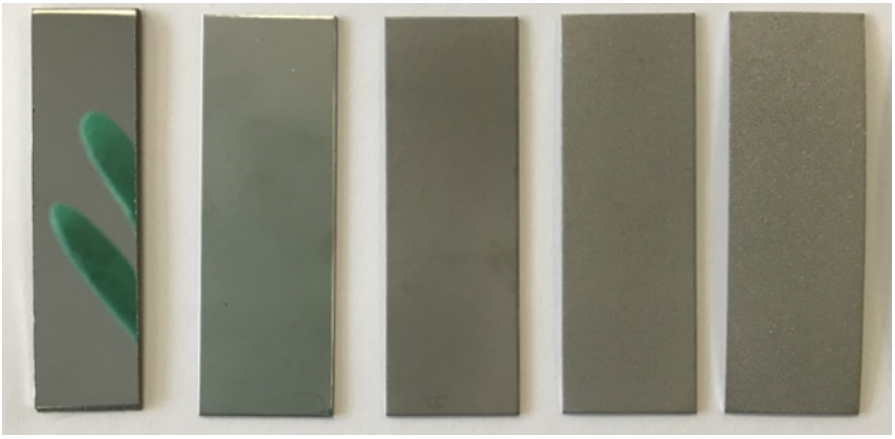

Figure 4.4 *Stainless steel substrates; Mirror finish, 2B Finish, Grit 100, Grit 60 and Grit 36*

4.3. Methodologies for topographic evaluation

Measurement of surface roughness and determination of statistical roughness parameters is a significant topic in surface science and engineering. There are various techniques and equipment available such as confocal microscopes, mechanical profilometers, interferometry techniques, etc. For the roughness measurements in this project the following equipment was used; Atomic force microscopy (AFM), White light interferometry (WLI), Alicona microscope and surface profilometer (Surfcom). The reason for selecting a range of measurement equipment using different techniques was to compare the roughness parameters obtained and as each equipment has different resolution, this will provide information about a range of roughness from nano- to micro- scale.

AFM and Surface profilometer both are contact measurement equipment. The stylus type profilometers can give the information about the roughness profile if the stylus tip is smaller

compared to the lateral size of the surface irregularities. Surfcom gives only one-dimensional roughness data that is based on the average surface height deviations and is impractical to evaluate a two-dimensional surface. On the other hand AFM is a scanning probe microscope having higher resolution (sub-nanometer scale) that generates a 3D image of the evaluation area. Due to the limitations of the contact measurement techniques, interferometric methods have been developed. However interferometric techniques also have limitations; measurement based on fringe contrast requires that the roughness height must be a small fraction of the wavelength (Asakura, 1978). The more detailed information on each technique is described below.

4.3.1. Atomic force microscopy

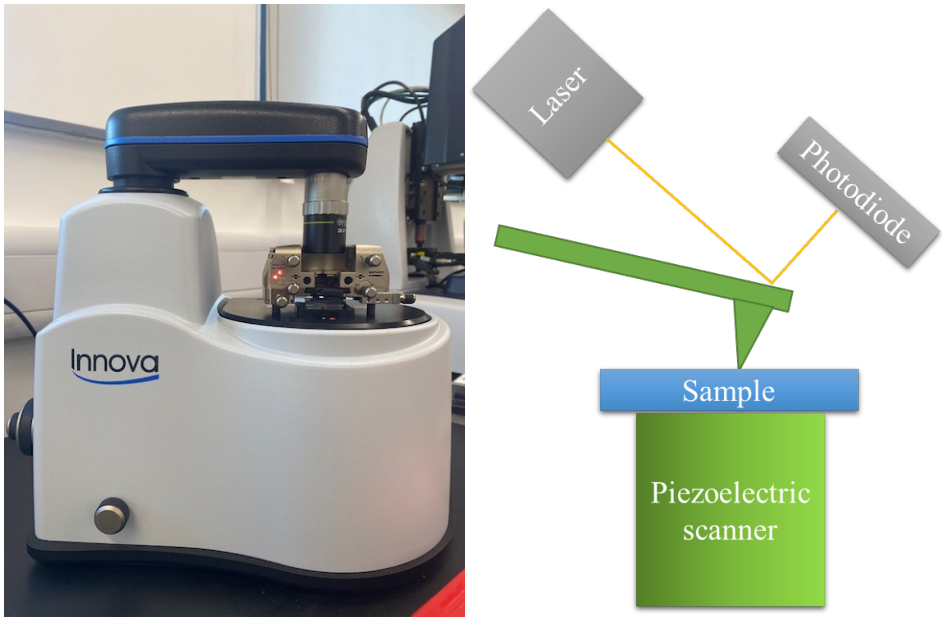

Figure 4.5 AFM used in this project and schematic of AFM technique

Atomic force microscopy provides a 3D profile by measuring the forces between the probe and the surface of the sample. The AFM tip touches the substrate and records the force. This force is described by Hooke's law (De Oliveira et al., 2012):

$$F = -k \times x \qquad 4.1$$

Where F is force, k is the spring constant and x the cantilever deflection. Force between the tip and the sample affects how the probe interacts with the sample. If there are repulsive forces, the probe will be in contact with the sample and in case of the attractive forces the probe will be in no contact with the sample. There are three modes for the imaging: contact, intermittent contact, and the non-contact mode. The movement of the tip is controlled by a

piezo-electric tube scanner. The very important component is a probe as different probes measure different properties. Also, probe defines the force that is applied on the sample and it has to be selected based on the imaging mode and the application (De Oliveira *et al.*, 2012). The Atomic Force Microscope used in this study was an Innova AFM (Bruker, Germany). Coating/substrate samples were cut in 2 x 1 cm and then placed on the positioning unit. The AFM used was operating in Peakforce Quantitative Nano-mechanical tapping mode using a silicon tip on a nitride cantilever probe (Bruker, nominal spring constant 0.4974 N/m, nominal resonance frequency of 70 kHz).

4.3.2. Surface Profilometer

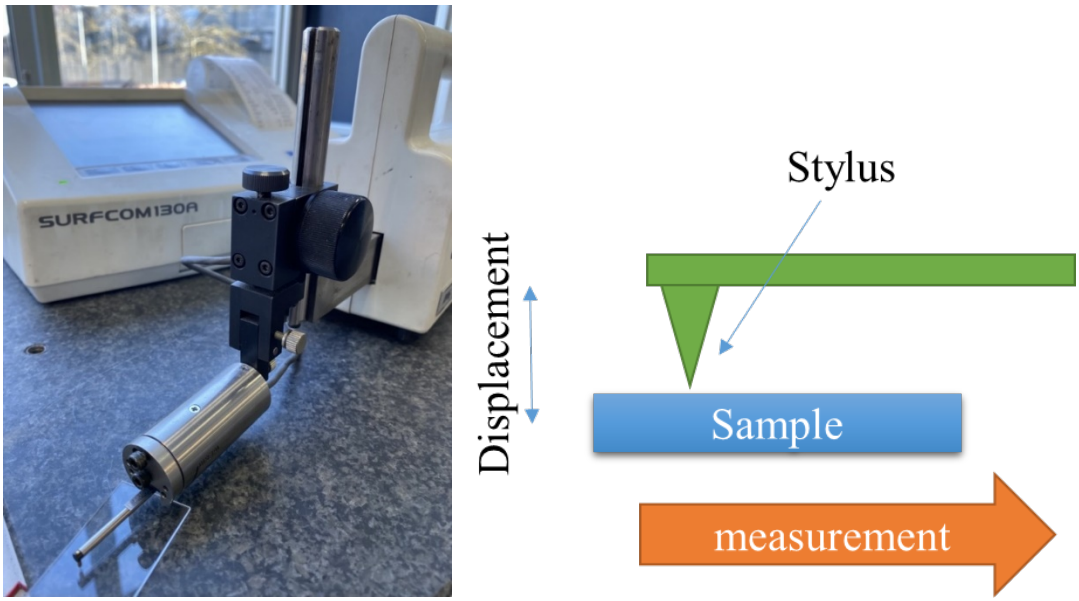

Figure 4.6 Photo of Zeiss Surfcom 130A and schematic

Zeiss Surfcom 130A is a stylus profilometer used to measure 2D roughness profile of a surface. Surfcom 130 is a tracing driver with free stylus-and-arm system (Figure 4.6). Similarly, to AFM, it uses a stylus (tip) to obtain roughness data. Waviness is measured through its 50 mm tracing driver while the roughness on radii is measured based on its 1.6 mm deflection range. The 10 mm evaluation length was used with the cut-off value of 0.8 mm to obtain the roughness data with surface profilometer.

4.3.3. White light Interferometry

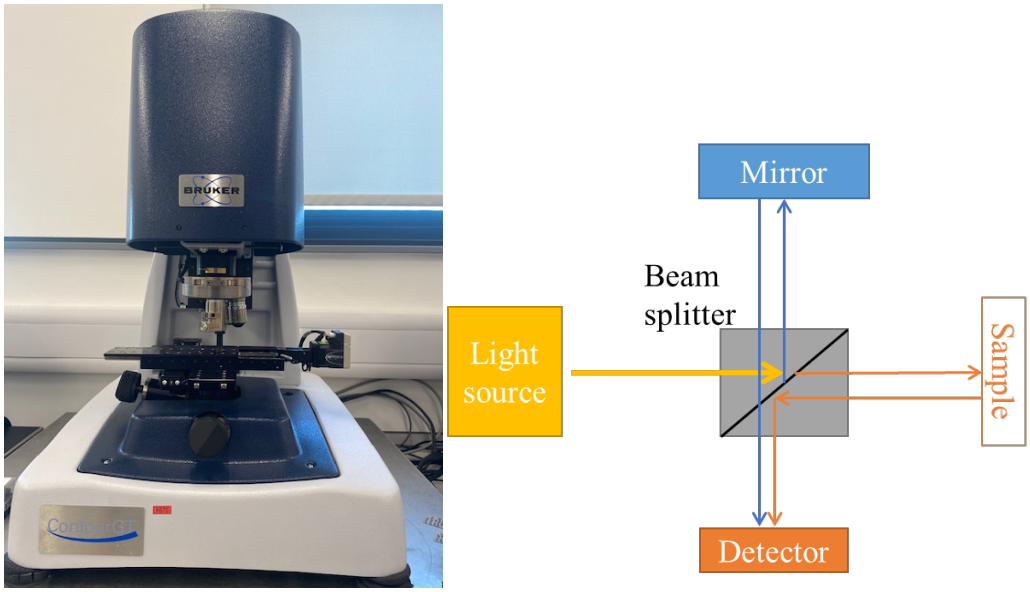

Figure 4.7 White Light Interferometry used and a schematic of process

The White Light Interferometry (WLI) is a non-contact optical measurement equipment. It provides a beam from the light source that is divided into two by a beam splitter. One beam is reflected from the reference mirror while the other is reflected from the sample. These two reflected beams are recombined by the beam splitter to create an interferogram (J.Schmit, 2013). For this study, 3D White Light Interferometer (WLI, Bruker Contour GT-K 3D Optical Microscope) was used to record three-dimensional surface topographies of substrates and coatings. The magnification lenses used in measurements were 2.5, 20 and 50. The Vertical Scanning Interferometry (VSI) mode with the white light source was used for substrates with high level of surface roughness while for the planar / smooth ones the Phase Shift Interference (PSI) mode was used. The obtained WLI datasets were filtered to remove the tilt from the profile and obtain roughness parameters. Examples of obtained WLI images are given in Figure 4.8.

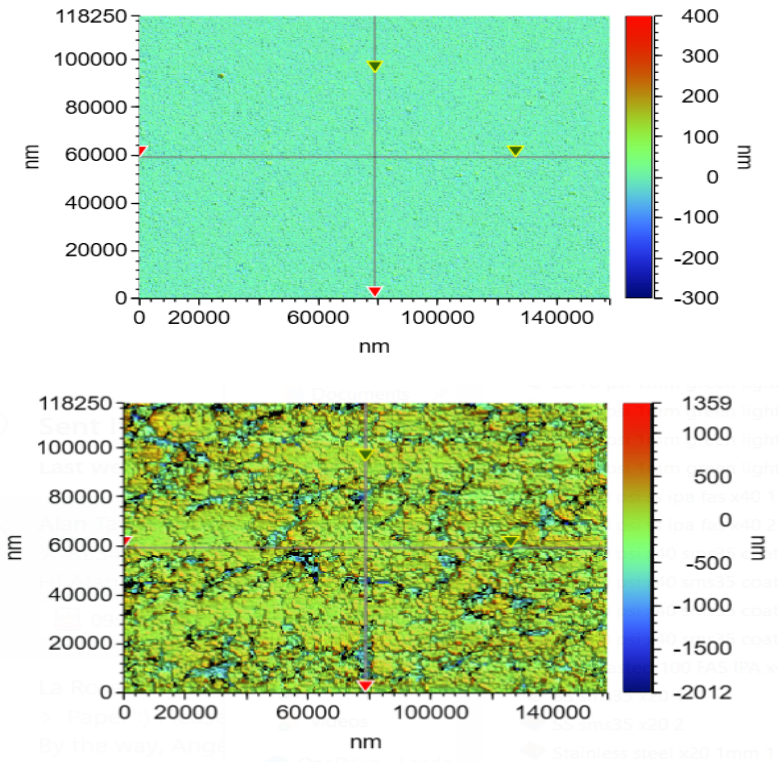

Figure 4.8 WLI of glass (top) and stainless steel 2B finish

4.3.4. Alicona microscope

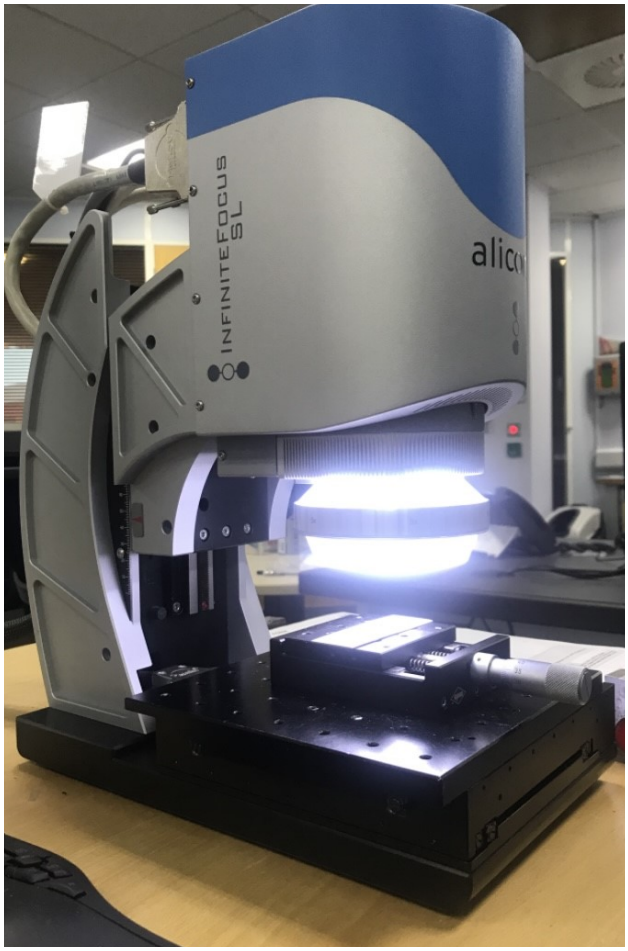

Figure 4.9 Alicona microscope

Alicona is an optical 3D measurement equipment with vertical resolution of up to 10nm. Alicona uses the method called focus variation to measure the form and roughness of the sample. The light from the white light source is focused onto the sample via the objective. The sample reflects the light back into different directions depending on the topography. All the light that is reflected back by the specimen is gathered by the light sensor behind the beam splitting mirror. Algorithms convert the collected data into 3D information and generate a true colour image with the full depth by the analysis of the focus variation. The Focus-Variation can measure surfaces with R_a value of as low as 0.009 µm (*Focus-Variation - The technical principle*, no date). The magnification used for the measurement of samples was 2.5. The obtained measurements / images were filtered to remove tilt after which the roughness parameters were obtained.

4.3.5. Roughness parameters

The roughness measurement equipment described above produces values of roughness parameters. However, the real surface topography is so complex that a finite number of parameters cannot provide a full description of it. There are a range of statistical roughness parameters that can be used to describe it and the use of increased number of parameters can provide a more accurate description. These parameters are generally categorised into three groups; amplitude parameters, spacing parameters, and hybrid parameters. The parameters used to characterise the surface topography in this project are described below. Parameters were selected to characterise roughness and to identify if there is a correlation between a specific roughness parameter and surface wettability.

4.3.5.1. The amplitude parameters

The Roughness average ($\boldsymbol{R_a}$) is a widely used height parameter as it is easily obtained. It is a mean of the absolute surface profile; it does not distinguish between peaks and valleys and thus it is not useful to characterise them. More refined parameters can be used for better characterisation. The Root mean square roughness ($\boldsymbol{R_q}$) is the square of the roughness average parameter. Maximum profile valley depth ($\boldsymbol{R_V}$), Maximum profile peak height ($\boldsymbol{R_{max}}$) and Maximum height of the profile ($\boldsymbol{R_T}$) give the values of the deepest valley, highest peak and the distance/height between them across the surface profile from the baseline respectively. The average values of these parameters can also be obtained. Ten-point average roughness ($\boldsymbol{R_Z}$) is the average of the five highest peaks added to the five deepest valleys (Gadelmawla *et al.*, 2002).

4.3.5.2. The Spacing parameters

Mean spacing ($\boldsymbol{R_{Sm}}$) describes the average spacing between the peaks in the length of evaluation.

4.3.5.3. Characteristics in the height direction

Skewness ($\boldsymbol{R_{sk}}$) measures the symmetry of the profile across the baseline. The symmetrical distribution with equal number of peaks and valleys would have a zero skewness. The positive value of skewness indicates that the topography mainly consists of peaks while the negative value indicates that there are more valleys. Skewness is a useful value to distinguish between profiles with similar mean roughness value as it helps to identify if their shape is similar. Kurtosis ($\boldsymbol{R_{ku}}$) is used to define the sharpness of the profile's probability density

curve. If the kurtosis value is less than three, the curve is platykurtoic which means that the profile has few high peaks and valleys. If the value is above three, the curve is leptokurtoic and has many high peaks and valleys. Root mean square slope (R_{dq}) is a mean absolute profile slope across the evaluation length. The property such as hydrodynamic lubrication is affected by this parameter (Gadelmawla *et al.*, 2002).

4.3.5.4. Parameters expressed as mathematical formulae

The parameters that were used in this project are described as mathematical formulae in the Table 4-1.

Table 4-1 Description of roughness parameters

Parameter	Mathematical Formula as expressed by Gadelmawla *et al.* (2002)
Roughness average ($\boldsymbol{R_a}$)	$R_a = \frac{1}{L}\int_0^L \lvert Z(x)\rvert \, dx$ 4.2
Root mean square roughness ($\boldsymbol{R_q}$)	$R_q = \sqrt{\frac{1}{L}\int_0^L \lvert Z^2(x)\rvert \, dx}$ 4.3
Maximum profile valley depth ($\boldsymbol{R_V}$)	$R_V = \lvert\min Z(x)\rvert \; for \; 0 \leq x \; \leq L$ 4.4
Maximum profile peak height ($\boldsymbol{R_{max}}$)	$R_p = \lvert\max Z(x)\rvert \; for \; 0 \leq x \; \leq L$ 4.5
Maximum height of the profile ($\boldsymbol{R_T}$)	$R_T = R_V + R_{max}$ 4.6
Average profile valley depth ($\boldsymbol{R_V}$)	$R_{vm} = \frac{1}{L}\sum_{i=x}^{L} R_{vi}$ 4.7
Average profile peak height ($\boldsymbol{R_c}$)	$R_c = \frac{1}{L}\sum_{i=x}^{L} R_{pi}$ 4.8
Average height of the profile ($\boldsymbol{R_{Tm}}$)	$R_{Tm} = \frac{1}{L}\sum_{i=x}^{L} R_{Ti} = R_{pm} + R_{vm}$ 4.9

Ten point average roughness ($\boldsymbol{R_Z}$)	$R_z = \frac{1}{n}\sum_{i=x}^{n} P_i - \sum_{i=1}^{n} V_i$ 4.10
Mean spacing ($\boldsymbol{R_{Sm}}$)	$R_{Sm} = \frac{1}{L}\sum_{i=1}^{1} S_i$ 4.11
Skewness ($\boldsymbol{R_{sk}}$)	$R_{sk} = \frac{1}{R_q^3}\int_{-\infty}^{\infty} y^3 p(y)dy$ 4.12 or $R_{sk} = \frac{1}{NR_q^3}(\sum_{i=1}^{N} Y_i^3)$ 4.13
Kurtosis ($\boldsymbol{R_{ku}}$)	$R_{ku} = \frac{1}{R_q^4}\int_{-\infty}^{\infty} y^4 p(y)dy$ 4.14 Or $R_{ku} = \frac{1}{NR_q^4}(\sum_{i=1}^{N} Y_i^4)$ 4.15
Root mean square slope ($\boldsymbol{R_{dq}}$)	$\boldsymbol{R_{dq}} = \sqrt{\frac{1}{L}\int_0^L (\theta(x) - \theta)^2 dx}$, 4.16 $\theta = \frac{1}{L}\int_0^L \theta(x)dx$ $\boldsymbol{R_{dq}} = \sqrt{\frac{1}{n-1}\sum_{i=1}^{n-1}\left(\frac{\delta_{yi}}{\delta_{xi}} - \theta_m\right)^2}$, 4.17 $\theta_m = \frac{1}{n-1}\sum_{i=1}^{n-1}\left(\frac{y_i - y_{i-1}}{x_i - x_{i-1}}\right)$

4.4. Wettability evaluation

4.4.1. Drop shape analyser

For the wettability evaluation a drop shape analyser (DSA) KRÜSS GmbH DSA-100 was used.

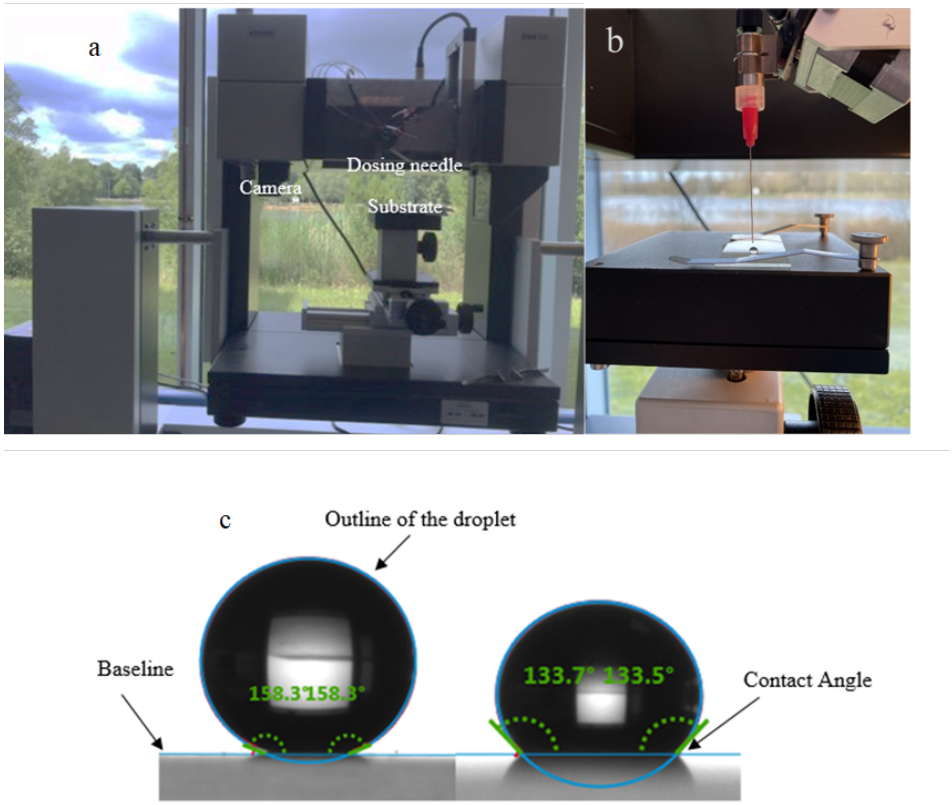

Figure 4.10 a. Drop Shape Analyser KRÜSS GmbH DSA-100 used in the study, b. dosing and deposition of the droplet, c. typical image of the contact angle measurement and the contour of the droplet

The DSA (Figure 4.10) operates by capturing the image of the deposited droplet and contouring its shape to determine the contact angle between the probe liquid and the sample (Figure 4.10). After the image has been captured, the DSA employs the ADVANCE software to evaluate the grey scale values of the image to detect the baseline (the contact line between the droplet and the sampling material) as well as the outline of the droplet.

The KRÜSS GmbH DSA-100 is capable of measuring contact angles of static sessile drops to evaluate the wettability with probe liquids and calculate the SFE of the substrate. It can also be used to obtain the surface tensions of the probe liquids via the pendant drop method. The DSA-100 used in this study is also equipped with the tilting table that can be automated

to tilt the sample at the specified rate while the goniometer captures the change in the contact angle of the deposited droplet. The detailed description of these techniques is given below.

4.4.2. Static contact angle measurements

Static contact angle is one of the essential parameters in surface science. It is considered that contact angle measurement provides a straightforward and reliable technique for the interpretation of surface energetics and SFE calculations (Lam *et al.*, 2001).

It should be highlighted that experimentally measured contact angles are macroscopic properties, and their value is a mean of many microscopic contact angles formed around the perimeter of the deposited droplet. It is generally considered that the macroscopic contact angle is the apparent contact angle (Chibowski and Jurak, 2013; Huhtamäki *et al.*, 2018). The static contact angle measurements were performed by depositing a 2 microliter droplet of the selected probe liquid on the test specimen by the automated syringe or the micro-pipette. The volume of 2 microliters was selected for measurements because it provides the droplet with the diameter below the capillary length of the probe liquids used and thus the gravitational effects on the drop may be neglected (*Effect of drop volume on static contact angles - TN310e*, 2004). When the droplet was deposited on the sample the goniometer measured the created contact angle every 1 second three times and the measurement was repeated for three different droplets on the same sampling material. The Young-Laplace fitting method was used to obtain the contour of the droplet. The total SFE was then calculated using the OWRK (Owens, Wendt, Rabel and Kaelble) method. The OWRK is a standard method for determining the SFE of a solid from the contact angle with several liquids. The theory behind it is described in chapter 2 (Owens and Wendt, 1969).

4.4.3. Probe liquids

Contact angles can be measured with a range of liquids and an appropriate selection of probe liquid is required to obtain useful wetting data. Van Oss (2006) has provided the data of the liquids most frequently used for the contact angle measurements. Table 4-2 provides the surface tensions and viscosity of some apolar and polar liquids used in the contact angle measurements.

Table 4-2 Surface tension of liquids and their viscosities at 20 ºC (data from Van Oss, 2006)

Liquid	Surface tension (mN/m)			Viscosity (poise)
	Disperse	Polar	Total	η
Non- polar				
Decane	23.8	0.0	23.8	0.0092
Tetradecane	26.6	0.0	26.6	0.0218
Pentadecane	27.1	0.0	27.1	0.0290
cis-Decalin	32.3	0.0	32.3	0.0338
Bromonaphtalene	44.4	0.0	44.4	0.0489
Diiodo-methane	50.8	0.0	50.8	0.0280
Polar				
Water	21.8	51.0	72.8	0.0100
Glycerol	34.0	30.0	64.0	14.9000
Formamide	39.0	19.0	58.0	0.0375
Ethylene glycol	29.0	19.0	48.0	0.1990

As mentioned in Chapter 2, the obtained contact angle depends on interfacial surface tension and thus the surface tension of the probe liquid. The section below describes the methodology of surface tension measurement.

4.4.4. Measurement of surface tension

The surface tension of liquids is most frequently determined by the Wilhelmy plate method. A rectangular plate (glass or platinum) is suspended on a micro-balance above the beaker containing the liquid of interest. The beaker with the liquid is raised to the plate and upon contact an additional force / weight (ΔW) is exerted on the plate. Where P_d is the plate periphery (Van Oss, 2006).

$$\gamma_L cos\theta = \frac{\Delta W}{P_d} \qquad 4.18$$

The method which was used to determine the surface tensions of LST probe liquids used in this thesis was the pendant drop method which is another reliable approach for measurement. The pendant drop (PD) method is an optical method for determining the surface tension of a drop of liquid by using the curvature of the drop profile. An advantage when compared with the frequently used methods based on force measurement, such as the Du Noüy ring measurement or the Wilhelmy plate measurement, is the very small sample volume required

(approx. 20-60 µL). In the pendant drop method, the liquid is suspended from the tip of a needle.

The pendant drop method involves the determination of the profile of a suspended drop. The profile is determined by the balance between gravity and surface forces. The equation of Bashforth and Adams which is based on Laplace's equation, relates the drop profile to the interfacial tension through a nonlinear differential equation which is given below (Arashiro and Demarquette, 1999):

$$\frac{1}{\frac{R_1}{a}} + \frac{\sin\varphi}{\frac{x}{a}} = -B\frac{z}{a} + 2 \qquad 4.19$$

Where:

$$B = \frac{a_d^2 g \Delta\rho}{\gamma} \qquad 4.20$$

Δρ is the difference between the densities of the two phases in contact, g is the gravitational constant, γ is the interfacial tension, a_d is the radius of curvature at the apex of the drop, x, z, φ are the coordinates defined as in Figure 4.11 and R1 is the radius of curvature at the point with coordinates (x, z).

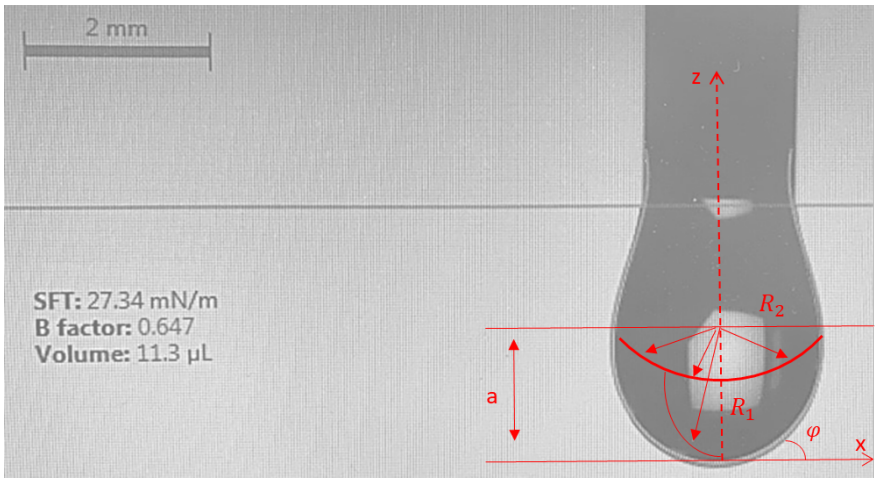

Figure 4.11 Geometry of the pendant drop

The shape of the pendant drop is dependent on a single dimensionless quantity, the Bond number (B). If the Bond number associated with a pendant drop is determined together with the drop radius (a) at the apex, the interfacial tension γ is then readily determined from the above equation. When performing the pendant drop measurements, it is important to have a sufficiently large drop to obtain an adequate deformation of the droplet for the measurement. In this study the Kruss DSA 100 was used for pendant drop measurements of probe liquids

to determine their surface tension. A needle with a diameter of 1.8mm was used to dose droplets of sufficient volume for the measurements and Kruss DSA was used for the surface tension determination.

To blend the water-ethanol probe liquids with specific surface tensions of 50 and 30 mN/m, a range of solutions with mole fraction of ethanol ranging from 0.02 to 0.75 were prepared. The surface tensions of blends were measured using the pendant drop method using Kruss DSA – 100 (see Figure 4.12) and the defined mole fraction of ethanol was used to prepare probe liquid blends with surface tensions of 50 mN/m (LST 50) and 30 mN/m (LST 30) (see Table 4-3).

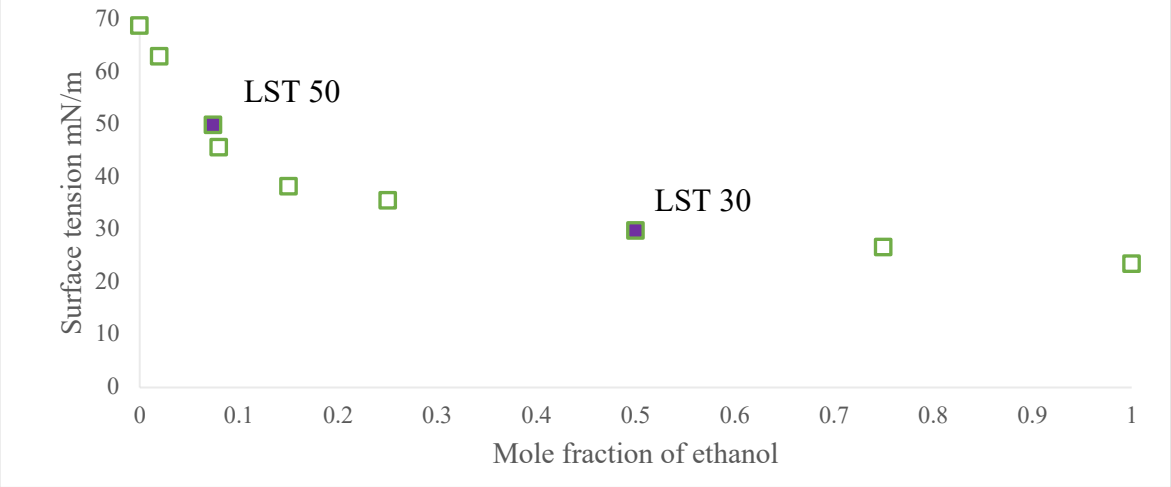

Figure 4.12 Surface tensions of water-ethanol probe liquids at various mole fractions of ethanol

For this study four probe liquids were selected with two water-ethanol blends with different surface tensions. The liquids were chosen based on the criteria that liquids should have a range of intermolecular forces and surface tension values of polar and non-polar parts. The liquids used for the measurements were water, diiodo-methane and water-alcohol blends with surface tensions of 30 mN/m and 50 mN/m and for some samples also the static contact angles with decane and o-xylene were assessed. These liquids were selected as water is a highly polar liquid while diiodo-methane does not have any polar component in its surface tension. Ethanol has one of the lowest surface tensions and is soluble in water, so the surface tension of the alcohol-water blend could be easily manipulated by changing the ratios of the blend. The surface tensions of probe liquids used in this study are given in Table 4-3.

Table 4-3 Probe liquids selected for surface energy analysis

Probe liquid	Surface Tension Disperse (γ_s^d) mN/m	Surface Tension Polar (γ_s^p) mN/m	Surface Tension Total (γ_s) mN/m
Water	22.6	50.2	72.8
Diiodo-methane	50.8	0.0	50.8
LST 50	-	-	46.6 (± 6.8)
LST 30	-	-	28.0 (±0.7)
Ethanol	18.8	2.6	21.4
o - Xylene	30.1	0.0	30.1
Decane	23.8	0.0	23.8

4.4.5. Dynamic contact angle measurement

It is frequently observed that the contact angle at the advancing side of a drop is larger than the contact angle at the receding side (Figure 4.13). Young's equation is valid for contact angles that are measured as advancing contact angles, in other words contact angles that have stopped to advance further. Advancing contact angles have been considerd to be a measure of apolar nature of the surface while the receding angle (retreating angle) a measure of its polar characteristics (Van Oss, 2006). One of the reasons for mainly using advancing contact angles for thermodynamic derivations/measurments is that receding contact angle reflects liquid retention by the solid and not a property of the solid on its own. In other words it is the measure of the contact angle with the surface that has been already wetted/contaminated with the probe liquid while for the advancing contact angle it is not the case (Lam *et al.*, 2001). The difference between these two contact angles is known as contact angle hysteresis (CAH). The presence of contact angle hysteresis in contact angle measurements complicates the contact angle interpretation in terms of Young's equation. The contact angle hysteresis has been studied comprehensively in the past; however, the origins of this phenomena are not completely understood. There are several interpretations and studies that attribute it to surface heterogeneity. Gaydos and Neumann (1994) determined that the minimum amount of surface heterogeneity to produce contact angle hysteresis was about 1 μm. Though, the

effect of surface roughness on the hysteresis may not only depend on the level of roughness but also on the type of surface topology (Chibowski and Jurak, 2013) (see chapter 2 for the discussion of CAH origins). One of the ways to determine contact angle hysteresis and liquid roll-off angle on the surface is to study droplet behavior on inclined surfaces. There is no standard procedure for it, but conditions such as drop volume and tilting speed must be taken into consideration when performing the measurement. Kruss DSA-100 has a function of tilting table that can be used for dynamic CA measurements. To perform dynamic contact angle measurement using Kruss DSA-100, the droplet has to be deposited on a level surface after which the DSA table is tilted at a specific speed (°/s) up to the tilt angle of 80°. The tilt angle refers to the critical angle between the tilting substrate and the horizontal surface. As the substrate is tilted, the images of droplet are captured at a specific rate (every second) to obtain measurements as a function of tilt. The obtained sequences of images are evaluated to determine the sliding angle (SA), advancing and receding contact angles and contact angle hysteresis. One of the main criterion for evaluation is movement of the three-phase contact point (CP); the receding (CP(R)) and advancing (CP(A)) points between surface, liquid and gas phase (Figure 4.14).

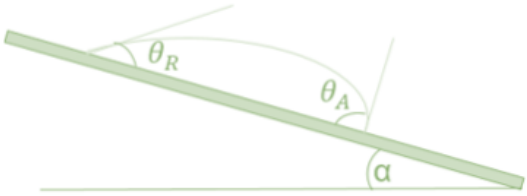

Figure 4.13 Dynamic contact angle measurement; advancing and receding contact angles on tilted surface

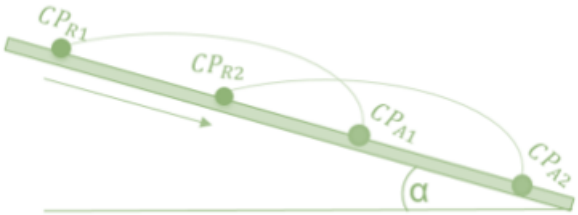

Figure 4.14 Dynamic contact angle measurement; movement of the three-phase contact point (CP) at receding (rear of the droplet) and advancing (front of the droplet)

The SA is an empirical quantity that depends on measurement parameters, such as the tilting speed or drop volume. For comparative measurements between different samples, it is therefore important to determine suitable measuring conditions according to the chosen criteria. For this study all the dynamic contact angle measurements were taken using the same volume of the droplet (20 microliters), the tilting speed used was constant (1 °/s) and measurements were taken every second. For the comparative measurements between samples the sliding angle was identified as the angle of inclination at which the position of the moving three-phase point is displaced by 40 pixels for both receding and advancing points (Figure 4.15). The roll-off angle or the point at which the droplet leaves the camera view was also captured. In case the droplet is pinned and does not leave the camera view even at the 80º tilt the sliding angle is determined as a comparison parameter between samples.

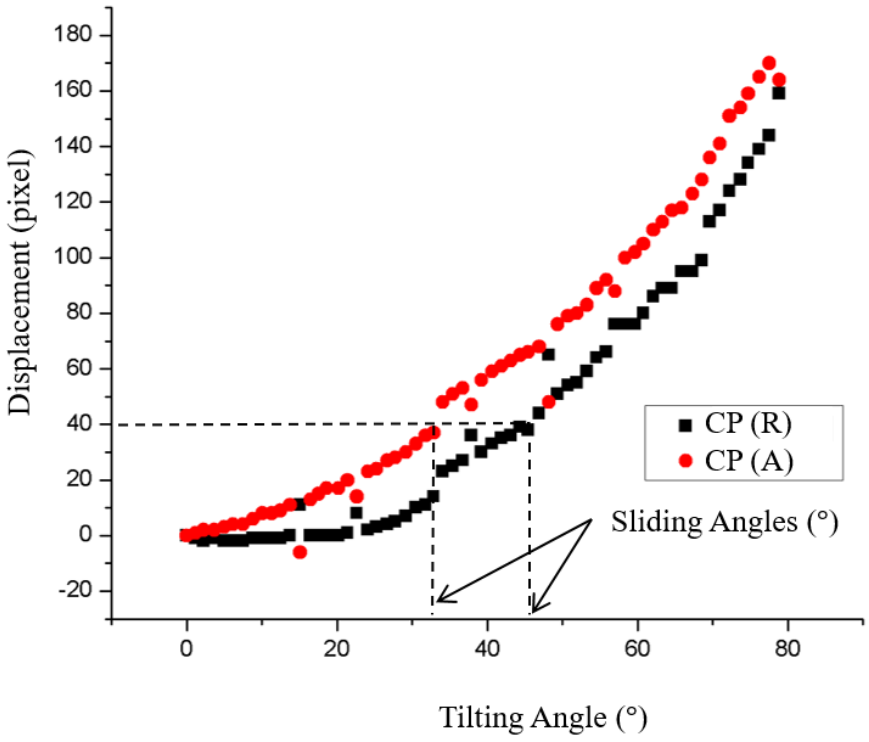

Figure 4.15 Determination of the Sliding Angle (SA) using the coordinates of the three phase points in the video image

The purpose of the dynamic contact angle measurements was to determine the contact angle hysteresis with a range of probe liquids (both polar and apolar) and to study the effect of

liquid properties on CAH on low SFE substrates. As well as to compare the CAH of fluorinated and un-fluorinated coating systems applied on roughened and planar substrates.

4.5. Scanning electron microscopy

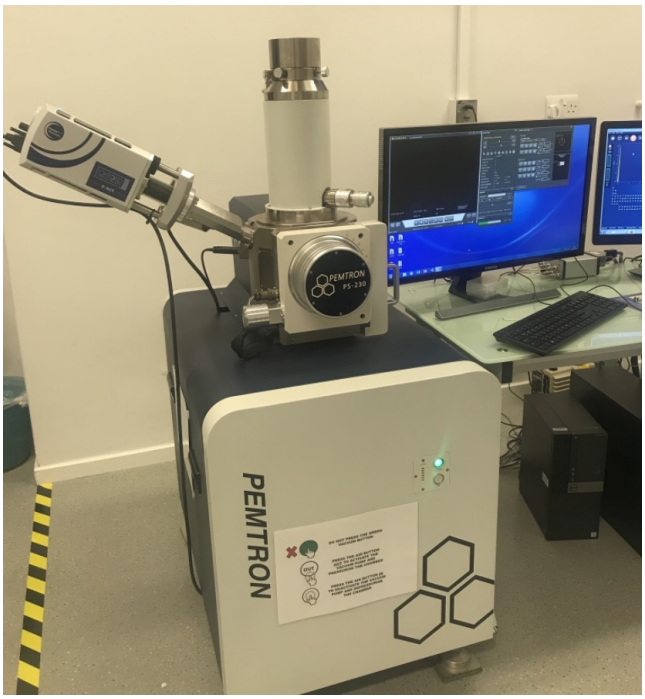

Figure 4.16 Pemtron PS-250

Scanning electron microscopy (SEM) is used for material characterization. SEM uses the electrons that are reflected off the sample to generate an image. The electrons are emitted from the source and are attracted to the positively charged anode. The path of the electrons is controlled by electromagnetic lenses; the condenser lens defines the size of the electron beam, and the objective lens focuses it on the sample. SEM uses the backscattered (BSE) and the secondary electrons (SE). The BSE is the primary electron beam that gets reflected from the sample and SE are created by the inelastic interactions of the beam with the sample. The SE provide information on the surface. The detectors identify the electrons, and the image is generated. The SEM measurements were performed on the surface to obtain the morphology of the deposited coating and to identify whether specific coating alters the substrate's surface topography. For scanning electron microscopy (SEM) measurements, the test specimens were prepared by applying a thin layer of gold sputter coating to prevent charging during the experiment. The thin layer of gold sputter with the estimated thickness of a few nanometres was applied via the Polaron equipment limited SEM coating unit E5100. The SEM used in this study was Pemtron PS-250.

4.6. Dynamic Light Scattering

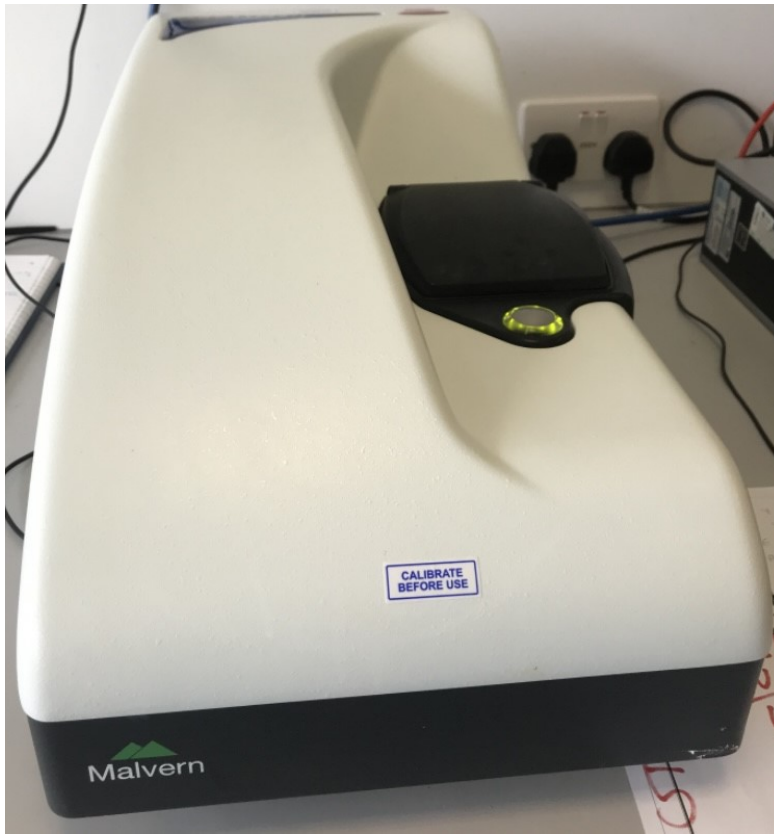

Figure 4.17 Dynamic Light Scattering (DLS)

One of the ways to obtain a super repellent surface with nano-scale topography is to follow the bottom-up fabrication approach. Bottom-up approach used in this thesis employed silica nanoparticles to build up the desired surface roughness at a nano-scale. Silica nanoparticles were synthesised using Stöber method described in detail in Chapter 7. In order to characterise and identify the size/diameter of the fabricated nanoparticles Dynamic Light Scattering (DLS) was used. Dynamic Light Scattering (DLS), also referred to as Photon Correlation Spectroscopy or Quasi-Elastic Light Scattering, is a technique used to measure the particle sizes in the sub-micron region. Dynamic Light Scattering measures Brownian motion and relates it to the particle size. The motion of the particles in the solution is random due to the solvent molecules that surround them, and this random motion is referred to as Brownian motion. The larger particles have slower Brownian motion but the smaller ones faster. The Brownian motion velocity is defined by the translational diffusion coefficient (given by the symbol D). The particle size can be calculated from the translational diffusion coefficient using the Stokes-Einstein equation:

$$d(H) = \frac{kT}{3\pi\eta D} \quad 4.21$$

Where d(H) is hydrodynamic diameter, D is the translational diffusion coefficient, k_B is the Boltzmann′s constant, T the absolute temperature, and η viscosity. The diameter measured by the DLS is the hydrodynamic diameter as it measures how a particle diffuses in a fluid. Thus, the particle diameter obtained is the diameter of a sphere with equal translational diffusion coefficient. Apart from the particle size the translational diffusion coefficient depends on the particle's surface structure, the concentration and nature of ions in the medium. A dynamic light scattering system uses a laser as a light source to illuminate a cuvette containing the sample. The laser beam passes through the sample but some light is scattered by the particles at different angles. A detector measures this scattered light, but its intensity needs to be within a defined range for the detector to effectively identify it. The DLS uses an attenuator to tune the intensity of the laser source to help with the detection of the scattered light. The light scattering intensity is distributed from the detector to a correlator (a processing board). The correlator matches the scattering intensity at consecutive time intervals to define the variation of the intensity rate. The information from the correlator is passed to a Nano software which analyses the data and derives the particle size information. One of the features of the Zetasizer Nano S is a Non-Invasive Backscatter Detection (NIBS). The Zetasizer Nano S detects the scattering information at 173 degrees, and this is acknowledged as backscatter detection. There is no contact between the sample and the detection optics thus it is said to be non-invasive, and this technique has the advantage as the laser does not have to travel through the whole sample and thus the multiple scattering effect is reduced where the light from one particle is scattered by the other particles. Contaminants in the dispersant are usually of the larger size than the sample and the larger particles scatter in the forward direction. Hence, backscattering reduces the effect of contaminants such as dust (*DLS technical note MRK656-01*, 2018).

ISO 22412:2017 (2017) standard describes the application of DLS to measure the mean hydrodynamic particle size and the size distribution (PdI) of sub micrometre particles dispersed in liquids. A typical DLS results report is presented in Figure 4.18. The Z-Average relates to the hydrodynamic diameter of the dispersed particles and the PdI specifies the size distribution of produced nano particles. A PdI value lower than 0.2 indicates that the suspension is monodisperse (Stetefeld, McKenna and Patel, 2016).

			Size (d.nm):	% Intensity:	St Dev (d.n...
Z-Average (d.nm):	44.18	Peak 1:	49.96	100.0	17.64
PdI:	0.111	Peak 2:	0.000	0.0	0.000
Intercept:	0.952	Peak 3:	0.000	0.0	0.000
Result quality :	Good				

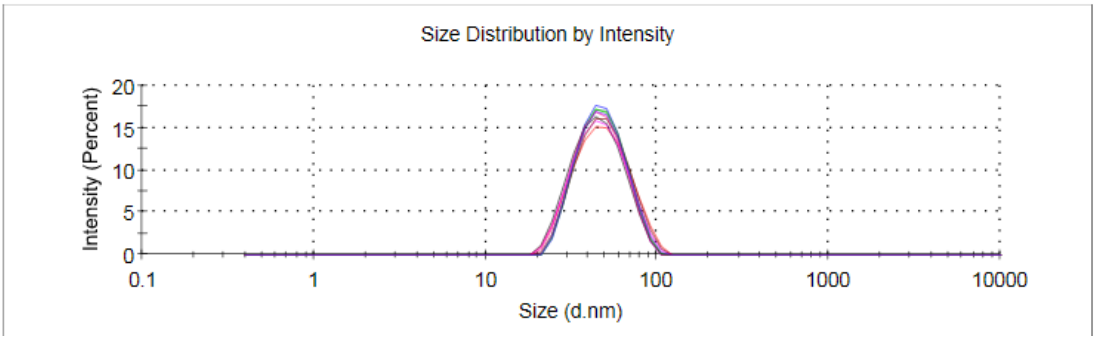

Figure 4.18 DLS results

The size (Z - average) and poly-dispersity index (PdI) of produced silica nanoparticles at every stage of fabrication and functionalisation were measured using the DLS technique. At least three measurement repeats were undertaken for each sample and the mean of Z-average was calculated.

4.7. Mechanical abrasion

As described in chapter 2 and 3, the hydrophobic and omniphobic coatings deposited on a variety of substrates can find applications such as in non-wetting, anti-contamination, stain resistance and easy clean surfaces. These properties can increase the surface value but in order to be useful it is important for them to maintain those characteristics and remain effective after exposure to abrasion or surface cleaning routine. Coatings with incorporated nanoparticles that promote repellence (described in chapter 7) were evaluated via comparison of the contact angle with water and diiodo-methane and the depreciation of those contact angles due to exposure to mechanical abrasion. The mechanical abrasion method for those thin coatings was selected to be a 50 cycle abrasion with steel wire wool. The steel wire-wool was used as an abradant to which the load of 0.45 kg was applied. The samples were subjected to 50 abrasive cycles by the abradant under the load. The wettability of the samples was assessed before and after the abrasive test.

4.7.1. Coating Visual Appearance

Figure 4.19 Novo-gloss IQ Goniometer

The application of aesthetically pleasing functional repellent coatings is increasing. Thus, it is important for the coatings to maintain their visual appearance after exposure to mechanical abrasion. The gloss and haze of coatings with incorporated silica nanoparticles that promote repellence were measured before and after mechanical abrasion described in section 4.8 to identify if the coatings can maintain their visual property. Gloss and haze of coatings were measured using a Novo-Gloss IQ Goniometer from Rhopoint Instruments, according to ASTM D523 –14 (for the gloss) and ASTM E430-19 (for the haze) ('ASTM D523-14, Standard Test Method for Specular Gloss', 2018; 'ASTM E430-19, Standard Test Methods for Measurement of Gloss of High-Gloss Surfaces by Abridged Goniophotometry', 2019). Value of gloss is obtained by irradiating a specific amount of light at a surface and quantifying the reflection. Three different angles of incidence may be used to measure the gloss of coatings. The incidence angle is selected depending on the type and roughness of the surface. Table 4-4 provides the commonly used principal of gloss measurement geometry selection.

Table 4-4 Incidence angles for gloss measurements

Gloss Range with 60° Gloss Meter	Measure With:
10 - 70 GU	60º
>70 GU	20º
<10 GU	85º

For the coatings prepared in this project the incidence angle used to measure haze and gloss was 20º.

4.8. Summary

The chapter provided a detailed description of the evaluation methodologies and characterisation techniques used in this project. The assessment/characterisation methodology focused on the surface topography, surface chemistry and more importantly wettability to various probe liquids.

CHAPTER 5. WETTABILITY EVALUATION OF PLANAR SURFACES

5.1. Introduction – wettability of surfaces

The majority of metallic and inorganic substrates are oleo or hydrophilic and yet there is no complete understanding of liquid-surface interaction. Liquid adsorption to the surface may be uniform or in isolated areas and it can be driven by different physical and chemical processes. The nature and extent of liquid-substrate interaction can be controlled by application of adhesive or abhesive treatment to the substrate.

In terms of surface interaction with water, surfaces become increasingly hydrophilic in the following order:

non-polar < polar, no hydrogen bonding < polar, hydrogen-bonding < hydroxylic < ionic

High contact angles with water are indicative of hydrophobicity however another important factor to consider is whether the adsorbed water (or liquid) is free or bound to the surface. Free water (or liquid) can be easily desorbed. If water remains bound to the surface and cannot be removed without heating the surface is considered hygroscopic (Arkles, Pan and Mi Kim, 2009).

Surface hydroxyl groups are present on the surface of metal oxide materials and various glasses. The hydroxyl or silanol groups can be of different types, the schematic of interacting, isolated, geminal silanols as well as the siloxane is presented in Figure 5.1. The neighbouring silanols are interacting and are capable of forming an H-bond if the distance between them is less than 3.3 Å (Dong, Pappu and Xu, 1998). The surface OH groups influence chemical properties as they act as adsorption sites and are capable of hydrogen bonding. To make surface more hydrophobic, the hydrogen bonding sites must be reduced, and the polar surface must be shielded by creating a non-polar interface.

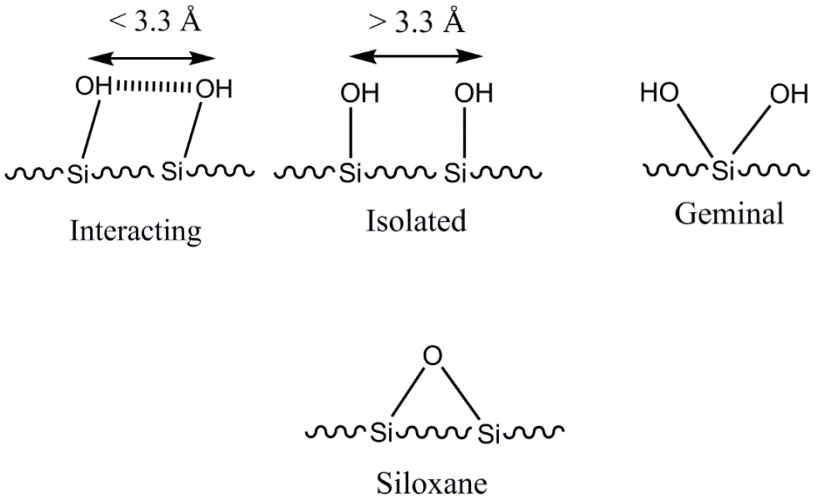

Figure 5.1 Surface functional groups on glass

Hydroxyl groups (Figure 5.1) can be transformed into oxane bond via the reaction with an organosilane. Silanes with aliphatic and fluorinated substituents are capable of making the surface more hydrophobic. Silanes also provide anchor points for the non-polar organic substituent that can shield the polar substrate from interaction with water. The factors that have to be taken into account are that not all hydroxyl groups may react leaving sites for possible hydrogen bonding or not all polar surface might be shielded by the organic substituents (Arkles, Pan and Mi Kim, 2009).

Therefore, factors that affect silane's ability to render surface hydrophobic are as follows (Arkles, Pan and Mi Kim, 2009):

- Silane's organic substituent
- Extent of surface coverage
- Residual unreacted groups
- Orientation of silane

The following chapter reviews various surface treatments and how they affect solid-liquid interaction by measuring the static and dynamic contact angle with a variety of polar and non-polar probe liquids.

5.2. Surface topography of substrates

The substrates studied in this chapter were planar with minimal surface roughness in order to minimise effect of surface topography on repellence and mainly concentrate on the effect of surface chemistry achieved by treatments. The substrates used were glass and stainless steel 304 with 2B and mirror finish. Surface roughness of selected substrates was measured using White Light Interferometry, Alicona and surface profilometer Surfcom.

5.2.1. White light Interferometry

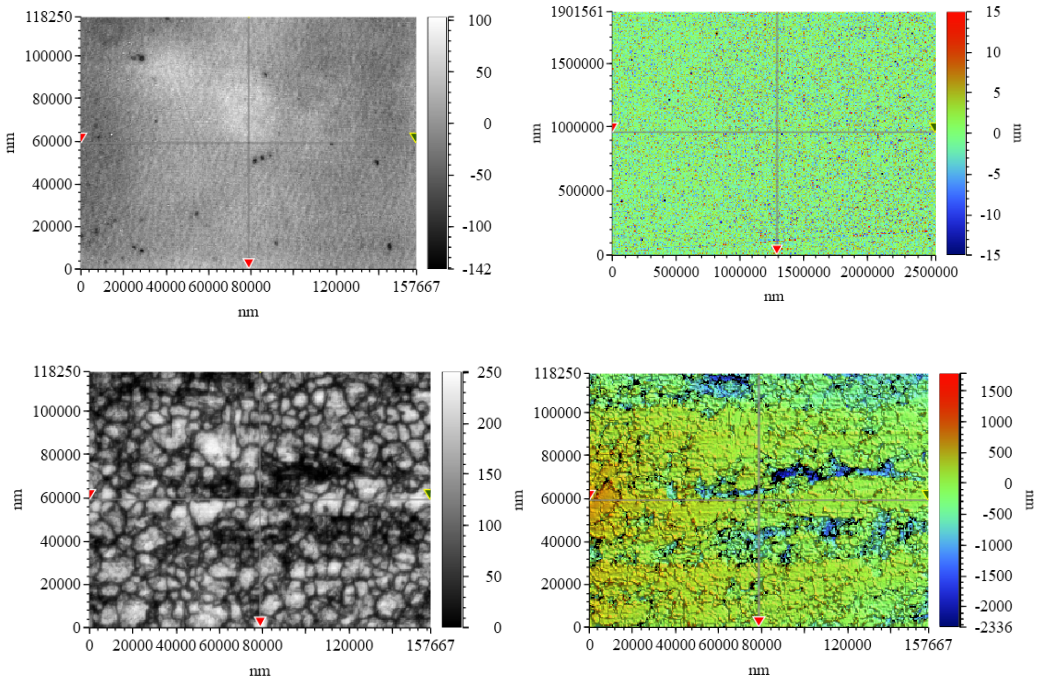

Figure 5.2 WLI images of glass (top) and stainless steel 2B finish (bottom).

Figure 5.2 presents the white light interferometry images of glass and stainless steel with 2B finish and in Table 5-1 are presented the roughness parameters measured via WLI.

Table 5-1 Roughness parameter values from WLI measurements

Parameter	Glass	Stainless steel 304 with 2B finish
Ra (nm)	7.07 (±0.29)	159.57 (±8.85)
Rp (nm)	76.07 (±41.09)	1431.87 (±120.79)
Rq (nm)	8.9 (±0.44)	238.97 (±8.62)
Rt (nm)	163.9 (±67.01)	3572.33 (±181.3)
Rv (nm)	-87.83 (±26.22)	-2140.5 (±123.31)
Surface area index	1.00 (±0.00)	1.13 (±0.01)

According to WLI measurements both substrates exhibit minimal surface roughness in the range of nanometers; for glass average roughness is 7 nm and for stainless steel 2B it is 160 nm. For comparison to planar substrates, the surface area index was obtained for both surfaces. Surface index is lateral area divided by surface area (similar to Wenzel roughness ratio parameter). Planar surfaces with no topographic characteristics have a surface index of one. For glass according to WLI measurements it is 1, meaning that surface is planar with no surface roughness. For stainless steel 2B finish it is 1.138, which means that some degree of roughness is present.

5.2.2. Alicona

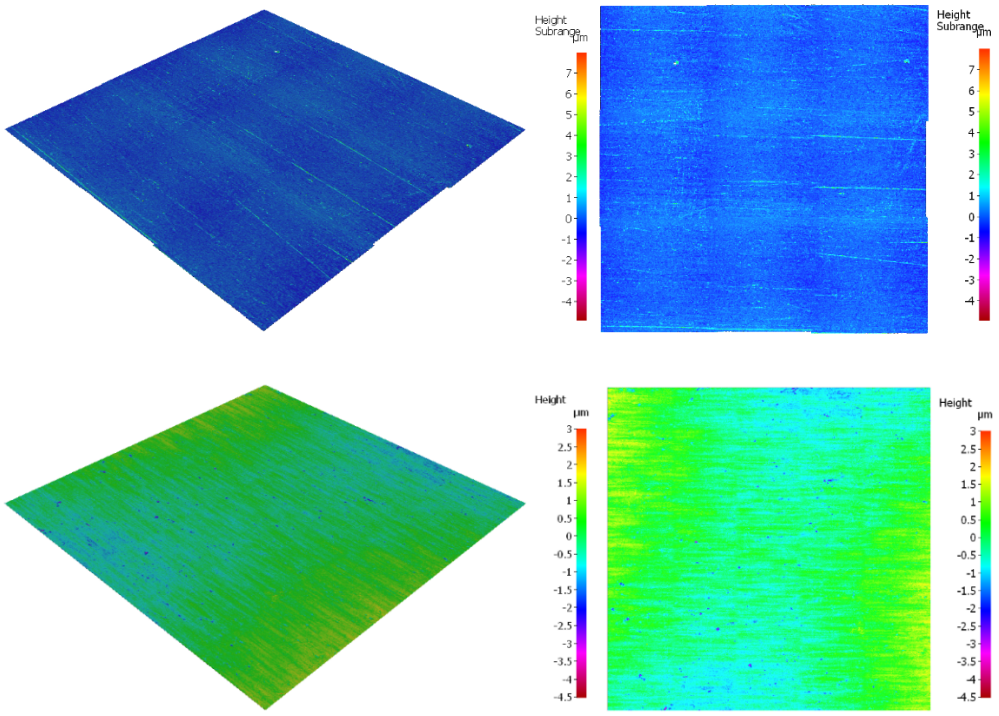

Figure 5.3 Alicona images of stainless steel 304 with mirror finish (top) and with 2B finish bottom

Figure 5.3 presents the Alicona images of stainless steel with mirror and 2B finish and Table 5-2 presents the roughness parameters.

Table 5-2 Roughness parameter values from Alicona measurements

Parameter	Mirror finish	2B finish
Ra (µm)	0.14 ± 0.01	0.14 ± 0.01
Rq (µm)	0.18 ± 0.01	0.18 ± 0.00
Rt (µm)	1.92 ± 0.00	1.36 ± 0.00
Rz (µm)	1.24 ± 0.00	1.10 ± 0.00
Rmax (µm)	1.74 ± 0.00	1.34 ± 0.00
Rp (µm)	1.30 ± 0.00	0.54 ± 0.10
Rv (µm)	0.61 ± 0.01	0.31 ± 0.43
Rc (µm)	0.71 ± 0.10	0.60 ± 0.03
Rsm (µm)	0.13 ± 0.03	0.11 ± 0.05
Rsk	0.75 ± 0.00	-0.53 ± 0.00
Rku	6.85 ± 0.00	4.05 ± 0.00
Rdq	0.03 ± 0.00	0.03 ± 0.00
Rt/Rz	1.55 ± 0.00	1.24 ± 0.00
Lc (µm)	800.00	800.00

According to Alicona measurements both substrates exhibit minimal surface roughness with roughness average being 140 nm.

5.2.3. Surface profilometry

Roughness of glass and stainless steel 304 with 2B and mirror/polished finish were also measured with Surfcom surface profilometer. The roughness data obtained is presented in Table 5-3.

Table 5-3 Roughness parameter values from Surfcom measurements

Substrate	Glass	SS mirror	SS 2B
Ra (µm)	0.02 (±0.00)	0.04 (±0.00)	0.16 (±0.01)
Rq (µm)	0.03 (±0.00)	0.05 (±0.00)	0.21 (±0.00)
Rsk	0.07 (±0.14)	-0.28 (±0.22)	-1.67(±0.50)
Rku	3.17 (±0.74)	3.22 (±0.31)	11.64 (±1.09)

5.2.4. Comparison of roughness data

The roughness data for the substrates studied in this chapter was measured using White Light Interferometry, Alicona and surface profilometer Surfcom. The WLI was used to measure the roughness data on stainless steel with 2B finish and glass. The reason for not measuring stainless steel with mirror finish is that it has a highly reflective surface and interferometric technique was not suitable for it. Alicona was used to collect data on stainless steel with 2B and mirror finish but not on glass as Alicona is not suitable for measuring transparent surfaces that are extremely smooth. Surfcom surface profilometer was used on all three substrates. As it is a contact stylus type apparatus the reflectance and transparency does not influence its measurement capabilities.

The data collected via three different techniques indicate that the substrate roughness increases from glass, stainless steel mirror finish to stainless steel with 2B finish. Glass according to both WLI and Surfcom measurements has the lowest roughness average which is in nanometre scale (7 -20 nm). All three measurement techniques indicate that stainless steel with 2B finish displays the highest roughness with roughness average being in the range of 140-160 nm. The WLI was used to obtain the surface area index of substrates. Surface area index is similar to the Wenzel roughness term, it is the ratio of the actual surface area to the projected one, ideally a smooth and planar surface would give a surface area index of 1. Table 5-1 presents the values generated by WLI software for glass and stainless steel with 2B finish. According to WLI measurements, glass has the ideal smooth surface with a index of 1 while stainless steel has the value of 1.13 which suggests that it has some degree of surface heterogeneity even though its roughness average value is in the nanometre scale. As mentioned in Chapter 2, roughness plays an important part in substrate's wettability. It can either enhance or reduce it. However, the degree of roughness that influences wettability has to be taken into account. As presented in Chapter 2, Figure 2.10, as the Wenzel's roughness parameter increases the wettability characteristic changes and according to the plot, an index of even 1.2 does not significantly affect the repellence/wettability. This suggests that the roughness of substrates in this study should not have a significant impact on their wettability. The main parameter that will affect it will be surface chemistry and this chapter will study its impact.

5.3. Glass and stainless steel 304 – surface dehydration, dihydroxylation, and rehydroxylation

Since the hydroxyl groups on surface are the reactive sites that are able to interact with silanes and water it is essential to understand how different surface treatments might affect it. In order to understand the surface properties of glass and stainless steel 304 substrates, they were subjected to dehydration at 150ºC for 18 hours in the oven, humidity treatment at 85% relative humidity at 85ºC for 18 hours and humidity treatment followed by 15 minutes drying in the oven at 150ºC. Prior to thermal and humidity treatments the substrates were cleaned via IPA wipe. Following surface treatments, contact angles with water and diiodo-methane probe liquids were measured immediately. Figure 5.4 presents the contact angles obtained.

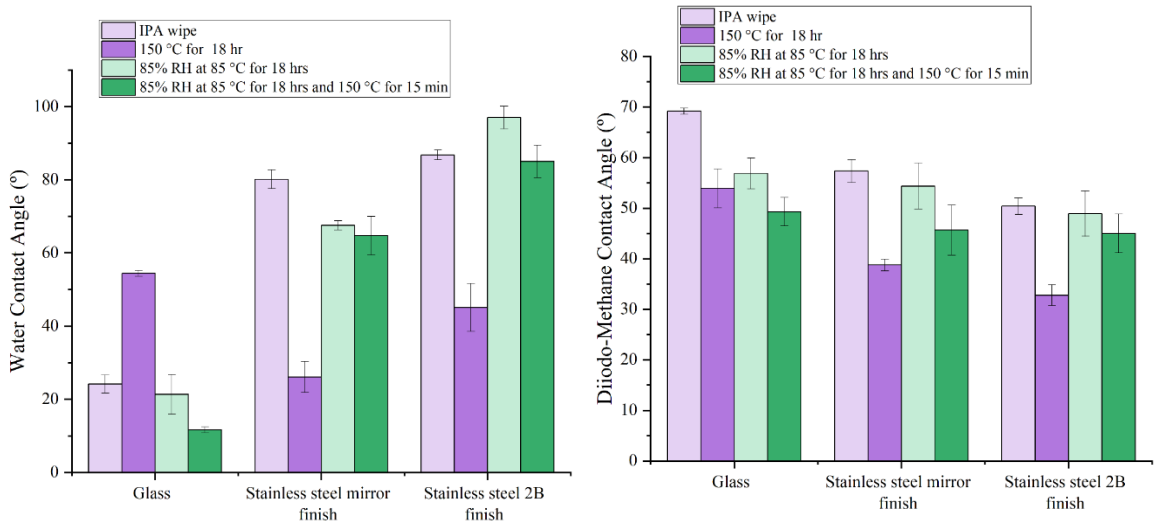

Figure 5.4 Water and diiodo-methane contact angles after surface treatments

The glass surface after IPA wipe was extremely hydrophilic with a water contact angle of just 24º. After surface dehydration at 150ºC, the surface becomes slightly less hydrophilic with CA increasing to 55º suggesting that the physiosorbed water on the surface had been removed with possibility of reduction of OH groups on the surface. On the other hand, humidity treatments make the glass surface even more hydrophilic with a decrease in WCA to 21º after air drying and to 11ºC after oven drying at 150ºC. Comparing the stainless steel substrate to glass, the IPA wiped stainless steel exhibited a much higher water contact angle of 87º for the 2B finish and 80º for the mirror finish sample. Considering that both stainless steels are of the same grade, 304, they should have similar chemical compositions and thus surface chemistry. The difference in the contact angle could be explained by the surface roughness which is depended on surface finish as described in Chapter 2 (Figure 2.10). After

heat treatment both the stainless steel substrates exhibited a drop in water contact angle to 45º (2B) and 26º (mirror), which could be explained by the decomposition of trace surface contaminants and rehydroxilation of the surface (Williams *et al.*, 2017). Whilst the humidity treatment decreased the WCA for the mirror finish surface, the 2B grade surface showed an increase in the WCA to 97º. Glass and stainless steel have different compositions and surface chemistries which have an influence on their surface hydroxy group coverage and dehydration mechanisms. Chromium-rich steels commonly terminate in a layer of hydroxide while in the absence of chromium frequently show the oxy-hydroxides (Castle, 2008). The metal surface is the base for the surface layers and, to some degree it guides the structure of those layers by the phenomenon of epitaxy. The segregation of non-metallic and metallic elements to free metal is of great importance in understanding metallurgical phenomena. Although their effect on the formation of an oxide layer may be minimal, sulphur is believed by some to influence the adhesion of oxides to metal surfaces (Castle, 2008). During interaction with water, chromium steels lose the iron constituent in their oxide by selective solution of Fe^{++} ions. In the presence of water vapour, the oxide converts to hydroxides. On heating, solid state reactions between the oxidised material and the underlying metal occur at a temperature of 200ºC. This leads to the more enriched surface in stable oxide (Castle, 2008). Takahashi *et al.* (2012) studied the hydrophilic states of stainless steels after heat treatments. In the study it was found that the hydrophilisation after heat treatments proceeded according to two mechanisms. One is the decomposition of surface contaminants. The other is the removal of surface hydroxyl groups followed by chemisorption of water on dehydroxylated sites. As a result of the fewer surface contaminants and the surface rehydration, the total number of surface hydroxyl groups on stainless steel became larger than that on the original surface (Takahashi and Fukuzaki, 2012).

In terms of diiodo-methane contact angles, the opposite effect was observed. DCA was the highest after IPA wipe and was reduced by heat and humidity treatments. As diiodo-methane is a non-polar liquid with liquid surface tension solely provided by Van der Waals (dispersion) forces, increasing the density of surface hydroxyl groups is expected to enhance DCA as the polar nature of the surface increases. Williams *et al.* (2017) studied the modification of stainless steel 316 by cold atmospheric plasma. To understand the changes in the SFE, XPS was used to analyse the surface for chemical changes induced by exposure to the plasma. The reduction in the carbon contamination at the surface was demonstrated. The increase in the polar component corresponded with an increase in oxygen on the surface. Similarly, an increase in the polar component of the SFE of 304 stainless steel was observed

after heat treatment Figure 5.5. Williams et al (2017) also observed that there may be a limit to the removal of carbon contaminant as the polar carbon is more strongly attached to the oxide surface. Therefore, the non-polar carbon is removed revealing a layer of oxygen containing polar carbon (Takahashi and Fukuzaki, 2012). Carbon contaminants on the surface could explain the change in the contact angle with diiodo-methane.

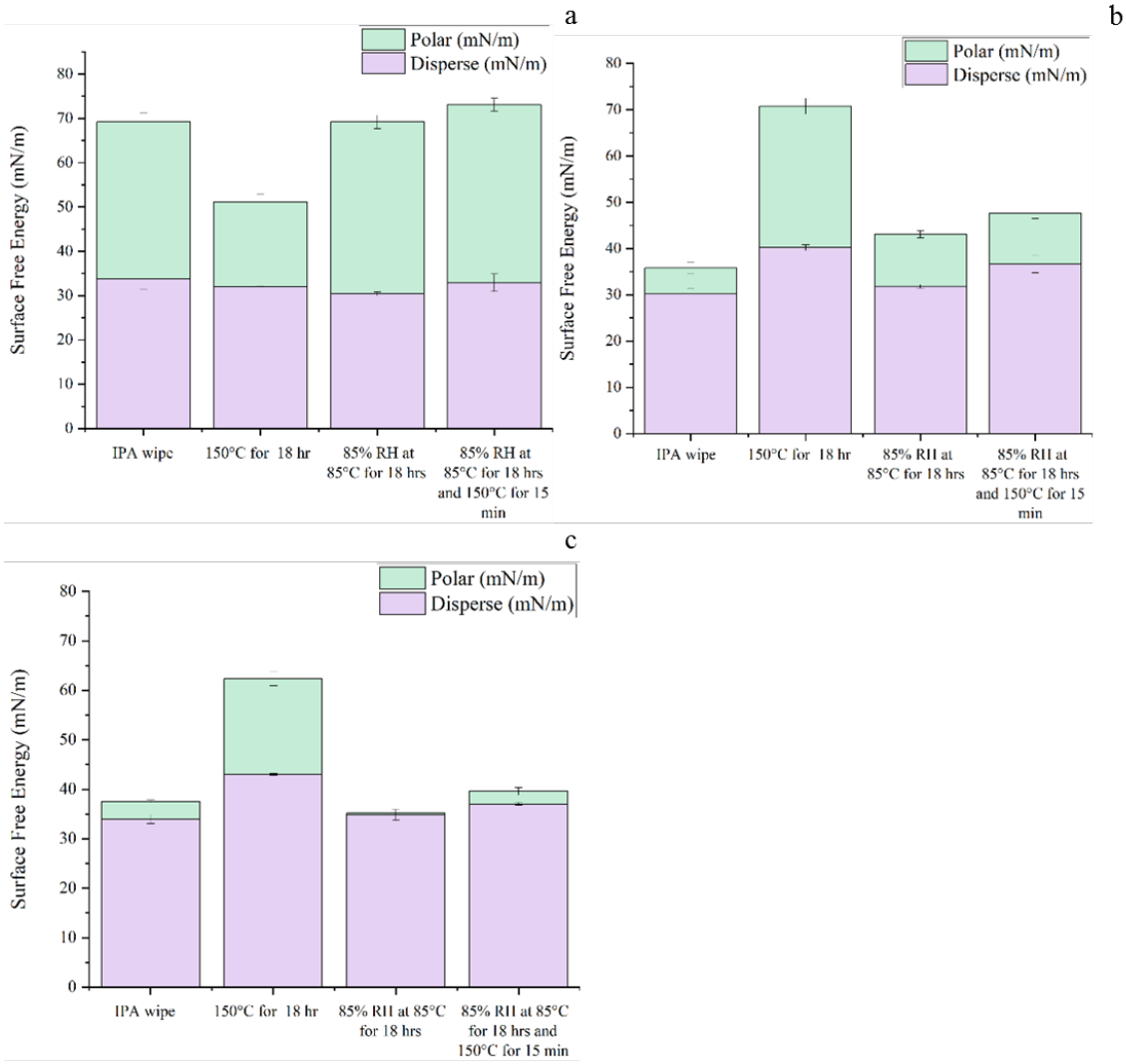

Figure 5.5 Surface free energy after treatments for glass (a), stainless steel mirror finished (b) and stainless steel 2B finished

The surface free energies of the substrates after thermal and humidity treatments were calculated using the OWRK method based on water and diiodo-methane contact angles presented in Table 5-4. This approach allowed the separation of the polar and disperse components of each of the surfaces investigated.

For the glass substrates, the polar component of the SFE was significantly affected by the heat or humidity while the disperse component remained relatively constant. The biggest change in the polar component was after the thermal treatment at 150ºC for 18 hours, which resulted in a significant decrease in the polar component. This can be explained by surface dehydration and as a consequence a decrease in the density of surface hydroxyl sites. There was little difference in the SFE of the samples subjected to different humidity treatments. Whilst there are minor differences in the measured WCA and DCA, the net effect is that these surfaces are broadly equivalent. This could mean that the surface had already adsorbed water at standard atmospheric conditions and further increase in humidity did not have an impact.

The stainless steel substrates have lower SFE polar component values compared to glass, but the disperse component exhibits greater variations after the various treatments. Contrary to the behaviour observed on the glass samples, the heat treatment increased the polar SFE component for both stainless steel materials, the disperse component also increased for both steel surfaces. The exposure to a humid environment however had the impact of a slightly increasing the polar term on the mirror finished surface compared to the IPA wiped surface. Under the same conditions the 2B grade surface exhibited a reduction in the polar term with the humidity treatment with no subsequent heating demonstrating a negligible contribution of the polar term to the observed SFE.

In summary, the SFE of the glass has a stable and constant disperse term. Heating and exposure to a humid environment had a negligible impact on this term, whilst the polar term showed considerable variation. Heating the glass appears to reduce the polar contribution whilst exposing it to humidity increases this term. A dehydration, rehydration mechanism would account for this behaviour. The steel surfaces show a far more complex behaviour. The disperse term is changed by heating at 150°C, the polar term also changes significantly by this treatment. The surface finish appears to have a notable effect on the polar term on exposure to damp heat. The behaviour of the steel therefore cannot be explained by a simple hydration model.

Table 5-4 CA and SFE of substrates after treatments

Substrate	Treatment	WCA [º]	DCA [º]	SFE [mN/m]	Disperse [mN/m]	Polar [mN/m]
Glass	IPA wipe	24.2 (±2.5)	69.2 (±0.6)	50.8 (±1.2)	33.8 (±2.5)	35.4 (±2)
	150 °C for 18 hr	54.4 (±0.8)	53.9 (±3.9)	51.1 (±1.9)	32.1 (±0.2)	19.0 (±1.9)
	85% RH at 85 °C for 18 hrs	21.3 (±5.4)	56.9 (±3.1)	69.2 (±2.0)	30.4 (±0.4)	38.8 (±1.5)
	85% RH at 85 °C for 18 hrs and 150 °C for 15 min	11.7 (±0.8)	49.3 (±2.8)	73.1 (±3.4)	32.9 (±2.0)	40.2 (±1.5)
Stainless steel (304) 2B finish	IPA wipe	86.8 (±1.3)	50.4 (±1.6)	37.5 (±1.2)	34.0 (±0.9)	3.6 (±0.3)
	150 °C for 18 hr	45.1 (±6.6)	32.8 (±2.0)	62.4 (±1.6)	43.0 (±0.2)	19.4 (±1.5)
	85% RH at 85 °C for 18 hrs	97.0 (±3.1)	48.9 (±4.5)	35.2 (±1.1)	34.9 (±1.1)	0.4 (±0.0)
	85% RH at 85 °C for 18 hrs and 150 °C for 15 min	85.0 (±4.4)	44.9 (±3.8)	39.6 (±0.9)	37.0 (±0.3)	2.6 (±0.7)
Stainless steel (304) mirror finish	IPA wipe	80.1 (±2.6)	57.3 (±2.3)	35.8 (±2.5)	30.1 (±1.3)	5.7 (±1.2)
	150 °C for 18 hr	26.1 (±4.3)	38.8 (±1.1)	70.7 (±2.1)	40.2 (±0.6)	30.5 (±1.7)
	85% RH at 85 °C for 18 hrs	67.5 (±1.2)	54.4 (±4.5)	43.1 (±1.1)	31.8 (±0.4)	11.3 (±0.8)
	85% RH at 85 °C for 18 hrs and 150 °C for 15 min	64.7 (±5.3)	45.7 (±4.9)	47.7 (±3.0)	36.6 (±1.8)	11.0 (±1.2)

5.3.1. Temperature effect on surface dehydration

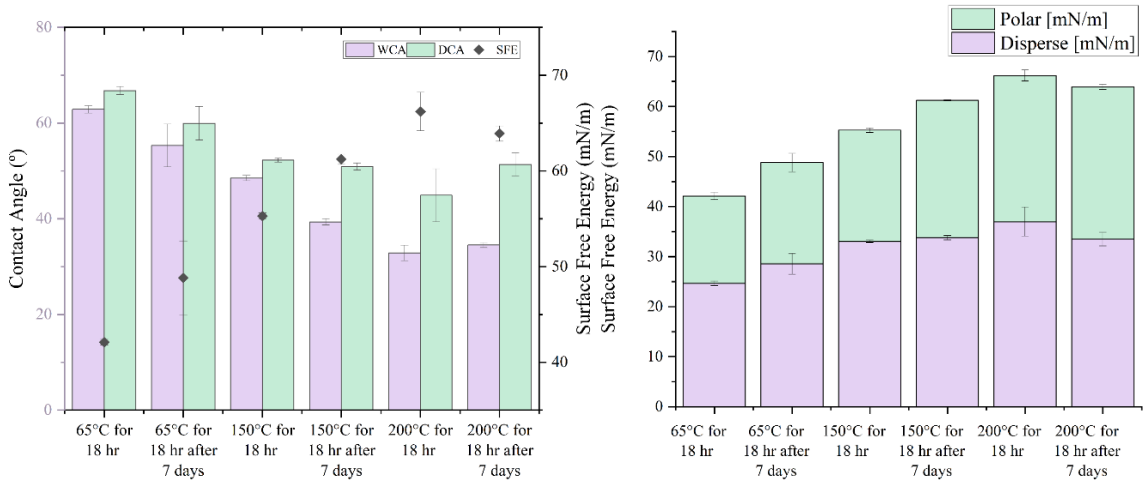

Figure 5.6 Probe liquid contact angles and surface free energy of glass after thermal treatments

To further study the effect of thermal treatment on the dehydration of glass slides, the substrates were subjected to 65ºC, 150ºC and 200ºC for 18 hours after which they were left under atmospheric conditions for 7 days to study the level of surface rehydration. The results of obtained contact angles and calculated surface free energies are presented in Figure 5.6 and Table 5-5.

The increase in temperature has a significant impact on the contact angles, the increased thermal treatment temperature causes both water and diiodo-methane contact angles to decrease. As presented earlier in Table 5-4, the water contact angle on glass after the IPA wipe and no thermal treatment is 24º. This means that the thermal treatment increases the hydrophobicity of the surface compared to samples that were not exposed to elevated temperature. However, as the temperature of thermal treatment is increased the contact angle decreases with it (Figure 5.6). Zhuravlev (1993) performed a survey on the properties of amorphous silica. He studied the temperature boundary of surface dehydration and dehydroxylation as well as the concentration of hydroxyl groups on the silica surface. Zhuravlev suggested that there may be two types of physically adsorbed water on the silica surface; one with activation energies of desorption in the range of 6–8 kcal/mol and another one in the range of 8–10 kcal/mol (Zhuravlev, 1993). Removal of physisorbed water or surface dehydration, occurs at low temperatures. The temperature related to the completion of dehydration and the beginning of dehydroxylation by condensation of surface OH groups is estimated to be 190ºC. Most of the physisorbed water is removed at about 150ºC and at 200ºC silica surface is made of single, geminal, vicinal, and terminal silanol groups and siloxane bridges (Roberts, W.O., & Bergna, 2005). Because of the shift in the electronic

density in going from O atom to Si atom, the formation of a hydrogen bond between the oxygen on the surface of the sample and water molecules is not favoured. Sufficient surface concentration of hydroxyl groups makes the surface hydrophilic while the predominance of siloxane bridges on the silica surface makes the surface hydrophobic.

The data presented in Figure 5.6 and Table 5-4 suggests that the surface dehydration occurred causing WCA to increase from 24º to 63º. According to Zhuravlev (1993), it would be expected for the surface to dehydroxylate at the elevated temperatures forming hydrophobic siloxane bridges. However, the surface became more hydrophilic. The reason behind the decreased water repellence might be that after the surface has undergone dehydration, it mainly consists of vicinal or geminal hydroxyl groups. As shown in Figure 5.1, vicinal groups can be either interacting or isolated. Interacting vicinal groups have less affinity to interact with water deposited on the surface compared to isolated hydroxyl groups. As the surface is subjected to higher temperatures, it starts to undergo dehydroxylation – it loses hydroxyl groups. Causing the surface hydroxyl density to decrease and therefore the distance between the hydroxyl groups increases, shifting interacting vicinal groups to become isolated. This shift might explain the increased hydrophilicity of the studied glass surface. In terms of the surface rehydration after 7 days at atmospheric conditions, the decrease in contact angle for treatments at 65ºC and 150ºC was observed. However, for 200ºC treatment there is no significant change even after 7 days. This supports the assertion that under these conditions the surface becomes dehydrated as well as dehydroxylated and so complete rehydroxylation cannot be achieved at atmospheric conditions.

Table 5-5 Values of probe liquid contact angles and surface free energy of glass after thermal treatments

	WCA [º]	DCA [º]	Surface free energy [mN/m]	Disperse [mN/m]	Polar [mN/m]
IPA wipe and 65°C for 18 hr	62.9 (±0.8)	66.8 (±0.8)	42.1 (±0.3)	24.7 (±0.5)	17.4 (±0.8)
IPA wipe and 65°C for 18 hr after 7 days	55.4 (±4.5)	60.0 (±3.5)	48.8 (±3.9)	28.6 (±2.0)	20.2 (±1.8)
IPA wipe and 150°C for 18 hr	48.5 (±0.6)	52.2 (±0.4)	55.3 (±0.3)	33.0 (±0.2)	22.3 (±0.4)
IPA wipe and 150°C for 18 hr after 7 days	39.4 (±0.6)	50.9 (±0.8)	61.2 (±0.5)	33.8 (±0.4)	27.5 (±0.1)
IPA wipe and 200°C for 18 hr	32.8 (±1.6)	44.9 (±5.5)	66.2 (±2.0)	37.0 (±2.9)	29.2 (±1.1)
IPA wipe and 200°C for 18 hr after 7 days	34.5 (±0.5)	51.3 (±2.4)	63.9 (±0.8)	33.5 (±1.4)	30.4 (±0.6)

5.4. Commercial repellent coating selection

Coatings are used for a variety of purposes, for example they are used to provide surface protection from external factors (chemical, mechanical), to give surface a specific property (such as wettability, repellence, etc.) or for aesthetics. There is a wide range of available coatings on the market to make surfaces of glass or metal products more repellent.

Various low SFE chemicals can be used to treat the materials and reduce their SFE. Silanes, fluoropolymers and silicones are amongst the most employed materials for the enhancement of the repellence on the surfaces. Silanes with the hydrolysable groups react with water to form silanols, which react with hydroxyl groups at the surface of substrates to provide a protective coating where the silane's alkyl group reduces the SFE of the substrate. Silanes can be applied via chemical vapour deposition (CVD) or solvent deposition in solvents such as alcohols (Li *et al.* 2016). The deposition of silanes might form self-assembled monolayers (SAMs) dependent on the deposition conditions (Flink *et al.* 2001). The properties of the SAMs are dependent on the reaction conditions such as water content, solvent, and temperature. The hydrolysis and subsequent condensation of a silane layer is dependent on the silane concentration in the solution and can take from minutes up to hours. The formation of oligomers and polymers may affect the achieved coverage of the coating. The oligomerization and polymerization can be avoided by controlling the water content in the coating solution. The thickness of the silane layer on the substrate is typically less than 1µm, thus it does not affect the topography of the substrate. The conversion of the hydrolysed silanes into covalent siloxane network requires aging or baking of the sample at around 100 °C for several hours (Li *et al.* 2016).

Table 5-6 Composition of studied coating systems

Coating system	Dynasynal Sivo EC	Avalon Glass	Gelest Aquaphobe CF	Sivo Clear k1	Sivo Clear K2	Sharc Sapphire
Binder base:	Silane	Mixture of silanes	Chlorinated fluoroalkylmethylsiloxane CAS: 908858-79-7 95-100%	fluoroalkylsilane	Catalyst Aqueous	organic polysiloxane CAS: 346577-55-7 10-30% aminosilane CAS: 919-30-2 1-5%
Solvent base:	Propanol CAS: 67-63-0 93% Dodecane CAS: 112-40-3 5%	Propanol CAS: 67-63-0 50-90%	none	Ethanol CAS: 64-17-5 96%	Propanol CAS: 67-63-0 > 20%	hydrocarbon solvent CAS: 64742-48-9 20-50% butyl acetate CAS: 123-86-4 20-50%
Data Source:	('Dynasylan ® SIVO CLEAR EC Safety Data Sheet', 2016)	('AVALON ® Glass Safety Data Sheet')	('AQUAPHOBE ® CF Safety Data Sheet', 2018)	('Dynasylan® SIVO CLEAR K1 Safety Data Sheet', 2018)	('Dynasylan® SIVO CLEAR K2 Safety Data Sheet', 2016)	('Sharc ® Sapphire Safety Data Sheet', 2019)

Coating system	Gelest Aquaphobe CM	Solarsharc	Tutoprom bright	Gelest siliclad	Aculon ON-305	Aculon ON-353
Binder base:	1,5-Dichloro-1,1,3,3,5,5-hexamethyltrisiloxane CAS: 3582-71-6 30-60% 1,3-Dichlorotetramethyldisiloxane CAS: 2401-73-2 20-50% 1,7-Dichlorooctamethyltetrasiloxane CAS: 2474-02-4 20-50%	Organic Polysilazane Functionalised silica nanoparticles	Organic polysilazane	Octadecylsilane derivative	Proprietary Polymer 5% Methyl Nonafluoroisobutyl Ether CAS: 163702-08-7 45%	Proprietary ingredient < 5%
Solvent base:	no	n-butyl acetate	n-butyl acetate	tertiary alcohols and diacetone alcohol	Isooctane CAS: 540-84-1 45% Isopropanol CAS: 67-63-0 5%	Aculon Fluorosolvent 1 20 – 80 % Aculon Fluorosolvent 2 20 – 80 % Proprietary ingredient < 5%
Data Source:	(‘AQUAPHOBE ® CM Safety Data Sheet’, 2018)		(‘tutoProm® bright Material Safety Data Sheet’)	(‘Siliclad® Safety Data Sheet’)	(‘Aculon ON-305 Materials Safety Data Sheet’)	(‘Aculon ON-353 Materials Safety Data Sheet’)

Table 5-7 Coating properties

Coating system	**Dynasynal Sivo EC**	**Avalon glass**	**Gelest Aquaphobe CF**	**Sivo clear k1**	**Sivo Clear K2**	**Sharc Sapphire**
Appearance:		Colourless liquid	Amber Liquid	Liquid colourless liquid		Liquid colourless liquid
Density:	0.79 g/cm3		1.4-1.43 specific gravity	0.8 g/cm3	0.89 g/cm3	
Condition of substrate:	Clean, dry					
Application:		ready to be used. Wipe coat and polish.	applied as 2-10 % solution in dry solvents such as hexane, methylene chloride or toluene.	Mix K1 and K2 components 1:1 by volume. Shake for 3 minutes and apply within one day. Wipe on the surface and polish.		Ready to use. Wipe coat and polish.
Substrate pre-treatment:	IPA wipe					
Drying /Curing:		Room temperature 1 hour	Heat curing at 110°C for 15-20 minutes in an exhausted oven.			Room temperature for 1 hour
Coating Thickness:			molecular			
Viscosity:	2.5 mPa.s		6-10 cSt.	2 mPa.s	3.7 mPa.s	
SFE of glass after treatment:			16-19 dynes/cm			
Data Source:	(‘Dynasylan ® SIVO CLEAR EC Product Information’)	(‘AVALON ® Glass Technical Data Sheet’)	(‘AQUAPHOBE ® CF Technical Data Sheet’)	(‘Dynasylan ® SIVO CLEAR K2 Dynasylan Product Information’, 2011)		(‘Sharc Sapphire Product Information’, 2011)

Coating system	Gelest Aquaphobe CM	Solarsharc	Tutoprom bright	Gelest siliclad	Aculon ON-305	Aculon ON- 353
Appearance:	Amber Liquid	colourless to pale yellow liquid	colourless to pale yellow liquid	Amber liquid	Liquid	Liquid
Density or specific gravity:	0.99-1.01 specific gravity	0.9 g cm3	ca. 0.86 g/cm3	0.88 specific gravity		1.52 specific gravity
Condition of substrate:	Clean, dry					
Application:	applied as 2-10 % solution in dry solvents such as hexane, methylene chloride or toluene.	Wipe coat under dry humid conditions				
Substrate pre-treatment:	IPA wipe					
Drying / Curing:	Heat curing at 110 °C for 15-20 minutes in an exhausted oven.	130 °C – 180 °C: for one hour. Alternatively ambient conditions for seven days	130 °C – 180 °C: for one hour			
Coating Thickness:	molecular	2 µm		molecular		
Viscosity:	3-6 cSt.			8-20 cSt.		
SFE of glass after treatment:	25 dynes/cm			31 dynes/cm		
Data source:	(‘AQUAPHOBE ® CM Technical Data Sheet’, no date)		(‘tutoProm® bright Technical Data Sheet’)	(‘Siliclad® Technical Data Sheet’, no date)	(‘Aculon ON-305 Materials Safety Data Sheet’)	(‘Aculon ON-353 Materials Safety Data Sheet’)

5.4.1. Commercial coating deposition method

The eleven coatings were deposited following recommendations in technical data sheets. In all cases the recommended deposition method was to pre-treat substrate with a cleaner that does not leave a residue. For this purpose, isopropanol alcohol was used. The coatings were wiped onto the surface, spread evenly and polished to remove excess wet film material. Several coating deposition methods were tried such as dip-coating and wipe coating. It was observed that dip-coating does not provide uniformly deposited coating and coating develops cracks. Wipe-coating application avoided this problem.

Gelest coatings Aquaphobe CM and CF were diluted with xylene according to the instructions and for the Siliclad water was used as the diluent.

Curing of the coatings was performed according to the supplier recommendations mentioned in Table 5-7.

5.5.Substrate topography after coating deposition

To confirm that the surface topography does not change after coating deposition and does not have an effect on wettability, the glass slides were measured and compared to the uncoated samples. Figure 5.7 shows WLI images of fluorinated and non-fluorinated silanes, siloxanes and silazanes deposited on the glass substrate. Figure 5.7 (a) shows Tutoprom, Figure 5.7 (b) shows Tutoprom deposited via dip-coating on glass and shows half of the glass covered by Tutoprom while the other half is untreated glass substrate. From the WLI image, the coating thickness after dip-coating was estimated to be around 0.7 μm. The wipe coated samples are so thin that they cannot be captured or measured by the Surfcom profilometer. The other WLI images are of Aquaphobe CM, Aquaphobe CF and Siliclad. Comparing the WLI images, it is apparent that wiping commercial coatings cover the surface uniformly. The roughness of the glass slides covered with commercial coatings was measured using Surfcom profilometer and the roughness parameter values obtained did not differ from untreated glass which once again confirms that the coatings do not seem to alter the surface topography or roughness and the effect of surface topography on wettability is kept at the minimum. The wettability and repellence data reported in chapter refer to the change of surface chemistry and not to the change in substrate roughness.

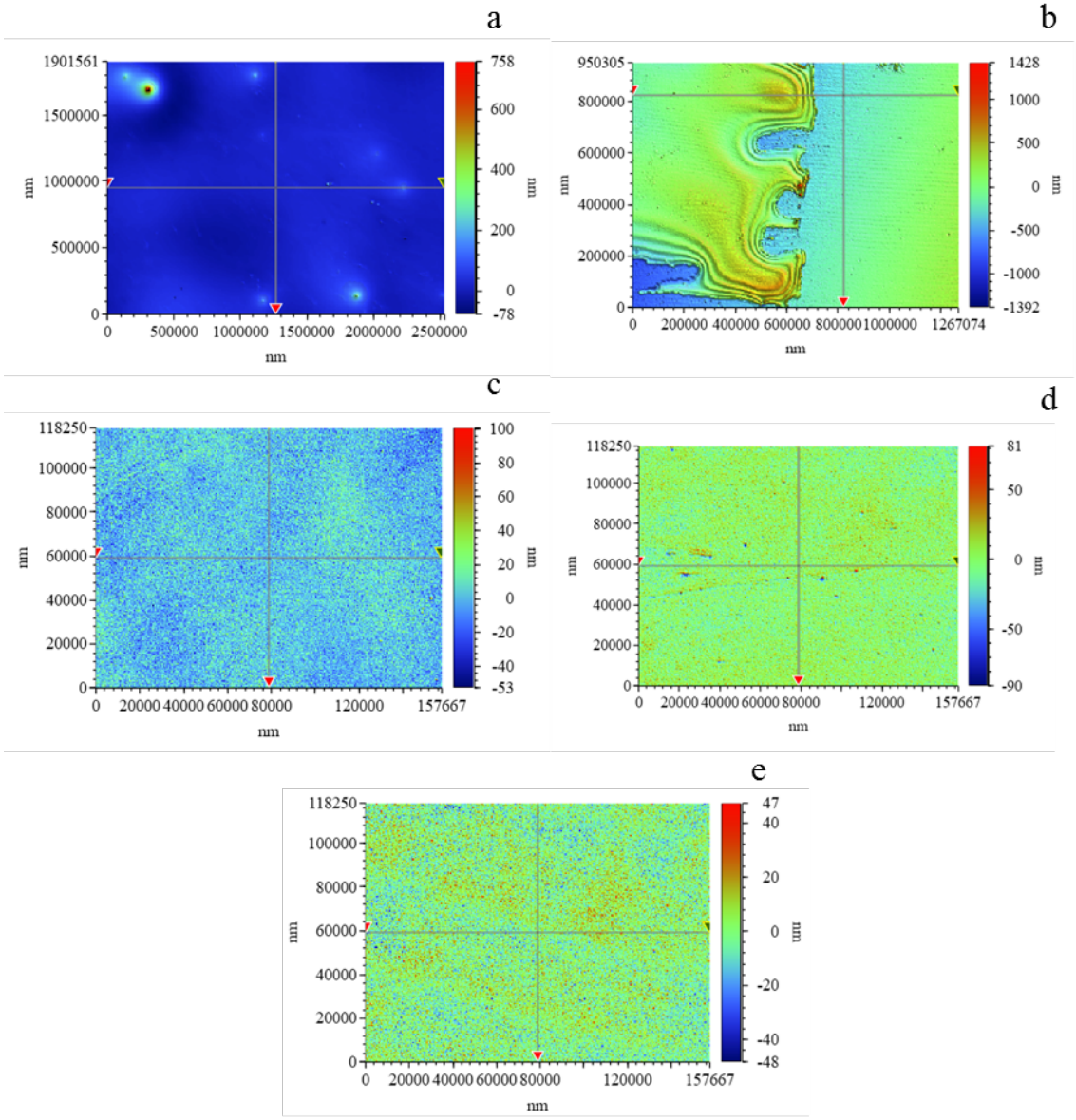

Figure 5.7 WLI images of glass substrates after coating deposition. Tutoprom wiped (a) and Tutoprom dip-coated (b), Aquaphobe CM (c), Aquaphobe CF (d), Siliclad (e)

5.6.Effect of surface pre-treatment on coating deposition

The effect of surface pre-treatment was studied to identify whether the change of the surface hydroxyl layer and physisorbed water caused by treatment affects adhesion of coating and thus affect final wettability of the substrate.

Three different pre-treatments were studied: IPA wipe, IPA wipe followed by 200º bake for 1 hour and sonic cleaning for 15 minutes in acetone solvent. Glass slide without coating,

with Sapphire coating and Sivo EC coating was studied. The same testing was performed on stainless steel. The results obtained are presented in Table 5-8.

Table 5-8 Effect of surface pre-treatment on CA

Coating	Substrate	Treatment	WCA [º]	DCA [º]
No coating	Glass	IPA wipe	24.2 (±2.5)	50.8 (±1.2)
		IPA wipe and 200 °C for 1 hr	35.9 (±0.9)	37.5 (±1.6)
		Sonic cleaning 15 min in acetone	35.6 (±2.8)	40.3 (±1.5)
	Stainless steel 304 mirror finish	IPA wipe	82.5 (±1.9)	60.1 (±3.1)
		Sonic cleaning 15 min in acetone	63.4 (±3.2)	45.5 (±3.0)
		IPA wipe and 200 °C for 1 hr	60.2 (±4.7)	33.1 (±2.0)
Sharc Sapphire	Glass	IPA wipe	104.4 (±0.2)	77.0 (±0.7)
		IPA wipe and 200 °C for 1 hr	93.0 (±0.9)	64.0 (±2.7)
Sivo EC Clear		IPA wipe	106.0 (±1.2)	92.9 (±2.0)
		IPA wipe and 200 °C for 1 hr	74.6 (±3.4)	90.2 (±1.0)
Sharc Sapphire	Stainless steel 304 mirror finish	IPA wipe	98.8 (±2.9)	72.6 (±2.3)
		IPA wipe and 200 °C for 1 hr	94.9 (±1.9)	63.5 (±2.3)
Sivo EC Clear		IPA wipe	109.7 (±1.0)	91.8 (±1.1)
		IPA wipe and 200 °C for 1 hr	110.7 (±0.7)	91.5 (±2.4)

Comparing the uncoated glass slides (Figure 5.8), additional heat treatment and sonic cleaning cause increase in water contact angle while decreasing the values of the DCA. As previously explained, this is caused by a decrease in the surface hydroxyl level. Stainless

steel shows, as expected, higher hydrophilicity after the heat treatment as well as after the acetone cleaning.

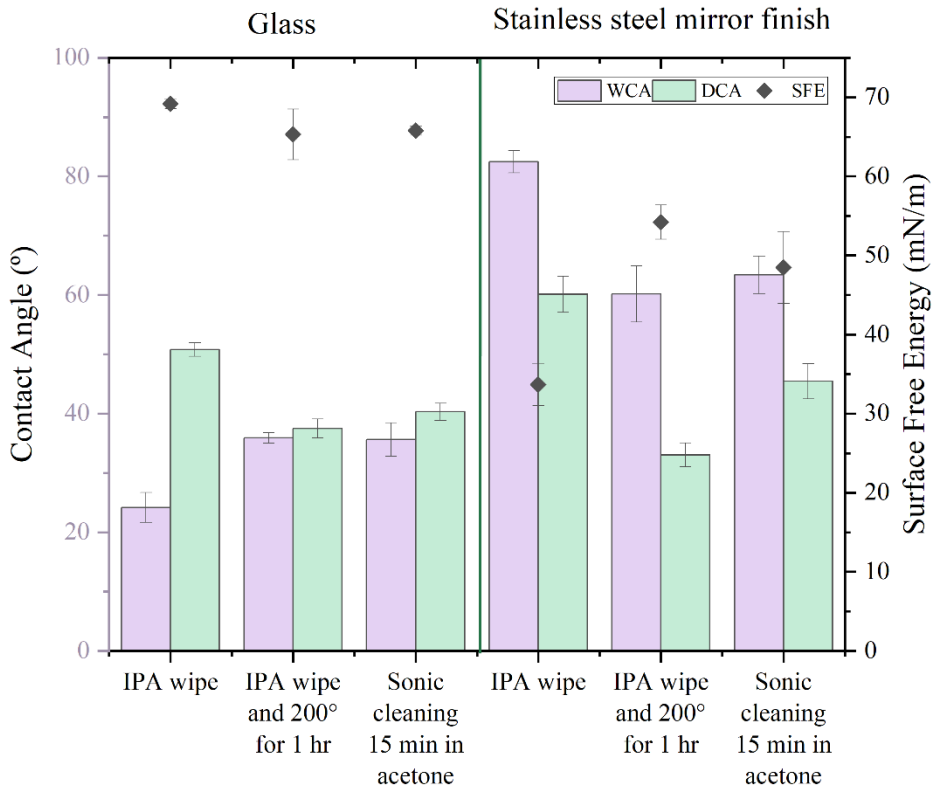

Figure 5.8 CA values for glass and stainless steel 304 without coating

Comparing the coated glass slides (Figure 5.9), additional heat treatment prior to the coating deposition decreased the final contact angles of both WCA and DCA. As studied earlier in this chapter, thermal treatment of the substrate affects its wettability. The wettability of the substrate is an important property that has an influence on the deposition and adhesion of the coating. The results obtained showed that pre-treatment had a slight effect on the final contact angles with probe liquids. The coated stainless-steel slides (Figure 5.9) showed a slight change in contact angles but the decrease was not as significant as for glass. Comparing the fluorinated treatment (Sivo EC) and non – fluorinated treatment (Sharc Sapphire) on IPA wiped glass. The water contact angle was identical for both treatments showing WCA of ~105º. However, WCA for Sivo EC after thermal pre-treatment showed more significant decrease than SharcSapphire indicating that less of the coating adhered to the dehydrated surface. Despite Sivo EC and Sharc Sapphire showing identical WCA on glass, the DCA was significantly higher for fluorine containing coating (Sivo EC). Zisman (1964) found that the SFE depends on the constituent groups in polymers, as follows: CH2 (36mN/m) > CH3 (30 mN/m) > CF2 (23 mN/m) > CF3 (15 mN/m). He reported that the

replacement of a single fluorine atom by a hydrogen atom in a terminal -CF 3 group more than doubles the critical surface energy. Fluorinated surface treatments have lower SFE and therefore display higher contact angles with low surface tension probe liquids.

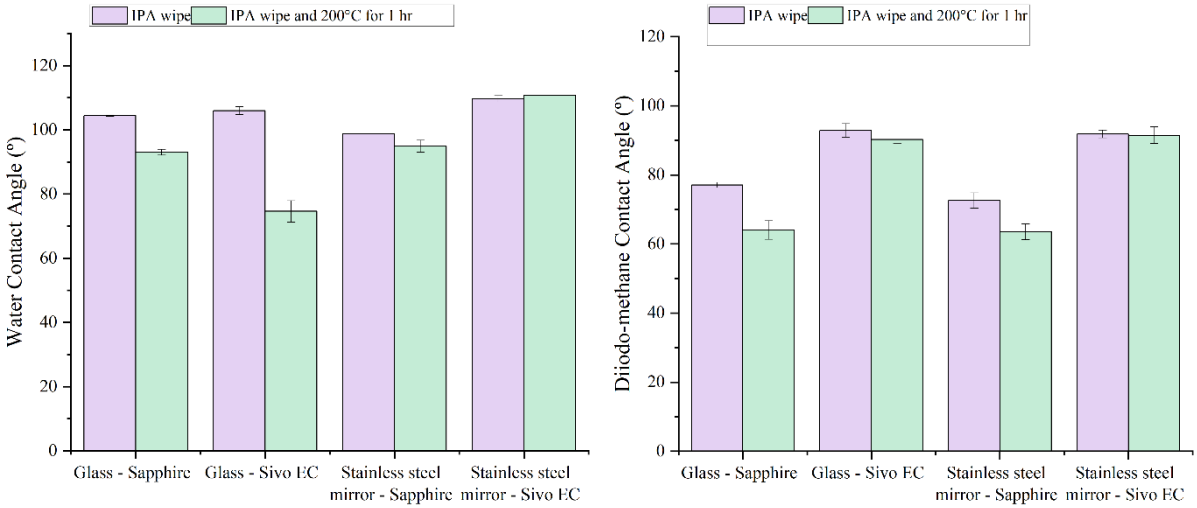

Figure 5.9 Water and diiodo-methane contact angles after coating deposition

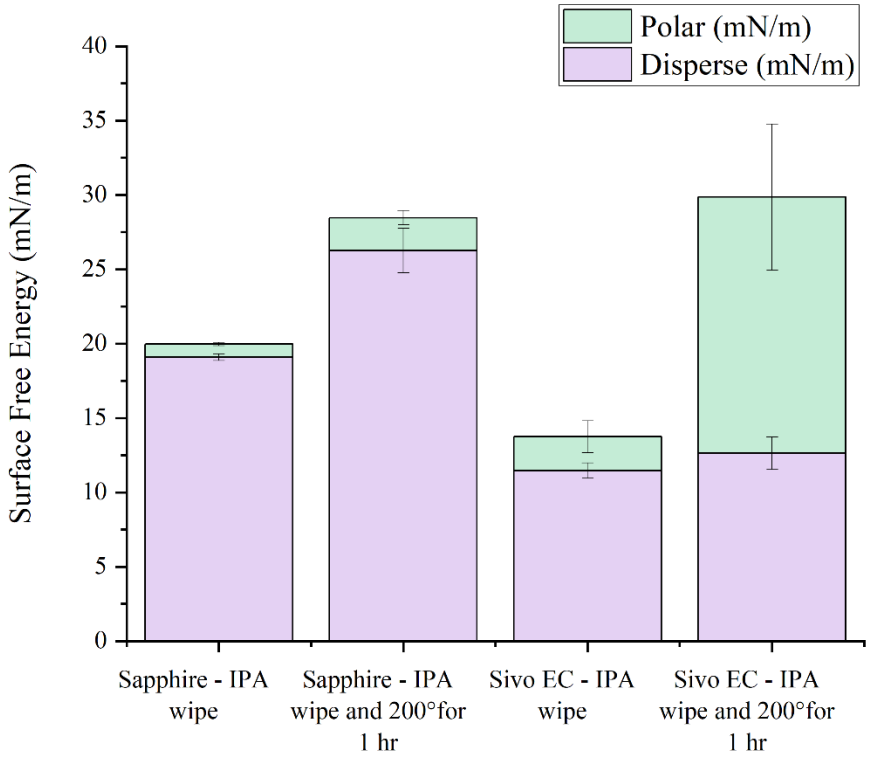

Figure 5.10 Surface free energy of glass

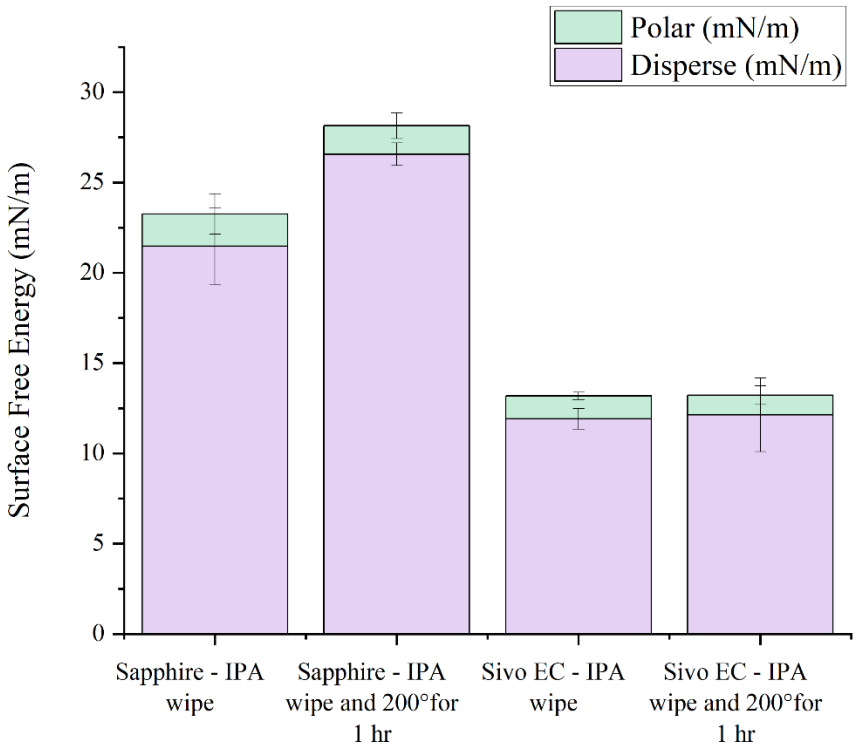

Figure 5.11 Surface free energy of stainless steel

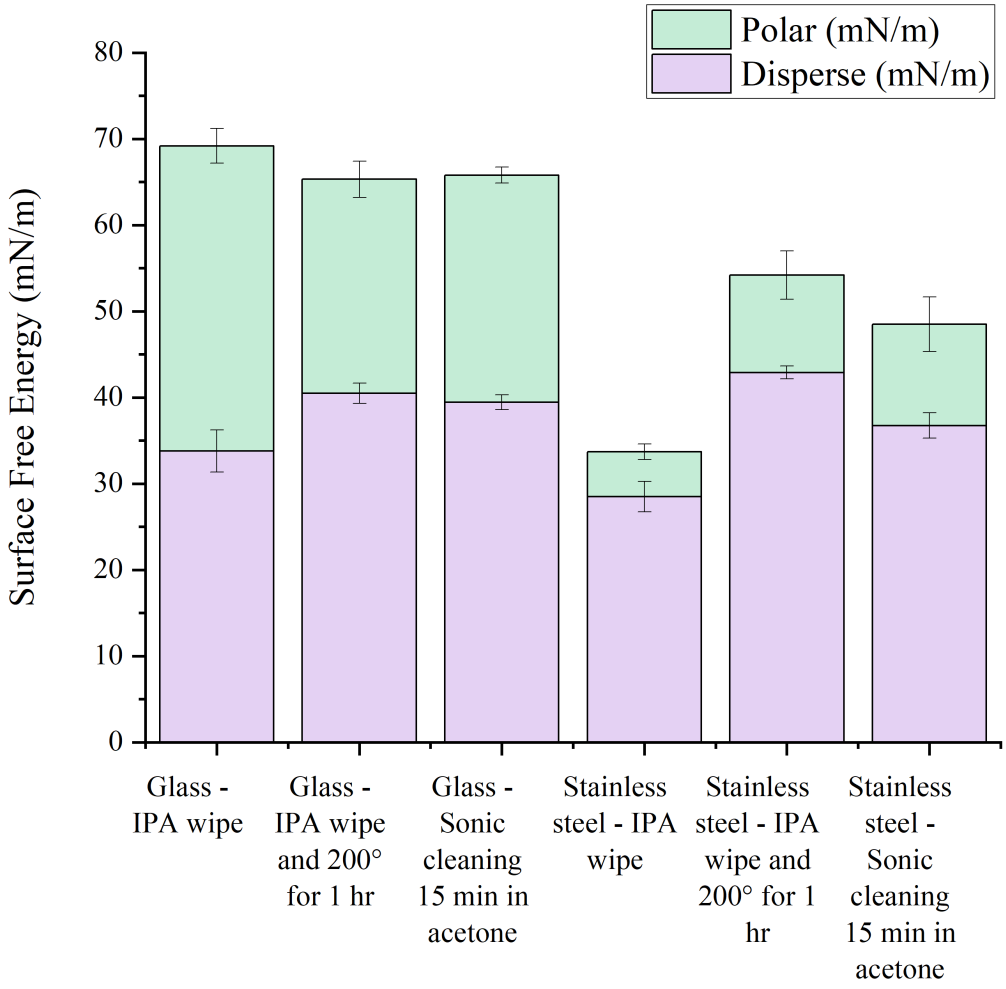

Figure 5.12 Surface free energy of substrates without coating

The surface free energies of treated (Figure 5.10) and untreated glass (Figure 5.12) and stainless steel 304 treated (Figure 5.11) and untreated (Figure 5.12) are presented. On the glass substrate, after the IPA wipe, Sapphire exhibits higher disperse SFE compared to Sivo EC. The polar part of SFE is identical for both treatments hence the main factor dictating differences in SFE is the disperse part. The fluorinated treatment has higher level of lipophobicity, the higher contact angle with DCA is considered in the SFE calculation, which brings the overall SFE down. The thermal pre-treatment increases the polar part of SFE for Sivo EC and disperse part for Sapphire treated glass. On stainless steel substrates there is no significant change in polar component depending on substrate, pre-treatment or chemical treatment. On the glass slides without coatings, pre-treatments decrease the polar component and increase disperse part while on stainless steel the polar component is increased.

5.6.1. Wettability after surface treatment with commercial coatings

Coating performance was assessed by the sessile drop measurement performed with Kruss DSA 100, the measurement methodology for determining contact angles using the Kruss DSA equipment is described in Chapter 4.

For the initial wettability the measurement of static contact angles was undertaken using water and diiodo-methane as the probe liquids. Water contact angle (WCA) and diiodo-methane contact angle (DCA) were used to calculate surface free energy (SFE) of the coated substrate using OWRK method.

Table 5-9 presents values of WCA, DCA and SFE for coatings that were deposited on glass and stainless steel 304 with 2B finish.

Table 5-9 Commercial coating WCA, DCA and SFE on glass

Coating	WCA [º]	DCA [º]	Disperse [mN/m]	Polar [mN/m]	SFE [mN/m]
Sivo EC	95.3 (±4.4)	84.8 (±3.5)	15.1	4.4	19.6
Avalon Glass	88.9 (±3.5)	85.8 (±6.4)	14.7	7.3	22.0
Aquaphobe CF	94.1 (±5.8)	78.2 (±1.5)	18.4	3.9	22.3
Sivo Clear K1 + K2	88.9 (±11.3)	85.1 (±6.7)	15.0	7.5	22.5
Sharc Sapphire	97.4 (±0.1)	72.9 (±0.4)	21.3	2.0	23.3
Aquaphobe CM	92.3 (±1.3)	67.4 (±3.2)	24.3	2.8	27.2
SolarSharc	88.1 (±5.5)	66.6 (±1.4)	24.8	4.2	29.0
Tutoprom Bright	86.6 (±2.8)	64.0 (±2.3)	26.3	4.2	30.5
Siliclad	89.2 (±1.8)	58.5 (±3.9)	29.4	2.6	32.1
Aculon 305	77.2 (±1.1)	67.2 (±1.8)	24.7	9.3	34.1
Aculon 353	67.3 (±2.9)	63.0 (±2.6)	26.8	13.6	40.4

As can be seen from the table, the commercial coatings on glass gave WCA values in the range of 67 to 96º, DCA values in the range of 63 to 84º and SFE values between 20 and 40 mN/m.

Table 5-10 Commercial coating WCA, DCA and SFE on stainless steel 304 with 2B finish

Coating	WCA [º]	DCA [º]	Disperse [mN/m]	Polar [mN/m]	SFE [mN/m]
Sivo EC	112.7 (±2.1)	91.1 (±4.6)	12.3	0.7	13.0
Avalon Glass	115.9 (±0.8)	89.3 (±0.2)	13.0	0.3	13.3
Aquaphobe CF	114.9 (±1.9)	89.3 (±2.8)	13.0	0.4	13.4
Sivo Clear K1 + K2	114.7 (±1.8)	89.4 (±4.8)	13.1	0.4	13.4
Sharc Sapphire	108.1 (±1.2)	85.3 (±3.9)	14.9	1.0	15.9
Aquaphobe CM	101.6 (±1.7)	73.7 (±1.7)	20.8	1.2	22.0
SolarSharc	98.6 (±3.4)	70.1 (±3.9)	22.8	1.5	24.3
Tutoprom Bright	96.8 (±4.0)	69.0 (±4.6)	23.5	1.8	25.3
Siliclad	106.6 (±7.5)	63.8 (±7.9)	26.4	0.2	26.6
Aculon 305	97.6 (±0.6)	48.7 (±2.3)	35.0	0.3	35.3
Aculon 353	93.6 (±4.8)	43.9 (±2.7)	37.6	0.7	38.3

Coatings on stainless steel gave higher WCA values in the range of 94 to 113º, DCA values in the range of 44 to 91º and SFE values from 13 to 38 mN/m.

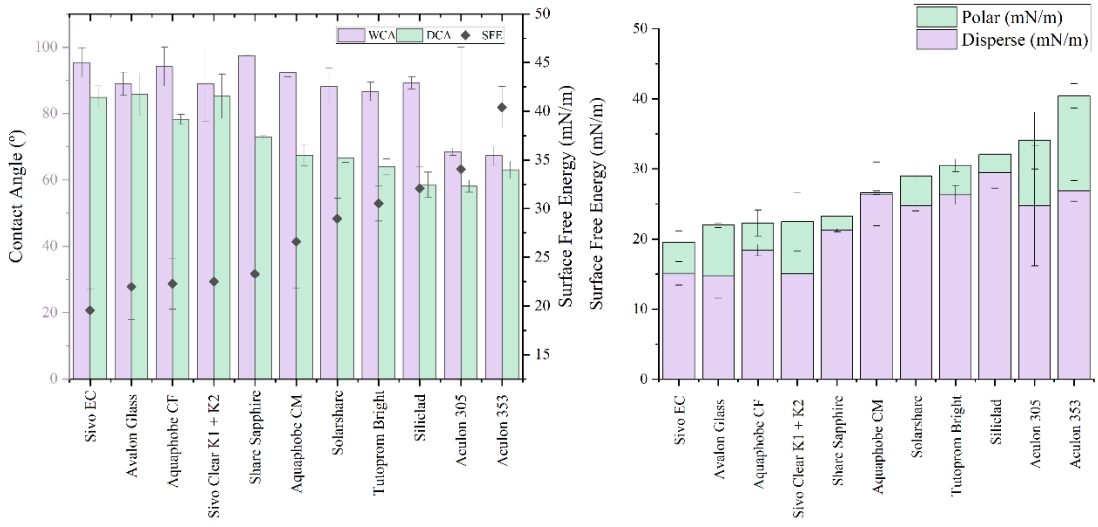

Figure 5.13 Contact angles and SFE for coatings deposited on glass

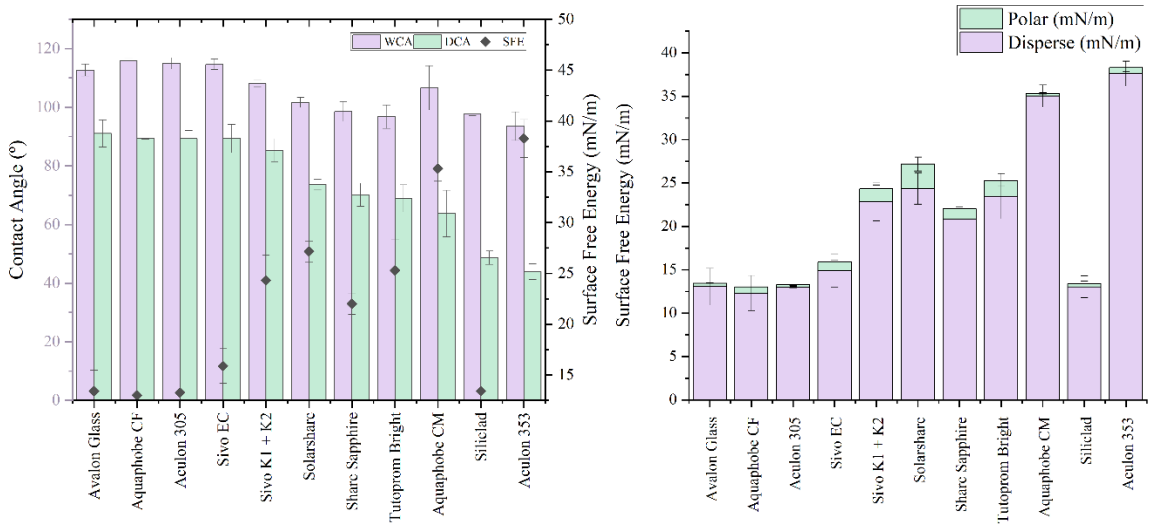

Figure 5.14 Contact angles and SFE for coatings deposited on stainless steel

Figure 5.13 presents the WCA, DCA and SFE values of the coatings deposited on glass and stainless steel. The coatings that showed highest values of both WCA and DCA on both substrates were the fluorinated silane-based coatings; Sivo EC, Avalon Glass, Aquaphobe CF, Sivo K1 + K2. The only non-fluorinated coating that showed similarly high WCA was Sharc Sapphire which is not a silane but a polysilazane coating. Comparing the SFE components, glass exhibits higher polar component values compared to stainless steel whose SFE consists mainly of the disperse component. For the glass substrates, Sharc Sapphire, Aquaphobe CM and Siliclad all decreased the polar part of the SFE the most compared to other coatings. None of these coatings contain fluorine, Siliclad is octadecylsilane derivative, Sharc Sapphire is methyl containing polysilazane and Aquaphobe CM consists of dichloro-hexamethyltrisiloxane, dichloro-tetramethyldisiloxane and dichloro-octamethyltetrasiloxane.

According to the initial wettability assessments, the coatings with the highest and lowest repellency on both glass and stainless steel were selected for more detailed investigation and were subjected to drop shape analysis using LST 50 and LST 30 probe liquids.

The results of these assessments are presented in Table 5-11 and Table 5-12.

Table 5-11 Contact angles with probe liquids – coatings deposited on glass

Coating	WCA (º)	DCA (º)	LST 50 (º)	LST 30 (º)
Avalon Glass	88.9	85.8	77.1 (±2.5)	24.4 (±5.2)
Aquaphobe CF	94.1	78.2	77.4 (±3.3)	34.3 (±3.7)
Aquaphobe CM	92.3	67.4	80.7 (±2.9)	37.4 (±1.8)
Siliclad	89.2	58.5	66.9 (±1.1)	25.8 (±3.8)
Aculon 353	67.3	63.0	62.8 (±4.0)	25.5 (±3.4)

On the glass it can be seen that LST 50 contact angles were in the range of 63 to 81º and LST 30 of 24 to 37º. LST 50 and diiodo-methane have similar surface tension of around 50mN/m, the difference is that LST is polar while diiodo-methane is apolar. LST 50 showed lower contact angles on fluorinated coatings (Aquaphobe CF, Avalon Glass) compared to diiodo-methane. Meanwhile a different trend can be seen with non-fluorinated treatments where LST 50 exhibited higher contact angles. According to Zisman (1964) the SFE depends on the constituent groups in polymers, as follows: CH_2 (36mN/m) > CH_3 (30 mN/m) > CF_2 (23 mN/m) > CF_3 (15 mN/m). It was also reported that the replacement of a single fluorine atom by a hydrogen atom in a terminal -CF 3 group more than doubles the critical surface energy. According to Zisman's study on surface free energies, it would be expected for coatings containing fluorinated group to exhibit increased contact angles with LST 50. Perfluorinated alkanes are known to have lower water solubilities than the corresponding hydrocarbons, while exhibiting high level of lipophobicity. The thought-provoking observation regarding the low SFE reported by Zisman is that the free energy of hydration per unit hydrophobic surface area is similar for hydrocarbons and fluorocarbons. C-F bond also exhibits higher dipole moment than the C-H bond and due to that a stronger binding with dipolar water might be expected. The dispersion interactions of C-F are expected to be more attractive than those of C-H with water due to the polarizability of F in the C-F bond being higher than that in the C-H bond. The fluorocarbon surface could be argued to be more hydrophilic than hydrocarbon surfaces based on the contact angle data presented in Table 5-11. However, this contrasts with common knowledge on fluorinated coatings as described

by Zisman (1964) that the replacement of a single hydrogen atom by a fluorine atom in a terminal -CH 3 group more than halves the SFE.

Table 5-12 Contact angles with probe liquids – coatings deposited on stainless steel 304 2B finish

Coating	WCA (º)	DCA (º)	LST 50 (º)	LST 30 (º)
Avalon Glass	112.7	91.1	89.1 (±3.3)	35.7 (±7.0)
Aquaphobe CF	115.9	89.3	91.5 (±1.3)	46.7 (±1.3)
Aquaphobe CM	106.6	63.8	81.2 (±3.6)	12.2 (±1.6)
Siliclad	97.6	48.7	75.9 (±2.6)	18.7 (±7.6)
Aculon 353	93.6	43.9	68.4 (±1.4)	28.1 (±2.7)

On the stainless steel it can be seen that LST 50 contact angles were in the range of 68 to 91º and LST 30 of 12 to 47º. Similarly, for the observation on glass substrate; LST 50 showed similar contact angles on fluorinated coatings (Aquaphobe CF, Avalon Glass) to diiodo-methane. Meanwhile a different trend can be seen with non-fluorinated (Aquaphobe CM, Siliclad, Aculon 353) treatments where LST 50 exhibited higher contact angle.

Comparing wettability data on glass (Table 5-11) and stainless steel (Table 5-12). Contact angles on stainless steel were higher for Avalon Glass and Aquaphobe CF. While for other coatings contact angle values were either comparable or lower. This difference in values between the same coatings can be attributed to the substrate roughness effect or the ability of the coating to adhere to a specific surface.

5.7.Commercial coating treatment - Dynamic contact angle study

Dynamic contact angle measurements were performed on Aquaphobe CM, Aquaphobe CF and Siliclad coatings deposited on glass. This method was used to determine contact angle hysteresis, sliding angle and liquid roll-off angle as a function of the surface tilt. There is no standard procedure for this method, but conditions such as drop volume and tilting speed must be taken into consideration when performing the measurement. The methodology used is described in detail in Chapter 4. The obtained contact angle values at varying surface tilt from 0 to 80º were evaluated to determine the sliding angle (SA), advancing and receding contact angles and contact angle hysteresis. One of the main criteria used for evaluation was movement of the three-phase contact point (CP); the receding (CP(R)) and advancing (CP(A)) points between surface, liquid and gas phase. The sliding angle was identified as the angle of inclination at which the position of the moving three-phase point is displaced

by 40 pixels for both receding and advancing points and roll-off angle was taken as a value of the surface tilt at which a droplet leaves the camera view.

The receding and advancing water CAs and CPs measured by Kruss DSA are plotted in Figure 5.16 as a function of surface tilt. As can be seen from contact angle measurements, as the surface is being tilted the receding side exhibits bigger change in CA compared to the advancing one. As the tilting angle increases, the advancing contact angle becomes higher and with it hysteresis grows. For all three coatings the hysteresis is in the range of 10-23º with the highest hysteresis value at roll off tilt. As previously mentioned, the difference between the advancing and receding CAs is contact angle hysteresis (CAH) and it is used as a measure of how well a droplet can pin to the surface. The CAH should be minimal for the droplet to desorb easily. In terms of contact point values, the CP points were converted from millimetres to pixels to allow for the comparison between different measurements and magnifications. From the plots, it can be seen that both advancing and receding sides start movement at the same tilt angle. The hysteresis of contact points (CPH = CP advancing – CP receding) is not evident from these plots. In order to compare the differences in advancing and receding sides for both CA and CP Figure 5.17 presents CAH and CPH as a function of surface tilt angle. The CAH begins to increase before the movement of droplet, and it increases inversely with tilt. Contact points start the motion only after a certain degree of CAH is achieved and show hysteresis of about 10 px. The hysteresis between advancing and receding points suggest that receding CP remains pinned and starts motion later than advancing side. The values of measured roll-off angles and sliding tilts together with CAH are presented for each coating in Table 5-13 for water and Table 5-14 for diiodo-methane. Comparing the repellency performance of Siliclad, Aquaphobe CM and Aquaphobe CF. Aquaphobe CM and Aquaphobe CF showed the lowest water roll-off tilts of ~ 40º. While Siliclad has an average roll-off tilt of 58º. In comparison to water, diiodo-methane did not exhibit either roll-off or pinning of the droplet. Instead, it spread out and created a film on the surface. The spreading action took place at a very low tilt angle of approximately 7-9º and the CAH measured was very high 31-48º. For all three coatings the same action was observed. It is considered that CAH provides information on the pinning/adhesion force of the droplet to the surface, but CAH on its own does not provide information whether the droplet is exhibiting a film forming behaviour, whether it is spreading and wetting out a surface or whether it easily de-wets and rolls off without leaving a film behind. To provide information on the dynamic wetting behaviour that CAH is lacking, the CPH parameter was developed and studied. Identifying and calculating CPH parameters adds value to the

dynamic contact angle measurements. As demonstrated in this section, CPH provides insights in identifying the type of wetting behaviour taking place and in distinguishing if the dewetting is taking place or the receding side remains pinned. Which is an important behaviour in surface wettability that cannot be easily described by static contact angles, dynamic contact angles or even contact angle hysteresis.

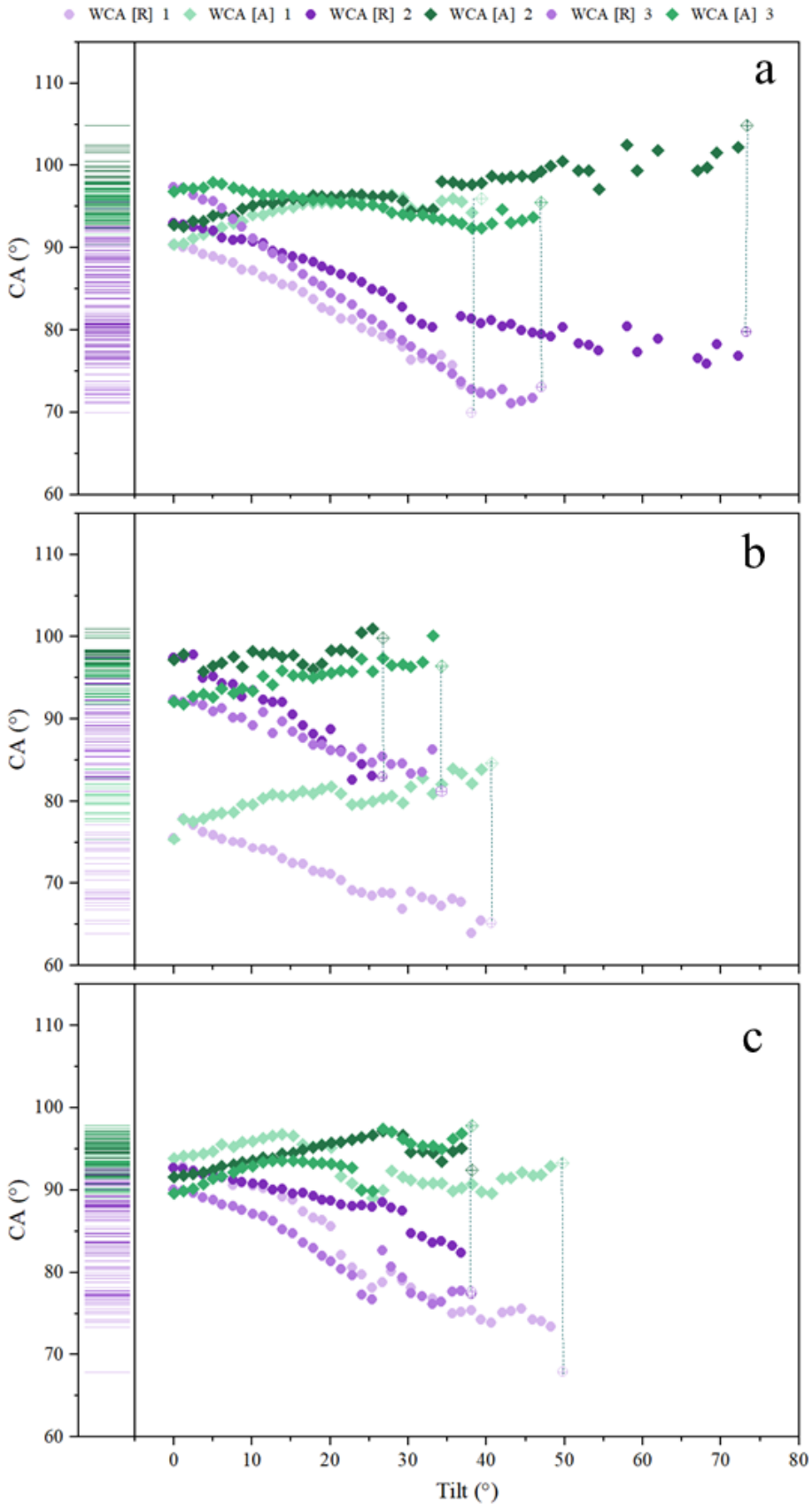

Figure 5.15 Dynamic contact measurements on Siliclad (a), Aquaphobe CM (b) and Aquaphobe CF (c).

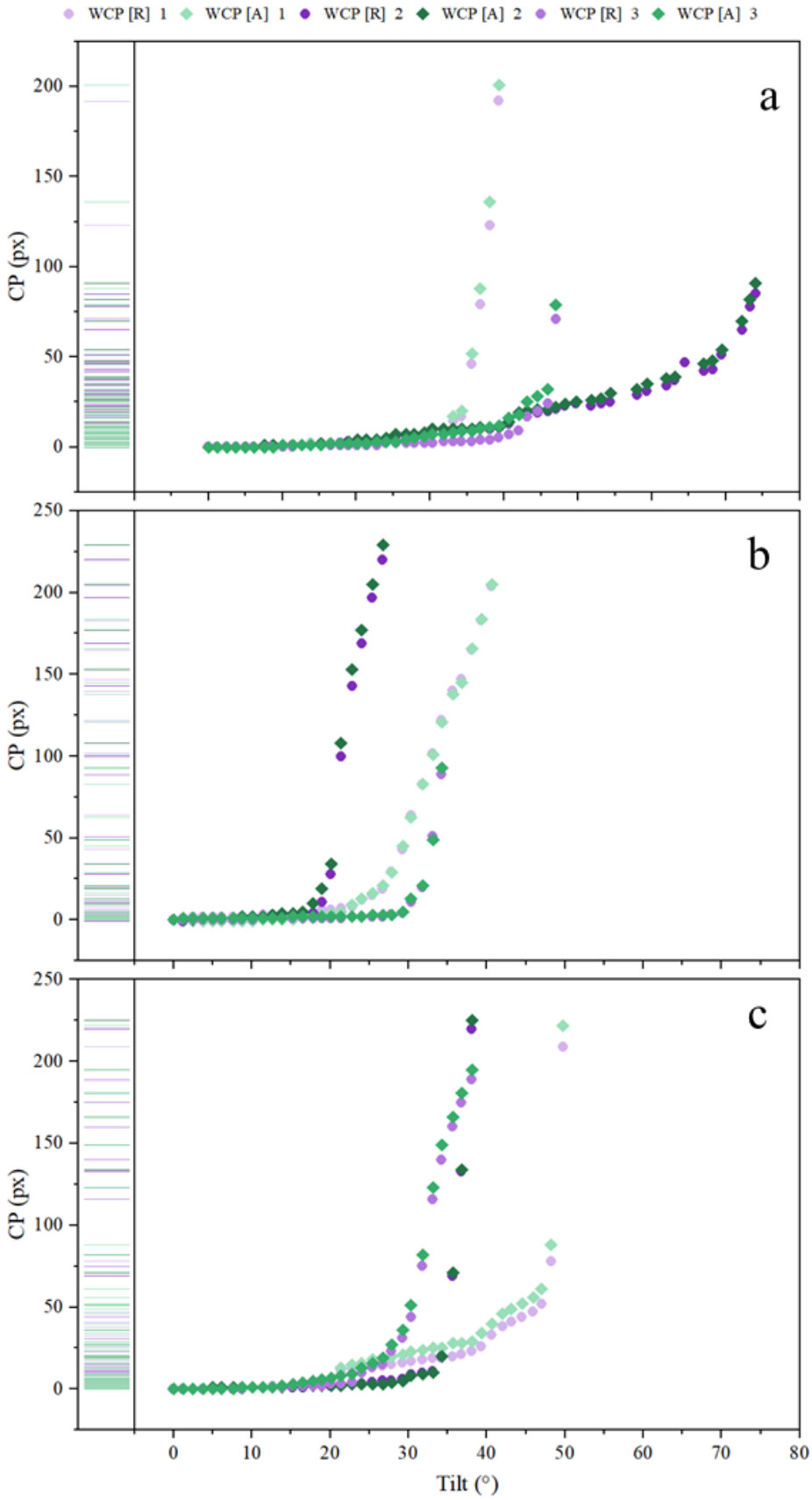

Figure 5.16 Dynamic contact measurements on Siliclad (a), Aquaphobe CM (b) and Aquaphobe CF (c).

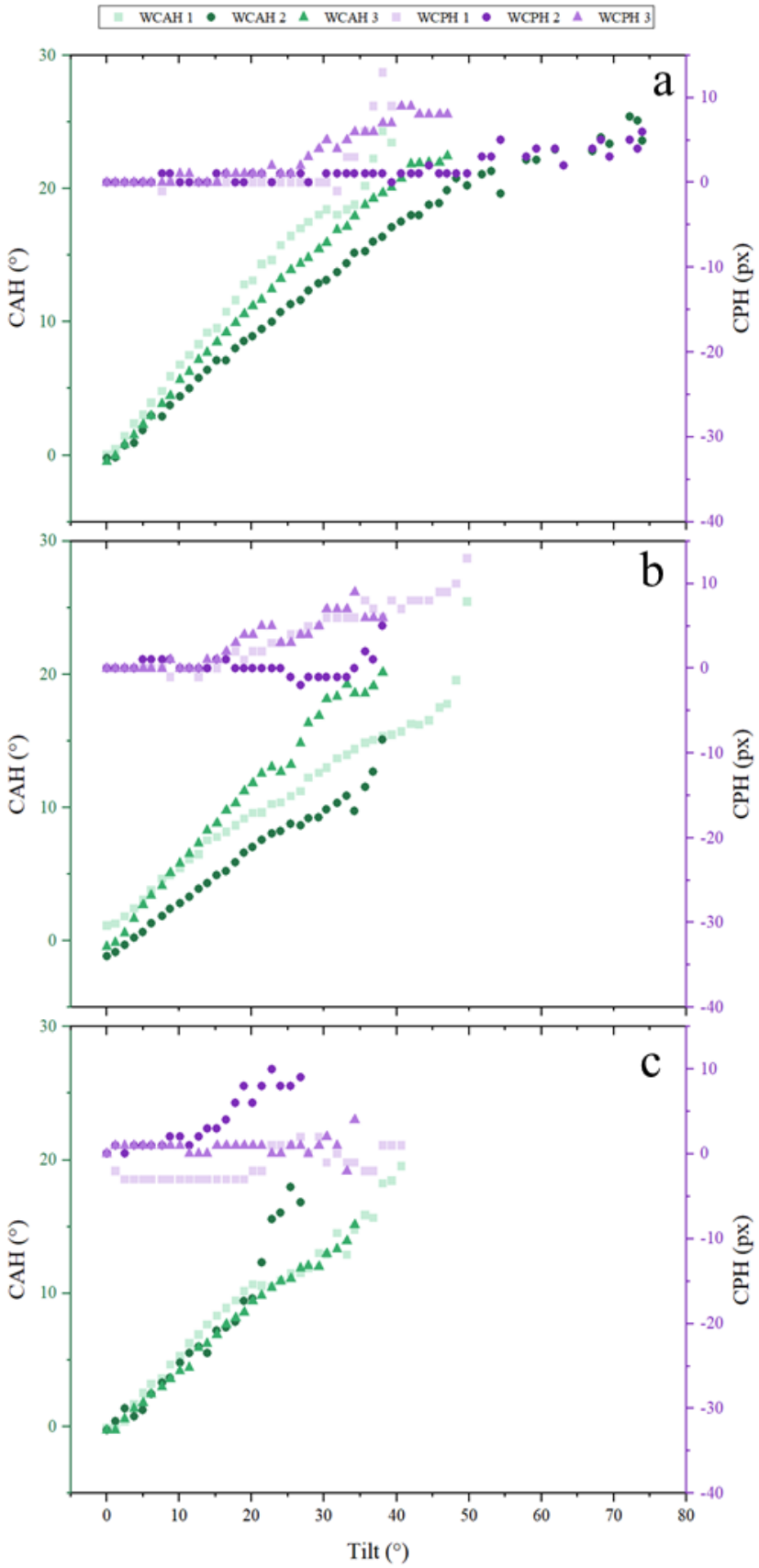

Figure 5.17 Contact angle hysteresis (CAH) and Contact point hysteresis (CPH) as a function of tilt angle on Siliclad (a), Aquaphobe CM (b) and Aquaphobe CF (c).

Table 5-13 Water contact angle movement

Movement	Siliclad				Aquaphobe CM				Aquaphobe CF			
	Tilt (˚)	CA [R] (˚)	CA [A] (˚)	CAH (˚)	Tilt (˚)	CA [R] (˚)	CA [A] (˚)	CAH (˚)	Tilt (˚)	CA [R] (˚)	CA [A] (˚)	CAH (˚)
10 px	38.3 (±5.0)	76.0 (±5.0)	95.3 (±2.5)	19.3 (±2.5)	24.3 (±5.5)	79.7 (±9.5)	91.0 (±9.5)	11.3 (±1.5)	26.0 (±6.2)	81.0 (±3.6)	92.3 (±2.5)	11.3 (±1.5)
40 px	50.0 (±15.7)	75.0 (±2.0)	97.0 (±1.7)	22.0 (±1.0)	27.7 (±6.1)	80.0 (±11.3)	92.7 (±11.0)	12.7 (±1.5)	36.3 (±6.5)	78.3 (±4.2)	94.3 (±2.1)	16.0 (±3.6)
roll off	53.7 (±18.9)	72.3 (±1.2)	95.7 (±0.6)	23.3 (±0.6)	42.0 (±20.2)	76.3 (±9.9)	93.7 (±7.8)	17.3 (±2.5)	42.0 (±6.9)	74.3 (±5.5)	94.3 (±3.2)	20.0 (±5.0)

Table 5-14 Diiodo-methane contact angle

	Siliclad	Aquaphobe CM	Aquaphobe CF
roll off tilt	7.0 (±1.7)	8.3 (±2.1)	9.0 (±1.0)
CA [R] roll off	58.3 (±28.6)	45.7 (±8.0)	60.0 (±3.6)
CA [A] roll off	96.0 (±9.6)	94.0 (±11.3)	91.7 (±14.0)
CAH roll off	37.7 (±21.2)	48.3 (±18.9)	31.7 (±17.2)

5.8. Summary

This chapter provided a review on various surface treatments and how they affect solid-liquid interaction by measuring the static and dynamic contact angle with a variety of polar and non-polar probe liquids. The substrates reported in this chapter were planar with minimal surface roughness in order to minimise the effect of surface topography on repellence and mainly concentrate on the effect of surface chemistry achieved by treatments. The surface roughness of selected substrates (glass, stainless steel 304 with 2B finish and mirror finish) was measured using White Light Interferometry, Alicona and surface profilometer Surfcom. The data collected via three different measurement technique are in agreement that the substrate roughness increases from glass, stainless steel mirror finish to stainless steel with 2B finish.

In terms of surface treatments, different cleaning approaches, thermal and humidity treatments were studied and their effect on substrates wettability, SFE and contact angles after final coating deposition were assessed. The main findings for thermal and humidity treatments were that the glass has a stable and constant disperse SFE term. Heating and exposure to a humid environment had a negligible impact on it, whilst the polar term showed considerable variation. Heating the glass appears to reduce the polar contribution whilst exposing it to humidity increases this term. A dehydration, rehydration mechanism would account for this behaviour. The steel surfaces show a far more complex behaviour. The disperse term is changed by heating at 150°C, the polar term also changes significantly by this treatment. The surface finish appears to have a notable effect on the polar term on exposure to damp heat. The behaviour of the steel therefore cannot be explained by a simple hydration model.

Eleven coatings (fluorinated and non-fluorinated) deposited on glass and stainless steel were studied. The commercial coatings deposited on glass gave static WCA values in the range of 67 to 96º, DCA values in the range of 63 to 84º and SFE values between 20 and 40 mN/m. Coatings on stainless steel gave higher WCA values in the range of 94 to 113º, DCA values in the range of 44 to 91º and SFE values from 13 to 38 mN/m. The coatings that showed highest values of both WCA and DCA on both substrates were the fluorinated silane-based coatings. The studied coatings were also exposed to LST probe liquid assessment. The

assessment showed that polar LST 50 exhibits higher contact angles on non-fluorinated coatings compared to diiodo-methane. From the obtained results it could be argued that fluorocarbon surface is more hydrophilic than hydrocarbon surfaces.

The wettability of commercial coatings Aquaphobe CM, Aquaphobe CF and Siliclad were studied via dynamic contact angle measurements to obtain CAH and CPH values. The obtained data showed that CAH begins to increase before the movement of droplets, and it increases inversely with the tilt angle. Contact points start the motion only after a certain degree of CAH is achieved. The hysteresis between advancing and receding points suggest that receding CP remains pinned and starts motion later than the advancing side. It is considered that CAH provides information on the pinning/adhesion force of the droplet to the surface, but CAH on its own does not provide information whether the droplet is exhibiting a film forming behaviour, whether it is spreading and wetting out a surface or whether it easily de-wets and rolls off without leaving a film behind. To provide information on the dynamic wetting behaviour that CAH is lacking, the CPH parameter was developed and studied in this chapter. Identifying and calculating CPH parameters adds value to the dynamic contact angle measurements. As demonstrated in this section, CPH provides insights in identifying the type of wetting behaviour taking place and in distinguishing if the dewetting is taking place or the receding side remains pinned. Which is an important behaviour in surface wettability that cannot be easily described by static contact angles, dynamic contact angles or even contact angle hysteresis.

CHAPTER 6. ENGINEERED ROUGHNESS – MICRO SCALE

6.1.Introduction

The wetting of substrates is significantly influenced by their surface topographic characteristics or in other words surface roughness. As described in Chapter 2, Wenzel and Cassie Baxter models explain that the apparent contact angle on a rough surface differs from the inherent contact angle. The wettability can either be enhanced or reduced by the increase in surface roughness (Figure 6.1).

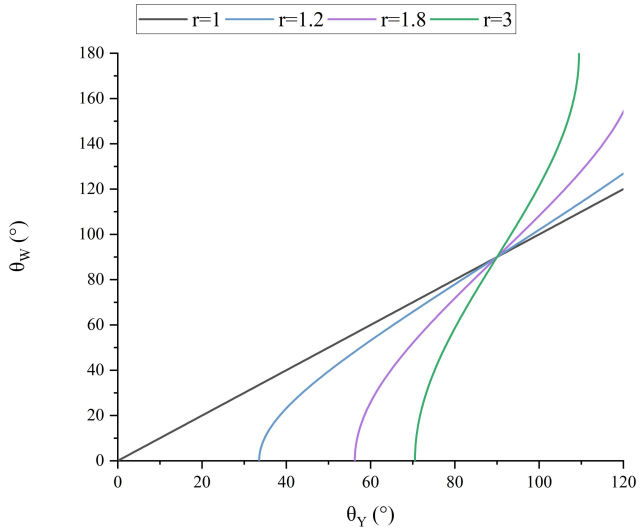

Figure 6.1 Apparent contact angle versus inherent contact angle

The complex interaction of surface chemistry and roughness, appealing to both adsorption and mechanical interlocking theories of adhesion, are used to explain the increased adhesion resulting from micro or nano rough surfaces. It is well known that to achieve improved abhesion the specific surface area should be minimised. Critical factors affecting wettability and adhesion are SFE and surface roughness. Deeper understanding on how surface roughness in combination with SFE affect wettability by a variety of liquids could help develop surface treatments for industrial applications.

Therefore, the wettability of the surface can be tuned not only by changing its surface chemistry (as described in Chapter 5) but also by altering the topographic characteristics.

This chapter overviews the engineered surface topography of the micro scale level and its effect on wetting by a range of probe liquids, both polar and non-polar.

6.2. Substrates and surface roughness

Grit blasting was chosen to generate substrates with different levels of roughness in the micro-scale range. It was intended that the process would minimise the variability that might arise from surface treatments such as chemical etching and provide reproducible method. The grit blasting process used alumina abrasive media particles with grit sizes of 240, 220, 100, 60, 36 blasted at pressures of 40, 40, 40, 50 and 70 psi, respectively. SS304 coupons with 2B finish were used as a basis for grit blasting. The roughness of the stainless-steel substrates before and after blasting was evaluated by confocal microscope and surface profilometer. Alicona confocal microscope with the vertical resolution of up to 10 nm was used. Zeiss Surfcom 130 stylus profilometer was used to measure 2D roughness profile of a surface. Surfcom 130 is a tracing driver with free stylus-and-arm system. The evaluation length was set up to 10 mm. The AFM and SEM were used to generate substrates' surface morphology images before and post surface treatment. The methodology of surface roughness measurement as well as grit blasting process is described in Chapter 4.

The roughness parameters obtained are presented in Table 6-1 and roughness profile, kurtosis and skewness are presented in Figure 6.2, Figure 6.3 and Figure 6.4 respectively. The topography images taken with Alicona are presented in Figure 6.5.

The Alicona images demonstrate that the untreated stainless-steel substrates are completely planar with minimal surface roughness features. The increase in the grit size promotes the increase in height and depth of the peaks and valleys for all samples.

Table 6-1 Alicona measurments

Parameter	mirror SS304	SS 2B finish	SS 240	SS 220	SS 100	SS 60	SS 36
R_a (µm)	0.14 ± 0.01	0.14 ± 0.01	1.19 ± 0.06	1.34 ± 0.06	1.34 ± 0.05	1.71 ± 0.14	2.91 ± 0.39
R_q (µm)	0.18 ± 0.01	0.18 ± 0.00	1.51 ± 0.08	1.71 ± 0.08	1.72 ± 0.04	2.16 ± 0.19	3.82 ± 0.56
R_t (µm)	1.92 ± 0.00	1.36 ± 0.00	10.23 ± 0.92	11.67 ± 0.58	12.03 ± 1.11	13.17 ± 1.03	24.45 ± 4.09
R_z (µm)	1.24 ± 0.00	1.10 ± 0.00	7.50 ± 0.52	8.57 ± 0.47	8.98 ± 0.41	10.03 ± 1.03	17.86 ± 2.06
R_{max} (µm)	1.74 ± 0.00	1.34 ± 0.00	9.65 ± 1.28	11.31 ± 0.60	11.39 ± 1.13	12.88 ± 0.97	23.13 ± 4.89
R_p (µm)	1.3.0 ± 0.00	0.54 ± 0.10	5.14 ± 0.72	5.89 ± 0.67	5.82 ± 0.26	6.53 ± 1.07	9.94 ± 1.23
R_v (µm)	0.61 ± 0.01	0.31 ± 0.43	5.10 ± 0.50	5.78 ± 0.13	6.21 ± 0.85	6.65 ± 0.35	14.51 ± 4.57
R_c (µm)	0.71 ± 0.10	0.60 ± 0.03	4.67 ± 0.10	5.35 ± 0.35	5.61 ± 0.26	6.58 ± 0.26	11.46 ± 1.26
R_{sm} (µm)	0.13 ± 0.03	0.11 ± 0.05	111.14 ± 4.33	126.58 ± 14.89	125.90 ± 12.88	126.27 ± 3.02	162.33 ± 13.49
R_{sk}	0.75 ± 0.00	-0.53 ± 0.00	0.14 ± 0.06	0.00 ± 0.09	-0.01 ± 0.02	-0.06 ± 0.13	-0.58 ± 0.60
R_{ku}	6.85 ± 0.00	4.05 ± 0.00	3.38 ± 0.26	3.51 ± 0.05	3.48 ± 0.32	3.10 ± 0.17	4.41 ± 1.43
R_{dq}	0.03 ± 0.00	0.03 ± 0.00	0.15 ± 0.01	0.15 ± 0.01	0.16 ± 0.01	0.18 ± 0.01	0.25 ± 0.03
R_t/R_z	1.55 ± 0.00	1.24 ± 0.00	1.37 ± 0.16	1.36 ± 0.03	1.33 ± 0.06	1.32 ± 0.06	1.36 ± 0.08
L_c (µm)	800.00						

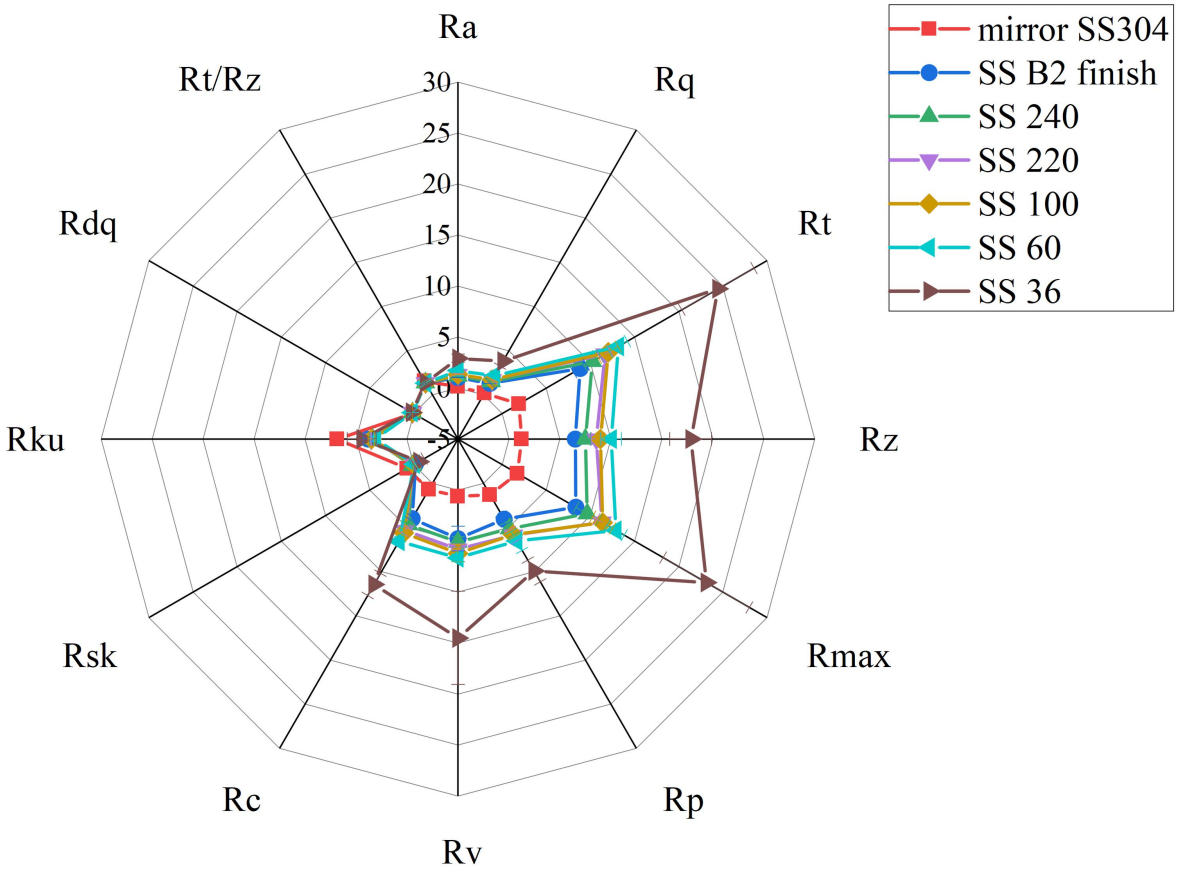

Figure 6.2 Roughness profile parameters according to Alicona measurements

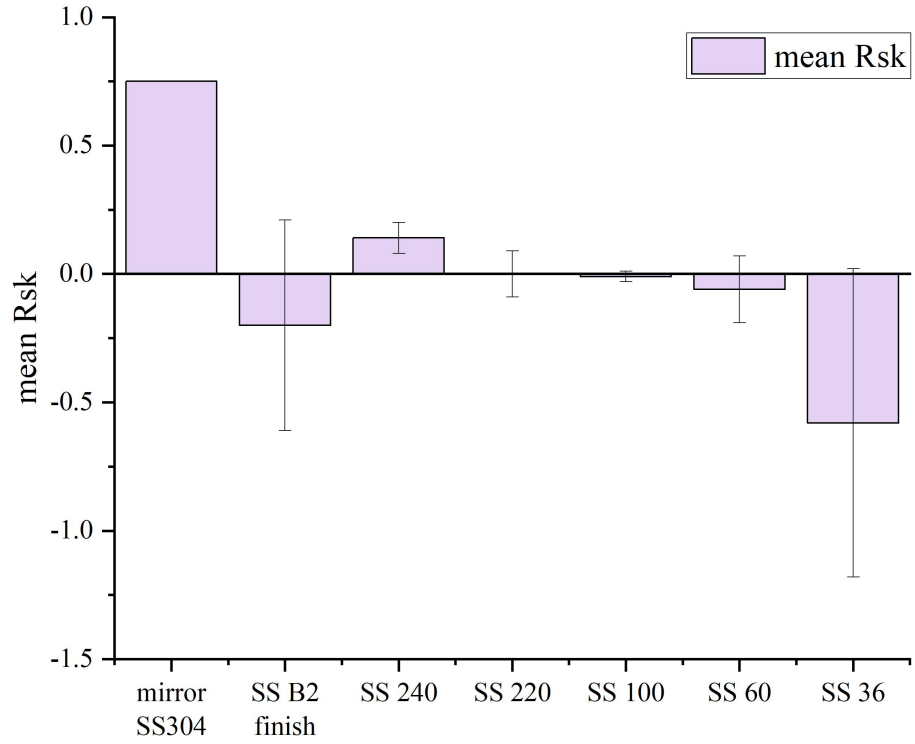

Figure 6.3 Roughness profile skewness for stainless steel substrates

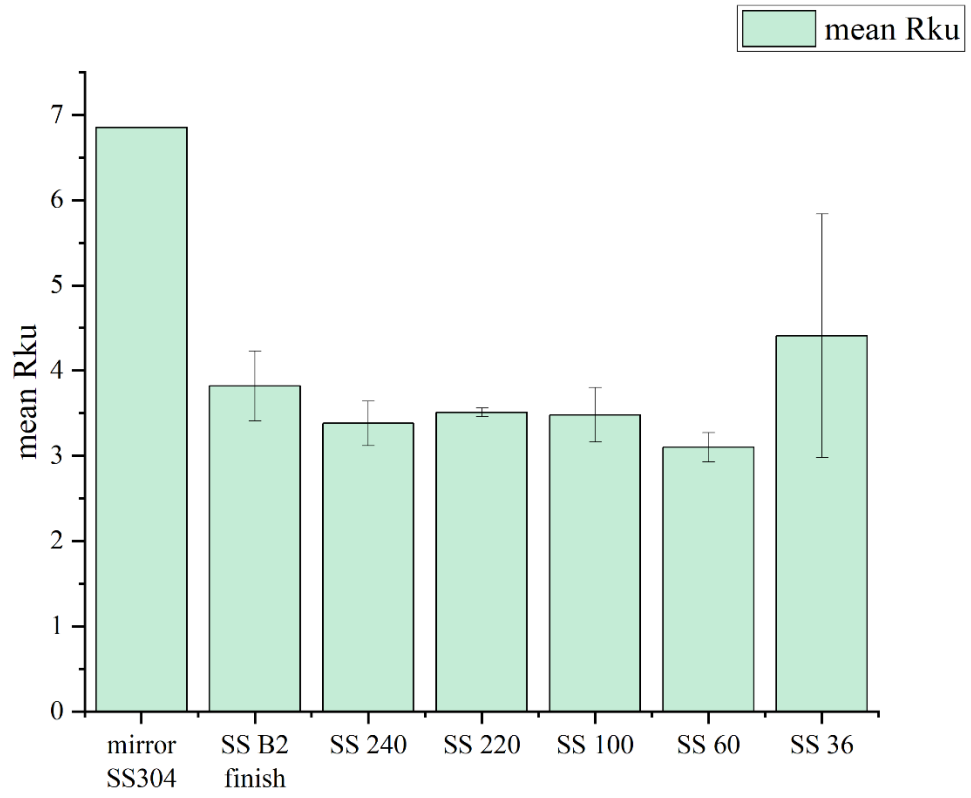

Figure 6.4 Roughness profile kurtosis for stainless steel substrates

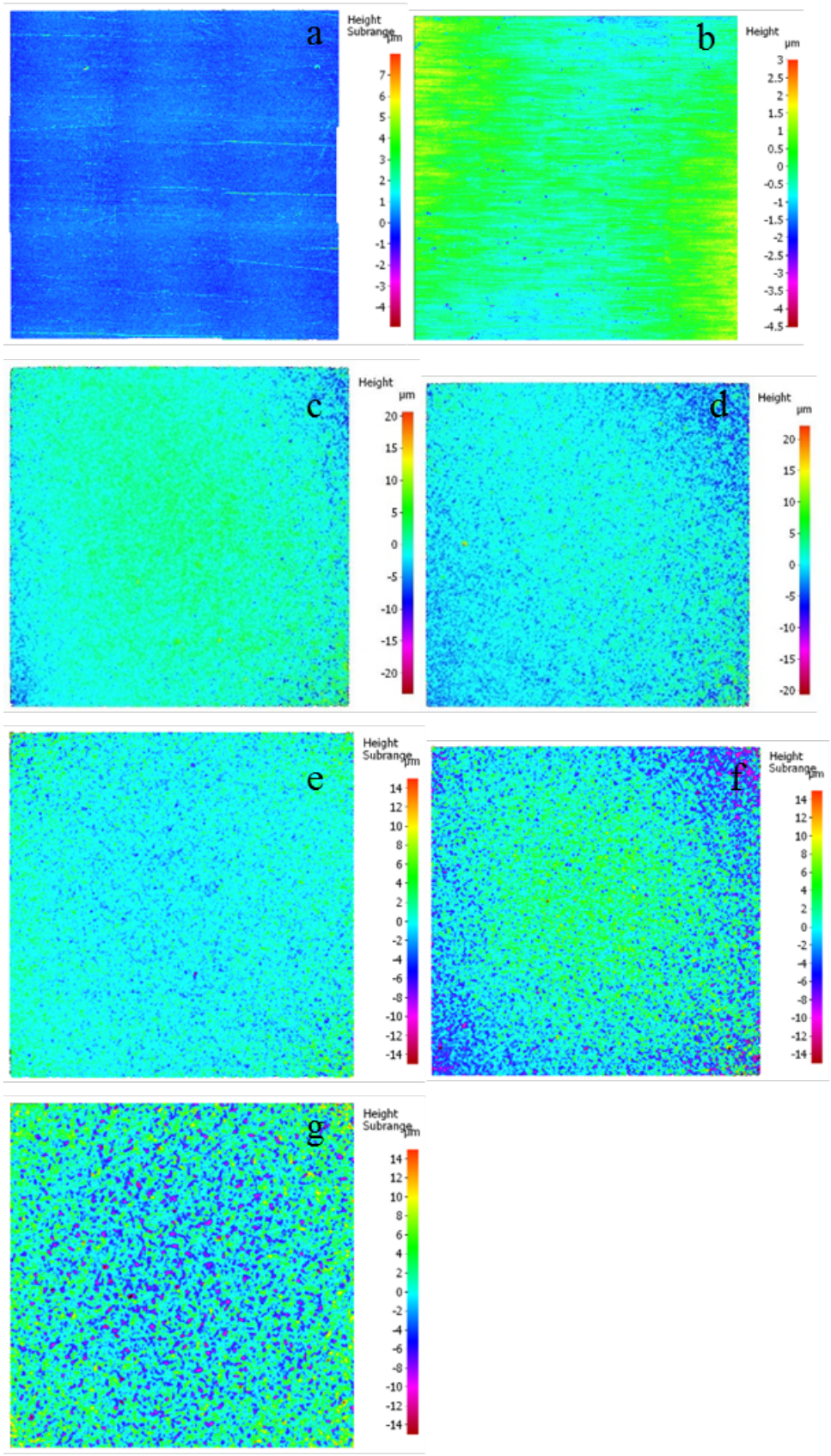

Figure 6.5 Surface topography images taken with Alicona; Stainless steel mirror finish (a), Stainless steel 2B finish (b), Grit 240 (c), Grit 220 (d), Grit 100 (e), Grit 60 (f), Grit 36 (g)

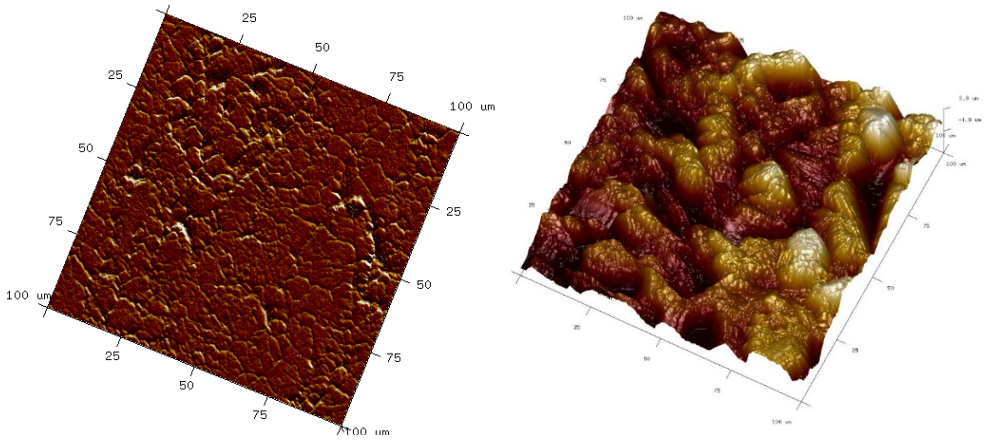

Figure 6.6 (a) Stainless steel 304 2B finish AFM image (b) Stainless steel 304 grit blasted with grit 100 at 40 psi

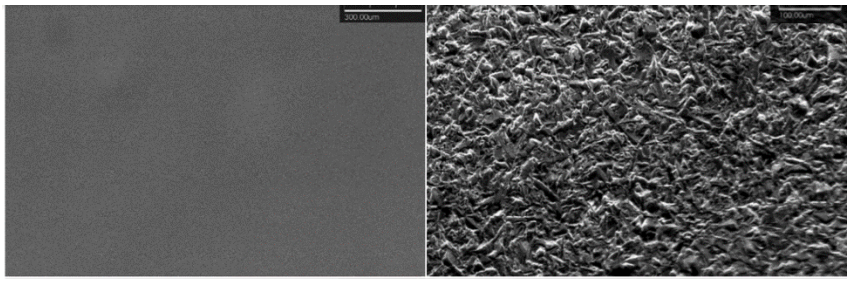

Figure 6.7 SEM images; (a) Stainless steel with mirror finish, (b) Stainless still grit blasted with Grit 100

Table 6-2 Surface roughness measured by Surfcom and Alicona

Equipment used	Parameter (µm)	mirror SS304	normal ss304	Grit 100	Grit 60	Grit 36
Surfcom 130A	R_a	0.04 ± 0.00	0.16 ± 0.01	1.34 ± 0.01	2.28 ± 0.17	4.01 ± 0.14
	R_q	0.05 ± 0.00	0.21 ± 0.00	1.70 ± 0.01	2.88 ± 0.2	5.14 ± 0.17
	R_{sk}	-0.28	-1.67	-0.11	-0.2	-0.02
	R_{ku}	3.22	11.64	3.38	3.34	4.07
Alicona	R_a	0.14 ± 0.01	0.14 ± 0.01	1.34 ± 0.05	1.71 ± 0.14	2.91 ± 0.39
	R_q	0.18 ± 0.01	0.18 ± 0.00	1.72 ± 0.04	2.16 ± 0.19	3.82 ± 0.56
	R_{sk}	0.75	0.00	-0.01	-0.06	-0.58
	R_{ku}	6.85	4.05	3.48	3.10	4.41

Surface roughness values are dependent on the measuring technique, selected surface spatial wavelengths included, and the lateral resolution of the measuring method used. The variation in the optical and mechanical profile roughness is caused by differences in lateral resolution. The optical interferometric methods are limited by the resolution of the optical systems, while the resolution of the mechanical methods depends on the contact area of the stylus on the surface peaks/valleys (Bennett, 1985). Comparing the roughness values obtained by surface profilometer and Alicona in Table 6-2, there is a slight variation in the measurements. However, measurements agree on roughness increasing from mirror finish to Grit 36 blasted stainless steel. The surface roughness values presented are average of at least three measurements and the standard deviation confirms that the blasting method provides reproducible surface topographies. The AFM and SEM images (Figure 6.6 and Figure 6.7) demonstrate the morphology of substrates before and after roughening treatment. Grit blasting creates surfaces with stochastic topographic pattern with reproducible statistic roughness parameters. As presented in Figure 6.2 the shape of the profile for all blasted substrates is the same; all the measured parameters increase with increase in the size of the grit used. This increase is coherent and consistent across samples. The significant change is demonstrated by substrates blasted with grit 36 demonstrating the highest values in height of the roughness profile's peaks and valleys. However, it still maintains the same shape of the profile. As the profile exhibits consistent shape for all the grits used and all the parameters show an increase, it does not matter which specific parameter is used to describe the surface as the increase is consistent across them.

The skewness of the profile is presented separately to compare the height distribution across all samples in Figure 6.3. Grit blasted samples demonstrated negative skewness with the only outlier being grit 240. Negative skewness means that the height distribution of the profile is below the mean plane/baseline, thus the profile has more roughness valleys/pits than peaks. Another parameter that is presented is kurtosis in Figure 6.4. Kurtosis is a measure of the sharpness of the profile. The values for grit blasted samples suggest that their profiles are spiked with grit 36 having the sharpest profile among all the blasted substrates.

6.3. Wettability assessment of substrates

6.3.1. Static contact angle measurements

Glass and stainless steel samples with roughness average varying from 0.1 μm to 4 μm (mirror finish, 2B finish, grit blasted with grit sizes of 100, 60, and 36) were selected for wettability assessment. Grit 240 and 220 were not included in the study as their roughness is not significantly different from grit 100. The wettability was evaluated by Kruss DSA 100 with the evaluation methodology described in Chapter 4. The obtained contact angles are reported in Table 6-3.

Table 6-3 No coating

Substrate	Ra (μm)	WCA (º)	DCA (º)	LST 50 (º)	LST30 (º)
Glass	0.0	24.2 (±2.5)	69.2 (±0.6)	25.4 (±0.5)	<10
SS Mirror finish	0.1	80.1 (±2.6)	57.3 (±2.3)	61.4 (±0.3)	<10
2B	0.1	86.8 (±1.3)	50.4 (±1.6)	77.4 (±2.3)	<10
Grit 100	1.3	93.3 (±5.9)	67.2 (±5.5)	18.1 (±1.5)	<10
Grit 60	1.7	63.5 (±2.9)	43.8 (±3.8)	33.8 (±4.8)	<10
Grit 36	2.9	43.8 (±7.0)	59.9 (±2.4)	75.3 (±3.7)	<10

The increase in surface roughness from 0.01 μm to 4 μm for the uncoated substrates results in a rise of static contact angles for probe liquids. For liquids with lower SFE that are LST 30, gave static contact angles below 10°. According to Wenzel the greater the deviation from 90° on a smooth surface (Figure 6.1), the greater will be the influence of introduced roughness. Thus, if the contact angle is below 90°, the introduction of surface roughness is expected to decrease the contact angle further, however the obtained values do not seem to follow this trend. Introduction of roughness increased the contact angle even though the starting contact angle was below 90° for all liquids studied. The highest contact angle achieved was on SS304 blasted with grit 100 for water, on glass for diiodo-methane and on SS304 2B finish for LST50. In the Wenzel equation chemical composition and the shape of roughness profile are ignored (Islam, Tong, and Falzon 2014; Nakajima 2011). However, these are very important factors for wettability of substrates. Another parameter that might affect this relationship is the droplet size. It was reported that the Wenzel approximation improves with increase in droplet size in comparison to roughness profile size. However, the limit of roughness size is still to be fully understood (Wolansky and Marmur 1998; Islam, Tong, and Falzon 2014).

To assess the effect of surface chemical treatment on roughened substrates, five commercial coatings were selected; Aculon 353, Tutoprom Bright, Sharc Sapphire, Avalon Glass and Sivo EC. The coating composition, preparation, deposition and drying/curing method was the same as for planar surfaces described in Chapter 5. The wettability assessment values for coated substrates are reported in Table 6-4, Table 6-5, Table 6-6, Table 6-7 and Table 6-8. The contact angle data is presented in Figure 6.8, Figure 6.9, Figure 6.10, Figure 6.11, Figure 6.12 and Figure 6.13.

Table 6-4 Aculon 353

Substrate	R_a (µm)	WCA (º)	DCA (º)	LST 50 (º)	LST 30 (º)
Glass	0.0	67.3 (±2.9)	63.0 (±2.6)	62.8 (±4.0)	25.5 (±3.4)
SS Mirror finish	0.1	93.7 (±2.3)	69.6 (±1.4)	84.2 (±3.2)	51.3 (±2.7)
2B	0.1	93.6 (±4.8)	43.9 (±2.7)	68.4 (±1.4)	28.1 (±2.7)
Grit 100	1.3	103.2 (±4.3)	61.9 (±5.2)	94.3 (±3.7)	80.9 (±5.6)
Grit 60	1.7	113.8 (±6.4)	82.5 (±3.9)	82.0 (±3.9)	40.4 (±3.3)
Grit 36	2.9	113.0 (±5.1)	88.8 (±3.7)	87.8 (±5.2)	47.4 (±3.4)

Table 6-5 Tutoprom Bright

Substrate	R_a (µm)	WCA (º)	DCA (º)	LST 50 (º)	LST 30 (º)
Glass	0.0	86.6 (±2.8)	64.0 (±2.3)	76.2 (±3.8)	58.7 (±2.2)
SS Mirror finish	0.1	98.6 (±1.0)	70.1 (±1.1)	87.5 (±5.2)	52.1 (±5.4)
2B	0.1	96.8 (±4.0)	69.0 (±4.6)	86.9 (±3.0)	76.9 (±8.9)
Grit 100	1.3	118.9 (±3.5)	90.5 (±3.8)	100.7 (±3.8)	69.0 (±1.4)
Grit 60	1.7	128.9 (±2.1)	92.5 (±5.6)	110.3 (±7.8)	75.8 (±2.8)
Grit 36	2.9	119.6 (±1.5)	86.3 (±1.6)	112.6 (±2.2)	73.6 (±2.6)

Table 6-6 Sapphire

Substrate	R_a (µm)	WCA (º)	DCA (º)	LST 50 (º)	LST 30 (º)
Glass	0.0	97.4 (±0.1)	72.9 (±0.4)	96.9 (±2.3)	73.8 (±2.9)
SS Mirror finish	0.1	99.7 (±1.4)	72.6 (±1.6)	84.5 (±3.2)	75.1 (±3.8)
2B	0.1	98.6 (±3.4)	70.1 (±3.9)	101.0 (±1.7)	80.3 (±2.8)
Grit 100	1.3	127.5 (±2.2)	94.9 (±1.4)	111.5 (±5.6)	82.2 (±3.8)
Grit 60	1.7	127.7 (±1.0)	90.8 (±3.0)	116.2 (±6.7)	66.6 (±2.6)
Grit 36	2.9	123.7 (±2.1)	92.2 (±1.4)	108.0 (±4.3)	59.4 (±2.6)

Table 6-7 Avalon Glass

Substrate	R_a (µm)	WCA (º)	DCA (º)	LST 50 (º)	LST 30 (º)
Glass	0.0	88.9 (±3.5)	85.8 (±6.4)	77.1 (±2.5)	24.4 (±5.2)
SS Mirror finish	0.1	98.8 (±3.0)	76.2 (±3.6)	92.9 (±3.1)	59.1 (±4.3)
2B	0.1	112.7 (±2.1)	91.1 (±4.6)	89.1 (±3.3)	35.7 (±7.0)
Grit 100	1.3	129.3 (±3.0)	117.4 (±2.8)	119.9 (±5.2)	88.7 (±5.1)
Grit 60	1.7	132.0 (±1.3)	116.8 (±1.8)	121.6 (±1.9)	72.2 (±2.9)
Grit 36	2.9	131.4 (±0.6)	112.6 (±2.5)	119.4 (±6.0)	64.7 (±3.9)

Table 6-8 Sivo EC

Substrate	R_a (µm)	WCA (º)	DCA (º)	LST 50 (º)	LST 30 (º)
Glass	0.0	95.3 (±4.4)	84.8 (±3.5)	96.9 (±2.3)	93.7 (±1.7)
SS Mirror finish	0.1	107.0 (±2.2)	86.4 (±3.1)	94.8 (±1.2)	86.4 (±1.8)
2B	0.1	114.7 (±1.8)	89.4 (±4.8)	112.2 (±2.1)	100.8 (±1.7)
Grit 100	1.3	134.2 (±1.1)	118.7 (±3.4)	128.2 (±1.3)	114.1 (±6.9)
Grit 60	1.7	133.8 (±2.1)	123.4 (±1.9)	120.4 (±2.5)	69.2 (±3.2)
Grit 36	2.9	134.1 (±0.3)	122.0 (±0.5)	109.6 (±2.8)	67.8 (±2.9)

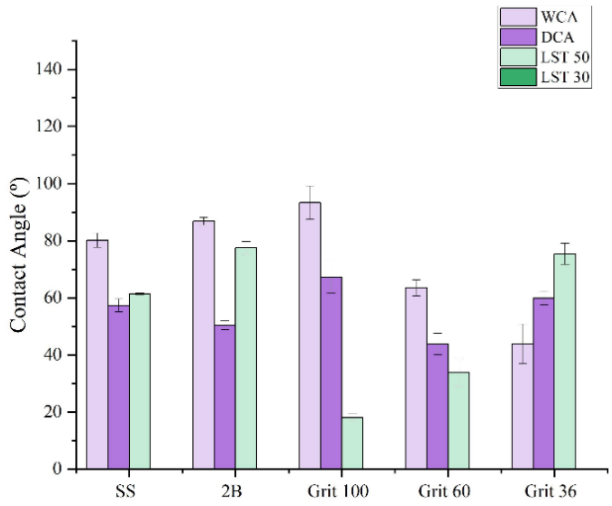

Figure 6.8 No coating

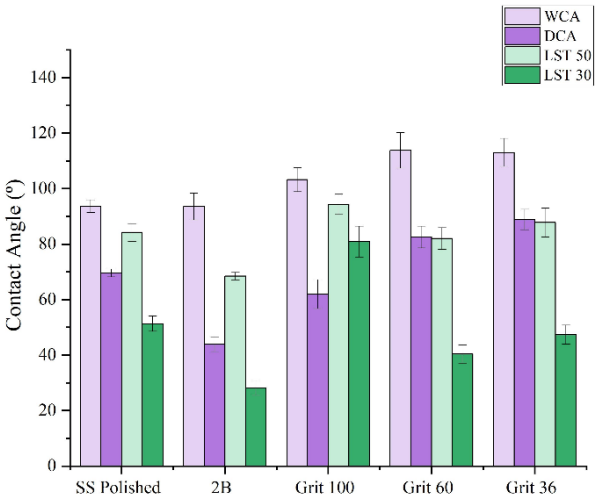

Figure 6.9 Aculon 353

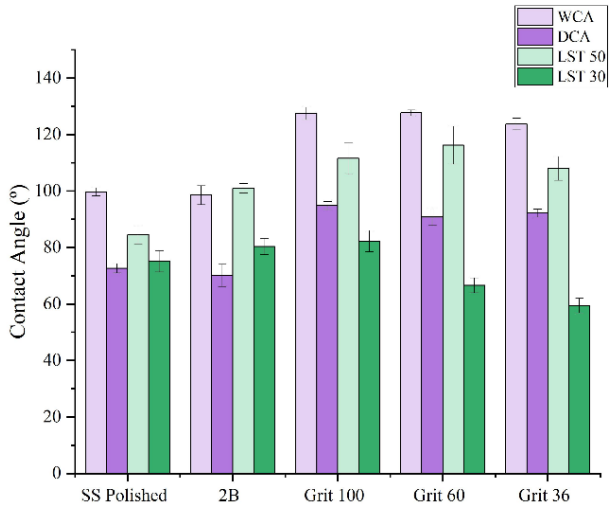

Figure 6.10 Sapphire

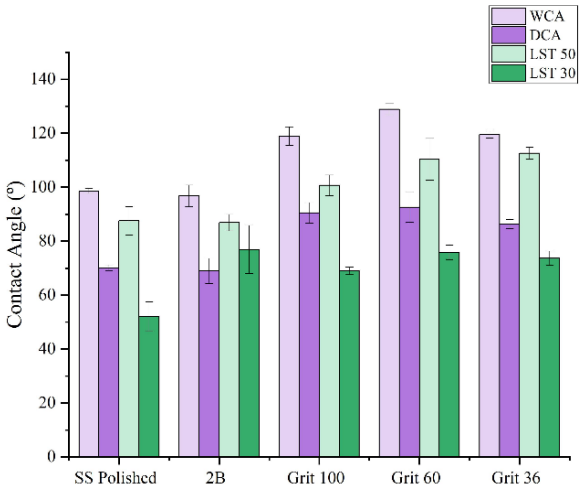

Figure 6.11 Tutoprom

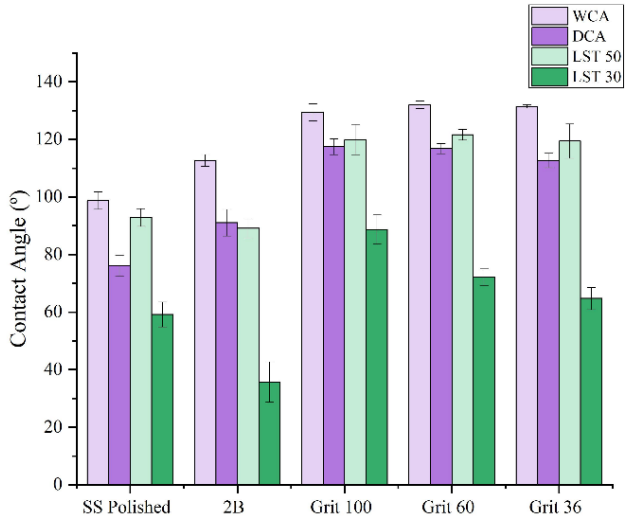

Figure 6.12 Avalon glass

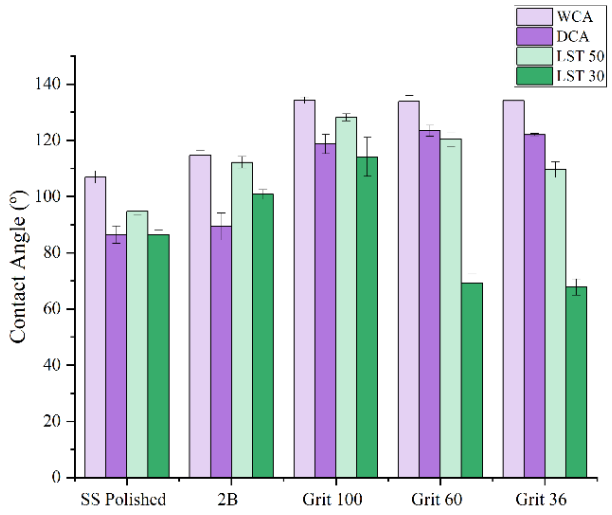

Figure 6.13 Sivo EC

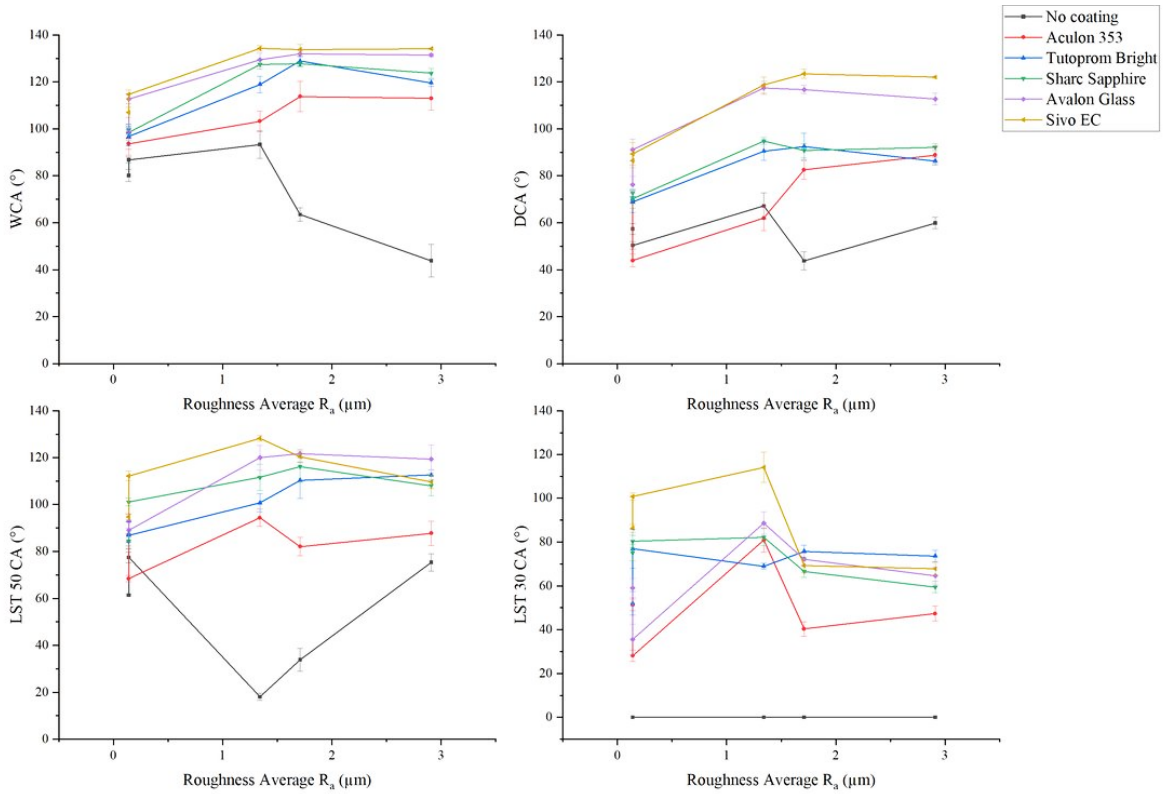

Figure 6.14 Repellence as a function of roughness average

To assist with the visualisation of the obtained CA data with water, diiodo-methane, LST 50 and LST 30 the values are presented in Figure 6.14 as a function of surface roughness. As can be observed from the plots (Figure 6.8 to Figure 6.14) increase in surface roughness significantly enhances the water and diiodo-methane abhesion on coated substrates. For the stainless-steel substrate without any coating the increase in water contact angle is maintained up to 1.3 after which it decreases. The diiodo-methane and LST 50 follow the different trend, the CA for both liquids decreases up to a roughness value of 1.3-1.7 µm after which it exhibits an uplift.

In terms of the substrates with deposited coating, the chemical treatment enhances contact angle for all probe liquids. Water exhibits consistent increase up to a roughness average value of 1.7 µm after which the increase in roughness does not have an influence on the CA value. The coating has a significant influence on the uplift of the CA on substrates with high roughness average value (Grit 36 blasted – R_a 2.9 µm). Deposition of the coating enhanced the WCA from 40 º (on uncoated substrate) to a value of 100-130 º (on coated substrates). The coating does not seem to have such a significant influence on the wettability/repellence of smooth/planar substrate. Comparing the values on the SS304 with mirror finish the

coating deposition increased the initial WCA from 80 º to 97-107 º with the highest values achieved on fluorinated surfaces.

Diiodo-methane and LST 50 on coated substrates show similar trend to water, there is an uplift in CA with increased roughness and after roughness average of 1.7 µm the CA is not influenced by increase in roughness.

The deposited fluorinated coatings together with roughness increased LST 30 CA from 0 to 70-110º. However, for LST 30 this effect is maintained up to a surface roughness average of 1.7 µm after which increase in roughness causes probe liquid to penetrate the roughness grooves and thus a decrease in CA. This is opposite to the effect seen with water, diiodo-methane and LST50.

For some of the blasted samples standard deviation values were higher compared to mirror finish ones. This agrees with the assumption that heterogeneous surfaces exhibit more than one local contact angles. The contact angle varies along the three-phase contact line for a liquid drop deposited on a rough surface (Jaroslaw W Drelich, 2019). Thus, it creates a variation in the observed contact angles (Méndez-Vilas *et al.*, 2006).

6.3.2. Wettability by Xylene and Decane

Sharc Sapphire and Sivo EC coated mirror finish and grit 100 blasted stainless steel substrates were subjected to a further wettability assessment by o-xylene and decane probe liquids. The obtained values are reported in Table 6-9. The un-fluorinated coating (sapphire) showed complete wetting with decane. On the other hand the fluorinated surface treatment (Sivo EC) maintained decane and o- xylene repellence on both smooth and roughened substrates Figure 6.15. The surface energies of the substrates are reported in Table 6-10.

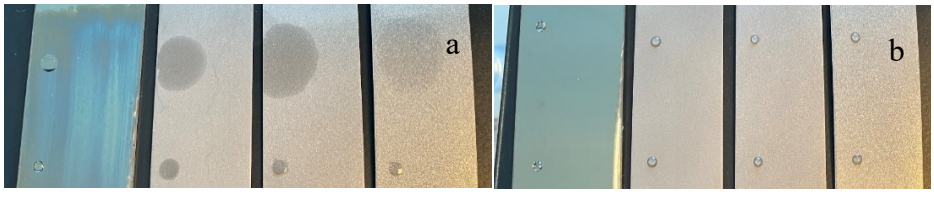

Figure 6.15 Sapphire coating on (a), Sivo EC coating (b)– (left to right) mirror finish, Grit 100, Grit 60, Grit 36. Decane droplet (top) and Xylene droplet (bottom).

Table 6-9 Wettability assessment with o-xylene and decane

Surface	**Surface treatment**	**CA with o-xylene (º)**	**CA with decane (º)**
Stainless steel	Grit 100	<10.0	<10.0
	Mirror finish	<10.0	<10.0
Sivo EC	Grit 100	52.0 ± 0.6	54.4 ± 7.6
	Mirror finish	55.7 ± 2.5	47.8 ± 4.3
Sapphire	Grit 100	21.6 ± 2.0	<10.0
	Mirror finish	24.9 ± 2.1	15.9 ± 5.1

Table 6-10 Surface free energies of coated and uncoated mirror finish and blasted steel substrates

Surface	**Surface treatment**	**SFE (mN/m)**	**Disperse (mN/m)**	**Polar (mN/m)**
Stainless steel	Grit 100	27.6 ± 5.1	24.5 ± 3.1	3.1 ± 2.0
	Mirror finish	35.8 ± 2.5	30.1 ± 1.3	5.7 ± 1.2
Sivo EC	Grit 100	3.6 ± 0.6	3.5 ± 0.7	0.1 ± 0.1
	Mirror finish	15.7 ± 1.3	14.3 ± 1.5	1.3 ± 0.5
Sapphire	Grit 100	10.7 ± 0.6	10.7 ± 0.6	0.0 ± 0.0
	Mirror finish	22.9 ± 0.9	21.4 ± 0.9	1.5 ± 0.3

The SFE for each substrate was calculated using Owens, Wendt, Rabel and Kaelble (OWRK) method based on water and diiodo-methane contact angle values. The most significant decrease was for fluorinated treatment (Sivo EC), the SFE decreased from 15.7 mN/m to 3.6 mN/m. Both the disperse and polar parts of the surface tension decreased. For all samples

increase in roughness provided a decrease in SFE (Table 6-10). Probe liquids do not penetrate in the roughness grooves of the substrate if the roughness profile can maintain capillary pressure and create air pockets inside the grooves. The decrease in the interfacial surface area provides uplift in repellence. This means that the decrease in SFE values is not attributed to the actual change in SFE but to the increase in contact angles based on which SFE is being calculated.

6.3.3. Dynamic contact angles

Treated and untreated grit blasted stainless steel substrates were subjected to dynamic contact angle measurements. The methodology used is described in Chapter 4.

6.3.3.1. Dynamic contact angles on uncoated substrates

The results of the assessment are reported in Table 6-11 and Table 6-12 for uncoated surfaces. For all stainless-steel substrates studied, none of them exhibited a water roll – off. Diiodo-methane did not exhibit the roll-off of the droplet, when the substrates were tilted all of them exhibited film formation which is caused by the lower surface tension of diiodo-methane compared to water.

Table 6-11 Water Roll off angles on uncoated substrates

	Tilt 0 º		**Tilt 80 º**			**Comments**
	CA [R] (º)	**CA [A] (º)**	**CA [R] (º)**	**CA [A] (º)**	**CAH (º)**	
Mirror finish	77.1	76.9	52.4	84.5	32.1	**no roll off**
2B finish	71.4	75.5	54.3	89.4	35.1	**no roll off**
Grit 100	88.9	88.2	59.5	88.2	28.7	**no roll off**
Grit 36	74.7	76.1	51.5	81.0	29.6	**no roll off**

Table 6-12 Diiodo-methane roll-off angles on uncoated substrates

	Tilt 0 º		**Sliding tilt**				**Comments**
	CA [R] (º)	**CA [A] (º)**	**Sliding tilt (º)**	**CA [R] (º)**	**CA [A] (º)**	**CAH (º)**	
Mirror finish	65.8	61.4	7.7	42.3	87.0	44.7	**film**
2B finish	63.2	51.8	13.0	13.3	144.9	131.6	**film**
Grit 100	71.0	61.2	18.0	19.6	127.8	108.3	**film**
Grit 36	62.9	63.5	17.0	25.4	108.6	83.2	**film**

6.3.3.2. Dynamic contact angle measurements on coated substrates

For the substrates treated with coatings a similar trend was observed. Water did not exhibit roll-off on roughened substrates while probe liquids with lower surface tensions exhibited film formation. The dynamic contact angle data are presented in tables in Appendix A for each coating (Tutoprom, Sapphire, Sivo EC, Avalon Glass and Aculon 353) deposited on glass, SS304 with mirror finish, SS304 with 2B finish, SS304 blasted with grit 100, 60 and 36. The dynamic contact angle values were measured with water, diiodo-methane, LST 50 and LST 30 probe liquids. The data presented in the tables are values at the roll-off point taken across three samples and averaged. The tables present roll-off contact angles at receding and advancing side, the roll-off tilt as well as contact points at receding and advancing sides. The contact points were measured to calculate the diameter of each droplet and study its spreading at roll-off. The contact angles were used to get the values of contact angle hysteresis at roll-off. The roll-off in this study refers to the tilt angle at which the droplet is leaving the camera view. In case of no-roll off, the maximum tilt of 80 º is presented as a roll-off angle meaning that the droplet remained pinned even at the maximum tilt of the DSA tilting table. To help with the visualisation, CAH (at roll-off tilt), the droplet diameter (at roll-off tilt) and the roll-off tilt are plotted for water and LST 50 in Figure 6.16 to Figure 6.21. Water displayed the lowest roll-off tilt for all coating systems on glass and mirror finish stainless steel 304 (Figure 6.16). On planar surfaces the fluorinated Sivo EC showed the lowest roll-off tilt of 45° on glass and Sapphire on mirror finish stainless steel 304. As roughness increased non-fluorinated coating systems (apart from Sapphire) showed no roll-off (petal effect). On SS304 blasted with grit 36 (4 μm roughness average) the only coating that displayed roll-off was Sapphire. In terms of contact angle hysteresis at roll-off tilt, no massive variation was seen across the coatings with CAH ranging from ~ 20-25° for most coatings (Figure 6.17). On grit 36 the lowest CAH was exhibited by Sapphire, which explains its roll-off capability. Across all the samples the lowest water CAH for all coating systems was observed on samples with lowest roughness (glass). To study the spreading of the droplet at roll-off, its diameter was calculated. The value is presented in pixels in Figure 6.18. The values were converted from millimetres to pixels to normalise and account for the possible differences in magnification factor across the measurements. No significant change in droplet diameter was observed across the samples, but the lowest diameter was exhibited on the roughest substrate (grit 36) for all coating systems. LST 50 showed similar trend to

water, with the lowest roll-off tilt being on planar substrates (glass, SS304 mirror finish, SS304 2B finish) while the substrate roughness enhanced the pining effect. The contact angle hysteresis on the other side was much higher compared to water with values ranging from 20-50 ° on planar surfaces while on roughened ones the increase up to 85-95 ° was observed which suggests very high pinning as well as film formation due to LST 50's lower surface tension. The diameter of the droplet was also observed to be higher than for water. In case of Diiodo-methane and LST 30, those probe liquids showed film formation at low roll-off tilts and high CAH values on all substrates (Figure 6.22).

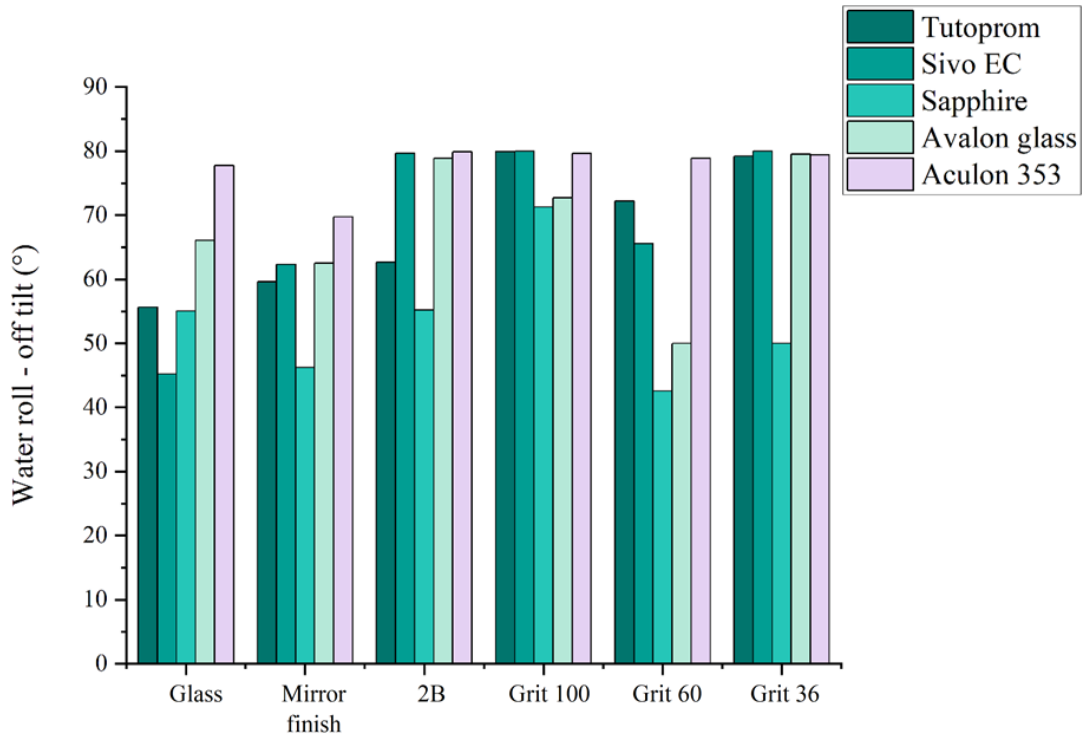

Figure 6.16 *Water droplet roll off tilt*

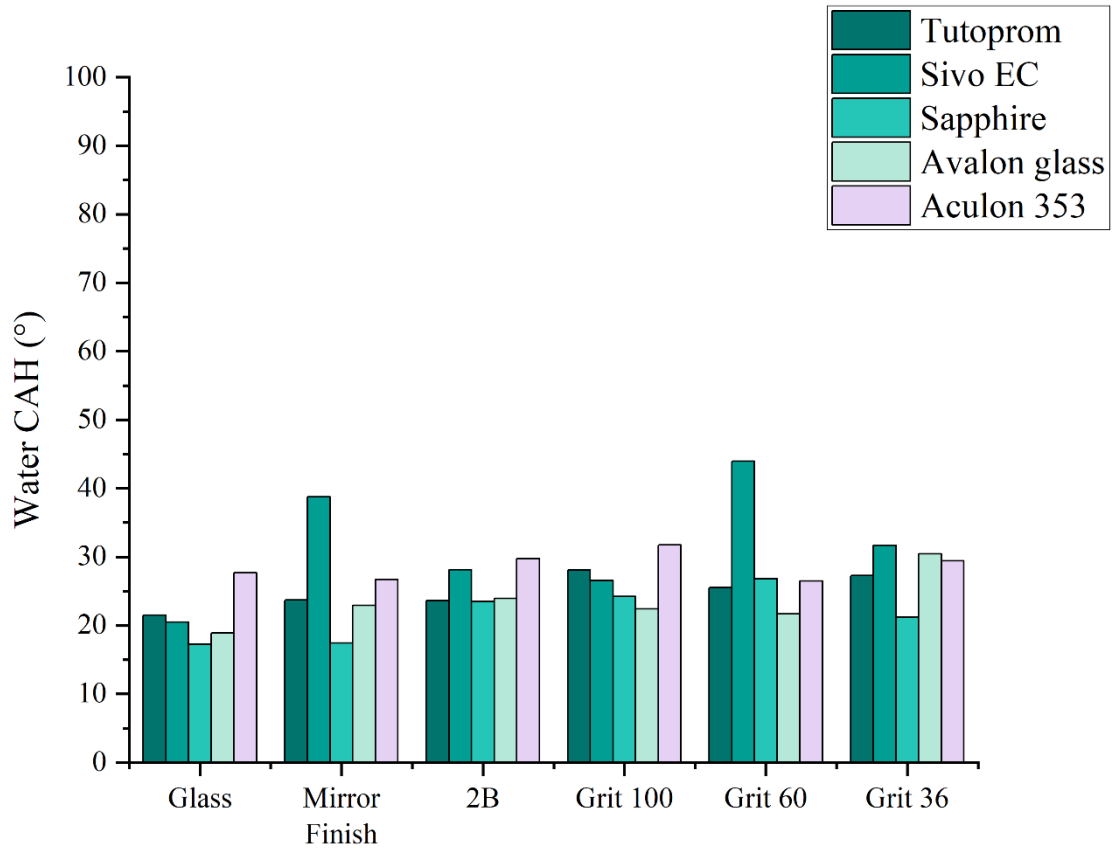

Figure 6.17 Water droplet contact angle hysteresis at roll off tilt

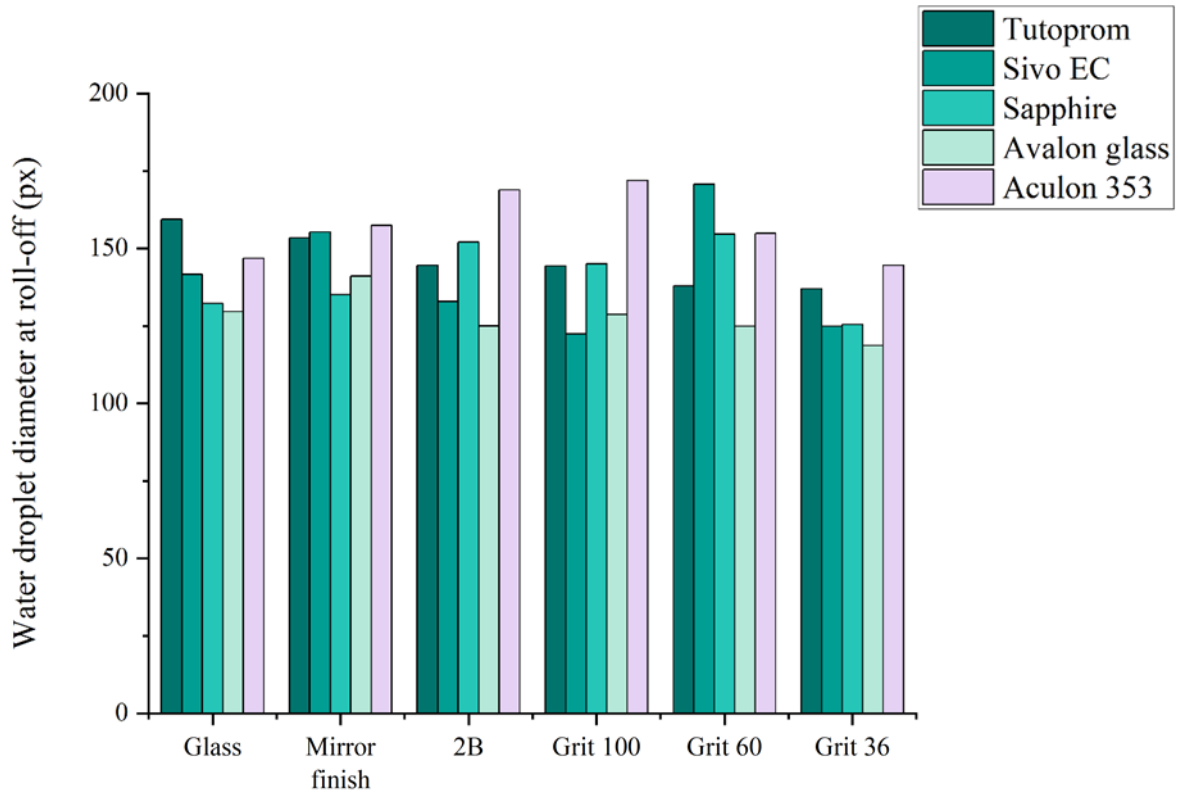

Figure 6.18 Water droplet diameter at roll off tilt

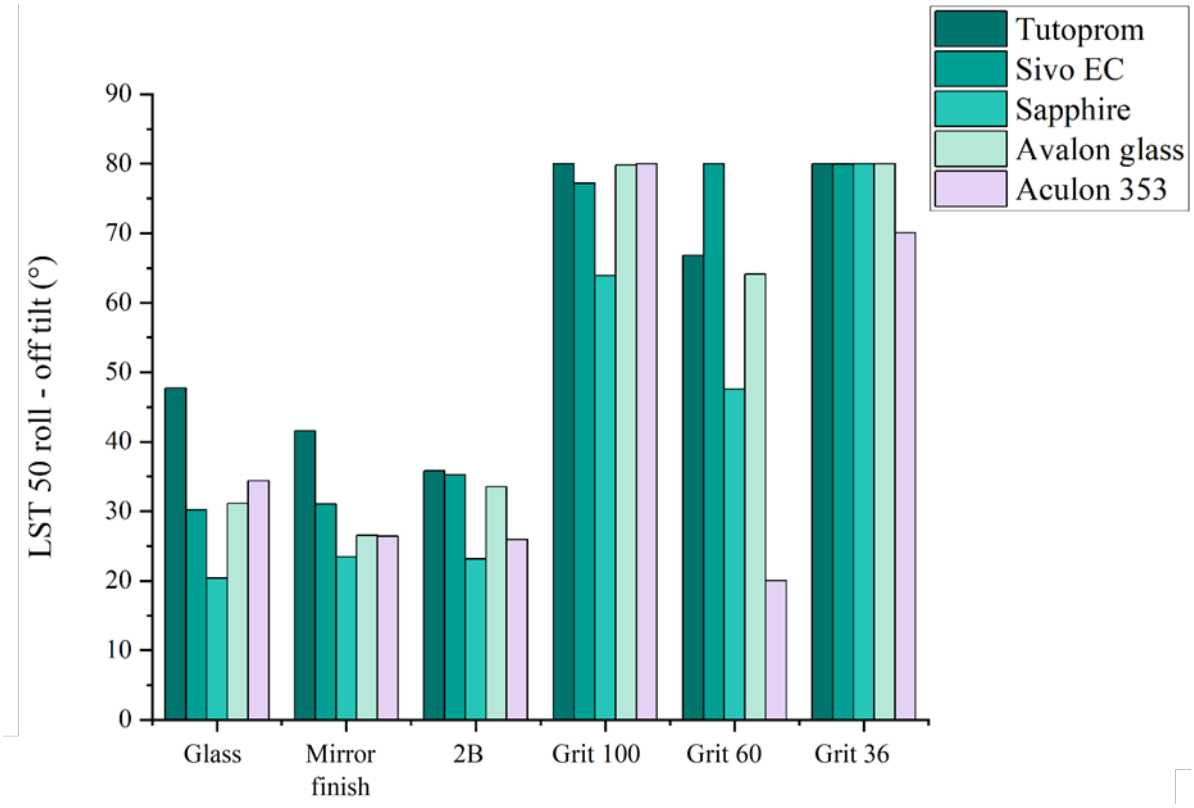

Figure 6.19 LST 50 droplet roll off tilt

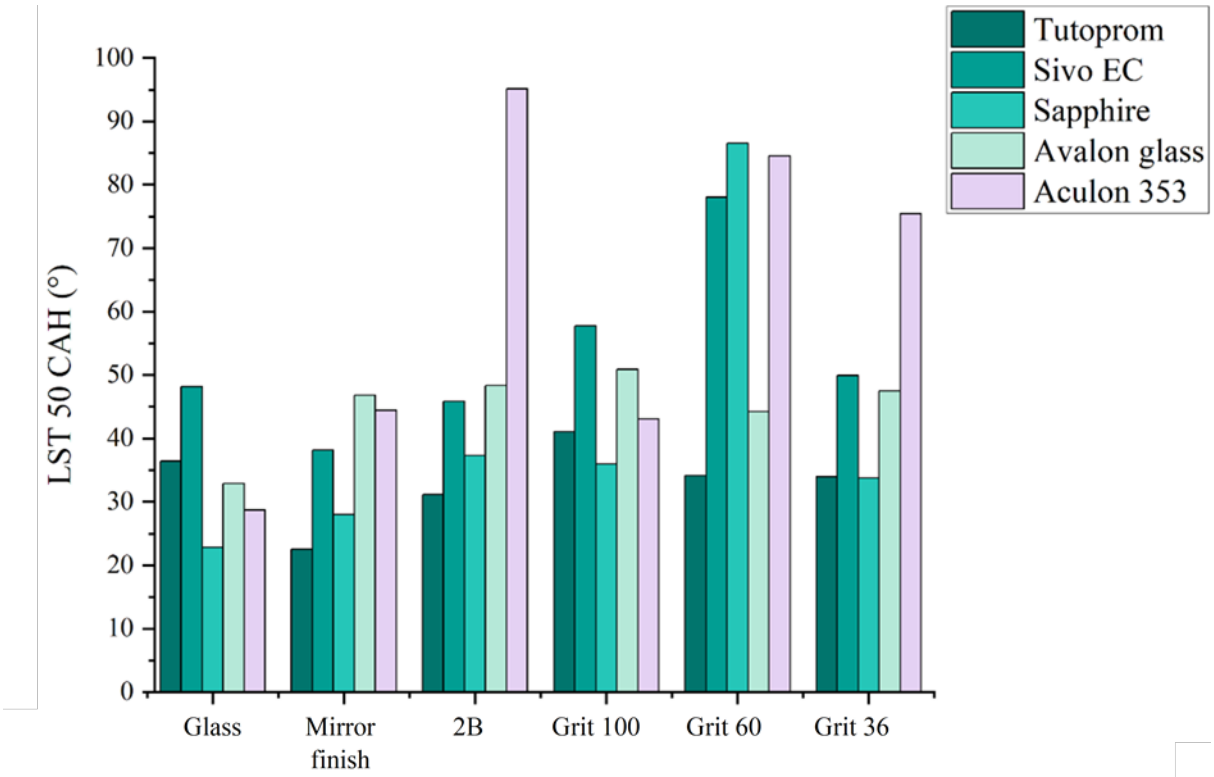

Figure 6.20 LST 50 droplet contact angle hysteresis at roll off tilt

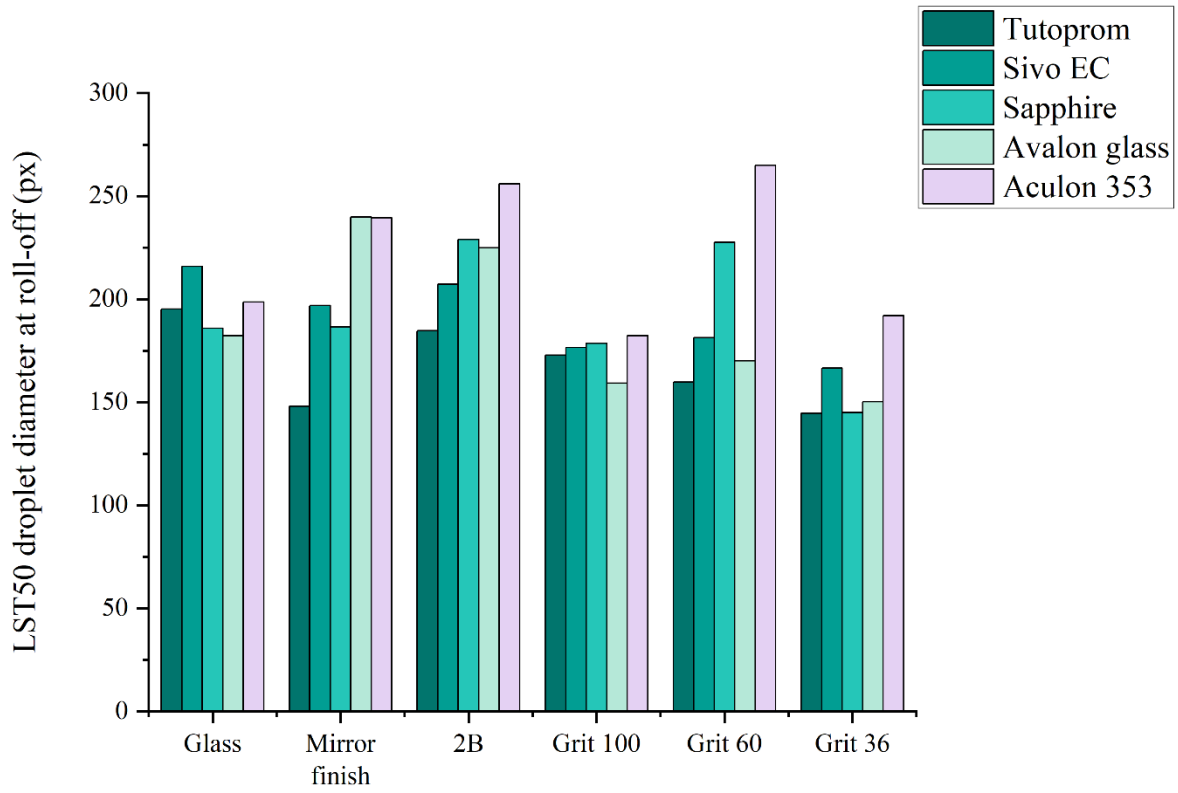

Figure 6.21 LST 50 droplet diameter at roll off tilt

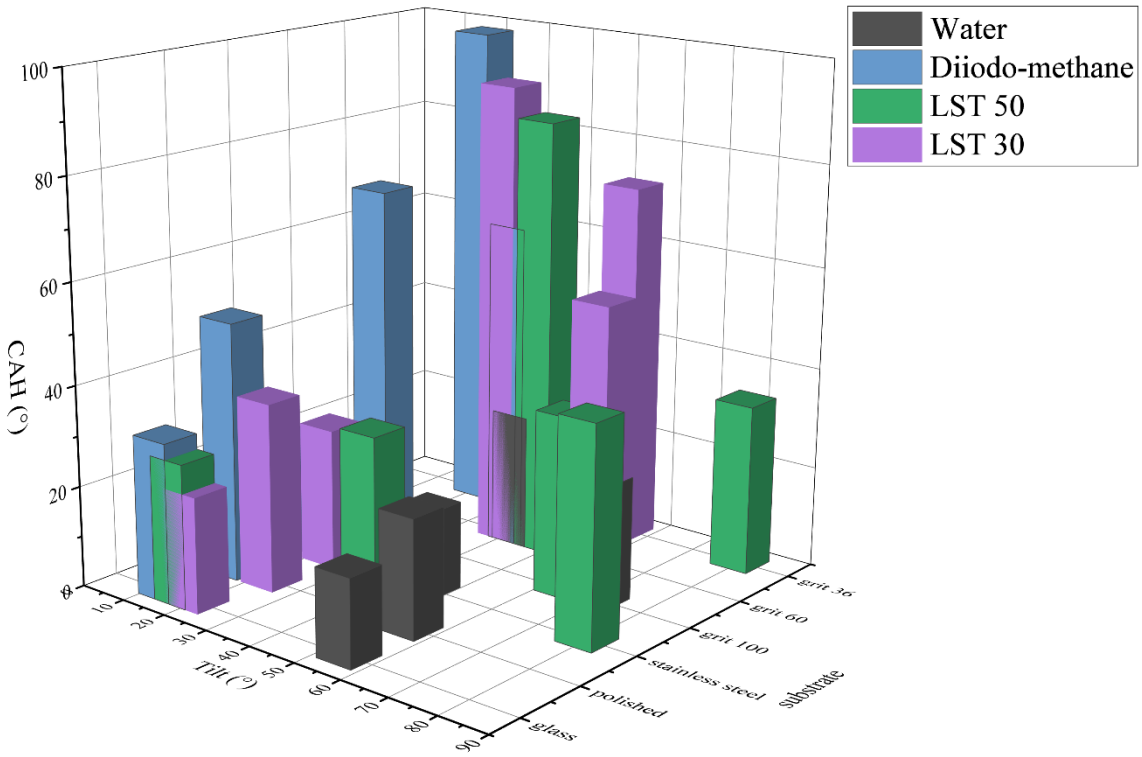

Figure 6.22 Contact angle hysteresis at roll-off tilt plotted as a function of roll-off tilt and substrate used

Figure 6.22 presents contact angle hysteresis at roll-off tilt plotted as a function of roll-off tilt and substrate used. The values presented are for Sapphire coating system. As can be seen from the plot, water is the probe liquid with the lowest CAH value across all substrates but does not exhibit low roll-off angle. The lowest roll-off was measured on the not roughened stainless steel 304. LST 50 also exhibited roll-off on planar/smooth substrates, but as the roughness increased it increased the CAH and caused a film forming behaviour. Meanwhile, diiodo-methane displays highest CAH across all substrates. Its roll-off angle appears to be one of the lowest, however it exhibited film formation due to the high CAH. A similar behaviour was observed with LST 30 probe liquid. Similar behaviour was observed for other coating systems, data is available in Appendix A.

6.4. Summary

The objective of Chapter 6 is to understand the impact of surface micro-level roughness on wettability/repellence. The roughness studied in this chapter was primarily obtained by surface blasting with different size grit and blasting pressures. The immediate effect of grit blasting is seen as changes in surface topography (Figure 6.5 and Figure 6.6). The roughness parameter values obtained by Surfcom and Alicona are very similar. The grit blasted surface gives roughness average values ranging from (Ra) of 1 μm to 4 μm with negative roughness skewness (Rsk) which means that height distribution is skewed below the mean plane (Figure 6.3). This was expected as the grit blasting was employed to introduce surface roughness to the substrates. For the mirror finish stainless steel substrate the roughness profile seems to be planar and roughness average parameter is in the range of 0.04-0.14 μm as expected.

The effect of grit-blasting and surface treatment on repellence were studied by wettability assessments. The static contact angles with 2μL droplets of water, diiodo-methane, LST 50, LST 30, Xylene and Decane were measured. The increase in surface roughness from 0.01 μm to 4 μm for the uncoated substrates results in a rise of static contact angles for probe liquids. For liquids with lower SFE that are LST 30, Xylene and Decane the deposited probe liquid gave contact angles below 10°. According to Wenzel the greater the deviation from 90° on a smooth surface, the greater will be the influence of introduced roughness. Thus, if the contact angle is below 90°, the introduction of surface roughness is expected to decrease the contact angle further, however the obtained values do not seem to follow this trend. Introduction of roughness enhanced contact angle even though the starting contact angle was below 90° for all liquids studied.

For the coated substrates, a similar effect was observed; increase in surface roughness enhances repellence of all liquids except for Xylene and Decane. Comparing fluorinated and un-fluorinated silane treatments, the coating containing fluorine exhibited higher contact angles on both roughened and smooth surfaces for all liquids. This effect can be seen more evidently for low SFE disperse liquids; Xylene and Decane. Even for the lowest liquid surface tension liquid (23.8 mN/m) the contact angle is maintained at 47-54°. On the polysiloxane based coating polar probe liquids (water, LST 50, LST 30) exhibit high contact angle values but for disperse probe liquids (Diiodo-methane, Xylene, Decane) the same

effect cannot be achieved and for Xylene and Decane even additional surface roughness does not enhance contact angle values.

The SFE values were calculated for mirror finish, and grit 100 blasted stainless steels coated with Sivo EC and Sharc Sapphire. The SFE for each substrate was calculated using Owens, Wendt, Rabel and Kaelble (OWRK) method based on water and diiodo-methane contact angle values. For all samples increase in roughness provided a decrease in SFE (Table 6-10). Probe liquids do not penetrate in the roughness grooves of the substrate if the roughness profile can maintain capillary pressure and create air pockets inside the grooves. This means that the decrease in SFE values is not attributed to the actual change in SFE but to the increase in contact angles based on which SFE is being calculated.

The dynamic contact angle assessment showed that the roughened substrates with micro scale roughness exhibit high contact angle hysteresis, no roll-off or film formation for liquids with low surface tensions. Water droplets remain pinned to the surface even at a tilt of 80 º while diiodo-methane spreads on the surface and forms a film. As mentioned in Chapter 2, super repellent surfaces that will eliminate pinning of droplets should have a minimal contact angle hysteresis; less than 10º. Which in the case of grit blasted surfaces was not achieved.

CHAPTER 7. NANO-SCALE ROUGHNESS

7.1. Introduction

The work reported in this Chapter 7 relates to the investigation into the effect of nano-scale roughness on surface wettability and repellence for a variety of probe liquids. Nano-scale roughness is introduced to the surface by silica nanoparticles deposition (Figure 7.1) while low SFE is achieved by surface functionalisation of nanoparticles with silanes. As previously reviewed in Chapter 2 and 3, smaller nano-pore/capillary diameters between neighbouring particles inhibit liquid penetration and therefore enhance repellence.

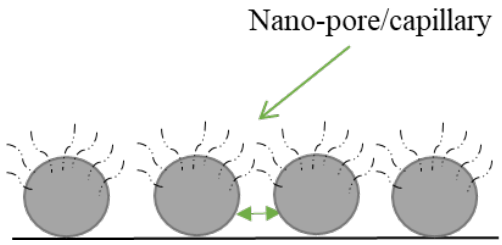

Figure 7.1 Silica nanoparticles deposited onto the substrate

7.2. Silica nanoparticles

Two types of silica nanoparticles (SNPs) were used in the study; synthesised by sol-gel method (SMS35) and commercial fumed silica particles (Aerosil 200).

7.2.1.Stöber silica nanoparticles

Previous work at TWI has established a reproducible methodology for synthesis of silica nanoparticles via Stöber method (Bourebrab *et al.*, 2018; La Rosa, 2020). This method was used within this project to obtain nanoparticles with a diameter of ~35 nm, these particles are labelled as SMS35.

The silica particle synthesis by hydrolysis and condensation of alkoxysilanes was first mentioned by Stöber and Fink (1968). Producing SNPs via the Stöber process is a very attractive method as it allows synthesis of SNPs with very low impurity levels, small particle size and narrow particle size distribution (Suratwala *et al.*, 2003).

To synthesis SNPs via Stöber method, the silane source TEOS was added to ethanol in the presence of water and ammonia. The following reaction takes place in the process:

$$Si(OC_2H_5)_4 + xH_2O \rightarrow Si(OC_2H_5)_4{-}x(OH)_x + xC_2H_5OH \quad 7.1$$

$$\equiv Si{-}OC_2H_5 + HO{-}Si \equiv \rightarrow \equiv Si{-}O{-}Si \equiv + C_2H_5OH \quad 7.2$$

$$\equiv Si{-}OH + HO{-}Si \equiv \rightarrow \equiv Si{-}O{-}Si \equiv + H_2O \quad 7.3$$

The reactions above provide an overview description of the hydrolysis and condensation reactions that take place during the Stöber synthesis method. The outline method used to produce the SMS35 particles is shown in Figure 7.2.

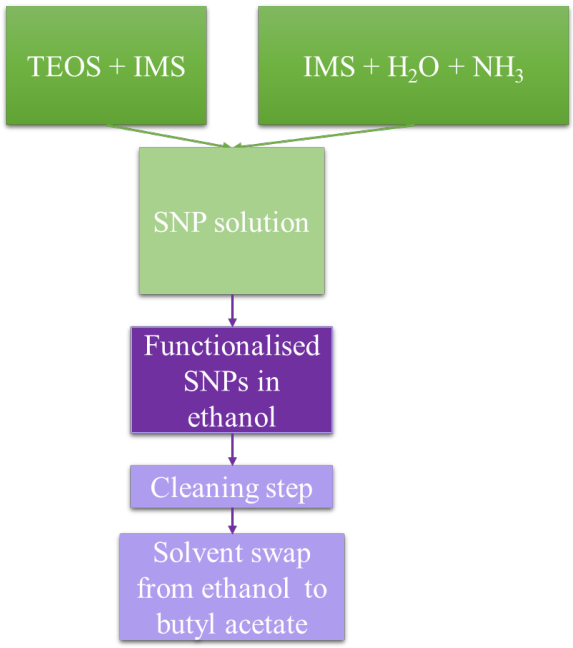

Figure 7.2 SNP synthesis process via sol-gel

The size (Z - average) and poly-dispersity index (PdI) of the SMS35 suspensions were measured using the dynamic light scattering (DLS) using the Zetasizer Nano S Malvern Panalytical. The obtained results are presented in section 7.2.4. The methodology behind DLS measurements is described in Chapter 4.

7.2.2.Aerosil 200®

The Aerosil® process produced silica (and other metal oxide) nanoparticles via a pyrogenic route, these materials are often referred to as “fumed silica”. Typically, silicon tetrachloride is passed through a flame at ~2500-3000°C, this oxidises the feedstock and generates spherical silica nanoparticles of size 7-15nm in diameter. These dense particles aggregate into complex secondary structures and have surface areas that are dictated by the primary

particle size. The material used in this project had a specific surface area of ~200m^2/g according to the manufacturer.

7.2.3. Silica nanoparticle functionalisation

Zhuravlev (1993) described the surface chemistry of SNPs and concluded that the surface hydroxyl density to be 4.6 OH/nm^2 and 4.9 OH/nm^2 calculated by the least-squares method and the arithmetical mean, respectively. These values are widely recognised and quoted (Mueller *et al.*, 2003; Spyrogianni *et al.*, 2017).

SNPs similarly to glass are inherently hydrophilic as the surfaces are dominated by hydroxyl groups (Figure 7.3, Figure 7.4). As previously discussed in Chapter 5 surface hydroxyl groups are the main bonding/adsorption sites for water and should be eliminated to decrease wettability.

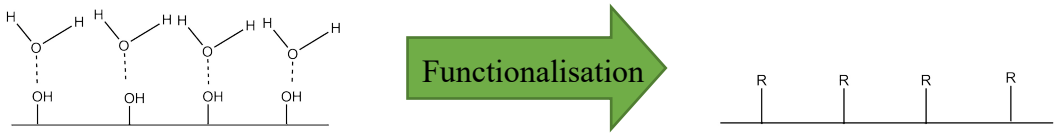

Figure 7.3 Glass surface with sites for water adsorption and glass surface functionalised with silanes

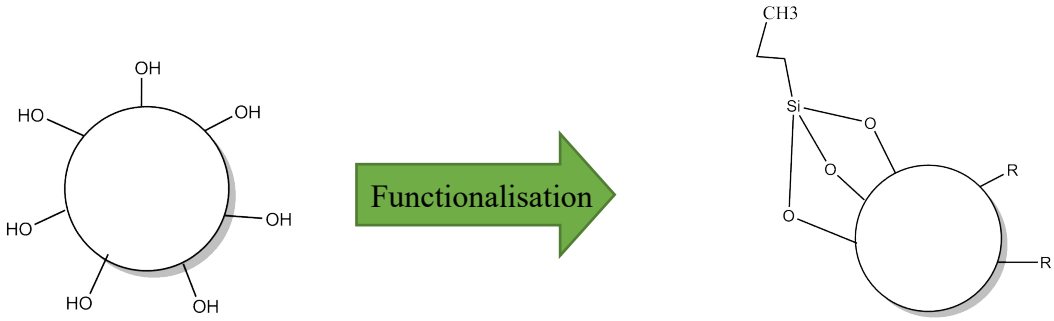

Figure 7.4 SNP surface with sites for water adsorption and SNP surface functionalised with silanes

Both Stöber and fumed SNPs were functionalised to eliminate surface hydroxy groups and to increase their hygrophobicity. Two types of silane functionalisation agent were used, one fluorinated and one non-fluorinated. The silanes used were hexamethyldisilazane (HMDZ- CAS Number: 999-97-3) and 3,3,3- trifluoropropyltriethoxysilane (333 - CAS number 681-97-0). Functionalisation using HMDZ was performed on both the Aerosil 200 and the SMS35 whilst the functionalisation with fluorinated silane 333 was performed only on Stöber SNPs.

HMDZ reacts with the surface hydroxyl groups to graft trimethylsilyl (TMS) groups on to the surface. The replacement of polar, protic hydroxyls with low polarity, aprotic trimethylsilyl ligands has a profound effect on the surface chemistry of silica and silicates (Currell and Parsonage, 1981; Ettlinger, Ladwig and Weise, 2000; Frahn *et al.*, 2001). The surface is transformed from behaving in a hydrophilic manner to hydrophobic.

Functionalisation of SNPs with hexamethyldisilazane can be undertaken in the vapour phase or in solution/suspension. Suratwala *et al.* (2003) reacted Stöber silica with HMDZ in solution/suspension and studied both reaction time as well as concentration on the level of trimethylsilyl (TMS) functionalisation. The reaction time of 7 days together with excess sylilating agent increased the amount of grafted TMS on the surface of the SNPs and facilitated sufficient surface coverage. This methodology used by Suratwala was used as the basis for the HMDZ treatment of the SMS35 material in suspension.

The approach to functionalisation is shown schematically in Figure 7.5.

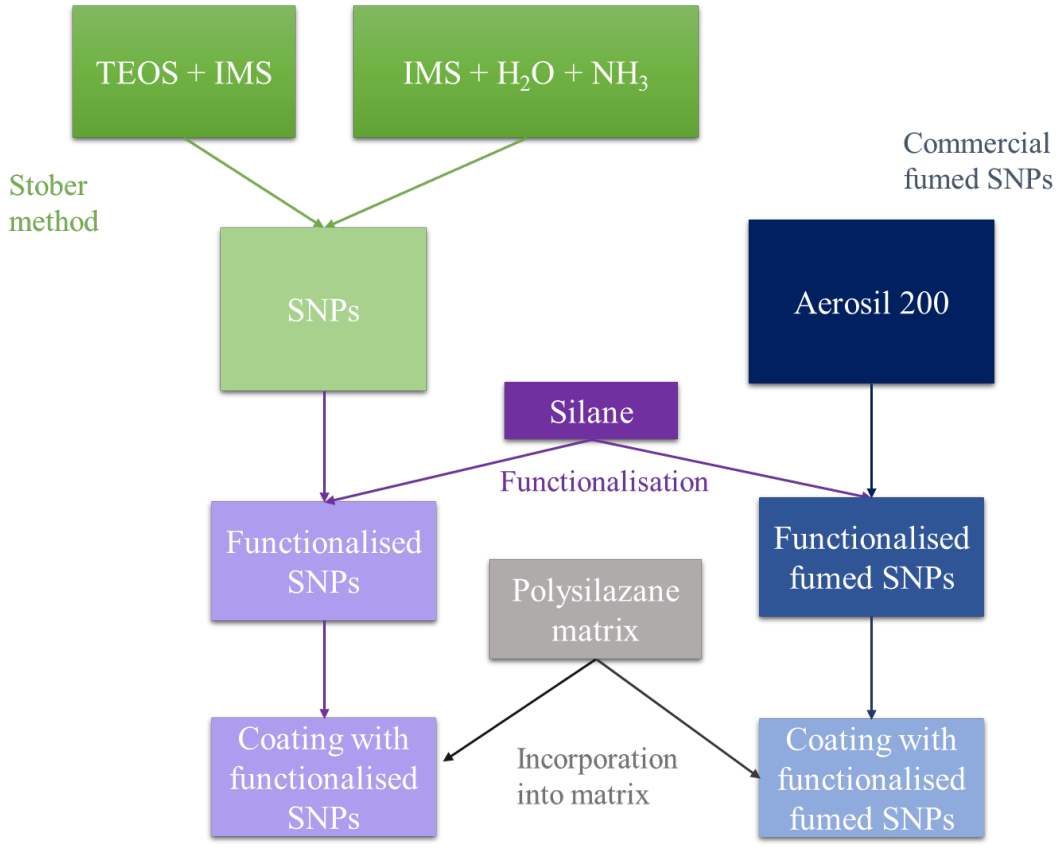

Figure 7.5 SNPs and functionalisation used in Chapter 7

The single HMDZ functionalisation on the SMS35 functionalisation was performed at T4 level, where the T level is defined as:

$$T\ level = \frac{mass\ of\ silane\ (HMDZ)}{mass\ of\ silica}$$

The HMDZ was added to the SMS35 suspension (~4.4% solids in IMS) and the vessel was sealed and heated at 65°C for 7 days to ensure a high TMS coverage. Excess silane was required to accommodate the reaction between HMDZ and alcohol which is competitive with the HMDZ-silanol reaction. After 7 days the solvent was exchanged for fresh IMS to reduce the pH of the suspension.

The Aerosil 200 silica was functionalised by adding 5 grams of HMDZ to a suspension of 5 grams Aerosil 200 in 70 grams of butyl acetate. The suspension with added silane was shaken for 48 hours. After which it was dried out for 72 hrs at 65 ºC to remove all the solvent and obtain functionalised SNP powder.

To undertake the functionalisation with the 3,3,3- trifluoropropyltriethoxysilane, a T level 0.125 was used in conjunction with ammonia as catalyst and the functionalisation was performed at 65 ºC for 18 hours. The role of the ammonia was to hydrolyse the alkoxy groups on the silane and to promote condensation of these onto the silica surface. Ammonia could not be used with HMDZ functionalisation since this silane does not possess alkoxy groups.

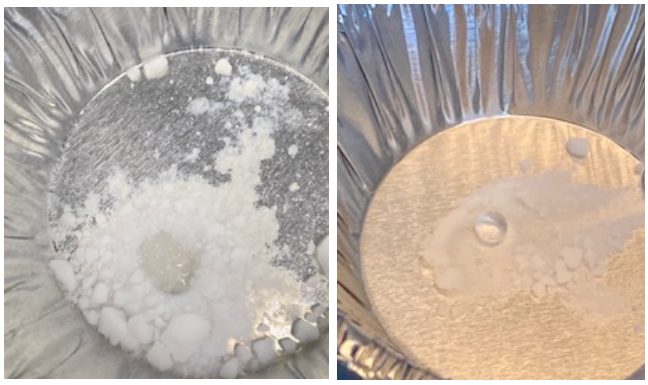

Figure 7.6 water drop wettability test; (a) un-functionalised Aerosil 200, (b) HMDZ functionalised Aerosil 200

The dried fumed SNP powder was assessed for surface functionalisation with a simple water drop wettability test. The droplet of water was deposited on the SNPs to assess if it would wet their surface. As shown in Figure 7.6, the unfunctionalised powder is wetted easily while the HMDZ functionalised one exhibits a very high contact angle suggesting that functionalisation was successful.

7.2.4. Dynamic Light Scattering

The average size and size distribution of the particles at every stage of the SMS35 fabrication and functional process is presented in Table 7-1 and in Table 7-2.

Table 7-1 DLS data for un-functionalised SMS35

SNPs	Solution	Z-average (d. nm)	PdI
Un-functionalised SMS35	Ethanol	47.54	0.159

Table 7-2 DLS data for functionalised SMS35

SNPs	Solution	Z-average (d. nm)	PdI
HMDZ functionalised SMS35	Ethanol	44.18	0.111
	Ethanol after cleaning	50.01	0.126
	Butyl Acetate	31.33	0.264

It can be seen that the primary particle size of the SMS35 was 47.54 nm which is within the specification for this material. The polydispersity index (PdI) value of 0.159 is also considered acceptable and within the specification. Functionalisation with the HMDZ caused an apparent decrease in the particle size but did not have a significant effect on the particle size distribution as shown in figure 7.7b and in the measured PdI. This behaviour is in line with previous experience with this material.

Due to the aggregated nature of the Aerosil 200, particle size analysis of the dispersed material was not undertaken.

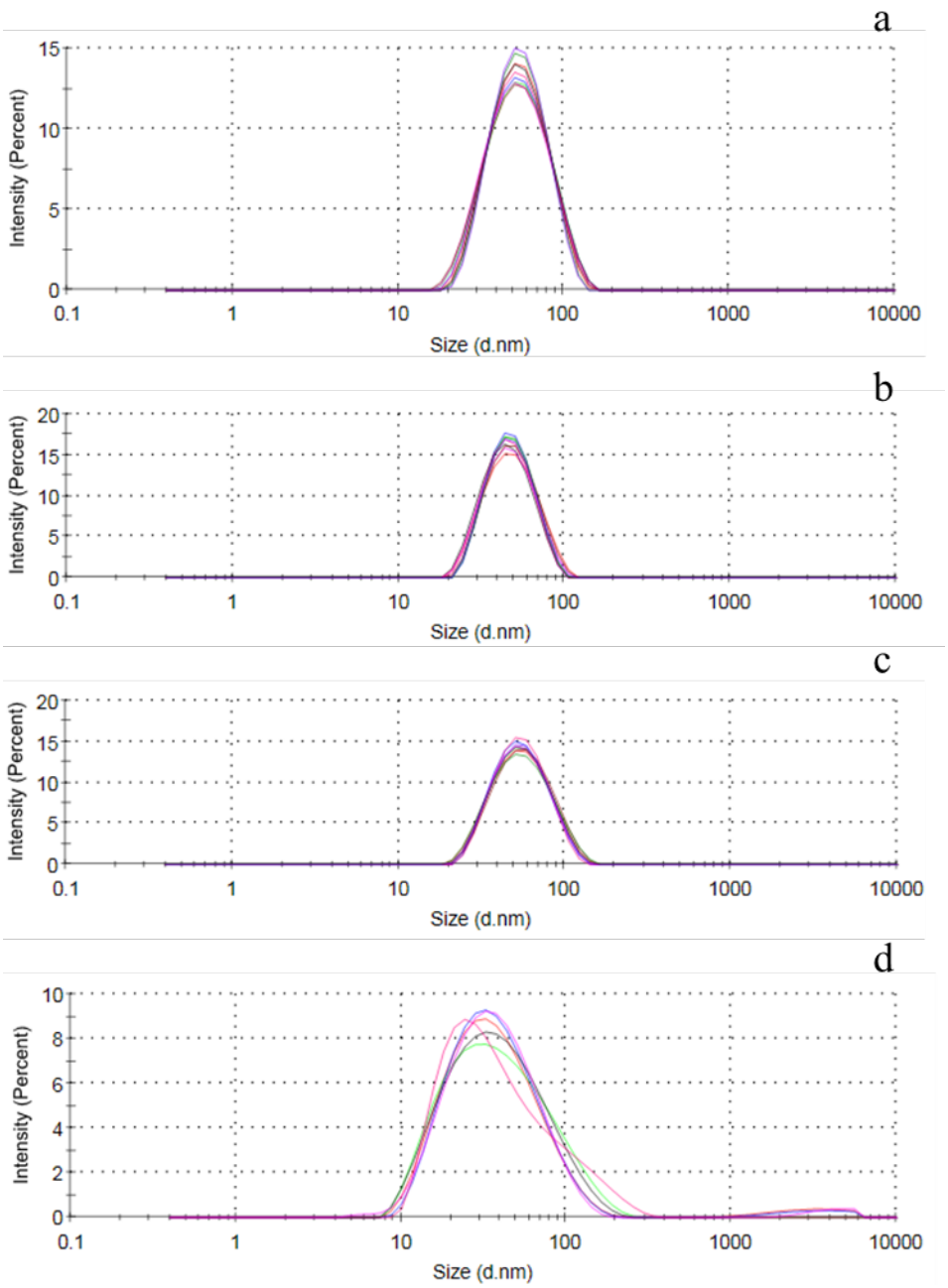

Figure 7.7 DLS size distribution by intensity measurements; before functionalisation dispersed in ethanol (a), after functionalisation dispersed in ethanol (b), after functionalisation and cleaning (c), after functionalisation solvent swapped in butyl acetate (d)

7.3. Coating deposition via dip coating

The prepared coating formulations as well as the nanoparticle suspensions reported in this chapter were deposited via dip coating method. Dip coating involves dipping a substrate in a coating solution and then vertically lifting it with a specific velocity v_0. This results in a wet film with a thickness λ. Dip coating is a simplistic method to deposit films but it involves a complex interaction between several counteracting factors such as: viscous drag upward

on the liquid by the substrate, gravitational force on the wet film, surface tension in the meniscus between the substrate and the solution, surface tension gradient along the film height caused by drying effect, the disjoining or conjoining pressure specifically in the films with thickness less than 1μm and etc. (Brinker *et al.*, 1992). The wet film thickness can be estimated from the relationship by Landau and Levich (1942):

$$\lambda = 0.94 \frac{(\eta v_0)^{\frac{2}{3}}}{\lambda_{LV}^{\frac{1}{6}} \sqrt{\rho g}}$$

Where λ_{LV} is the liquid surface tension at the meniscus, g is the gravitational acceleration (9.81 m/s^2) and η is viscosity. The advantage of the dip coating technique is that it is a simple method and it can be used for coating of irregular and complex shapes. Drying establishes the shape of the fluid profile, the deposition time as well as the magnitude of the forces exerted on the solid phase. As can also be seen from the relationship the velocity or rate of dipping plays an important part in the coating thickness and the thickness of the wet film can be precisely controlled or tuned to obtain the desired thickness. The coating protocols should be defined to tailor the deposition process to the specific application.

The dip coating routines used for the samples reported in this chapter were performed at a range of dipping rates varying from 50 mm/min to 500 mm/min to establish the effect of coating thickness on its wettability, roughness, and resistance to abrasion. After the withdrawal of the slide, the wet film was dried by heating in air at 150°C for 1 hour.

7.4. Silica nanoparticle deposition without a matrix

To study the effect of SNP deposition on surface topography, WLI images were taken of glass slides after dip-coating into a suspension of HMDZ functionalised SMS35 at a deposition rate of 100 mm/min, these are shown in Figure 7.8.

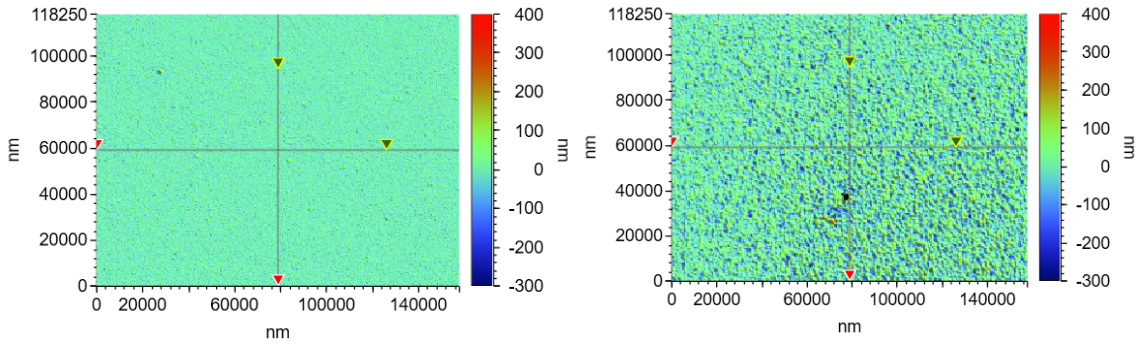

Figure 7.8 WLI image of glass without any treatment (left), glass slide with deposited HMDZ functionalised SMS35 silica nanoparticles (right)

The deposited film increased the roughness average from 9 nm to 11 nm and the root mean square deviation from 35 to 45 nm. To assess if SMS35 HMDZ film had been deposited as a monolayer, the surface was scratched to remove the particles from the surface and expose the substrate underneath, after which the WLI measurement was undertaken (Figure 7.9).

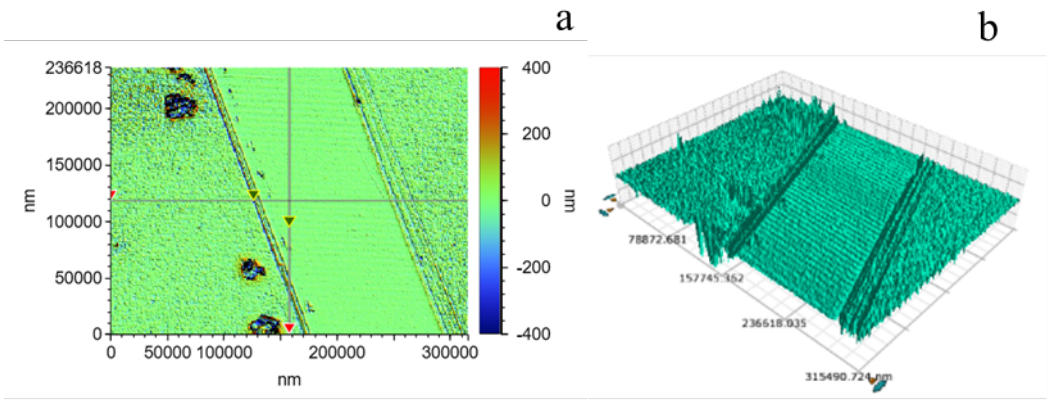

Figure 7.9 WLI of SMS35 functionalised with HMDZ on a glass substrate; top view (a) and 3D side view (b)

The measured region of the sample is presented in Figure 7.9. The roughness profile was used to calculate the height difference between the coated region and the exposed glass substrate. The height difference value obtained was 30 nm. From the DLS data it was confirmed that the Z-average of functionalised SMS35 nanoparticles was 31 nm. The value of just 30 nm obtained from WLI image suggests that the film consisted of nanoparticles assembled as a monolayer.

AFM images were taken of the deposited HMDZ functionalised SMS35 on glass (Figure 7.10), from the phase image (Figure 7.10 a) single SNPs can be identified. The roughness profile (Figure 7 10 c) was obtained for the selected nanoparticle presented in Figure 7.10 b

and its diameter was measured to be approximately 38 nm. The diameter of the deposited SNPs obtained by AFM correlates well with the DLS and WLI data. It can also be seen that the nanoparticle deposit in a film forming fashion. This effect can also be observed from the structural colour of the thin film formed by SNPs (Figure 7.11).

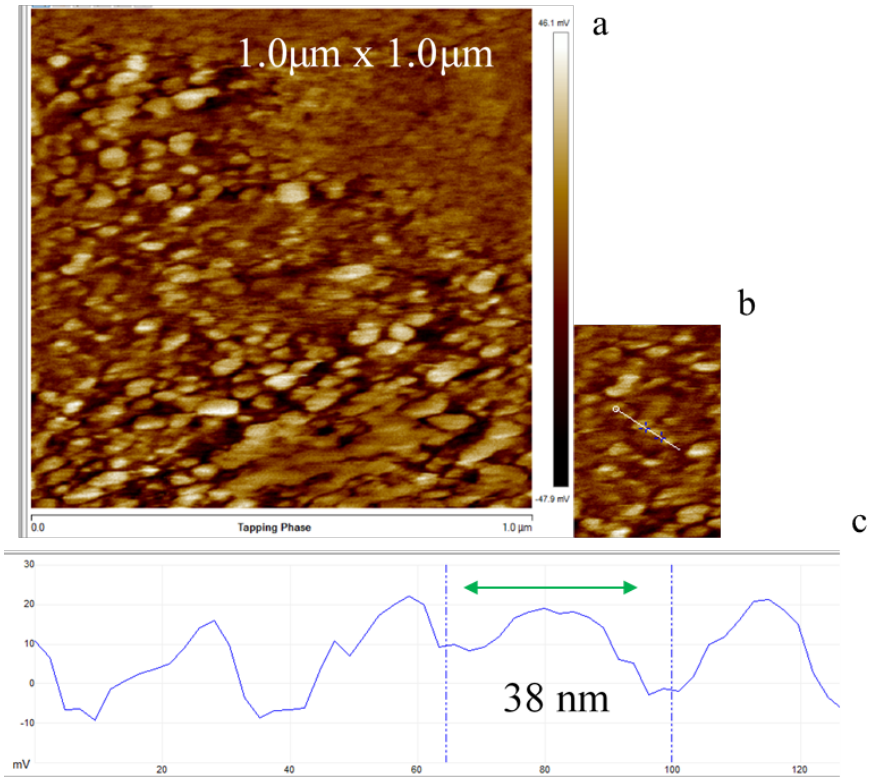

Figure 7.10 AFM image and profile of SNPs deposited on glass

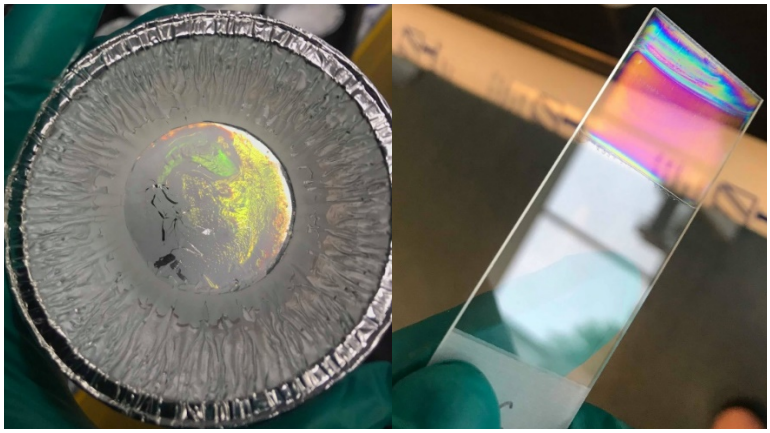

Figure 7.11 Structural colour of deposited SNPs film (SMS 35 functionalised with HMDZ)

7.5. Silica nanoparticle incorporation into the matrix

7.5.1.Nanocomposite coating preparation

The functionalised silica suspensions; SMS35 HMDZ, SMS35 333 and Aerosil 200 HMDZ were all dried out via evaporation to remove all volatile materials. The dried materials were then dispersed into fresh butyl acetate at a nominal loading to match the NVC value of the polysilazane coating solution (Sharc Sapphire®). The relative amounts of the functionalised SNP suspensions and polysilazane coating solution were adjusted to give the required loading of the functionalised SNP. This is shown schematically in Figure 7.12.

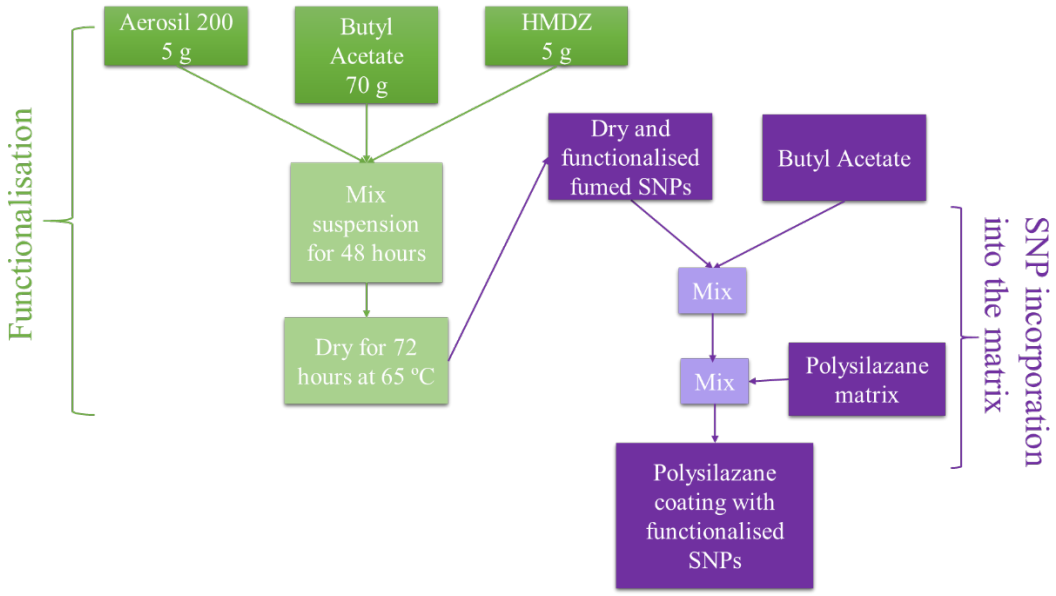

Figure 7.12 Fumed silica functionalisation and incorporation into the matrix process

7.5.2.Matrix for silica nanoparticles

The polysilazane coating Sharc Sapphire® was selected as a matrix for the functionalised SNPs.

For the SMS35 SNPs two levels of particle loading in the matrix were investigated 1:1 ratio (matrix: SNP ratio - 50% loading) and 1:3 ratio (75% loading). The functionalised Aerosil 200 functionalised SNP powder was incorporated into the matrix at 1:1 matrix to SNP ratio (50% loading).

The non-volatile content (NVC) is a measure of the amount of a non-volatile/solid contained in a solvent solution/suspension (ASTM D1644-01, 2017). The NVC of coating matrix was analysed by drying the aliquot of the material in an oven at 65°C for 18 hours. The NVC value was calculated as a percentage:

$$NVC\ (\%) = \frac{mass\ of\ non-volatile\ material}{mass\ of\ the\ solution} \times 100$$

The NVC of Sharc Sapphire coating was calculated to be 14.63% (± 0.32), the measure is based on 3 samples. The dried SNPs were therefore re-dispersed in butyl acetate at a nominal 15% to match the non-volatile (solid) content of the Sharc Sapphire coating which consists of polysilazane (solids) in butyl acetate (BA).

Deposition of the functionalised coating formulations was via dip coating as described earlier (section 7.3). The coated samples were dried and cured at 150°C for 1 hour in an air atmosphere.

7.5.3.White Light Interferometry

The surface roughness of matrix (Sapphire) and matrix modified with SNPs was studied using WLI. The WLI assessment was undertaken to confirm that the incorporation of SNPs into the coating matrix does not give rise to a levelling effect, that the SNPs are well distributed and provide nano-scale topography to the surface. Figure 7.13 shows the WLI images of the 2B stainless steel substrate uncoated, coated with the parent polysilazane and with SMS 35HMDZ modified polysilazane. Images of the coating and the coating edge were taken as was the modified coating on glass for comparison.

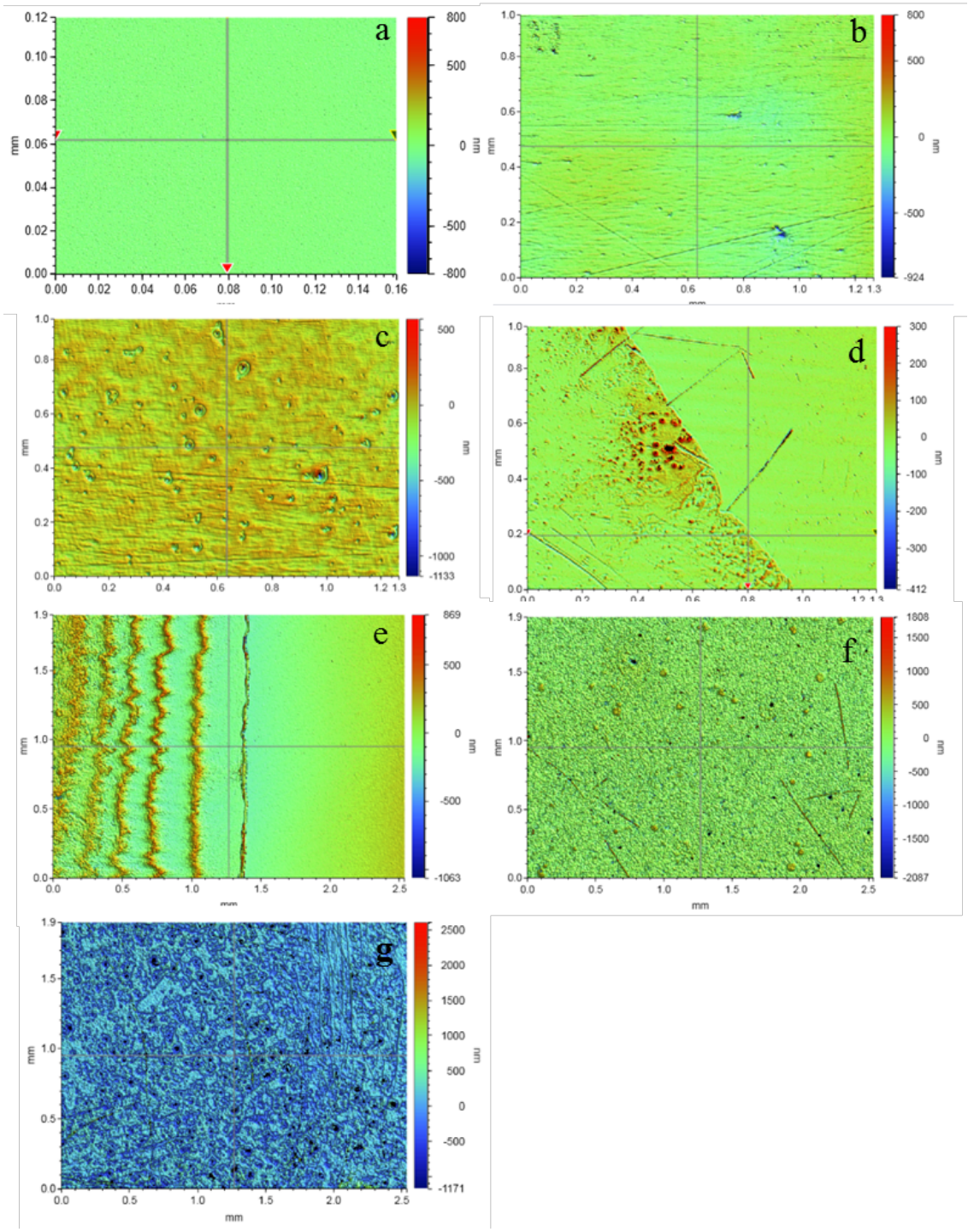

Figure 7.13 White Light Interferometry images of a. glass, b. Stainless steel, c. stainless steel coated with Sapphire d. edge of Sapphire coating and stainless steel, e. edge of Sapphire coating on glass with incorporated functionalised SNPs (75% loading) deposited by dip coating, f. Sapphire coating on glass with incorporated functionalised SNPs (75% loading) deposited by dip coating g, aerosil 200 deposited on glass

The measured roughness of stainless steel on its own was 33.62 nm and Rq is 45.9 nm. The deposition of the parent polysilazane coating does not change the surface topography significantly, the roughness average measured on stainless steel with polysilazane coating is 38 nm and Rq 55 nm.

Figure 7.13 (d) shows the edge of parent polysilazane coating with the stainless steel substrate. A similar image is presented in Figure 7.13 (e) for modified polysilazane (SMS 35 HMDZ at 75% loading level) coating deposited via the dip-coating method on glass. For the modified coating perpendicularly, oriented stripes with SNPs can be observed. However, the stripes seem to appear at the edge with the glass and disappear where the coating reaches a constant thickness as seen in Figure 7.13 (f). When the coating film reaches its constant thickness, the particles appear well distributed in the coating. The modified polysilazane coating with SMS 35 HMDZ T4 functionalised SNPs at 75% loading level has a significant effect on the surface roughness. The roughness average of untreated glass is 9 nm while the glass coated with modified polysilazane coating has the roughness average value of 85 nm. The roughness value demonstrates that the SMS35 HMDZ particles at 75% loading increased the roughness of the polysilazane coating. Furthermore, at this loading level the matrix did not give rise to a levelling effect and so the use of the functionalised SNPs enabled the achievement of nano-topography. A similar effect was observed with commercial SNPs. Glass deposited with polysilazane coating modified with Aerosil 200 (HMDZ functionalised and incorporated at 50% solid loading level) increased the surface roughness of glass to 176 nm. This suggests that Aerosil 200 modified coating provides rougher nano-scale topography compared to SMS 35. The roughness average for commercial SNPs is more than double the value of that of SMS 35.

7.5.4.Atomic force microscopy

The atomic force microscopy images, at different resolutions, of the SNPs incorporated in the matrix were obtained using the tapping mode. The methodology used for AFM measurement is described in Chapter 4. The images shown in Figures 7.14 – 7.18 clearly show the SMS 35 HMDZ functionalised silica particles uniformly distributed in the polysilazane matrix. Even at high resolution, image area of 400 x 400nm there is no evidence of clustering or aggregation of the HMDZ functionalised SMS 35 silica nanoparticles.

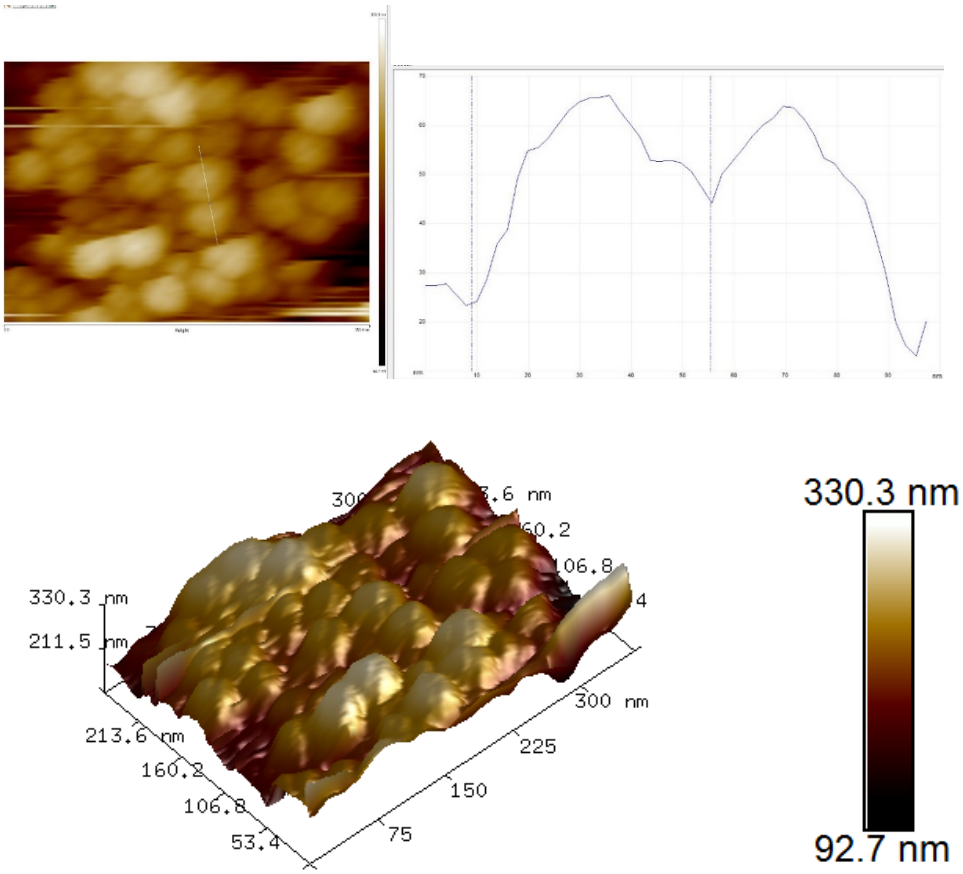

Figure 7.14 AFM topography images (400 nm area) of Sapphire with incorporated SMS 35 HMDZ T4 functionalised at 50% loading level deposited at a dipping rate of 10 mm/min on glass.

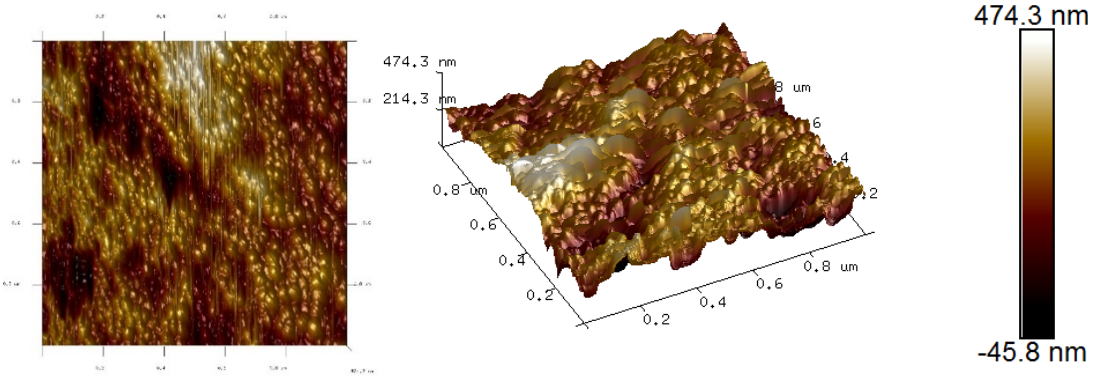

Figure 7.15 AFM topography image (1 µm area) of Sapphire coatings incorporated with SMS 35 HMDZ T4 functionalised at 50% loading level deposited at a dipping rate of 10 mm/min on glass

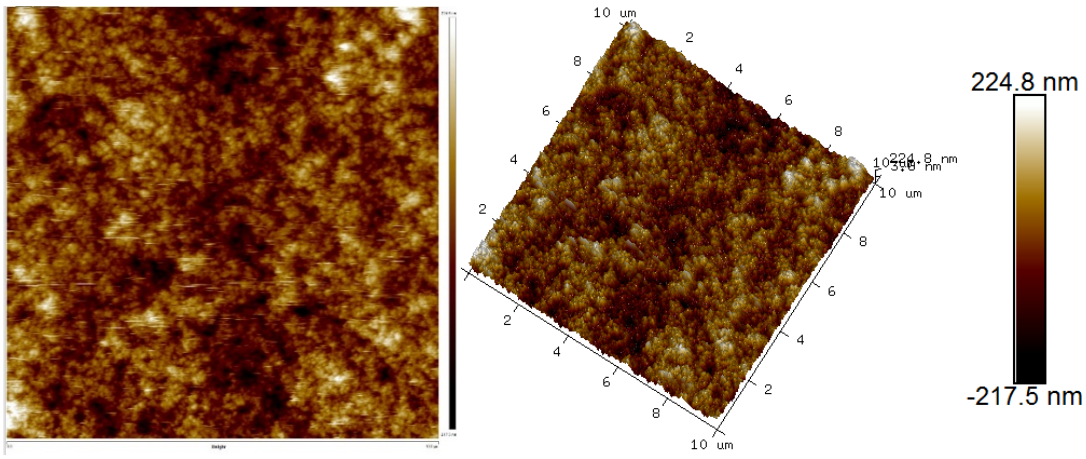

Figure 7.16 AFM topography image (10µm area) of Sapphire with incorporated SMS 35 HMDZ T4 functionalised at 50% loading level deposited at a dipping rate of 10 mm/min on glass

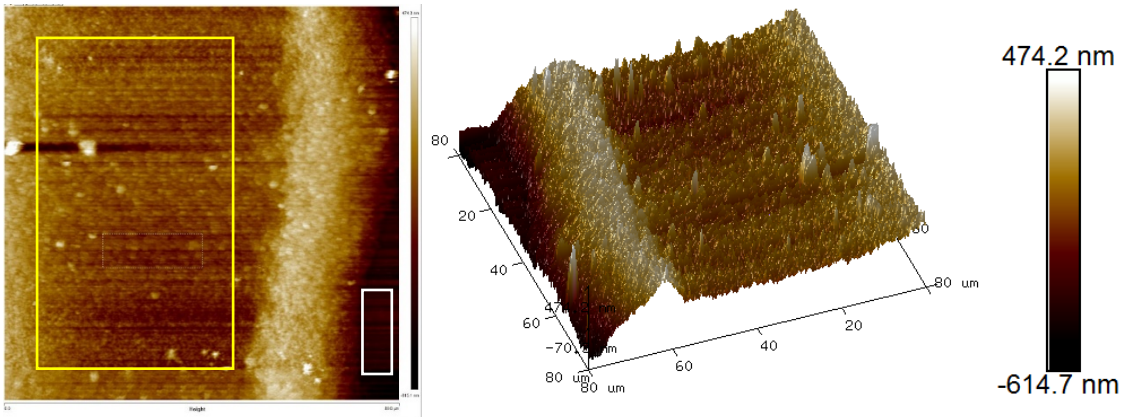

Figure 7.17 AFM topography image showing the edge of the modified coating (Sapphire with SMS 35 HMDZ T4 functionalised at 50% loading level) on glass

The AFM image in Figure 7.14 provides the roughness profile of the SNPs deposited on glass. From the obtained roughness profile the diameter of the single nanoparticle was measured to be 48 nm. Figure 7.17 shows the 80 µm area of the coating edge with glass topography generated by AFM in a tapping mode. The roughness average of glass (white square area in the AFM image) is 30.1 nm whilst the same parameter has a value of 56.2 nm in the coated area (yellow square area in the AFM image). This supports the findings of the WLI analysis showing that the presence of the nanoparticles introduces nanoscale roughness into the coating. The AFM study also supports the WLI finding that the SNPs are well distributed in the coating matrix.

7.6. Visual appearance

7.6.1. Effect of deposition rate

The effect of deposition rate on the visual appearance was studied using gloss meter. The methodology used is described in Chapter 4. The values obtained are presented in Table 7-3. There was no significant change observed in gloss or haze. The measured values seem to be independent of the deposition rate for SNPs F333 T0.125 75% sapphire deposited on stainless steel.

Table 7-3 Effect of deposition rate on visual appearance

Coating	**SNPs F333 T0.125 75 % sapphire deposited on stainless steel**		
Deposition rate	10.0 mm/m	100.0 mm/min	500.0 mm/min
Gloss	94.4 (± 4.4)	99.8 (± 3.0)	97.1 (± 3.5)
Rspec	52.5 (± 2.6)	61.6 (± 5.9)	43.7 (± 5.9)
Haze	18.0 (± 0.5)	23.1 (± 1.6)	20.4 (± 1.0)
DOI	81.8 (± 0.3)	84.4 (± 1.0)	70.9 (± 5.2)

7.7. Wettability tests

7.7.1. Incorporation of silica nanoparticles into the matrix

Wettability studies were performed using the DSA 100, the methodology used to determine wetting and to estimate the SFE of the specimens is described in Chapter 4.

Stainless steel samples with a 2B finish were dip-coated with the parent Sapphire coating solution the SMS 35 F333 suspension (no matrix) or the modified Sapphire coating containing the SMS 35 F333 nanoparticles at either 50% or 75% loading. All samples were dip coated at a rate of 100 mm/min and cured at 150 ºC in the oven. After which the contact angles with water and diiodo-methane were measured, these values are given in Table 7-4 and the data is presented in Figure 7.18.

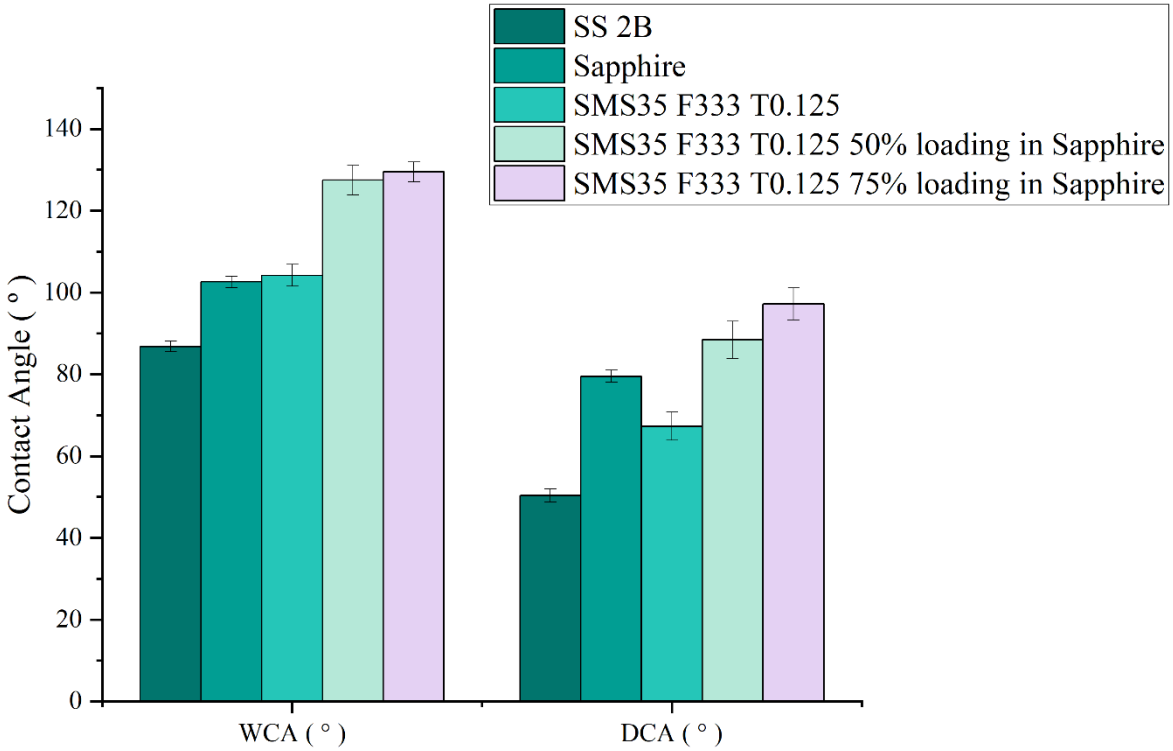

Figure 7.18 Wettability study before and after incorporation of SNPs

Table 7-4 WCA and DCA of coating matrix, SNPs, and matrix with SNPs

Sample	WCA (°)	DCA (°)
Stainless steel 2B finish	86.8 (±1.3)	50.4 (±1.6)
Sapphire on stainless steel 2B finish	102.6 (± 1.4)	79.5 (± 1.9)
SMS35 333 T 0.125 without Matrix	104.2 (± 2.7)	67.3 (± 3.4)
SMS35 333 T 0.125 50% loading with Sapphire	127.5 (± 3.6)	88.4 (± 4.5)
SMS35 333 T 0.125 75% loading with Sapphire	127.7 (± 1.4)	100.0 (± 0.3)

The parent Sapphire and functionalised SNPs (no matrix) give water contact angles values of approximately 100º. The sessile drop values for diiodo-methane ranged from 67º to 80º. There is an uplift in contact angles compared to the untreated stainless steel with 2B finish. However, the contact angles are lower compared to the modified coatings. This is likely to be due to the lack of a matrix which means the particles can be displaced, particularly by a dense liquid such as diiodo-methane. The incorporation of the functionalised SNPs into the Sapphire coating at 50% loading level elevated both contact angles to values of 128º and 88º for water and diiodo-methane respectively. Increased loading level maintained the water repellence at ~128º whilst the diiodo-methane contact angle increased to 100º.

The synergistic effect of the particles in the matrix is clear, a significant increase in repellence to both probe liquids was observed. However, whilst the increase in the repellence of diiodo-methane increased with loading from 50% to 75%, the hydrophobicity appeared to have plateaued for this type of additive.

Similar measurements were undertaken on the three different SNPs (HMDZ functionalised Aerosil 200, HMDZ functionalised SMS 35, and F333 functionalised SMS35) incorporated at different loading levels (50% and 75%) in the Sapphire polysilazane.

Table 7-5, Figure 7.19 and Figure 7.20 present the water and diiodo-methane contact angle values for silica nanoparticles incorporated into the Sapphire coating at 50% and 75% solid loading levels. The modified coatings were deposited on glass and stainless steel substrates (2B finish). There was no significant difference observed in contact angles between the coated glass and stainless-steel substrates. This indicates that these coatings provide effective coverage of both substrates and that the measured behaviour is independent of the substrate. Whilst this is perhaps no surprise, it is useful confirmation of this fact given that this was not the case for some of the silane-based coatings reported in chapter 5.

For the functionalised SMS 35 additives, increasing the loading level did not significantly increase the contact angle with water. This is likely to be due to some limit being achieved with regard to the surface chemistry and all samples showing similar roughness types and/or values. However, an increase was observed for the diiodo-methane probe liquid for the fluorinated additive on both substrates. The increase in DCA values can be attributed to the increased fluorine content in the coating that makes the surface more oleophobic (as described and observed in Chapter 5) but does not significantly affect hydrophobicity.

What was particularly notable, was the much higher repellence to both water and diiodo-methane exhibited by the coatings containing the functionalised Aerosil. Given the similar surface chemistry (trimethylsilyl functionality) this difference is most likely to be due to either different roughness levels or potential differences in the coverage of the functional groups on the silica. The WLI assessment showed that coating modified with Aerosil 200 HMDZ has the surface roughness average of 176 nm while for SMS 35 HMDZ additive this value is only 86 nm.

Table 7-5 Contact angle values for 50% and 75% particle loading levels

Particles	Deposition rate mm/min	Particle loading level in matrix	Probe liquids (º)	Substrates	
				CA (º) on glass	CA (º) on stainless steel
Aerosil 200 HMDZ T4	100	50%	WCA	145.3 (± 0.7)	145.8 (± 0.1)
		50%	DCA	106.9 (± 1.8)	108.8 (± 7.8)
SMS 35 HMDZ T4		50%	WCA	124.6 (± 1.1)	132.0 (± 0.7)
		50%	DCA	77.4 (± 1.2)	77.7 (± 2.8)
		75%	WCA	127.4 (± 1.5)	128.3 (± 1.4)
		75%	DCA	79.3 (± 2.1)	81.2 (± 0.4)
SMS 35 333 T0.125		50%	WCA	129.6 (± 1.1)	127.5 (± 3.6)
		50%	DCA	77.9 (± 1.6)	88.4 (± 4.5)
		75%	WCA	130.9 (± 3.3)	127.7 (± 1.4)
		75%	DCA	92.6 (± 7.1)	100.0 (± 0.3)

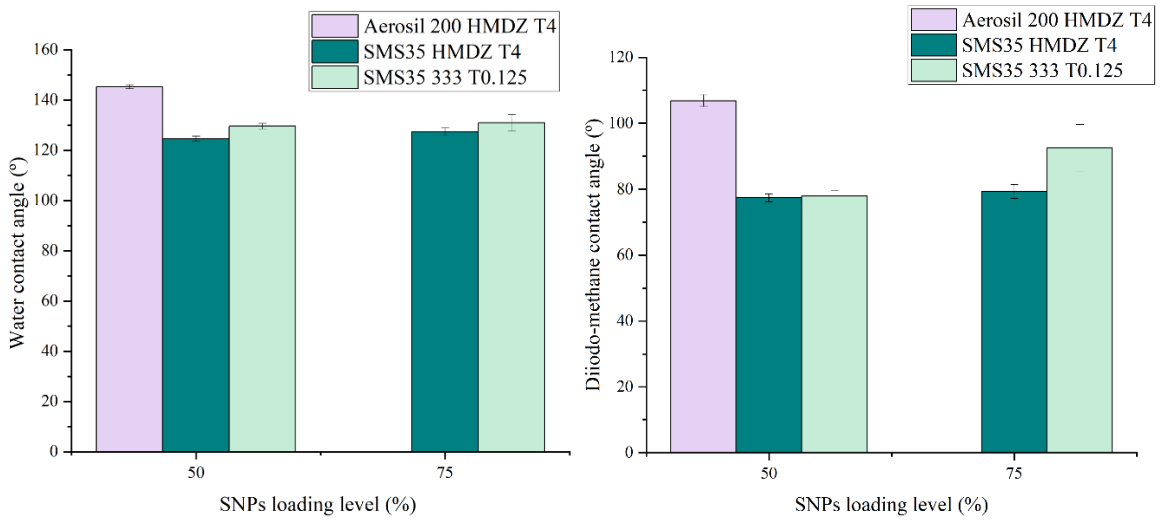

Figure 7.19 Water and diiodo-methane contact angle values for 50% and 75% loading levels deposited on glass

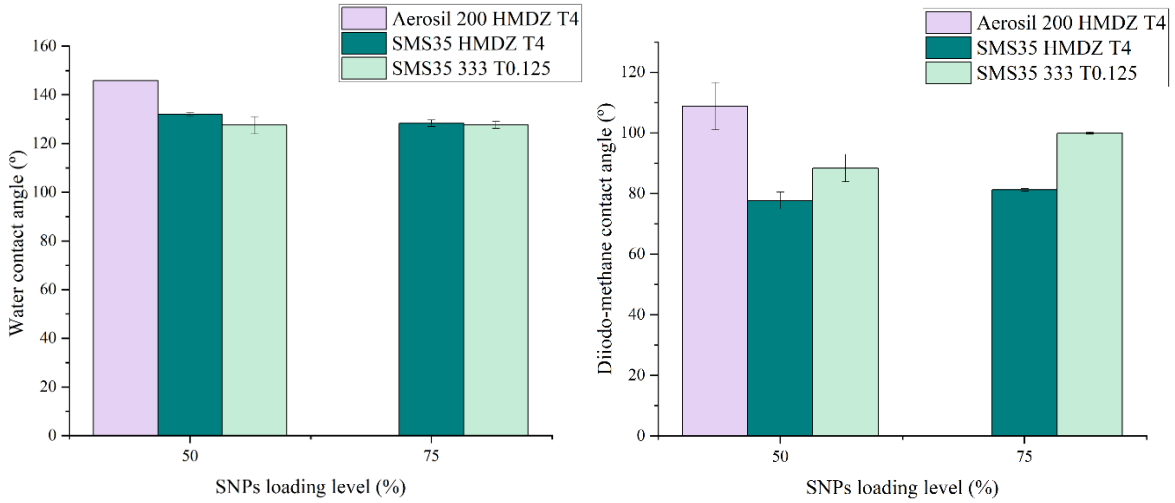

Figure 7.20 Water and diiodo-methane contact angle values for 50% and 75% loading levels deposited on stainless steel

7.7.2. Effect of deposition rate

The deposition rate determines the thickness of the final coating. The deposition rates of 10, 100 and 500 mm/min were used to study the effect of coating thickness on wettability. As can be seen in Table 7-6 the wettability for water does not change with deposition rate for both glass and stainless steel substrates. Similarly, the DCA values show little variability except for the coating deposited onto glass at 100mm/min. Given that no impact of the substrate was observed on these or the other modified polysilazane coatings, and the narrow distribution of DCA values for the other dip coating rates, this data point is viewed as an outlier.

Table 7-6 deposition rates and associated wettability data

	SNPs F333 T0.125 at 50% with Sapphire		
Deposition rate	Contact angle	substrates	
		Glass	Stainless steel 2B
10mm/min	WCA	126.4 (± 2.7)	129.6 (± 0.6)
	DCA	91.6 (± 2.5)	93.1 (± 4.3)
100mm/min	WCA	129.6 (± 1.1)	127.5 (± 3.6)
	DCA	77.9 (± 1.6)	88.4 (± 4.5)
500mm/min	WCA	130.3 (± 1)	127 (± 1.4)
	DCA	95.1 (± 1.6)	88.9 (± 4.7)

7.7.3. Effect of nano-scale and dual-scale roughness

The Sapphire polysilazane coatings incorporated with functionalised SNPs were deposited on grit blasted stainless steel substrates to create a dual-scale topography combining both the micro-scale topography (as described in Chapter 6) and the nano-scale topography described in this chapter. The SNPs used in this dual scale roughness study were the SMS 35 HMDZ functionalised silicas and were incorporated at 50 % solid loading level. The substrates were dip coated at 100 mm/min rate, to provide comparative data planar glass and stainless steel 304 (2B finish) were used, whilst grit blasted stainless steel panels were prepared as described in Chapter 4. The usual curing regime of 1 hour at 150º C was used after which the wettability was studied with water and diiodo-methane as the probe liquids. The measured contact angles are presented in Figure 7.22, Figure 7.23 and Table 7-7.

The grit blasting of stainless steel elevated the water contact angles on grit 100 and grit 20 while other blasted surfaces showed an increase in wetting. For the diiodo-methane the increase was observed with grit 100 and grit 36. On the coated substrates the water contact angle increased consistently with the increase in the substrate's micro-scale roughness until Grit 36 which exhibited a water contact angle of 154º. The surface with greater micro-roughness, prepared by blasting with grit of size 20, showed a slight reduction in the water contact angle which was measured at 132º. The diiodo-methane showed a similar trend with an increase in contact angle value with increasing micro-scale until the surface prepared with grit 60. Further increases in micro-roughness led to a reduction in the DCA. This behaviour is likely to be due to some key topographic thresholds being passed, each threshold being dictated by the specific characteristics of the probe liquids.

The overall impact of the use of dual-scale roughness on water repellence was immense. Figure 7.21 shows the stainless steel slide blasted with grit 100. Half of the slide was coated with the modified coating while the other half was left without any chemical treatment to enhance repellence. The uncoated side showing super hydrophilic behaviour whilst the coated side exhibiting behaviour close to superhydrophobic.

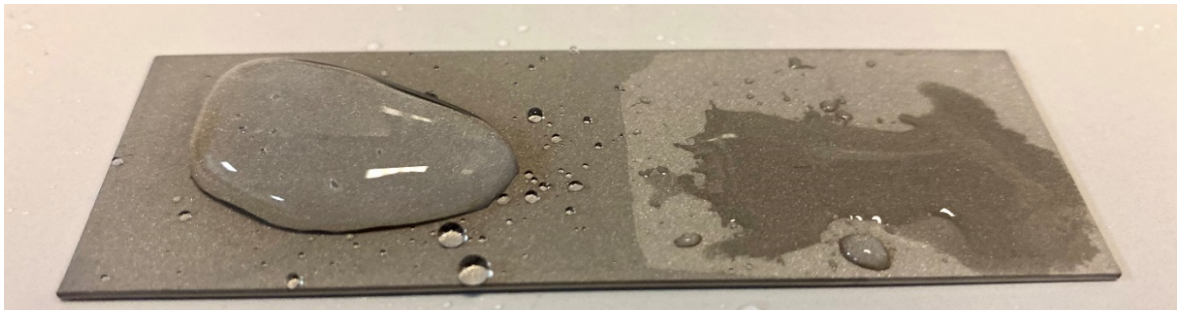

Figure 7.21 The droplets of water on SS304 blasted with grit 100. The Sapphire coating incorporated with SMS 35 HMDZ SNPs loaded 50 % (left) and no-coating (right)

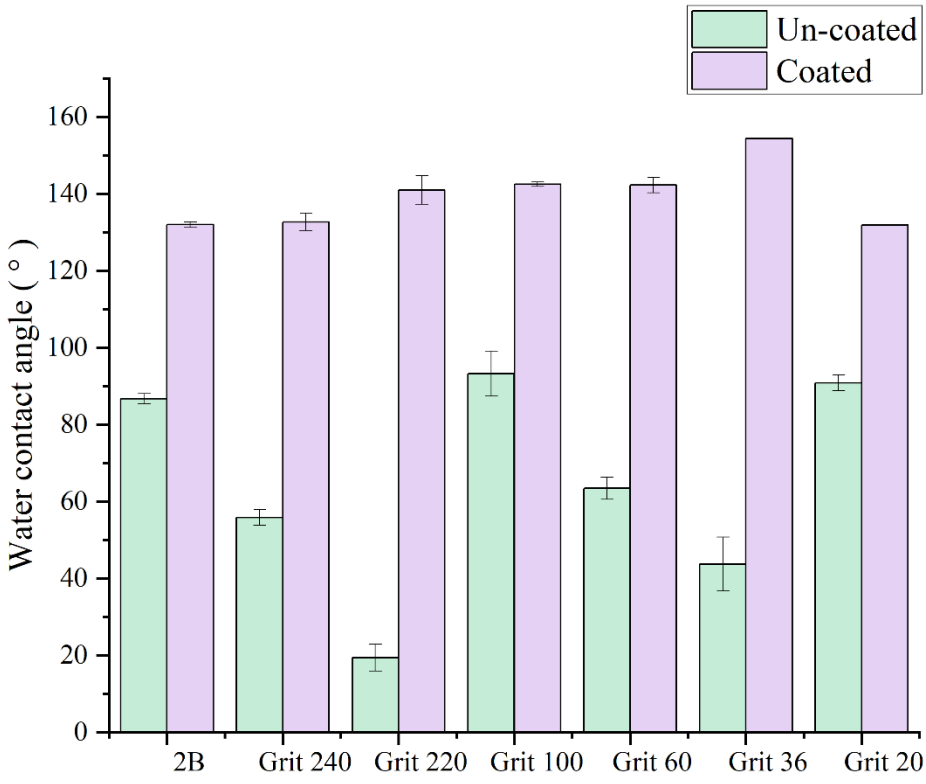

Figure 7.22 WCA for SMS 35 HMDZ T4 at 50% loading in Sapphire

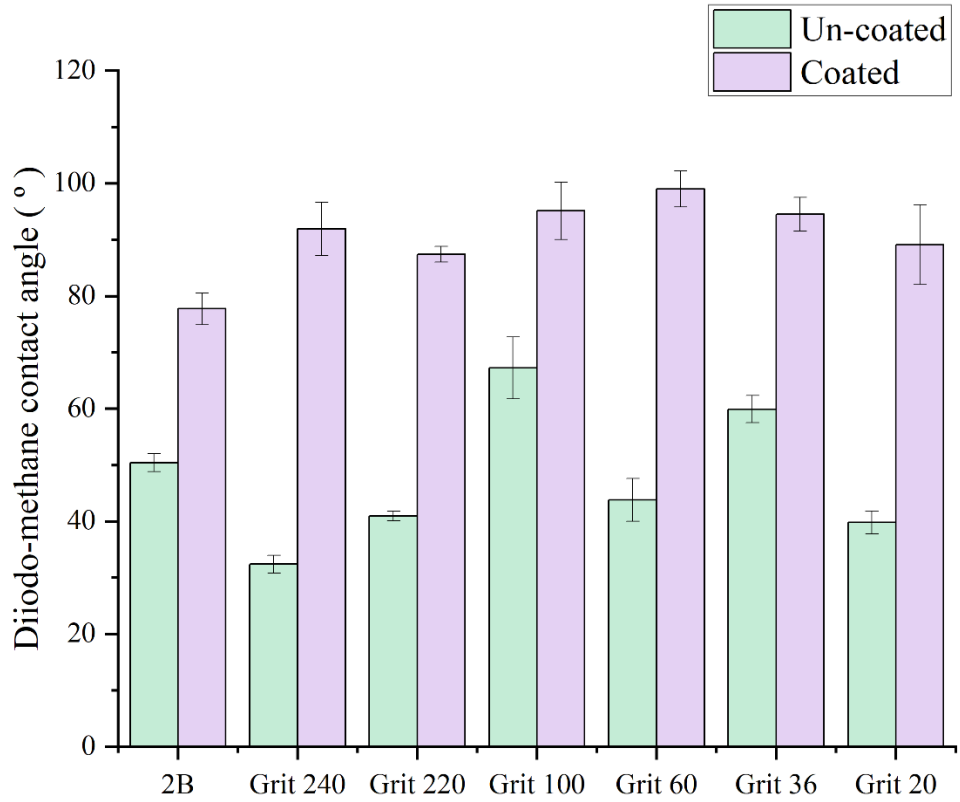

Figure 7.23 DCA for SMS 35 HMDZ T4 at 50% loading in Sapphire

Table 7-7 WCA and DCA for steel substrates with different surface finishes with and without the Sapphire coating containing the SMS 35 HMDZ SNPs at 50% loading

Particle	loading level	Matrix	Stainless steel surface finish	R_a (µm) of the substrate	WCA	DCA
SNPs HMDZ T4	50 %	Sapphire	2B	0.14 ± 0.01	132.0 (± 0.7)	77.7 (± 2.8)
SNPs HMDZ T4	50 %	Sapphire	Grit 240	1.19 ± 0.06	132.7 (± 2.2)	91.9 (± 4.7)
SNPs HMDZ T4	50 %	Sapphire	Grit 220	1.34 ± 0.06	141 (± 3.7)	87.4 (± 1.4)
SNPs HMDZ T4	50 %	Sapphire	Grit 100	1.34 ± 0.05	142.5 (± 0.6)	95.1 (± 5.1)
SNPs HMDZ T4	50 %	Sapphire	Grit 60	1.71 ± 0.14	142.3 (± 2.0)	99.0 (± 3.2)
SNPs HMDZ T4	50 %	Sapphire	Grit 36	2.91 ± 0.39	154.4 (± 0.1)	94.5 (± 3.0)
SNPs HMDZ T4	50 %	Sapphire	Grit 20	2.34 ± 0.04	131.9 (± 0.1)	89.1 (± 7.1)

7.7.3.1. Dynamic contact angles

The dynamic contact angle measurements were undertaken on the samples to determine their roll-off angle and contact angle hysteresis at roll-off. Figure 7.24 presents the contact angle hysteresis at roll-off for water droplets. From the plot it can be seen that the loading level of SNPs in the coating system does not notably affect roll-off or contact angle hysteresis. However, it can be seen that the both roll-off and CAH are very significantly affected by the substrate's roughness. The increased micro-scale roughness of the substrate reduced CAH from 25 º to below 10 º and the roll-off tilt from 80 º (no droplet roll-off) to below 10º. The findings in Chapter 6 showed that micro-scale roughness does not lead to low contact angle hysteresis or the roll off angle. The nano-scale roughness presented in this chapter also shows very high contact angle hysteresis and roll off tilt. However, by the specific combination of both micro and nano-scale roughness the low CAH and roll-off angles are achievable as presented in Figure 7.24. This suggests that the dual-scale topography is important to satisfy super repellence with water.

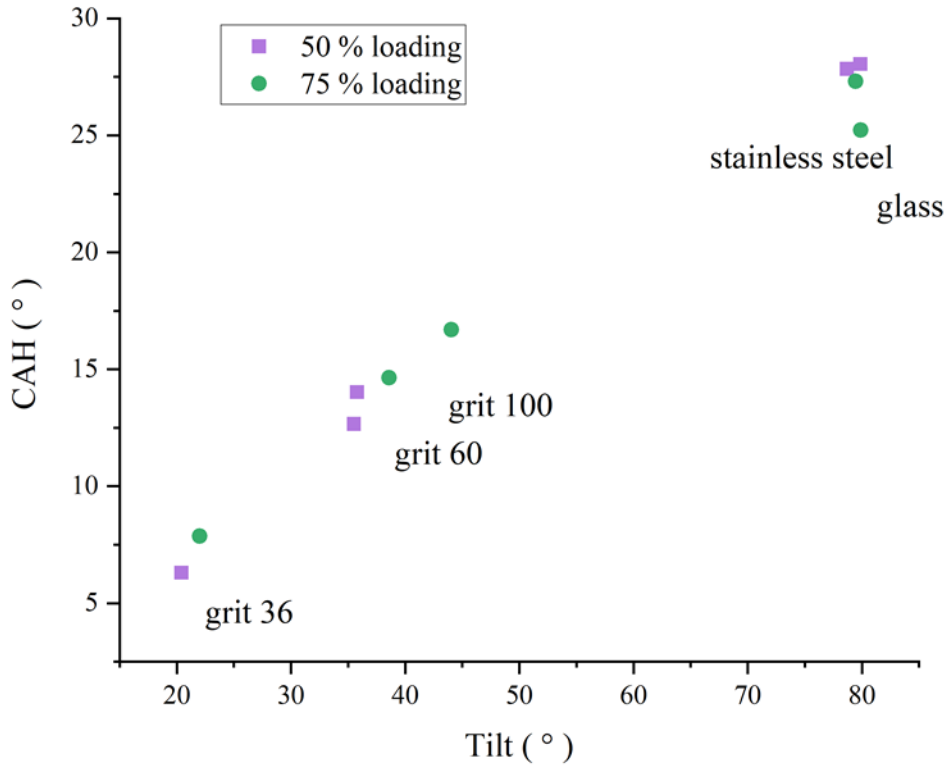

Figure 7.24 Water CAH at roll off angle as a function of roll off tilt

The similar graph to Figure 7.24 was plotted for diiodo-methane probe liquid in Figure 7.25. For all the samples studied the diiodo-methane probe liquid showed the film-formatting behaviour instead of rolling-off. This can be observed from the very high CAH of 60-80º.

The roll-off angle is in the range of 15-30º. However, it is not the true roll-off as the probe liquid left a mark/film after itself when rolling-off. In case of diiodo-methane the increase in the substrate's roughness did not influence roll-off, CAH or film forming behaviour. The water and diiodo-methane probe liquids show completely different wetting/repellence behaviour on the same substrates. The difference lies in the probe liquid properties. Water is polar and has significantly higher surface tension which allows it to bead up and roll-off the surface more freely. The diiodo-methane on the other hand is non-polar and has lower surface tension. As presented in Chapter 2, the surface tension of liquid has an influence on its penetration into the capillary/tube. The liquid penetration is also highly affected by the surface chemistry of the contacting solid (surface of the capillary). The behaviour of diiodo-methane on the surface suggests that the essential topographic thresholds are passed for its surface tension which causes its increased wettability.

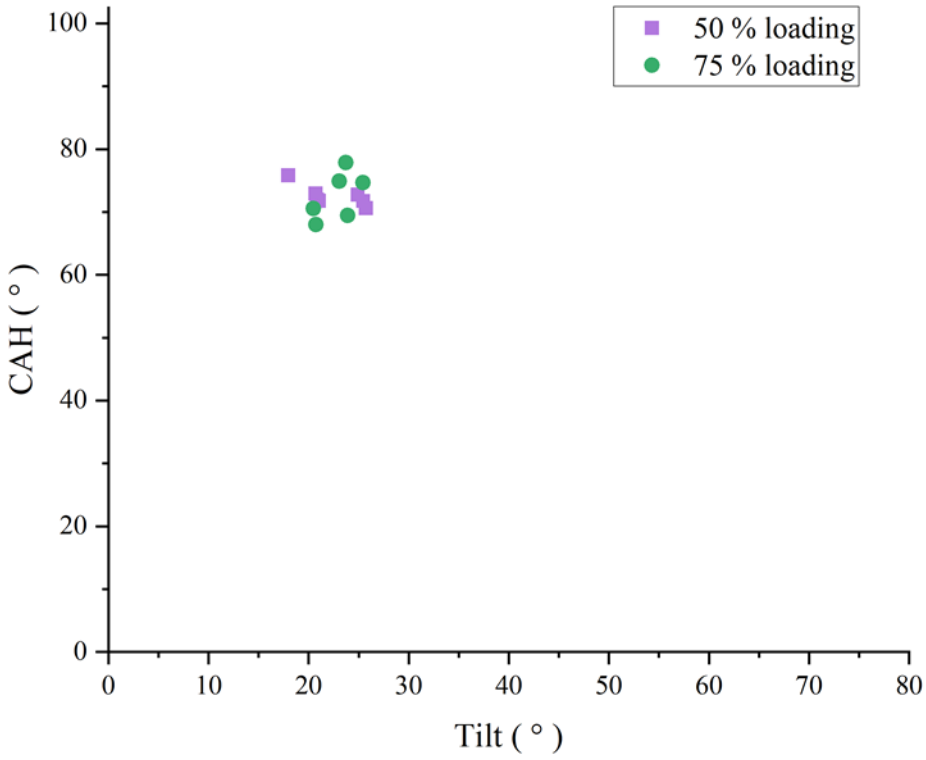

Figure 7.25 Diiodo-methane contact angle hysteresis at roll off tilt as a function of roll off tilt

7.7.4. Assessment with LST probe liquids

Further wettability assessment with LST liquids was undertaken on both types of SNP with HMDZ functionalisation. From the obtained data, it can be seen that the high static contact angle with water does not guarantee the highest repellence with low surface tension polar liquids. The highest contact angle for the LST 50 probe liquid was a value of 132º and was

measured on the SMS 35 HMDZ incorporated at 50% in the Sapphire coating which was deposited on SS304 blasted with grit 100. While the DCA on the same surface was 95 º. As the total surface tension value for both diiodo-methane and LST50 is similar, it would be expected for them to exhibit the similar contact angles unless there is a difference in polarity of the surface or probe liquid. From the obtained values the higher contact angle is observed with LST 50, the polar liquid which suggests that surface has higher level of hydrophobicity than lipophobicity. Blending LST probe liquids at various surface tensions provide insights into the wettability of the surface at the specific surface tension of the probe liquid. Their contact angles can also be used for comparison with non-polar liquids to get insights into the hydrophobic/oleophobic behaviour of the surface treatments. In terms of LST 30 the best performing coating giving the value of 61º was SNPs HMDZ T4 50% solid loading level in sapphire deposited on SS 304. The higher loading level of SNPs does not seem to enhance the CA with LST liquids.

Table 7-8 Contact angles with probe liquids for SNPs functionalised with HMDZ T4

Particle	Loading level	Substrate	Deposition rate (mm/min)	WCA (º)	DCA (º)	LST 50 (º)	LST 30 (º)
Aerosil 200 HMDZ	50 %	Glass	100	145.3 (± 0.7)	106.9 (± 1.8)	120.5 (± 6.9)	19.1 (± 0.6)
Aerosil 200 HMDZ	50 %	2B	100	145.8 (± 0.1)	108.8 (± 7.8)	118.3 (± 4.0)	56.7 (± 1.4)
SMS 35 HMDZ	50 %	Stainless steel	100	132.0 (± 0.7)	77.7 (± 2.8)	116.4 (± 4.3)	61.0 (± 2.5)
SMS 35 HMDZ	50 %	Grit 100	100	142.5 (± 0.6)	95.1 (± 5.1)	131.7 (± 0.3)	57.2 (± 1.2)
SMS 35 HMDZ	75 %	Glass	100	127.4 (± 1.5)	79.3 (± 2.1)	105.8 (± 1.7)	45.8 (± 6.1)
SMS 35 HMDZ	75 %	Stainless steel	100	128.3 (± 1.4)	81.2 (± 0.4)	105.7 (± 4.9)	56.4 (± 0.7)

7.8. Abrasion resistance

The abrasion resistance of the modified coatings was assessed by 50 cycles of wire-wool abrasion testing. After which the wettability and visual appearance of the coatings was measured. The methodology used is described in Chapter 4. The substrates used in this study were stainless steel 304 panels to which sapphire coatings incorporated with SNPs F333 T0.125 at 50 % and 75 % solid loading level were applied. The coatings were applied at the deposition rates of 10, 100 and 500 mm/min. The visual appearance assessed with gloss meter was performed on coatings deposited at 100 mm/min rate. The wettability data is presented in Table 7-9 and visual appearance data in Table 7-10.

The water and diiodo-methane contact angles in all cases after 50 cycles of abrasion decreased, apart from the coating deposited on SS304 blasted with grit 100. On Grit 100, further abrasion with wire-wool increased the diiodo-methane contact angles, the water contact angle increased for the coating with 75% loading level of nanoparticles. This increase in wettability could be explained by increase in the roughness. Comparing the coatings deposited on SS304 2B, the coating with 75% loading maintained the WCA above 110º and DCA above 79º while for 50% loading the values were above 105º for water and 71º for diiodo-methane. In terms of visual appearance, Sapphire without any coating after abrasion showed increase in gloss from 81 to 117, which could be attributed to the removal of the coating and the polishing effect. For the modified coatings, abrasion decreased the gloss from 95 to 75 for 75% loading level and from 87 to 49 for 50% loading level. The Haze showed increase in value to 21 for both coating systems. The abrasion also has an effect of distinctiveness of the image (DOI) value which is another characterisation of the coating/surface related to the reflectance of light from the surface. It is used to define how reflected light is scattered, the increase in scatter causes the distinctiveness of the image to decrease, in other words makes the image blurrier.

Table 7-9 Wettability after abrasion test

Particles	Substrate	Deposition rate (mm/min)	Probe liquid	50 % particle loading		75 % particle loading in Sapphire	
				Before abrasion	After abrasion	Before abrasion	After abrasion
				Contact angles (°)			
SNPs F333 T0.125	Stainless steel	10	Water	123.8 (± 3.1)	106.4 (± 1.3)	129.2 (± 1.3)	113.3 (± 0.6)
		10	Diiodo-methane	91.5 (± 2.6)	76.3 (± 1.5)	93.3 (± 5.2)	78.8 (± 0.4)
		100	Water	123.1 (± 4.4)	105.4 (± 0.8)	124.1 (± 2.0)	114.7 (± 3.7)
		100	Diiodo-methane	87.1 (± 4.1)	76.8 (± 3.3)	93.7 (± 1.4)	81.2 (± 5.7)
		500	Water	125.9 (± 2.2)	106.3 (± 1.4)	127.0 (± 2.1)	116.4 (± 1.7)
		500	Diiodo-methane	87.4 (± 0.4)	70.5 (± 6.1)	95.5 (± 1.2)	81.7 (± 1.7)
SNPs F333 T0.125	Grit 100	100	Water	137.6 (± 1.9)	134.1 (± 2.8)	131.9 (± 1.8)	136.4 (± 6.8)
		100	Diiodo-methane	97.3 (± 2.6)	103.6 (± 1.9)	96.3 (± 4.0)	114.1 (± 3.3)

Table 7-10 Visual appearance after abrasion test

Parameter	Stainless steel 304 2B finish	Sapphire	after 50 cycles	SNPs F333 75% Sapphire 100mm/m	After 50 cycles	SNPs F333 50% Sapphire 100mm/m	After 50 cycles
WCA (º)	86.8 (± 1.3)	102.6 (± 1.4)	85.6 (± 2.1)	124.1 (± 2.0)	114.7 (± 3.7)	123.1 (± 4.4)	105.4 (± 0.8)
DCA (º)	50.4 (± 1.6)	79.5 (± 1.9)	51.5 (± 3.3)	93.7 (± 1.4)	81.2 (± 5.7)	87.1 (± 4.1)	76.8 (± 3.3)
Gloss	138.6 (± 0.7)	80.8 (± 3.7)	117.4 (± 3.3)	95.3 (± 6.0)	74.7 (± 8.7)	87.3 (± 6.5)	49.4 (± 1.6)
Haze	26.7 (± 0.0)	20.5 (± 2.9)	26.7 (± 3.0)	19.3 (± 0.8)	20.5 (± 1.0)	17.2 (± 0.3)	20.6 (± 0.3)
DOI	82.9 (± 0.1)	73.3 (± 7.4)	74.3 (± 2.2)	83.5 (± 5.7)	74.7 (± 4.6)	78.9 (± 4.2)	60.4 (± 5.8)

7.9. Discussion

The work reported in this chapter related to the investigation of the effect of nano-scale roughness on surface wettability and repellence for a variety of probe liquids. Nano-scale roughness was introduced to the surface by the presence of silica nanoparticles, while low SFE was achieved by the surface functionalisation of these nanoparticles with silanes. As previously reviewed in Chapter 2 and 3, small diameter nano-pores/capillaries between the neighbouring particles should reduce liquid penetration and therefore enhance repellence. Two types of silica nanoparticles (SNPs) were used in the study; those synthesised by a sol-gel method and commercial fumed silica particles (Aerosil 200). The obtained particles were functionalised with fluorinated and non-fluorinated silanes; 333 and HMDZ. The DLS as well as WLI and AFM studies confirmed the diameter of the sol-gel synthesised nanoparticles to be in the range of 40-50 nm. It was shown that the nanoparticles could be used to obtain repellence via a bottom-up approach. When substrates are dip coated into the SNP suspension, the SNPs form a film that builds up the nano-roughness on the substrate while the surface functionalities on the SNPs provide low SFE. This combination gave the static CA of 104º for water and 67º for diiodo-methane on a glass substrate. However, the deposited nanoparticles without a matrix to hold the self-assembled nanoparticles together was not durable. The droplets would remain pinned to the surface and the diiodo-methane displayed film forming behaviour. To maintain repellence and increase durability, the obtained functionalised nanoparticles were incorporated into the commercial polysilazane coating Sharc Sapphire. Assessment with WLI confirmed that the modified coating has nano-scale roughness, and the coating does not cause the levelling of the nano-particles. Two loading levels were studied in this chapter: 50 % and 75 % solid loading. The incorporation of the functionalised SNPs into the Sapphire coating at 50% loading level elevated static contact angles to values of 128º (water) and 88º (diiodo-methane) respectively. Increasing the loading level to 75% did not change the repellence with water (128º) but did increase the repellence to diiodo-methane to 100º

The influence of the dip-coating deposition rate on wettability and visual appearance (haze, gloss) was examined. The three rates examined, 50, 100 and 500 mm/min were found not to have a significant impact on wettability, visual appearance or even resistance to abrasion of the coatings.

As mentioned, the increase in SNP loading level in the coating did not significantly increase the WCA but did increase the DCA when the SNPs had been subject to functionalisation with a fluoroalkyl containing silane (F333). For the F333 functionalised SNPs the DCA increased from 78º (at 50% loading) to 93º (at 75% loading). In terms of the HMDZ functionalisation the values were in the range of 77-79º. The increase in DCA values can be attributed to increased fluorine content in the coating that makes the surface more oleophobic (as described and observed in Chapter 5) but does not significantly affect hydrophobicity.

The abrasion resistance of the modified coatings was assessed by 50 cycles of wire-wool abrasion testing. After which the wettability and visual appearance of the coatings was measured. The water and diiodo-methane contact angles in all cases after 50 cycles of abrasion decreased, apart from the coating deposited on SS304 blasted with grit 100. On Grit 100, the further abrasion with wire-wool increased the diiodo-methane contact angles, the water contact angle increased for the coating with 75% loading level of nanoparticles. This increase in wettability could be explained by an increase in the roughness.

The modified coatings were deposited on grit blasted stainless steel substrates to create a dual scale topography that combines both the micro-scale topography (reported in Chapter 6) and the nano-scale topography studied in this chapter. The SNPs used in this dual-scale roughness study were functionalised with HMDZ and incorporated at 50% solid loading level into the Sapphire coating. On the coated substrates the water contact angle increased consistently with increase in the substrate's micro-scale roughness until grit 36 where the WCA of 154º was achieved. The surface with greater micro-roughness, prepared by blasting with grit of size 20, showed a slight reduction in the water contact angle which was measured at 132º. The diiodo-methane showed a similar trend with an increase in contact angle value with increasing micro-scale until the surface prepared with grit 60 where its contact angle reached 99º. Further increases in micro-roughness led to a reduction in the DCA. This behaviour is likely to be due to some key topographic thresholds being passed, each threshold being dictated by the specific characteristics of the probe liquids.

In terms of the CAH at roll-off and the roll-off tilt, the loading level of SNPs in the coating system did not have an influence. However, both roll-off and CAH are affected by the substrate's roughness in combination with the nano-scaled roughness. The increased micro-scale roughness of the substrate reduced CAH from 25 º to below 10 º and the roll-off tilt from 80 º (no droplet roll-off) to below 10º. The results in this study show that the high contact angle with the probe liquid does not guarantee the abhesive behaviour. It is important

to study the roll-off angles to confirm the repellent behaviour to specific liquids. The nano-scale topography studied in this chapter provided high static contact angles with probe liquids as well as high contact angle hysteresis and high roll-off angles/or no roll-off. The micro-scale topography studied in Chapter 6 provided similar results. However, the combination of both of these nano and micro-scale topographies provided high contact angles, low contact angle hysteresis and low roll-off tilts for water. This specific dual scale topography does satisfy the criteria for super repellence with water. However, this same combination of surface characteristics does not satisfy the probe liquids with lower surface tensions and different surface tension components (polar part/disperse part). Changing the micro and nano-scale topography as well as surface chemistry exhibits the range of wetting behaviours with various probe liquids. These behaviours provide design rules to achieving the omniphobicity. Whilst the clear critical parameters to achieving it are still unclear, this work sheds light on the parameters that have to be considered and the methods to elucidate them.

CHAPTER 8. METHODOLOGY FOR COMPARATIVE ASSESSMENT

8.1. Introduction

Selecting the correct surface chemistry and surface roughness for the utmost abhesive behaviour requires a variety of factors to be taken into account. This chapter introduces a new approach for the assessment of the repellence behaviour of coatings and surfaces. The methodology presented in this chapter helps to classify coatings and surface roughness characteristics according to their ability to repel various liquid not only in terms of static contact angles, but also in terms of contact angle hysteresis and roll-off tilt. The aim is to provide a plot of wettability data that enables the effective and comprehensive comparison of different surface chemistries and topographies to a range of probe liquids.

8.2. Assessment criteria

To provide a meaningful plot, the spider, or radar, diagram was selected as it allows for a range of experimental data points to be presented in a single graph. In the spider diagram each axis represents a different variable. The properties presented on each axis are: static contact angle (CA); contact angle hysteresis (CAH); the roll-off tilt angle (ROT) and the diameter of the droplet at roll-off (D). The probe liquids used were water (W), diiodo-methane (D), ethanol/water mix with a surface tension of 50mN/m (LST 50) and ethanol/water mix with a surface tension 30mN/m (LST 30).

Figure 8.1 presents the schematic spider diagram proposed in this study. Further explanation and information on the metrics used can be found in Table 8-1.

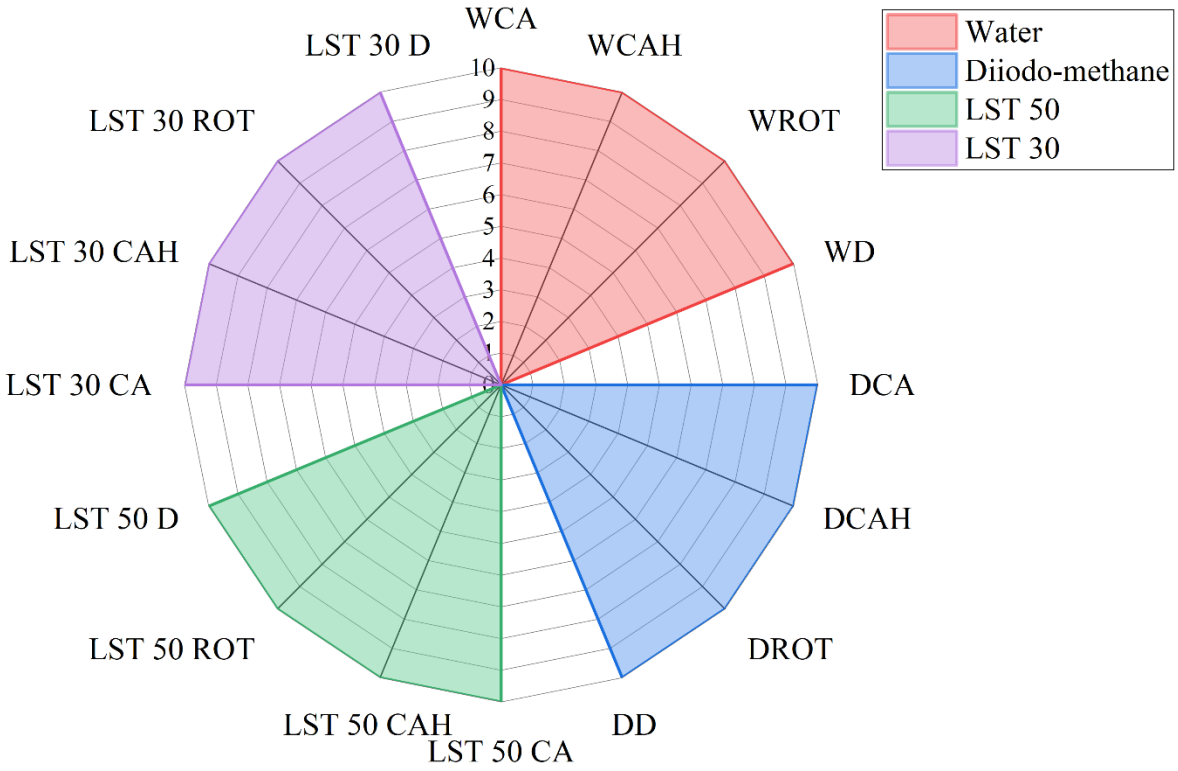

Figure 8.1 Spider diagram proposed for assessment

The spider diagram is split into four quarters: first quarter representing repellence to water, second to diiodo-methane, the third to LST 50 and the fourth to LST 30. This segmentation allows for easy comparison of wettability by different liquids. To normalise the parameters and allow for ready comparison of performance each parameter was given a score/value from 1 to 10; 1 being the poorest (least repellence) performance while 10 being the best (most repellence) performance. The score system and definition of each score/point is presented in Table 8-1.

Table 8-1 Spider diagram metrices and scoring system

Spider diagram value	Static contact angle (CA)	Contact angle hysteresis (CAH) at roll-off	Roll-off tilt (ROT)	Diameter at roll-off (D)
1	0 to 40	≥81	80	≥231
2	41 to 50	71 to 80	71 to 79	211 - 230
3	51 to 60	61 to 70	61 to 70	201-210
4	61 to 70	51 to 60	51 to 60	191-200
5	71 to 80	41 to 50	41 to 50	181-190
6	81 to 90	31 to 40	31 to 40	171-180
7	91 to 100	21 to 30	21 to 30	161-170
8	101 to 110	11 to 20	11 to 20	151- 160
9	111 to 119	6 to 10	6 to 10	141-150
10	≥120	0 to 5	0 to 5	≤140

The high static contact angles (above 120º), low contact angle hysteresis and low roll-off angles (up to 5º) are given a score of 10. The diameter of the droplet at roll-off was also assessed. Assessing the diameter provides an understanding as to whether the droplet is spreading out/wetting the surface during the roll off. The droplets were photographed and their diameters was measured in pixels to normalise the values and account for the magnification differences between measurements (if any as the same magnification factor was used across all the measurements). The best performing coating/surface would score 10 points on each radii and therefore occupy the largest area while the worst performing one would score less points and occupy a smaller area on the diagram.

8.3. Assessment of surface chemistries

The proposed assessment methodology was used to assess the repellence of the commercial coatings discussed in Chapter 5. The five selected coatings (Sapphire, Sivo EC, Aculon 353, Tutoprom and Avalon glass) were deposited onto mirror finished stainless steel 304 and the wetting behaviour to the four probe liquids was assessed. The contact angles, hysteresis, roll-off tilts and droplet diameters were given scores according to the criteria introduced earlier in Table 8-1. The obtained data are presented in Table 8-2. The values obtained are plotted as spider diagrams in Figure 8.2.

Table 8-2 Repellence data and associated scores of selected coatings on stainless steel 304 with mirror finish

Parameter	Sapphire	Sapphire - score	Sivo EC	Sivo EC - score	Aculon 353	Aculon 353 - score	Tutoprom	Tutoprom - score	Avalon glass	Avalon glass - score
WCA (°)	99.7 (±1.4)	7	107 (±2.2)	8	93.7 (±2.3)	7	98.6 (±1.0)	7	98.8 (±3.0)	7
WCAH (°)	23.5 (±0.4)	7	38.7 (±24.0)	6	26.7 (±1.2)	7	23.7 (±1.1)	7	22.9 (±2.2)	7
WROT (°)	55.2 (±5.8)	4	62.3 (±30.6)	3	69.8 (±13.0)	3	59.6 (±3.1)	4	62.5 (±15.7)	3
WD (px)	152.1 (±12.7)	8	155.3 (±19.4)	8	157.4 (±6.6)	8	153.3 (±0.7)	8	141 (±1.5)	9
DCA (°)	72.6 (±1.6)	5	86.4 (±3.1)	6	69.6 (±1.4)	4	70.1 (±1.1)	4	76.2 (±3.6)	5
DCAH (°)	51.2 (±10.6)	4	33.2 (±9.8)	6	25.2 (±7.0)	7	49 (±1.3)	5	49 (±7.8)	5
DROT (°)	14.6 (±6.1)	8	34 (±39.9)	6	7.3 (±1.8)	9	10.5 (±0.9)	9	15.1 (±11.7)	8
DD (px)	215.1 (±7.9)	2	181.6 (±1.1)	5	191 (±5.8)	4	213.7 (±21.9)	2	201.4 (±3.1)	3
LST 50 CA (°)	84.5 (±3.2)	6	94.8 (±1.2)	7	84.2 (±3.2)	6	87.5 (±5.2)	6	92.9 (±3.1)	7
LST 50 CAH (°)	36.6 (±3.8)	6	29.8 (±7.3)	7	23.7 (±0.6)	7	22.5 (±1.4)	7	32.4 (±0.1)	6
LST 50 ROT (°)	46.8 (±26.4)	5	36.1 (±14.6)	6	28.5 (±0.9)	7	41.6 (±1.8)	5	23.1 (±0.6)	7
LST 50 D (px)	172.4 (±9.7)	6	176.1 (±0.5)	6	169.5 (±0.5)	7	148 (±7.3)	9	195.2 (±1.7)	4

LST 30 CA (°)	75.1 (±3.8)	5	86.4 (±1.8)	6	51.3 (±2.7)	3	52.1 (±5.4)	3	59.1 (±4.3)	3
LST 30 CAH (°)	37.3 (±1.5)	6	38.2 (±0.6)	6	44.4 (±3.8)	5	22.6 (±0.0)	7	46.8 (±3.5)	5
LST 30 ROT (°)	23.1 (±1.1)	7	31.1 (±2.7)	6	26.4 (±1.2)	7	34.5 (±1.5)	6	26.5 (±1.4)	7
LST 30 D (px)	228.9 (±2.8)	2	196.9 (±7.5)	4	239.5 (±7.5)	1	163.5 (±2.4)	7	239.9 (±8/0)	1

Figure 8.2 Assessment of surface chemistries

As can be seen in Figure 8.2 all the coatings had WCA values in the range of 7-8, while roll-off tilt remains very high in the range of 3-4 for all coatings. The water diameter is relatively low across samples (score 8-9) suggesting that droplet does not spread out on the surface/wet it. The interesting observation is that water repellence performance of all coatings is similar, irresponsible of surface chemistry. There are greater differences between coatings when the probe liquid is diiodo-methane. The DCA is relatively low compared to water (score 4-6), but it exhibits better roll-off (6-9). However, the diameter of the diiodo-methane droplet is larger with scores ranging from 2 to 5 suggesting that more wetting/spreading is taking place due to lower surface tension of the probe liquid. Comparing the data of the LST50 and diiodo-methane, the LST50 exhibits higher contact angles, lower CAH and roll-off tilt. The roll-off tilt is lower but it also exhibits less spreading (lower value of droplet diameter) which suggests that it shows less film-forming behaviour. LST 30 also shows similar roll-off tilts but the large diameter value suggests that it is more likely to spread out and leave the film behind.

Comparing the fluorinated (Sivo EC) and non-fluorinated (Sapphire) surface treatments, the water repellence is similar on both surfaces. The main difference observed is with diiodo-methane wetting. The Sivo EC treatment exhibited a higher DCA (6 compared to 5), the DCAH was also higher (6 compared to 4) suggesting less droplet pinning, however the roll-off tilt was lower (6 compared to 8). Which would be assumed as a decrease in repellence towards diiodo-methane, but if the droplet diameter is taken into the account it can be observed that the droplet size is lower during the roll-off on Sivo EC coating. This suggests that on fluorinated treatment less wetting is taking place by the diiodo-methane (Figure 8.3).

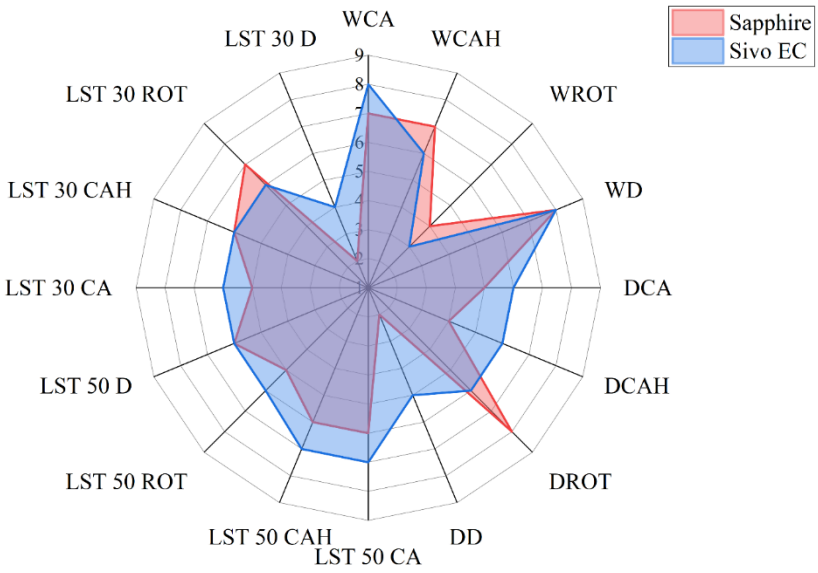

Figure 8.3 Diagrams for Sivo EC and Sapphire

8.4. Assessment of surface roughness

The effect of micro-scale surface roughness on repellence was assessed with the proposed criteria. The coating selected for the assessment was Sapphire deposited on grit blasted surfaces to provide the roughness; the data used was presented in Chapter 6. The repellence data was converted into scores as defined by the criteria highlighted above and is presented in Table 8-3.

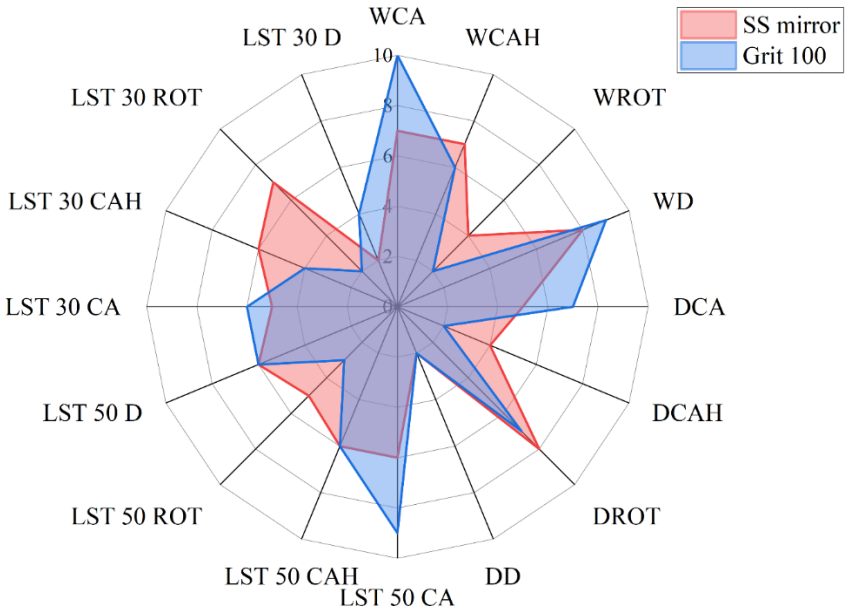

Figure 8.4 Effect of blasting with grit 100 on repellence

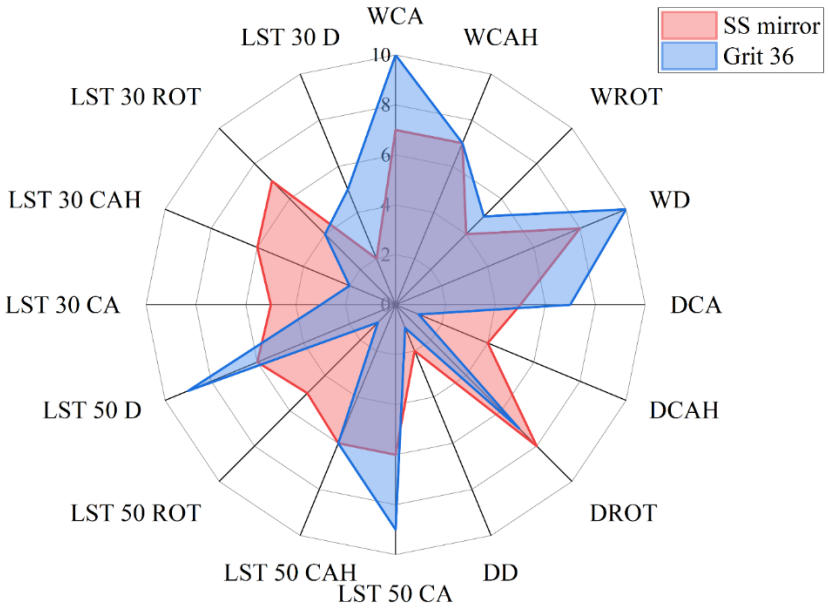

Figure 8.5 Effect of blasting with grit 36 on repellence

Table 8-3 The Repellence data and associated scores of Sapphire coating on blasted stainless steel 304

Parameter	SS mirror finish	SS mirror finish - score	SS 304 2B	SS 304 2B - score	Grit 100	Grit 100 - score	Grit 60	Grit 60 - score	Grit 36	Grit 36 - score
WCA (°)	99.7 (±1.4)	7	98.6 (±3.4)	7	127.5 (±2.1)	10	127.7 (±1.0)	10	123.7 (±2.1)	10
WCAH (°)	23.5 (±0.4)	7	17.4 (±1.9)	7	24.2 (±0.4)	6	26.8 (±13.2)	7	21.2 (±0.7)	7
WROT (°)	55.2 (±5.8)	4	46.2 (±7.1)	5	71.3 (±14.9)	2	42.6 (±12.9)	5	50.0 (±0.0)	5
WD (px)	152.1 (±12.7)	8	135.1 (±1.0)	10	145 (±16.6)	9	154.6 (±59.7)	8	125.5 (±2.5)	10
DCA (°)	72.6 (±1.6)	5	70.1 (±3.9)	4	94.9 (±1.4)	7	90.8 (±3.0)	7	92.2 (±1.4)	7
DCAH (°)	51.2 (±10.6)	4	23.5 (±9.0)	7	71.8 (±1.5)	2	64.8 (±32.5)	3	98.4 (±15.3)	1
DROT (°)	14.6 (±6.1)	8	13.5 (±1.4)	8	22.5 (±11)	7	41.6 (±33.3)	5	20.8 (±2.0)	7
DD (px)	215.1 (±7.9)	2	163.6 (±20.2)	7	225.5 (±13)	2	207.5 (±61.8)	3	255.3 (±1.7)	1
LST 50 CA (°)	84.5 (±3.2)	6	101 (±1.7)	8	111.5 (±5.6)	9	116.2 (±6.7)	10	108.0 (±4.3)	9
LST 50 CAH (°)	36.6 (±3.8)	6	43.2 (±0.3)	5	36 (±11.3)	6	86.5 (±1.1)	1	33.7 (±0.3)	6
LST 50 ROT (°)	46.8 (±26.4)	5	80.0 (±0.0)	1	63.9 (±27.9)	3	47.6 (±2.5)	5	80.0 (±0.0)	1
LST 50 D (px)	172.4 (±9.7)	6	185.8 (±0.0)	5	178.6 (±12.4)	6	227.6 (±5.7)	2	144.9 (±3.9)	9

LST 30 CA (°)	75.1 (±3.8)	5	80.3 (±2.8)	5	82.2 (±3.8)	6	66.6 (±2.6)	4	59.4 (±2.6)	3
LST 30 CAH (°)	37.3 (±1.5)	6	28 (±0.3)	7	58.8 (±1.2)	4	92.3 (±15.4)	1	72.2 (±15.0)	2
LST 30 ROT (°)	23.1 (±1.1)	7	23.4 (±0.6)	7	71.1 (±15.5)	2	39.2 (±1.9)	6	55 (±9.8)	4
LST 30 D (px)	228.9 (±2.8)	2	186.6 (±1.1)	5	192.2 (±28.9)	4	224.9 (±1.7)	2	189 (±13.1)	5

The obtained data for stainless steel with mirror finish and grit 100 were plotted on Figure 8.4. The plot shows the effect of blasting with grit 100 on repellence. Blasting with grit 100 created a surface with a roughness average of 1µm as presented in Chapter 6. The effect of grit 100 on water repellence is increase in the static contact angle and contact angle hysteresis which suggests that the substrate exhibits higher degree of droplet pinning which can also be observed by a significant decrease in the roll-off angle. Despite increase in CAH and decrease in the roll-off tilt, the droplet diameter is smaller on a blasted surface. This suggests that there might be capillary action that prevents water to completely penetrate into the roughness groves/capillaries to increase the interfacial surface area. This increase in the static contact angle for the roughened substrate is in line with the Wenzel's wetting model as described in Chapter 6. In terms of diiodo-methane wetting, the static contact angle is increased on the roughened substrate however a similar effect to water is observed in terms of CAH and roll-off tilt. The roughening does not seem to significantly change the diameter/spreading of diiodo-methane droplet on the surface. The same behaviour is observed with the other probe liquids, diiodo-methane, LST 50 and LST 30. The only difference is the droplet diameter which seems not to exhibit significant change for diiodo-methane and decreases with LST 30. Comparing the values for diiodo-methane and LST 50, even though their total surface tension values are similar there is a different wetting behaviour observed. The static contact angle is higher with LST 50 liquid, The CAH is much lower with LST50 as well as the diameter which suggests lower wetting/spreading of the liquid. The roll-off tilt seems to be lower with diiodo-methane but as already discussed this is due to the film-formation and not to repellence. This difference in the behaviour can be explained by the polar or disperse nature of the liquid/surface as already discussed in Chapter 5. The disperse probe liquid seems to be more compatible with the studied surface. Hence better wetting. The comparison between diiodo-methane and LST50 wetting behaviour is a valuable tool as it provides insight into the surface chemistry of the studied coating/substrate and its wetting behaviour with polar/disperse liquids. The comparison of diodo-methane with water does not provide as much insights because water has a very high surface tension which creates an uplift in repellence. The increased repellence has to be attributed to the increased surface tension and not to the specific polar/disperse interaction and therefore the data is not easily comparable.

In terms of wettability with LST 30 on stainless steel 304 with mirror finish and blasted with grit 100 coated the Sapphire coating, the static contact angle with LST30 is increased by the increase in roughness. The initial static contact angle with LST30 is 75º and blasting with grit 100 creates an uplift to 82º. This increase is not in line with the Wenzel wetting model. The contact angle of 75º suggests that the surface is inherently philic to the probe liquid and the increased roughness would increase the interfacial surface area and therefore wettability. However, this is not observed on the sample blasted with grit 100. Comparing the other studied parameters CAH and roll-off tilt however shows that the increase in roughness causes the wettability to increase. This observation suggests that the static contact angle can be a misleading parameter and in order to obtain deeper insights into repellence/wetting more parameters have to be considered with a range of probe liquids.

Blasting with grit 36 enhanced the mentioned behaviour further as seen in Figure 8.5. The repellence/wettability behaviour on the surface blasted with grit 36 seems to be more complex. In terms of water, there is an increase in the static contact angle, no significant change in CAH value and there is a slight decrease in the roll-off tilt and the diameter of the droplet is also smaller (suggesting less spreading). All of which agrees with Wenzel wetting model. The behaviour of diiodo-methane is very similar to the one observed on SS304 grit 100, but there is also an increase in droplet diameter (more spreading) and all the other parameters show increased wetting. The LST50 on the other hand shows decrease in diameter with increase in surface roughness. The LST30 liquid exhibits a decrease in static contact angle on grit 36, which differs from the behaviour observed on grit 100. However, the wetting on grit 36 agrees with Wenzel model wetting. The initial contact angle of 75º decreased to 60º with introduction of surface topography. This switch from repellence to wetting is different for each liquid and it seems to be determined by the specific characteristics of the probe liquids.

8.5. Assessment of nanoscale and dual-scale roughness

The effect of nano-scale and dual-scale surface roughness on repellence was assessed with the proposed criteria. The coating selected for the assessment was SMS3 35 HMDZ loaded at 50 % in the Sapphire coating as presented in Chapter 7. The repellence data converted into scores as defined by the above criteria is presented in Table 8-4. For the nano-scale and dual-scale roughness only the repellence with water and diiodo-methane were studied and so the proposed criteria was modified accordingly. The score system remained the same, but the spider diagram changed to the one presented in Figure 8.6. Half of the diagram is dedicated to the repellence data with water and the half to diiodo-methane.

The data from Chapter 7 for SMS35 HMDZ 50 % in sapphire coating system deposited on stainless steel 2B finish, Grit 100, Grit 60 and Grit 36 was scored according to the criteria. The values are presented in Table 8-4.

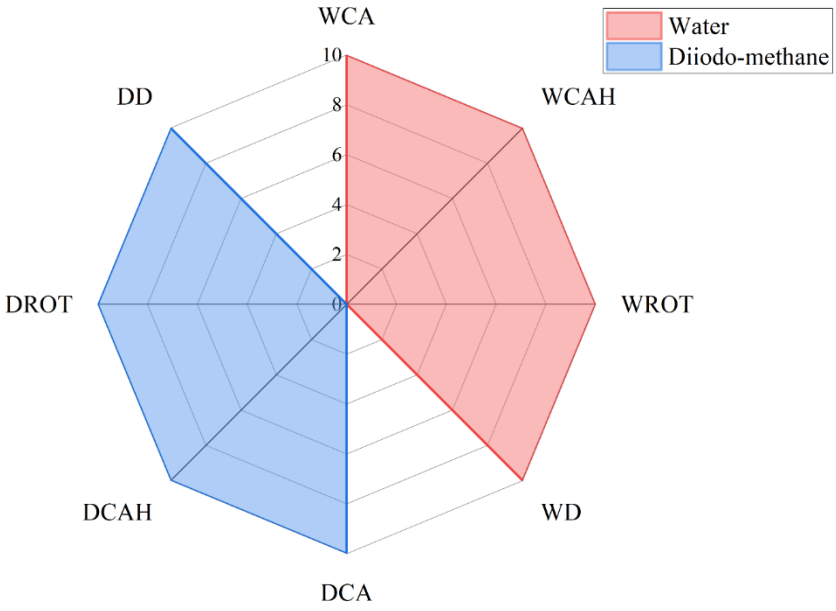

Figure 8.6 Spider diagram for water and diiodo-methane repellence study

Table 8-4 Repellence data and associated spider diagram score on nano-scale and dual scale topography

Parameter	SNPs HMDZ T4 50 % in sapphire							
	SS 304 2B	SS 304 2B - score	Grit 100	Grit 100 - score	Grit 60	Grit 60 - score	Grit 36 - score	Grit 36 - score
WCA (º)	132.0 (± 0.7)	10	142.5 (± 0.6)	10	142.3 (± 2.0)	10	154.4 (±0.1)	10
WCAH (º)	28.1 (±2.5)	7	14.0 (±9.1)	8	12.7 (±5.9)	8	6.3 (±1.1)	9
WROT (º)	79.9 (±0.2)	1	35.8 (±19.8)	6	35.5 (±12.1)	6	20.4 (±2.6)	8
WD (px)	124.2 (±1.7)	10	105.0 (±4.3)	10	102.6 (±4.1)	10	95.0 (±1.1)	10
DCA (º)	77.7 (±2.8)	5	95.1 (±5.1)	7	99.0 (±3.2)	7	94.5 (±3.0)	7
DCAH (º)	71.8 (±3.8)	2	100.1 (±14.1)	1	72.8 (±1.2)	2	71.8 (±2.7)	2
DROT (º)	21.0 (±2.2)	7	26.7 (±3.2)	8	24.9 (±0.1)	7	25.5 (±4.6)	7
DD (px)	244.7 (±5.4)	1	237.1 (±25.6)	1	227.8 (±6.3)	2	217.8 (±26.1)	2

Figure 8.7 presents the data for the nanoparticle containing Sapphire coating system deposited on stainless steel 2B finish, Grit 60, Grit 100 and Grit 36 blasted SS304. The plot presents the effect of nano-scale and dual-scale topography on the repellence with water and diiodo-methane. The most significant change is the roll-off tilt and contact angle hysteresis with water. The combination of nano-scale and micro-scale topography enables water droplet to roll-off the surface. As the micro-scale roughness is increased from grit 100 to grit 36 the uplift in the performance is clearly seen.

In terms of the diiodo-methane, the contact angle is enhanced by the addition of micro-scale roughness however the high CAH is maintained as well as the droplet diameter. The roll-off tilt therefore represents not the true roll-off, but the film forming behaviour of the probe liquid.

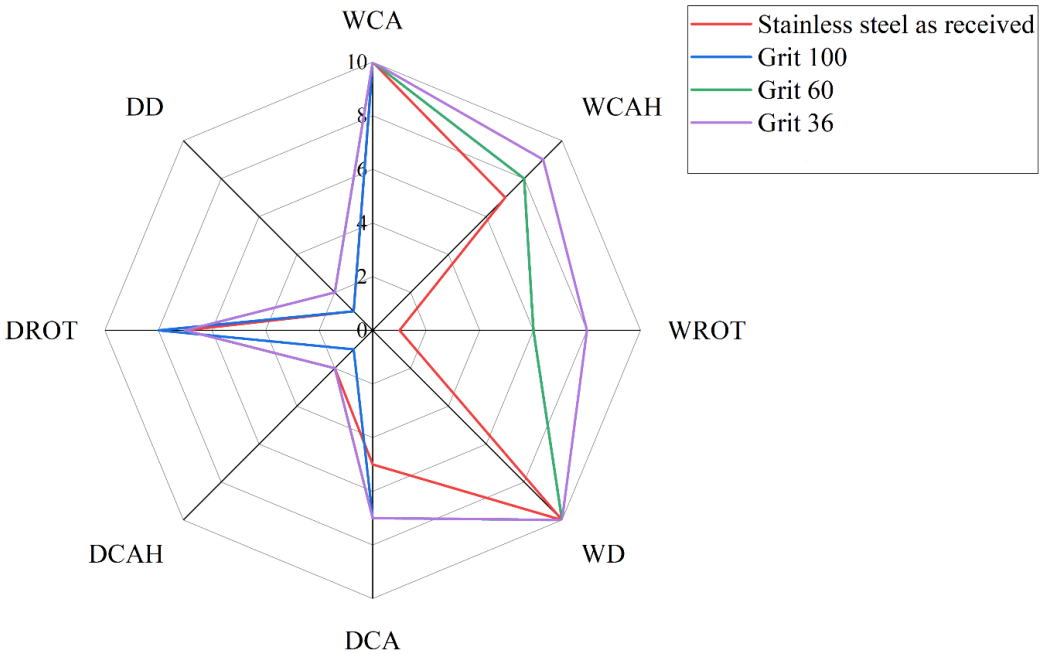

Figure 8.7 Effect of nano-scale and dual-scale topography

Figure 8.8 presents the comparison of nano-scale, micro-scale and dual scale topography. From the plot it can be observed that the micro-scale roughness has a more significant influence on the water roll-off tilt than nano-scale topography on its own. In terms of diido-methane the only surface that provided the uplift in contact angles, roll-off tilt and decrease in droplet diameter was stainless steel 304 treated with sapphire (planar substrate with minimal roughness). The introduction of roughness to the substrate causes the wettability

towards the low surface tension probe liquid (diiodo-methane) to increase while enhancing repellence of water.

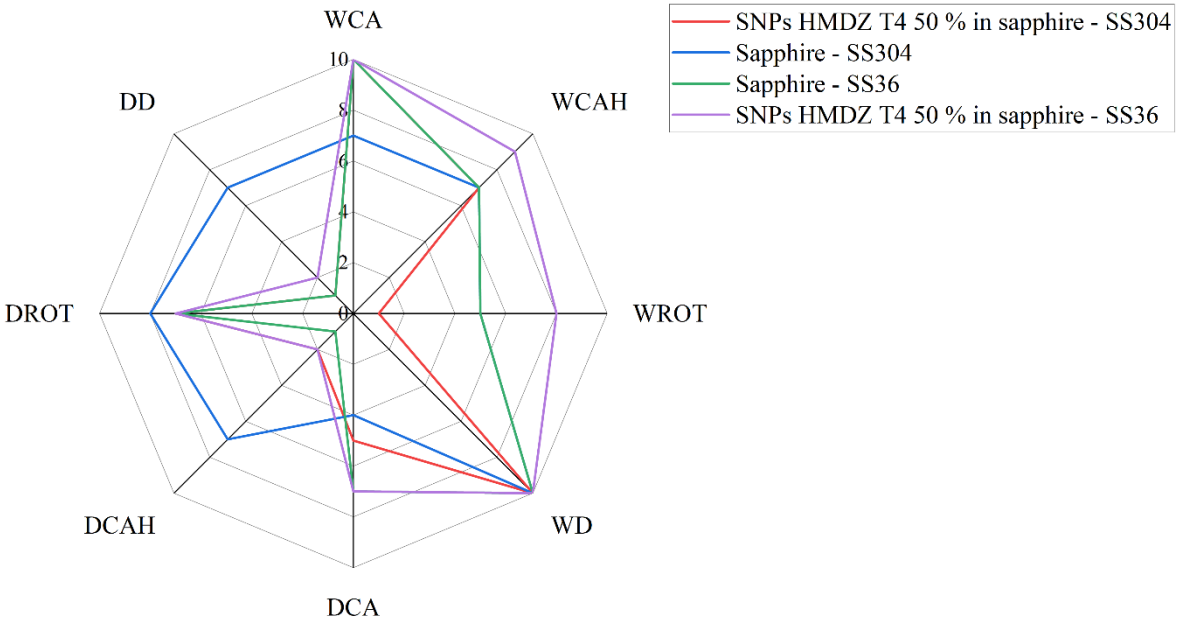

Figure 8.8 Comparison of nano-scale, micro-scale and dual-scale topography

8.6. Summary

Selecting the correct surface chemistry and surface roughness for the utmost abhesive behaviour requires a variety of factors to be taken into the account. A new assessment approach for the repellence evaluation of surfaces has been proposed in this chapter. The methodology presented in this chapter helps to classify coatings and surface roughness characteristics according to their ability to repel various liquids not only in terms of static contact angles but also in terms of contact angle hysteresis and roll-off tilt. The spider diagram was used to present the experimental data points in a single graph. Each repellence parameter was plotted on a spider diagram whose axes reflected static contact angles, contact angle hysteresis at roll-off, the roll-off tilt and the diameter of the droplet at roll-off for each liquid studied. As identified in previous chapters (Chapter 6 and 7) a high contact angle with a probe liquid does not guarantee an abhesive behaviour and can be misleading. It is important to study the roll-off angles to confirm the repellent behaviour to a specific liquid. Another valuable parameter to be considered is the droplet diameter at roll-off. It provides insight into the droplet spreading/wetting behaviour that cannot be easily identified by the static contact angle or even the contact angle hysteresis. The proposed evaluation approach allows for the easy comparison of a number of parameters with a range of liquids and

provides valuable insight. Assessment with a range of liquids is essential as probe liquids with different polar/disperse SFE components will provide different wetting behaviours even if their surface tension values are similar.

The proposed assessment methodology was used to assess the repellence data collected in this project. It included the effect of surface chemistry on repellence (Chapter 5), the effect of micro-scale surface roughness (Chapter 6) and the effect of nano-scale and dual-scale roughness (Chapter 7).

The coatings studied on planar smooth surfaces (SS304 with mirror finish) exhibited high WCA while the roll-off tilt remained very high for all coatings. The water repellence performance of all coatings was similar, irrespective of surface chemistry. More variability across coatings was observed with diiodo-methane. The probe liquids with lower surface tensions showed more droplet spreading/film forming behaviour on planar substrates compared to water. Comparing the fluorinated (Sivo EC) and non-fluorinated (Sapphire) surface treatments, the water repellence was similar on both surfaces, however an uplift in diiodo-methane repellence was observed suggesting that fluorine containing treatments enhance oleophobicity of the substrates as mentioned in Chapter 5. The hydrophobicity can be achieved by employing non-fluorine containing coatings/surface treatments, but fluorine is likely to be necessary for lower surface tension liquid that have a low polar nature.

The introduction of micro-scale topography showed an increase in static WCA but also increased the hysteresis and thus introduced the droplet pinning effect. The same behaviour was observed with diiodo-methane, LST 50 and LST 30 on substrates blasted with grit 100. Comparing the values for diiodo-methane and LST 50, even though their total surface tension values are similar there is a different wetting behaviour observed. The static contact angle is higher with LST 50 liquid, The CAH is much lower as well as the diameter which suggests lower wetting. The roll-off tilt seems to be lower with diiodo-methane but as already discussed this is due to film-formation and not to repellence. This difference in the behaviour can be explained by the polar or disperse nature of the liquid/surface as already discussed in Chapter 5. The disperse probe liquid seems to be more compatible with the studied surface. Hence better wetting. The comparison between diiodo-methane and LST50 wetting behaviour is a valuable tool as it provides insight into the surface chemistry of the studied coating/substrate and its wetting behaviour with polar/disperse liquids. The direct comparison of diodo-methane with water does not provide as much insight because water has a very high surface tension which creates an uplift in repellence. The increased

repellence has to be attributed to the increased surface tension and not to the specific polar/disperse interaction and therefore the data are not easily comparable. The use of LST50 avoids this and provides readily comparable values.

In terms of the repellence with lower surface tension liquid LST30, the initial static contact angle with LST30 is 75º and blasting with grit 100 creates an uplift to 82º. This increase is not in line with the Wenzel wetting model. The contact angle of 75º suggests that the surface is inherently philic to the probe liquid and the increased roughness would increase the interfacial surface area and therefore wettability. However, this is not observed on the sample blasted with grit 100. Comparing the other studied parameters CAH and roll-off tilt however shows that increase in roughness causes the wettability to increase. This observation suggests that the static contact angle can be a misleading parameter and to obtain deeper insight into repellence/wetting more parameters have to be considered with a range of probe liquids. The proposed evaluation approach allows for the easy comparison of a number of parameters and provides valuable insights into wetting.

The surface blasted with coarser grit 36 showed a more complex behaviour compared to grit 100. The increased roughness elevated the repellence/wettability characteristics. However, a noticeable difference was in the switch of the repellence of LST 30. The grit 100 provided an uplift in the static contact angle from the initial 75º to 82º but grit 36 enhanced wettability and decreased the contact angle to 60º. This switch from repellence to wetting is different for each liquid and it seems to be determined by the specific characteristics of the probe liquids.

The effect of nano-scale and dual-scale surface roughness on repellence was assessed with the proposed criteria with water and diiodo-methane as probe liquids. The micro-scale roughness has a more significant influence on the water roll-off tilt than nano-scale topography on its own. In terms of diiodo-methane the only surface that provided the uplift in contact angles, roll-off tilt and decrease in droplet diameter was stainless steel 304 treated with sapphire (planar substrate with minimal roughness). The introduction of roughness to the substrate causes the wettability towards the low surface tension probe liquid (diiodo-methane) to increase. The most significant change observed by the introduction of dual-scale roughness (combination of both nano-scale and micro-scale) was the roll-off tilt and contact angle hysteresis with water. The combination of nano-scale and micro-scale topography enables water droplet to roll-off the surface. The easy abhesion with water suggests that dual-scale topography is important for hydrophobicity.

CHAPTER 9. CONCLUSIONS AND FUTURE WORK

9.1. Summary of main results and conclusions

A deeper understanding of the key chemical and topographic characteristics that dictate super repellent behaviour would provide the enabler for the engineering of anti-contamination, anti-sticking and self-cleaning materials. This thesis provided insight into the design rules for the fabrication of surfaces that will be repellent not only to water but liquids with lower surface tensions too. The reported research provides understanding of the relative roles of surface chemistry and surface roughness and has allowed the development of a new methodology for assessing wettability.

A review on surface treatments and how they affect solid-liquid interaction by measuring the static and dynamic contact angle with a variety of polar and non-polar probe liquids has been presented (Chapter 5). To decouple the effects of surface roughness/topography from the surface chemistry contributions planar substrates with minimal surface roughness were used (glass and stainless steel 304 with mirror and 2B finish). The roughness data for the substrates studied was measured using White Light Interferometry (WLI), Alicona and surface profilometer Surfcom. Surface roughness values depend on the measuring technique, the surface spatial wavelengths used, and the lateral resolution of the measuring method. Variation in the optical and mechanical profile roughness is caused by differences in lateral resolution. The data collected via three different techniques agree on the substrate roughness increases from glass, stainless steel mirror finish to stainless steel with 2B finish. According to WLI measurements, glass has the ideal smooth surface with a roughness index of 1 while stainless steel 2B has the value of 1.13 which suggests that it has some degree of surface heterogeneity even though its roughness average value is in the nanometre scale. As mentioned in Chapter 2, roughness plays an important part in substrate's wettability. It can either enhance or reduce it. However, the degree of roughness that influences wettability has to be taken into account. As presented in Chapter 2, Figure 2.10, as the Wenzel's roughness parameter increases the wettability with 2B and mirror finish should not have a significant impact on their wettability. The main parameter that will affect it will be surface chemistry and Chapter 5 provided a study on its impact. In terms of the surface treatments of the substrates, different cleaning approaches, thermal and humidity treatments were studied as well as their effect on the substrate wettability, SFE and contact angles.

The main findings (Chapter 5) for thermal and humidity treatments were that the glass has a stable and constant disperse SFE term. Heating and exposure to a humid environment had a negligible impact on it, whilst the polar term showed considerable variation. Heating the glass appears to reduce the polar contribution whilst exposing it to humidity increases this term. A dehydration, rehydration mechanism would account for this behaviour. To further study the effect of thermal treatment on the dehydration of glass slides, the substrates were subjected to 65ºC, 150ºC and 200ºC for 18 hours (Chapter 5). The contact angles with both water and diiodo-methane decreased with increase in temperature of the thermal treatment. The reason behind the decreased water repellence might be that after surface had undergone dehydration, it mainly consists of vicinal or geminal hydroxyl groups. The vicinal groups can be either interacting or isolated. Interacting vicinal groups have less affinity to interact with water deposited on the surface compared to isolated hydroxyl groups. As the surface is subjected to higher temperatures, it starts to undergo dehydroxylation – it loses hydroxyl groups causing the surface hydroxyl density to decrease and therefore the distance between the hydroxyl groups increases, shifting interacting vicinal groups to become isolated. This shift might explain the increased hydrophilicity of the studied glass surface. In terms of the surface rehydration after 7 days at atmospheric conditions, the decrease in contact angle for treatments at 65ºC and 150ºC was observed. However, for 200ºC treatment there is no significant change even after 7 days which supports the assertion that under these conditions the surface becomes dehydrated as well as dehydroxylated and so complete rehydroxylation cannot be achieved at atmospheric conditions. The steel surfaces show a far more complex behaviour. Its disperse term is changed by heating at 150°C, the polar term also changes significantly by this treatment. The surface finish appears to have a notable effect on the polar term on exposure to damp heat. The behaviour of the steel therefore cannot be explained by a simple hydration model.

In terms of chemical surface treatments to reduce the SFE of the glass and stainless steel, eleven coatings were studied (Chapter 5), including fluorinated and non-fluorinated chemistries. The studied commercial coatings on glass all gave static water contact angles (WCA) values in the range of 67 to 96º, whilst the static diiodo-methane contact angles (DCA) values were in the range of 63 to 84º. The SFE values estimated for these coated glass substrates were therefore between 20 and 40 mN/m. When applied onto stainless steel these same coatings gave higher WCA values, between 94 and 113º, the corresponding DCA values were in the range of 44 to 91º and the SFE values ranged from 13 to 38 mN/m. The

wettability data showed variation across the samples however the obtained data can be clustered. The coatings that showed the highest values of both WCA and DCA on both substrates were the fluorinated silane-based coatings. In terms of the wettability assessment, the high water repellence did not guarantee decreased wettability with low surface tension liquids or with non-polar probe liquids. The greater differences between the coatings' repellent behaviour were identified when the probe liquid was diiodo-methane. To further examine the repellent behaviour of these studied coatings the sessile drop behaviour of probe liquids with lower surface tension values was investigated. This assessment showed that polar, protic liquid with a similar surface tension to diiodo-methane exhibited higher static contact angles on non-fluorinated coatings compared to diiodo-methane which contrasts with the perceived knowledge on fluorinated coatings. The initial wettability assessment with WCA and DCA suggested a superior repellence behaviour of fluorinated coatings compared to non-fluorinated treatments, however further assessment suggests that this might not be the case for lower surface tension polar probe liquids. The fluorine containing treatments enhance oleophobicity of the substrates. The hydrophobicity can be achieved by employing non-fluorine containing coatings/surface treatments, but fluorine is likely to be necessary for a lower surface tension liquid that have a low polar nature.

The repellent behaviour of commercial coatings deposited on smooth substrates was also studied via dynamic contact angle measurements to obtain contact angle hysteresis (CAH) values. The obtained data showed that CAH begins to increase before the movement of droplet, and it increases with the tilt angle. The position of the contact points (CP) starts to move only after a certain degree of CAH is achieved, in the studied samples the first movement was observed when the CAH value was in the range of 10-30º. Hysteresis between advancing and receding points suggests that the receding CP remains pinned and starts to move later than the advancing side. It is considered that CAH provides information on the pinning/adhesion force of the droplet to the surface, but CAH on its own does not provide information whether the droplet is exhibiting film forming behaviour, whether it is spreading and wetting out a surface or whether it easily de-wets and rolls off without leaving a film behind. To provide information on the dynamic wetting behaviour that CAH is lacking, an additional parameter that provides insight into the droplet movement or the change in droplet diameter has to be employed. Both the contact point hysteresis (Chapter 5) and the droplet diameter (Chapter 8) were studied to provide further understanding of different wetting/repellence behaviours. The hysteresis of contact points (CPH) is the difference between the CP movement at the advancing side and the CP movement at the

receding side of the droplet. The diameter of the droplet helps to identify the liquid spreading on the surface, large diameter suggests higher wettability and film forming behaviour. Identifying and calculating these parameters add value to the dynamic contact angle measurements and provide insight in identifying the type of wetting taking place as it cannot be easily described by static contact angles, dynamic contact angles or even contact angle hysteresis. Static WCA is a useful measure as it has value from a comparative perspective but is limited since water has a high surface tension and wishes to bead. Static DCA allows a more complete assessment of the surface and can be used together with WCA to provide SFE values and polar/disperse contributions. In order to get an understanding from the dewetting and roll-off point of view, dynamic contact angle measurement has to be undertaken since a high static contact angle does not guarantee low roll-off tilt or low contact angle hysteresis.

The impact of surface micro-level roughness on wettability/repellence behaviour was investigated (Chapter 6) by grit blasting stainless steel. Increasing the surface roughness from 0.01 μm to 4 μm resulted in a rise and then a fall in the static contact angles for the probe liquids employed. For liquids with low surface tensions (LST 30, xylene and decane) the deposited probe liquid gave contact angles below 10°. According to Wenzel the greater the deviation from 90° on a smooth surface, the greater will be the influence of introduced roughness on the apparent contact angle. Thus, if the contact angle is below 90°, the introduction of surface roughness is expected to decrease the contact angle further, however the obtained values do not seem to follow this trend. Introduction of roughness enhanced contact angles even though the starting contact angle was below 90° for all liquids studied. On the coated substrates, a similar effect was observed; increasing surface roughness enhanced repellence of all liquids except for xylene and decane. There could be two reasons for this uplift in contact angles on the inherently liquid-philic substrate. One of the reasons might be the topographic characteristics of the studied substrate; increased roughness might cause increased capillary action and prevent probe liquids from wetting the surface further. The second reason might be the need for further refinement to the Wenzel wetting model. As discussed in Chapter 2, there are different opinions on how to classify hydro/oleo-phobic and hydro/oleo-philic surfaces. In terms of contact angles with xylene and decane. Xylene has a low surface tension of 30 mN/m and its SFE consists only of a disperse component like decane having a disperse SFE of 24 mN/m. The starting contact angle on the smooth surface for Xylene treated with fluorinated coating (Sivo EC) was 56º while for non-

fluorinated treatment (Sapphire) it was 25º. For the decane, the values were 48º and below 10º respectively. The increased roughness together with the fluorinated treatments did not significantly change the CA values or slightly decreased them while more significant decrease was seen with non-fluorinated treatments suggesting that lower surfaces with inherently low CA values are more likely to agree with the Wenzel wetting model.

Comparing the effect of fluorinated and non-fluorinated coatings systems, the fluorinated coating provides higher contact angles on both roughened and smooth surfaces for all liquids. This effect can be seen more evidently for low surface tension liquids with low polar contributions. The dynamic contact angle assessment showed that the roughened substrates with micron-scale roughness exhibits high contact angle hysteresis, no roll-off or film formation for liquids with low surface tensions. Water droplets remain pinned to the surface even at a tilt of 80 º while diiodo-methane spreads on the surface and forms a film. As mentioned in Chapter 2, super repellent surfaces that will eliminate pinning of droplets should have a minimal contact angle hysteresis; less than 10º. In the case of the surfaces examined with roughness levels (R_a) in the range of 0.01 μm to 4 μm, there was no super repellent behaviour exhibited when treated with fluorinated or non-fluorinated coatings which had been demonstrated to significantly reduce the SFE of the surface. Therefore, achieving a high static CA was not sufficient to satisfy the conditions necessary to achieve super repellence.

The project investigated the effect of nano-scale and dual-scale roughness on repellence. Nano-scale roughness was introduced to the surface by incorporation of silica nanoparticles into candidate coatings, while low SFE was achieved by the surface functionalisation of these nanoparticles with silanes. Two types of silica nanoparticles (SNPs) were used in the study; those synthesised by a sol-gel method and commercial fumed silica particles (Aerosil 200). The obtained particles were functionalised with fluorinated and non-fluorinated silanes; hexamethyldisilazane (HMDZ) and 3,3,3- trifluoropropyltriethoxysilane (333). Dynamic light scattering (DLS) as well as WLI and Atomic force microscopy (AFM) studies confirmed the diameter of the sol-gel synthesised nanoparticles to be in the range of 40-50 nm. It was shown that the nanoparticles could be used to obtain repellence via a bottom-up approach by dip coated the SNPs from suspension onto glass slides. The SNPs form a film that builds up the nano-roughness on the substrate while the surface functionalities on the SNPs provide low SFE. This combination gave the static CA of 104º for water and 67º for diiodo-methane. To maintain the repellence and increase durability, the obtained

functionalised nanoparticles were incorporated into the commercial coating Sharc Sapphire. Sharc Sapphire was selected as it is a polysilazane based coating and not a silane as other surface treatments studied in Chapter 5. It has a film forming behaviour and it could act as a matrix for additives. Assessment with WLI confirmed that the modified coating has nano-scale roughness, and the coating matrix did not cause the levelling of the nano-particles. Two loading levels were studied (Chapter 7): 50 % and 75 % solid loading. The incorporation of the functionalised SNPs into the Sapphire coating at 50% loading level elevated the static contact angles to 128º from 103° (water) and to 88º from 80°(diiodo-methane) respectively. Increasing the loading level to 75% did not change the repellence with water (128º) but did increase the repellence to diiodo-methane to 93º (for F333 functionalisation). The increase in DCA values can be attributed to higher fluorine content in the coating that makes the surface more oleophobic (as described and observed in Chapter 5) but does not significantly affect hydrophobicity suggesting that the right surface chemistry is required in combination with the topography to satisfy the more demanding repellence conditions of diiodo-methane.

The modified coatings were deposited on grit blasted stainless steel substrates to create a dual scale topography that combines both the micro-scale topography (studied in Chapter 6) and the nano-scale topography (studied in chapter 7). The SNPs used in this dual-scale roughness study were functionalised with HMDZ and incorporated at 50% solid loading level into the Sapphire coating. On the coated substrates, the water contact angle increased consistently with increase in the substrate's micro-scale roughness until grit 36 (R_a 2.9µm) where the WCA of 154º was achieved. The diiodo-methane showed a similar trend with an increase in contact angle value with increasing micro-scale until the surface prepared with grit 60 (R_a 1.7 µm) where its contact angle reached 99º. Further increases in micro-roughness led to a reduction in repellence. This behaviour is likely to be due to some key topographic thresholds being passed, each threshold being dictated by the specific characteristics of the probe liquids. In terms of the CAH at roll-off and the roll-off tilt, the loading level of SNPs in the coating system did not have an influence. However, both roll-off and CAH were affected by the substrate's roughness in combination with the nano-scaled roughness. The increased micro-scale roughness of the substrate reduced water CAH from 25 º to below 10 º and the roll-off tilt from 80 º (no droplet roll-off) to below 10º. The results in this study show that a high contact angle with the probe liquid does not guarantee the abhesive behaviour. It is important to study the roll-off angles to confirm the repellent behaviour to specific liquids. The nano-scale topography provided high static contact angles with probe

liquids as well as high contact angle hysteresis and high roll-off angles/or no roll-off. The micro-scale topography studied in Chapter 6 provided similar results. However, the combination of both nano and micro-scale topographies provided high contact angles, low contact angle hysteresis and low roll-off tilts for water. This specific dual scale topography does satisfy the criteria for super repellence with water. However, this same combination of surface characteristics does not satisfy the conditions to achieve super repellence for probe liquids with lower surface tensions and different surface tension components (polar part/disperse part). Changing the micro and nano-scale topography as well as surface chemistry exhibited the range of wetting behaviours with various probe liquids. These behaviours provide some insight into the design rules to achieving omniphobicity as selecting the correct surface chemistry and surface roughness for the utmost abhesive behaviour requires a variety of factors to be taken into account. An assessment methodology (presented in Chapter 8) has been proposed for the evaluation of repellence of surfaces. This approach helps to classify coatings and surface roughness characteristics according to their ability to repel various liquids not only in terms of static contact angles but also in terms of contact angle hysteresis, roll off tilt and droplet diameter (film forming behaviour). Whilst the critical parameters to achieving omniphobicity are still unclear, this work sheds light on the parameters that have to be considered and the methods to elucidate them.

9.2. Recommendation for future work

The reported research work provides detailed understanding of the critical parameters for achieving superhydrophobicity, however further work is required to understand the design rules for superomniphobic surfaces.

The research presented in this thesis highlights the importance of dual-scale topography and further work should concentrate on study of various combinations of nano-scale and micro-scale topographies. The presented research included the study on the polysilazane coating incorporated with Stöber silica nanoparticles (diameter of 35 nm) used for the deposition onto a blasted substrates to obtain dual-scale topography. This work can be extended by incorporation of larger silica nanoparticles (diameter > 100 nm) into the coating and its deposition onto the substrates with a range of micro-scale roughnesses (< 1 μm and > 4 μm).

It was also highlighted that incorporation of fluorinated silica nanoparticles into the coating matrix enhances repellence, further work can be undertaken to study and compare different

fluorinated silanes and their effect on silica nanoparticle additive functionalisation and repellence.

Finally, as high static contact angles do not guarantee the abhesive behaviour, further work on repellence should include the study of the roll-off angles as well as film forming/rolling behaviour to confirm repellence to specific liquids.

References

‘Aculon ON-305 Materials Safety Data Sheet’. Aculon Inc.

‘Aculon ON-353 Materials Safety Data Sheet’.

Adam, N. K. and Jessop, G. (1925) ‘CCL.—Angles of contact and polarity of solid surfaces’, *J. Chem. Soc.{,} Trans.*, 127(0), pp. 1863–1868. doi: 10.1039/CT9252701863.

Alawajji, R. A., Kannarpady, G. K. and Biris, A. S. (2018) ‘Fabrication of transparent superhydrophobic polytetrafluoroethylene coating’, *Applied Surface Science*, 444, pp. 208–215. doi: 10.1016/j.apsusc.2018.02.206.

Anitha, C., S., S. A. and Mayavan, S. (2018) ‘Salvinia inspired fluroine free superhydrophobic coatings’, *Applied Surface Science*, 449, pp. 250–260. doi: 10.1016/j.apsusc.2017.11.120.

‘AQUAPHOBE ® CF Safety Data Sheet’ (2018). GELEST, INC.

‘AQUAPHOBE ® CF Technical Data Sheet’ (no date). GELEST, INC.

‘AQUAPHOBE ® CM Safety Data Sheet’ (2018). GELEST, INC, pp. 1–10.

‘AQUAPHOBE ® CM Technical Data Sheet’ (no date). GELEST, INC, p. 2484.

Arashiro, E. Y. and Demarquette, N. R. (1999) ‘Use of the pendant drop method to measure interfacial tension between molten polymers’, *Materials Research*, 2(1), pp. 23–32. doi: 10.1590/s1516-14391999000100005.

Arkles, B., Pan, Y. and Mi Kim, Y. (2009) ‘The role of polarity in the structure of silanes employed in surface modification’, *Silanes and other Coupling Agents*, 5, pp. 51–64.

Asakura, T. (1978) ‘CHAPTER 3 - SURFACE ROUGHNESS MEASUREMENT’, in ERF, R. K. (ed.) *Speckle Metrology*. Academic Press, pp. 11–49. doi: https://doi.org/10.1016/B978-0-12-241360-5.50009-1.

‘ASTM D523-14, Standard Test Method for Specular Gloss’ (2018). West Conshohocken, PA: ASTM International.

‘ASTM E430-19, Standard Test Methods for Measurement of Gloss of High-Gloss Surfaces by Abridged Goniophotometry’ (2019). West Conshohocken, PA: ASTM International.

‘AVALON ® Glass Safety Data Sheet’ (no date).

‘AVALON ® Glass Technical Data Sheet’ (no date). Milidyne, p. 33720.

Barthlott, W. and Neinhuis, C. (1997) ‘Purity of the sacred lotus, or escape from contamination in biological surfaces’, *Planta*, 202(1), pp. 1–8. doi: 10.1007/s004250050096.

Basu, B. J., Dinesh Kumar, V. and Anandan, C. (2012) ‘Surface studies on superhydrophobic and oleophobic polydimethylsiloxane- silica nanocomposite coating system’, *Applied Surface Science*, 261, pp. 807–814. doi: 10.1016/j.apsusc.2012.08.103.

Bennett, J. M. (1985) ‘Comparison Of Techniques For Measuring The Roughness Of Optical Surfaces’, *Optical Engineering*, 24(3), pp. 380–387. doi: 10.1117/12.7973493.

Bhushan, B. and Nosonovsky, M. (2010) ‘The rose petal effect and the modes of superhydrophobicity’, *Phil. Trans. R. Soc. A.* doi: 10.1098/rsta.2010.0203.

Bikerman, J. J. (2012) *Physical surfaces*. Elsevier.

Bourebrab, M. A. *et al.* (2018) ‘Influence of the initial chemical conditions on the rational design of silica particles’, *Journal of Sol-Gel Science and Technology*, 88(2), pp. 430–441. doi: 10.1007/s10971-018-4821-9.

Bouteau, M. *et al.* (2008) ‘Sliding behavior of liquid droplets on tilted Langmuir-Blodgett surfaces’, *Journal of Colloid and Interface Science*, 317(1), pp. 247–254. doi: 10.1016/j.jcis.2007.09.042.

Brinker, C. J. *et al.* (1992) ‘Review of sol-gel thin film formation’, *Journal of Non-Crystalline Solids*, 147–148, pp. 424–436. doi: https://doi.org/10.1016/S0022-3093(05)80653-2.

Byun, D. *et al.* (2009) ‘Wetting Characteristics of Insect Wing Surfaces’, *Journal of Bionic Engineering*, 6(1), pp. 63–70. doi: 10.1016/s1672-6529(08)60092-x.

Cassie, A. B. D. and Baxter, S. (1944) ‘Wettability of porous surfaces’, *Trans. Faraday Soc.*, 40(0), pp. 546–551. doi: 10.1039/TF9444000546.

Castle, J. E. (2008) ‘The composition of metal surfaces after atmospheric exposure: An historical perspective’, *Journal of Adhesion*, 84(4), pp. 368–388. doi:

10.1080/00218460802004477.

Caupin, F. *et al.* (2008) 'Absolute limit for the capillary rise of a fluid', *EPL (Europhysics Letters)*, 82(5), p. 56004. doi: 10.1209/0295-5075/82/56004.

Chibowski, E. (2003) 'Surface free energy of a solid from contact angle hysteresis', *Advances in Colloid and Interface Science*, 103(2), pp. 149–172. doi: 10.1016/s0001-8686(02)00093-3.

Chibowski, E. and Jurak, M. (2013) 'Comparison of contact angle hysteresis of different probe liquids on the same solid surface', *Colloid and Polymer Science*, 291(2), pp. 391–399. doi: 10.1007/s00396-012-2777-9.

Currell, B. R. and Parsonage, J. R. (1981) 'Trimethylsilylation of Mineral Silicates', *Journal of Macromolecular Science: Part A - Chemistry*, 16(1), pp. 141–166. doi: 10.1080/00222338108082045.

Dalawai, S. P. *et al.* (2020) 'Recent Advances in durability of superhydrophobic self-cleaning technology: A critical review', *Progress in Organic Coatings*, 138, p. 105381. doi: 10.1016/j.porgcoat.2019.105381.

Dalili, N., Edrisy, A. and Carriveau, R. (2009) 'A review of surface engineering issues critical to wind turbine performance', *Renewable and Sustainable Energy Reviews*, 13(2), pp. 428–438. doi: https://doi.org/10.1016/j.rser.2007.11.009.

Dalvi, V. H. and Rossky, P. J. (2010) 'Molecular origins of fluorocarbon hydrophobicity', *Proceedings of the National Academy of Sciences*, 107(31), pp. 13603–13607. doi: 10.1073/pnas.0915169107.

Dillard, D. A., Pocius, A. V and Chaudhury, M. (2002) *Adhesion science and engineering*. Elsevier.

DLS technical note MRK656-01 (2018).

Dong, Y., Pappu, S. V and Xu, Z. (1998) 'Detection of Local Density Distribution of Isolated Silanol Groups on Planar Silica Surfaces Using Nonlinear Optical Molecular Probes', *Analytical Chemistry*, 70(22), pp. 4730–4735. doi: 10.1021/ac9805697.

Dopierala, K. *et al.* (2013) 'Alkyl- and fluoroalkyltrialkoxysilanes for wettability modification', *Applied Surface Science*, 283, pp. 453–459. doi: 10.1016/j.apsusc.2013.06.130.

Drelich, Jaroslaw W. (2019) ‘Contact angles: From past mistakes to new developments through liquid-solid adhesion measurements’, *Advances in Colloid and Interface Science*, 267, pp. 1–14. doi: 10.1016/j.cis.2019.02.002.

Drelich, Jaroslaw W (2019) ‘Contact angles: From past mistakes to new developments through liquid-solid adhesion measurements’, *Advances in Colloid and Interface Science*, 267, pp. 1–14. doi: 10.1016/j.cis.2019.02.002.

‘Dynasylan® SIVO CLEAR K1 Safety Data Sheet’ (2018).

‘Dynasylan® SIVO CLEAR K2 Safety Data Sheet’ (2016). Evonik.

‘Dynasylan ® SIVO CLEAR EC Product Information’ (no date).

‘Dynasylan ® SIVO CLEAR EC Safety Data Sheet’ (2016).

‘Dynasylan ® SIVO CLEAR K2 Dynasylan Product Information’ (2011). Evonik Industries AG, pp. 2–4.

Eder, M., Amini, S. and Fratzl, P. (2018) ‘Biological composites{\textemdash}complex structures for functional diversity’, *Science*, 362(6414), pp. 543–547. doi: 10.1126/science.aat8297.

Effect of drop volume on static contact angles - TN310e (2004).

Esmeryan, K. D. (2020) ‘From Extremely Water-Repellent Coatings to Passive Icing Protection—Principles, Limitations and Innovative Application Aspects’, *Coatings*, 10(1). doi: 10.3390/coatings10010066.

Ettlinger, M., Ladwig, T. and Weise, A. (2000) ‘Surface modified fumed silicas for modern coatings’, *Progress in Organic Coatings*, 40(1), pp. 31–34. doi: https://doi.org/10.1016/S0300-9440(00)00151-X.

Flink, S., Van Veggel, F. C. J. M. and Reinhoudt, D. N. (2001) ‘Functionalization of self-assembled monolayers on glass and oxidized silicon wafers by surface reactions’, *Journal of Physical Organic Chemistry*, 14(7), pp. 407–415. doi: 10.1002/poc.372.

Focus-Variation - The technical principle (no date) *Alicona Imaging GmbH*. Available at: https://www.alicona.com/en/our-technology/focus-variation/.

Frahn, S. *et al.* (2001) ‘Surface modified fumed silicas’, *European Coatings Journal*, 40(3), pp. 98–105.

Furmidge, C. G. L. (1962) ‘Studies at phase interfaces. I. The sliding of liquid drops on solid surfaces and a theory for spray retention’, *Journal of Colloid Science*, 17(4), pp. 309–324. doi: 10.1016/0095-8522(62)90011-9.

Gadelmawla, E. S. *et al.* (2002) ‘Roughness parameters’, *Journal of Materials Processing Technology*, 123(1), pp. 133–145. doi: https://doi.org/10.1016/S0924-0136(02)00060-2.

Gaydos, J. and Neumann, A. W. (1994) ‘The shapes of liquid menisci near heterogeneous walls and the effect of line tension on contact angle hysteresis’, *Advances in Colloid and Interface Science*, 49, pp. 197–248. doi: https://doi.org/10.1016/0001-8686(94)80016-2.

Genzer, J. and Efimenko, K. (2006) ‘Recent developments in superhydrophobic surfaces and their relevance to marine fouling: a review’, *Biofouling*, 22(5), pp. 339–360. doi: 10.1080/08927010600980223.

Giese, R. F. and van Oss, C. J. (2002) *Colloid And Surface Properties Of Clays And Related Minerals*. CRC Press. doi: 10.1201/9780203910658.

Good, R. J. and Girifalco, L. A. (1960) ‘A THEORY FOR ESTIMATION OF SURFACE AND INTERFACIAL ENERGIES. III. ESTIMATION OF SURFACE ENERGIES OF SOLIDS FROM CONTACT ANGLE DATA’, *The Journal of Physical Chemistry*, 64(5), pp. 561–565. doi: 10.1021/j100834a012.

Herminghaus, S. (2000) ‘Roughness-induced non-wetting’, *Europhysics Letters ({EPL})*, 52(2), pp. 165–170. doi: 10.1209/epl/i2000-00418-8.

Huhtamäki, T. *et al.* (2018) ‘Surface-wetting characterization using contact-angle measurements’, *Nature Protocols*, 13(7), pp. 1521–1538. doi: 10.1038/s41596-018-0003-z.

Ilse, K. K. *et al.* (2018) ‘Fundamentals of soiling processes on photovoltaic modules’, *Renewable and Sustainable Energy Reviews*, 98(C), pp. 239–254. Available at: https://econpapers.repec.org/RePEc:eee:rensus:v:98:y:2018:i:c:p:239-254.

‘ISO 22412:2017’ (2017). ISO.

J.Schmit (2013) ‘An introduction to non-contact surface metrology’, *Technical Paper*. Available at: https://www.bruker.com/fileadmin/user_upload/8-PDF-Docs/SurfaceAnalysis/3D-OpticalMicroscopy/Webinars/An_introduction_to_non-contact_surface_metrology-Jun_2013.pdf.

Jeevahan, J. *et al.* (2018) ‘Superhydrophobic surfaces: a review on fundamentals,

applications, and challenges', *Journal of Coatings Technology and Research*, 15(2), pp. 231–250. doi: 10.1007/s11998-017-0011-x.

Kaynak, B. *et al.* (2017) 'Anti-adhesive layers on stainless steel using thermally stable dipodal perfluoroalkyl silanes', *Applied Surface Science*, 416, pp. 824–833. doi: 10.1016/j.apsusc.2017.04.197.

Kim, J. H. *et al.* (2018) 'Facile fabrication of superhydrophobic surfaces from austenitic stainless steel (AISI 304) by chemical etching', *Applied Surface Science*, 439, pp. 598–604. doi: 10.1016/j.apsusc.2017.12.211.

Krasovitski, B. and Marmur, A. (2005) 'Drops Down the Hill: Theoretical Study of Limiting Contact Angles and the Hysteresis Range on a Tilted Plate', *Langmuir*, 21(9), pp. 3881–3885. doi: 10.1021/la0474565.

Lam, C. N. C. *et al.* (2001) 'The effect of liquid properties to contact angle hysteresis', *Colloids and Surfaces A: Physicochemical and Engineering Aspects*, 189(1), pp. 265–278. doi: https://doi.org/10.1016/S0927-7757(01)00589-1.

Lam, C. N. C. *et al.* (2002) 'Study of the advancing and receding contact', *Advances in Colloid and Interface Science*, 96, pp. 169–191. doi: 10.1016/S0001-8686(01)00080-X.

Lautrup, B. (2011) 'Physics of Continuous Matter'. CRC Press. doi: 10.1201/9781439894200.

Lei, F. *et al.* (2018) 'Facile design and fabrication of highly transparent and hydrophobic coatings on glass with anti-scratch property via surface dewetting', *Progress in Organic Coatings*, 120, pp. 28–35. doi: https://doi.org/10.1016/j.porgcoat.2018.03.008.

Levich, B., & Landau, L. (1942) 'Dragging of a liquid by a moving plate', *Acta Physico Chimica*, Vol. XVII,.

Li, L. *et al.* (2016) 'Roles of silanes and silicones in forming superhydrophobic and superoleophobic materials', *Journal of Materials Chemistry A*, 4(36), pp. 13677–13725. doi: 10.1039/c6ta05441b.

Liu, X. *et al.* (2012) 'Extreme wettability and tunable adhesion: Biomimicking beyond nature?', *Soft Matter*, 8(7), pp. 2070–2086. doi: 10.1039/c1sm07003g.

Makkonen, L. (2016) 'Young's equation revisited', *Journal of Physics: Condensed Matter*, 28(13), p. 135001. doi: 10.1088/0953-8984/28/13/135001.

Makkonen, L. (2017) ‘A thermodynamic model of contact angle hysteresis’, *The Journal of Chemical Physics*, 147(6), p. 64703. doi: 10.1063/1.4996912.

Marczak, J. *et al.* (2016) ‘Modification of epoxy resin, silicon and glass surfaces with alkyl- or fluoroalkylsilanes for hydrophobic properties’, *Applied Surface Science*, 380, pp. 91–100. doi: 10.1016/j.apsusc.2016.02.071.

Méndez-Vilas, A. *et al.* (2006) ‘Looking at the micro-topography of polished and blasted Ti-based biomaterials using atomic force microscopy and contact angle goniometry’, *Colloids and Surfaces B: Biointerfaces*, 52(2), pp. 157–166. doi: 10.1016/j.colsurfb.2006.05.002.

Models for Surface Free Energy Calculation - Kruss TN 306 (1999).

Mueller, R. *et al.* (2003) ‘OH Surface Density of SiO2 and TiO2 by Thermogravimetric Analysis’, *Langmuir*, 19(1), pp. 160–165. doi: 10.1021/la025785w.

Nguyen-Tri, P. *et al.* (2019) ‘Recent progress in the preparation, properties and applications of superhydrophobic nano-based coatings and surfaces: A review’, *Progress in Organic Coatings*, 132(April), pp. 235–256. doi: 10.1016/j.porgcoat.2019.03.042.

De Oliveira, R. R. L. *et al.* (2012) ‘Measurement of the nanoscale roughness by atomic force microscopy: basic principles and applications’, *Atomic force microscopy-imaging, measuring and manipulating surfaces at the atomic scale*, 3.

Van Oss, C. J. (2006) *Interfacial forces in aqueous media*. CRC press.

Van Oss, C. J., Good, R. J. and Chaudhury, M. K. (1986) ‘The role of van der Waals forces and hydrogen bonds in “hydrophobic interactions” between biopolymers and low energy surfaces’, *Journal of Colloid and Interface Science*, 111(2), pp. 378–390. doi: 10.1016/0021-9797(86)90041-x.

Owens, D. K. and Wendt, R. C. (1969) ‘Estimation of the surface free energy of polymers’, *Journal of Applied Polymer Science*, 13(8), pp. 1741–1747. doi: 10.1002/app.1969.070130815.

Packham, D. E. (1996) ‘Work of adhesion: Contact angles and contact mechanics’, *International Journal of Adhesion and Adhesives*, 16(2), pp. 121–128. doi: 10.1016/0143-7496(95)00034-8.

Piscitelli, F. *et al.* (2020) ‘Superhydrophobic coatings as anti-icing systems for small

aircraft', *Aerospace*, 7(1). doi: 10.3390/aerospace7010002.

Quek, J. Y., Magee, C. L. and Low, H. Y. (2017) 'Physical Texturing for Superhydrophobic Polymeric Surfaces: A Design Perspective', *Langmuir*, 33(27), pp. 6902–6915. doi: 10.1021/acs.langmuir.7b01175.

Quéré, D. (2002) 'Rough ideas on wetting', *Physica A: Statistical Mechanics and its Applications*, 313(1), pp. 32–46. doi: https://doi.org/10.1016/S0378-4371(02)01033-6.

Quéré, D. (2008) 'Wetting and Roughness', *Annual Review of Materials Research*, 38(1), pp. 71–99. doi: 10.1146/annurev.matsci.38.060407.132434.

Roberts, W.O., & Bergna, H. E. (2005) *Colloidal Silica: Fundamentals and Applications*.

La Rosa, A. (2020) 'Understanding and Development of Functionalised Nanoscale Components for Advanced Composite Materials'.

'Sharc ® Sapphire Safety Data Sheet' (2019).

'Sharc Sapphire Product Information' (2011). Evonik Industries AG, pp. 2–4.

'Siliclad® Safety Data Sheet' (no date). GELEST, INC.

'Siliclad® Technical Data Sheet' (no date). GELEST, INC.

Spyrogianni, A. *et al.* (2017) 'The silanol content and in vitro cytolytic activity of flame-made silica', *Journal of Colloid and Interface Science*, 507, pp. 95–106. doi: https://doi.org/10.1016/j.jcis.2017.07.096.

Stetefeld, J., McKenna, S. A. and Patel, T. R. (2016) 'Dynamic light scattering: a practical guide and applications in biomedical sciences.', *Biophysical reviews*, 8(4), pp. 409–427. doi: 10.1007/s12551-016-0218-6.

Stöber, W. and and Fink, A. (1968) 'Controlled Growth of Monodisperse Silica Spheres in the Micron Size Range', *Journal of Colloid and Interface Science*, pp. 62–69.

Subhash Latthe, S. *et al.* (2012) 'Recent Progress in Preparation of Superhydrophobic Surfaces: A Review', *Journal of Surface Engineered Materials and Advanced Technology*, 02(02), pp. 76–94. doi: 10.4236/jsemat.2012.22014.

Suratwala, T. I. *et al.* (2003) 'Surface chemistry and trimethylsilyl functionalization of Stöber silica sols', *Journal of Non-Crystalline Solids*, 316(2–3), pp. 349–363. doi: 10.1016/S0022-3093(02)01629-0.

Szubert, K. *et al.* (2018) ‘Corrosion-protective coatings based on fluorocarbosilane’, *Progress in Organic Coatings*, 123(October 2017), pp. 374–383. doi: 10.1016/j.porgcoat.2018.07.030.

Takahashi, K. and Fukuzaki, S. (2012) ‘Super-Hydrophilicity of Stainless Steel Surface Induced by Heat Treatment with Gaseous Ozone’, *Ozone: Science \& Engineering*, 34(4), pp. 315–321. doi: 10.1080/01919512.2012.705248.

Tao, C. *et al.* (2016) ‘Sol-gel based antireflective coatings with superhydrophobicity and exceptionally low refractive indices built from trimethylsilanized hollow silica nanoparticles’, *Colloids and Surfaces A: Physicochemical and Engineering Aspects*, 509, pp. 307–313. doi: https://doi.org/10.1016/j.colsurfa.2016.08.055.

‘tutoProm® bright Material Safety Data Sheet’ (no date).

‘tutoProm® bright Technical Data Sheet’ (no date).

Valipour M., N., Birjandi, F. C. and Sargolzaei, J. (2014) ‘Super-non-wettable surfaces: A review’, *Colloids and Surfaces A: Physicochemical and Engineering Aspects*, 448(1), pp. 93–106. doi: 10.1016/j.colsurfa.2014.02.016.

Vazirinasab, E., Jafari, R. and Momen, G. (2018) ‘Application of superhydrophobic coatings as a corrosion barrier: A review’, *Surface and Coatings Technology*, 341(November 2017), pp. 40–56. doi: 10.1016/j.surfcoat.2017.11.053.

Vogler, E. A. (1998) ‘Structure and reactivity of water at biomaterial surfaces’, *Advances in Colloid and Interface Science*, 74(1–3), pp. 69–117. doi: 10.1016/S0001-8686(97)00040-7.

Wenzel, R. N. (1936) ‘Resistance of solid surfaces to wetting by water’, *Industrial \& Engineering Chemistry*, 28(8), pp. 988–994.

West, J. O. F. *et al.* (2016) ‘Development of a superhydrophobic polyurethane-based coating from a two-step plasma-fluoroalkyl silane treatment’, *International Journal of Adhesion and Adhesives*, 68, pp. 195–204. doi: 10.1016/j.ijadhadh.2016.03.007.

Williams, D. F. *et al.* (2017) ‘Surface analysis of 316 stainless steel treated with cold atmospheric plasma’, *Applied Surface Science*, 403, pp. 240–247. doi: 10.1016/j.apsusc.2017.01.150.

Wojdyla, A. M. *et al.* (2015) ‘Advanced low-energy durable coatings’, *International Journal of Energy Research*, 39(2), pp. 165–171. doi: https://doi.org/10.1002/er.3214.

Yong, J. *et al.* (2017) ‘Superoleophobic surfaces’, *Chemical Society Reviews*, 46(14), pp. 4168–4217. doi: 10.1039/c6cs00751a.

Yousefi, E. *et al.* (2018) ‘Preparation of new superhydrophobic and highly oleophobic polyurethane coating with enhanced mechanical durability’, *Applied Surface Science*, 454(April), pp. 201–209. doi: 10.1016/j.apsusc.2018.05.125.

Zhang, Z. *et al.* (2020) ‘Preparation of intricate nanostructures on 304 stainless steel surface by SiO2-assisted HF etching for high superhydrophobicity’, *Colloids and Surfaces A: Physicochemical and Engineering Aspects*, 586(66), p. 124287. doi: 10.1016/j.colsurfa.2019.124287.

Zhuravlev, L. T. (1993) ‘Surface characterization of amorphous silica-a review of work from the former USSR’, *Colloids and Surfaces A: Physicochemical and Engineering Aspects*, 74(1), pp. 71–90. doi: 10.1016/0927-7757(93)80399-Y.

Zisman, W. A. (1964) ‘Relation of the Equilibrium Contact Angle to Liquid and Solid Constitution’, *Advances in Chemistry*. AMERICAN CHEMICAL SOCIETY, pp. 1–51. doi: 10.1021/ba-1964-0043.ch001.

Appendix A

Table 9-1 Roll - off data for Tutoprom coating

Substrate	**Probe Liquid**	**CA [R] (º)**	**CA [A] (º)**	**Tilt (º)**	**Contact Point [R] (mm)**	**Contact Point [A] (mm)**
Glass	Water	71.5 (±5.7)	93.0 (±6.6)	55.7 (±12.1)	13.7 (±1.6)	18.5 (±1.7)
Glass	Diiodo-methane	44.2 (±5.6)	89.7 (±3)	9.6 (±1.3)	10.2 (±1.6)	16.6 (±1.4)
Glass	LST 50	42.7 (±0.3)	79.1 (±7.4)	47.7 (±7.4)	9.0 (±1.0)	14.8 (±1.1)
Glass	LST 30	42.5 (±0.1)	74.2 (±0.7)	38.4 (±7.1)	8.5 (±2.1)	14.4 (±2.1)
SS304 mirror finish	Water	76.3 (±1.9)	100.0 (±0.8)	59.6 (±3.1)	13.1 (±1.5)	17.7 (±1.5)
SS304 mirror finish	Diiodo-methane	46.0 (±4.7)	95.1 (±3.4)	10.5 (±0.9)	10.6 (±0.1)	17.0 (±0.8)
SS304 mirror finish	LST 50	70.6 (±0.4)	93.2 (±0.4)	34.5 (±1.5)	12.7 (±2.4)	17.6 (±2.3)
SS304 mirror finish	LST 30	70.3 (±0.3)	92.8 (±1.7)	41.6 (±1.8)	13.1 (±1.3)	17.5 (±1.5)
SS304 2B finish	Water	83.2 (±8.1)	106.8 (±10.1)	62.7 (±14.2)	12.8 (±2.0)	17.1 (±2.5)
SS304 2B finish	Diiodo-methane	35.3 (±12.5)	93.7 (±2.6)	16.4 (±7.6)	11.1 (±1.0)	17.7 (±1.2)
SS304 2B finish	LST 50	63.1 (±8)	89.1 (±8.6)	40.7 (±1.3)	10.0 (±2.1)	15.1 (±2.1)
SS304 2B finish	LST 30	44.8 (±29.1)	76.0 (±21.4)	35.8 (±17)	9.7 (±2.1)	15.2 (±0.5)

Grit 100	Water	85.4 (±10.3)	113.5 (±10.2)	79.9 (±0.1)	11.8 (±0.3)	16.2 (±0.5)
Grit 100	Diiodo-methane	24.7 (±1.3)	101.8 (±9.3)	25.9 (±1.3)	10.3 (±0.5)	17.4 (±0.4)
Grit 100	LST 50	52.6 (±2.6)	93.6 (±3.5)	80.0 (±0.0)	6.4 (±0.4)	11.5 (±0.4)
Grit 100	LST 30	26.5 (±0.4)	117.5 (±3.6)	39.8 (±0.9)	11.8 (±0.3)	18.5 (±0.2)
Grit 60	Water	90.1 (±13.1)	115.6 (±14.1)	72.2 (±12.8)	12.5 (±1.4)	16.7 (±1.8)
Grit 60	Diiodo-methane	23.5 (±0.2)	98.7 (±3.2)	23.9 (±0.0)	9.4 (±0.3)	16.5 (±0.6)
Grit 60	LST 50	66.4 (±2.1)	100.5 (±4.7)	66.8 (±21.8)	7.4 (±1.2)	12.1 (±1.5)
Grit 60	LST 30	28.6 (±1)	108.6 (±4.3)	48.1 (±1.8)	9.8 (±1.2)	16.1 (±1.4)
Grit 36	Water	87.5 (±8.3)	114.8 (±7.2)	79.2 (±0.7)	10.9 (±0.3)	15.0 (±0.1)
Grit 36	Diiodo-methane	23.1 (±3.8)	106.3 (±25.8)	22.9 (±0.9)	10.1 (±1.3)	17.1 (±2.0)
Grit 36	LST 50	69.4 (±1.3)	103.4 (±2.8)	80.0 (±0.0)	7.7 (±0.7)	12.0 (±0.6)
Grit 36	LST 30	31.9 (±4.9)	106.7 (±22.8)	44.9 (±6.1)	8.0 (±0.7)	14.5 (±1.5)

Table 9-2 Roll - off data for Aculon 353

Substrate	**Probe Liquid**	**CA [R] (º)**	**CA [A] (º)**	**Tilt (º)**	**Contact Point [R] (mm)**	**Contact Point [A] (mm)**
Glass	Water	72.2 (±0.9)	99.9 (±3.3)	77.7 (±3.3)	9.2 (±1.1)	13.6 (±1.2)
Glass	Diiodo-methane	62.8 (±5.6)	106.4 (±4.7)	9.6 (±1.5)	11.9 (±0.6)	17.6 (±0.6)
Glass	LST 50	39.5 (±7.1)	68.2 (±2.3)	34.4 (±7.5)	11.4 (±1)	17.4 (±1.2)

Glass	LST 30	19.9 (±2.3)	54.8 (±6.6)	19.1 (±0.7)	8.8 (±1.4)	16.1 (±1.7)
SS304 mirror finish	Water	68.5 (±0.3)	95.2 (±1.5)	69.8 (±13)	14.4 (±0.5)	19.1 (±0.3)
SS304 mirror finish	Diiodo-methane	61.0 (±7.9)	86.2 (±0.9)	7.3 (±1.8)	12.6 (±0.9)	18.3 (±0.7)
SS304 mirror finish	LST 50	67.0 (±0.7)	90.7 (±1.3)	28.5 (±0.9)	11.8 (±1.1)	16.9 (±1.1)
SS304 mirror finish	LST 30	24.0 (±0.6)	68.4 (±4.4)	26.4 (±1.2)	9.2 (±1.4)	16.4 (±1.1)
SS304 2B finish	Water	57.4 (±2.6)	87.1 (±3.2)	79.9 (±0.1)	8.9 (±0.3)	13.9 (±0.2)
SS304 2B finish	Diiodo-methane	20.9 (±3.5)	79.5 (±7.7)	10.7 (±1.9)	8.2 (±0.7)	16.2 (±1.8)
SS304 2B finish	LST 50	48.6 (±2)	91.6 (±3.7)	64.5 (±5.9)	11.5 (±0.2)	17 (±0.2)
SS304 2B finish	LST 30	20.0 (±2.0)	115.2 (±5)	25.9 (±2.6)	8.2 (±0.2)	15.9 (±0.1)
Grit 100	Water	60.1 (±6.5)	91.9 (±6.8)	79.6 (±0.5)	10 (±0.6)	15.2 (±0.7)
Grit 100	Diiodo-methane	18.9 (±0.6)	93.6 (±10.3)	17.9 (±0.8)	9.4 (±0)	16.5 (±0.3)
Grit 100	LST 50	42.7 (±3.5)	85.8 (±3.7)	80 (±0)	10.2 (±0.6)	15.6 (±0.6)
Grit 100	LST 30	17.1 (±1.9)	103.9 (±16.6)	23.3 (±1.9)	9.1 (±1.5)	16.8 (±1.4)
Grit 60	Water	77.9 (±2)	104.4 (±3.5)	78.9 (±1.6)	9.9 (±0.2)	14.6 (±0.1)
Grit 60	Diiodo-methane	42.8 (±29.3)	96.1 (±18.2)	18 (±2.8)	9 (±0.3)	15.3 (±0.8)
Grit 60	LST 50	16.7 (±1.9)	101.2 (±5.5)	20.1 (±1.2)	6.8 (±2.5)	14.7 (±3)

Grit 60	LST 30	58.2 (±2.1)	98.2 (±2.1)	80 (±0)	10.1 (±0.7)	14.9 (±0.7)
Grit 36	Water	77.2 (±2.5)	106.6 (±3)	79.4 (±0.8)	10.6 (±0.3)	14.9 (±0.3)
Grit 36	Diiodo-methane	36.3 (±0.2)	79.4 (±23.7)	31 (±12.1)	12.5 (±5.2)	16.9 (±2.8)
Grit 36	LST 50	35.4 (±3.2)	110.9 (±6.5)	70.1 (±16.7)	11.3 (±0.8)	17.1 (±0.3)
Grit 36	LST 30	57.3 (±9.6)	97.6 (±6.3)	80 (±0)	10.2 (±0.5)	15.1 (±0.4)

Table 9-3 Roll - off data for Avalon Glass

Substrate	**Probe Liquid**	**CA [R] (º)**	**CA [A] (º)**	**Tilt (º)**	**Contact Point [R] (mm)**	**Contact Point [A] (mm)**
Glass	Water	93.7 (±3.3)	112.6 (±4.5)	66.1 (±12.3)	12.5 (±1.8)	16.4 (±2)
Glass	Diiodo-methane	88.2 (±4.5)	116.0 (±1.9)	11.5 (±2.8)	9 (±0.4)	14.3 (±1.3)
Glass	LST 50	58.6 (±6.1)	91.5 (±9.6)	31.2 (±6.0)	9.3 (±0.1)	14.8 (±0.1)
Glass	LST 30	27.5 (±2.5)	71.1 (±4.7)	28 (±3.2)	9.8 (±1.0)	16.4 (±0.8)
SS304 mirror finish	Water	84.2 (±2.3)	107.1 (±4.5)	62.5 (±15.7)	12.8 (±2.0)	17 (±1.9)
SS304 mirror finish	Diiodo-methane	52.1 (±24.0)	101.1 (±16.1)	15.1 (±11.7)	11.7 (±1.9)	17.8 (±2.0)
SS304 mirror finish	LST 50	49.1 (±0.5)	81.6 (±0.6)	23.1 (±0.6)	13.2 (±0.4)	19.1 (±0.5)
SS304 mirror finish	LST 30	25.2 (±1.9)	72.0 (±5.4)	26.5 (±1.4)	9 (±0.5)	16.2 (±0.2)

SS304 2B finish	Water	91.1 (±6.0)	115.0 (±4.9)	78.8 (±1.2)	10.8 (±0.4)	14.6 (±0.2)
SS304 2B finish	Diiodo-methane	79.0 (±9.7)	116.3 (±6.4)	15.3 (±2.8)	9.2 (±1.1)	14.2 (±1)
SS304 2B finish	LST 50	48.3 (±6.6)	92.4 (±4)	42 (±5.3)	11.7 (±1.5)	17.3 (±2)
SS304 2B finish	LST 30	27.7 (±2.7)	76.1 (±0.6)	33.5 (±1.5)	8.5 (±1.5)	15.2 (±1.6)
Grit 100	Water	93.0 (±10.9)	115.4 (±11.6)	72.7 (±12.6)	11.6 (±0.1)	15.5 (±0.5)
Grit 100	Diiodo-methane	44.5 (±15.3)	103.3 (±13.3)	19.9 (±11.3)	11.6 (±2)	17.9 (±1.6)
Grit 100	LST 50	56.1 (±6.5)	106.9 (±3.3)	79.8 (±0.2)	10.5 (±0.2)	15.2 (±0.4)
Grit 100	LST 30	27.7 (±0.9)	115.0 (±8.7)	45 (±1.4)	9.7 (±2.1)	16.5 (±2)
Grit 60	Water	95.8 (±10.1)	117.5 (±7.9)	50.0 (±0.0)	9.7 (±0.2)	13.4 (±0.5)
Grit 60	Diiodo-methane	24.4 (±4.6)	109.0 (±21.3)	23.0 (±2.9)	9.8 (±0.6)	16.6 (±1.1)
Grit 60	LST 50	51.5 (±21.5)	95.7 (±17.5)	64.1 (±27.1)	9.7 (±0.4)	14.8 (±1.9)
Grit 60	LST 30	27.7 (±0.7)	109.3 (±5.1)	49.2 (±2.4)	10.7 (±0.4)	17.1 (±0.3)
Grit 36	Water	95.0 (±4.4)	125.4 (±1.2)	79.5 (±0.2)	10.6 (±0.1)	14.2 (±0.3)
Grit 36	Diiodo-methane	37.1 (±1.9)	113.7 (±1.9)	23.8 (±0.1)	9.3 (±0.6)	15.5 (±0.4)
Grit 36	LST 50	60.7 (±6.0)	108.2 (±3.8)	80.0 (±0.0)	9.5 (±0.5)	13.9 (±0.7)
Grit 36	LST 30	30.2 (±1.8)	116.5 (±3.3)	47.5 (±3.7)	7.9 (±0.5)	14.8 (±0.6)

Table 9-4 Roll - off data for Sapphire

Substrate	Probe Liquid	CA [R] (º)	CA [A] (º)	Tilt (º)	Contact Point [R] (mm)	Contact Point [A] (mm)
Glass	Water	91.7 (±2.8)	108.9 (±1.8)	55.0 (±4.9)	13.9 (±1.1)	17.9 (±1.2)
Glass	Diiodo-methane	81.9 (±26)	113.5 (±11.3)	13.5 (±3.3)	10.0 (±2.1)	14.8 (±2.3)
Glass	LST 50	53.0 (±0.8)	75.8 (±1.8)	20.4 (±1.4)	11.4 (±0.8)	16.9 (±0.9)
Glass	LST 30	52.7 (±4.5)	81.2 (±2.5)	17.5 (±0.1)	11.6 (±0.9)	17.7 (±0.7)
SS304 mirror finish	Water	92.2 (±2.8)	109.7 (±0.9)	46.2 (±7.1)	13.9 (±0.5)	17.9 (±0.5)
SS304 mirror finish	Diiodo-methane	104.7 (±17.1)	128.2 (±8.1)	13.5 (±1.4)	10.2 (±0.5)	15.1 (±1.1)
SS304 mirror finish	LST 50	45.1 (±1.1)	88.2 (±0.9)	80.0 (±0.0)	10.4 (±0.3)	16.0 (±0.3)
SS304 mirror finish	LST 30	52.3 (±1.3)	80.3 (±1.0)	23.4 (±0.6)	12.7 (±0.8)	18.3 (±0.8)
SS304 2B finish	Water	78.4 (±7.6)	102.0 (±7.2)	55.2 (±5.8)	12.4 (±2.2)	17.0 (±2.6)
SS304 2B finish	Diiodo-methane	39.5 (±14.4)	90.7 (±3.9)	14.6 (±6.1)	9.9 (±1.1)	16.3 (±0.9)
SS304 2B finish	LST 50	57.3 (±14.4)	94.0 (±10.6)	46.8 (±26.4)	14.2 (±0.2)	19.4 (±0.5)
SS304 2B finish	LST 30	27 (±2.7)	64.4 (±1.2)	23.1 (±1.1)	11.5 (±1.0)	18.3 (±0.9)
Grit 100	Water	85.9 (±11.5)	110.1 (±11.9)	71.3 (±14.9)	12.4 (±1.4)	16.7 (±1.9)
Grit 100	Diiodo-methane	33.3 (±14.7)	105.1 (±16.3)	22.5 (±11.0)	10.2 (±0.8)	17.0 (±1.2)

Grit 100	LST 50	52.0 (±12.0)	88.0 (±0.8)	63.9 (±27.9)	11.6 (±2.1)	16.9 (±1.7)
Grit 100	LST 30	43.4 (±10.7)	102.1 (±11.9)	71.1 (±15.5)	10.1 (±0.6)	15.8 (±1.4)
Grit 60	Water	76.3 (±45.4)	103.1 (±32.2)	42.6 (±12.9)	10.0 (±0.2)	14.7 (±2.0)
Grit 60	Diiodo-methane	46.1 (±41.6)	110.9 (±9.1)	41.6 (±33.3)	9.4 (±1.9)	15.6 (±0.1)
Grit 60	LST 50	28.7 (±0.7)	115.2 (±1.8)	47.6 (±2.5)	10.6 (±0.3)	17.4 (±0.5)
Grit 60	LST 30	25.2 (±1.3)	117.5 (±16.7)	39.2 (±1.9)	10.5 (±1.4)	17.2 (±1.5)
Grit 36	Water	93.9 (±0.4)	115.1 (±1.1)	50.0 (±0.0)	9.6 (±0.4)	13.4 (±0.5)
Grit 36	Diiodo-methane	21.0 (±1.1)	119.3 (±16.4)	20.8 (±2.0)	9.1 (±1.1)	16.8 (±1.1)
Grit 36	LST 50	65.0 (±3.2)	98.7 (±3.5)	80.0 (±0.0)	8.8 (±1.6)	13.2 (±1.5)
Grit 36	LST 30	28.0 (±1.6)	100.2 (±16.5)	55.0 (±9.8)	11.0 (±3.1)	16.7 (±3.4)

Table 9-5 Roll - off data for Sivo EC

Substrate	**Probe Liquid**	**CA [R] (º)**	**CA [A] (º)**	**Tilt (º)**	**Contact Point [R] (mm)**	**Contact Point [A] (mm)**
Glass	Water	87.1 (±3.1)	107.6 (±1.5)	45.2 (±7.0)	12.8 (±0.3)	17 (±0.2)
Glass	Diiodo-methane	76.9 (±5.4)	100.1 (±1.0)	9.7 (±2.1)	9.1 (±0.3)	14.1 (±0.4)
Glass	LST 50	32.3 (±7.4)	80.4 (±10.0)	30.2 (±5.7)	11.9 (±1.5)	18.4 (±1.5)
Glass	LST 30	32.0 (±1.4)	73.1 (±5.4)	24.9 (±1.2)	12.1 (±0.7)	18.8 (±0.8)

SS304 mirror finish	Water	73.5 (±28.1)	112.3 (±4.1)	62.3 (±30.6)	12.8 (±2.1)	17.5 (±1.5)
SS304 mirror finish	Diiodo-methane	69.5 (±22.5)	102.6 (±12.7)	34.0 (±39.9)	9.7 (±0.9)	15.1 (±0.9)
SS304 mirror finish	LST 50	54.7 (±1.9)	84.5 (±9.1)	36.1 (±14.6)	12.3 (±2.0)	17.6 (±2.0)
SS304 mirror finish	LST 30	45.1 (±2.9)	83.2 (±2.4)	31.1 (±2.7)	12.0 (±0.3)	17.9 (±0.5)
SS304 2B finish	Water	84.0 (±3.4)	112.2 (±2.1)	79.7 (±0.6)	10.0 (±1.9)	13.9 (±2.3)
SS304 2B finish	Diiodo-methane	36.6 (±14.3)	109.7 (±1.5)	19.1 (±7.2)	9.1 (±1.3)	15.7 (±2.1)
SS304 2B finish	LST 50	41.9 (±1.7)	105.3 (±1.3)	77.4 (±0.1)	14.1 (±0.4)	19.5 (±0.6)
SS304 2B finish	LST 30	38.2 (±7.2)	84.1 (±4.9)	35.3 (±3.5)	9.2 (±0.7)	15.4 (±0.9)
Grit 100	Water	97.7 (±12.1)	124.2 (±6.9)	80.0 (±0.0)	10.7 (±1.7)	14.4 (±1.7)
Grit 100	Diiodo-methane	40.9 (±0.7)	115.5 (±1.8)	25.6 (±4.1)	9.9 (±1.8)	15.9 (±1.9)
Grit 100	LST 50	45.4 (±6.5)	103.2 (±1.6)	77.2 (±2.7)	11.8 (±1.7)	17.1 (±1.7)
Grit 100	LST 30	59.6 (±22.7)	117.5 (±5.8)	79.9 (±0.1)	10.3 (±1.1)	15.1 (±2.0)
Grit 60	Water	46.8 (±7.2)	90.8 (±5.8)	65.6 (±25)	11.1 (±0.2)	16.2 (±0.4)
Grit 60	Diiodo-methane	48.0 (±17.8)	116.2 (±4.4)	26.4 (±1.9)	9.9 (±0.5)	15.4 (±1.4)
Grit 60	LST 50	38.0 (±0.5)	116.1 (±6.8)	80.0 (±0.0)	11.6 (±1.7)	17.1 (±1.8)
Grit 60	LST 30	35.4 (±0.7)	102.7 (±5.1)	78.2 (±1.9)	10.0 (±1.0)	15.0 (±1.3)

Grit 36	Water	83.3 (±8.1)	115.0 (±2.4)	80.0 (±0.0)	7.5 (±2.3)	11.3 (±2.6)
Grit 36	Diiodo-methane	45.7 (±11.9)	116.7 (±1.7)	22.9 (±2.5)	9.4 (±0.0)	15.6 (±1.0)
Grit 36	LST 50	45.1 (±4.2)	95.0 (±2.8)	79.9 (±0.1)	11.3 (±0.1)	16.3 (±0.1)
Grit 36	LST 30	42.4 (±0.9)	109.0 (±4.9)	79.0 (±1.0)	9.4 (±0.0)	14.4 (±0.1)